Report on hydrological and physical quantities under climate change scenarios within the cooperation area

Activity 4.1

Deliverable 4.1.1

Delivery date: 30 April 2020

Version 2.0

DELIVERABLE 4.1.1

PROJECT CHANGE WE CARE

https://www.italy-croatia.eu/web/changewecare

Work Package:	WP4
Activity:	4.1
Phase Leader:	CNR-ISMAR
Deliverable:	4.1.1: Report on hydrological and physical quantities under climate change scenarios within the cooperation area. The document will provide a prediction of the hydrological and hydrodynamic drivers of the coastal processes in the cooperation area. The first part will provide the generally accepted climate change forcings provided by coarse resolution climate models. A second step will focus on regional downscaling of such data, addressing and including more specifically local aspects (e.g. the influence of local winds in driving the circulation, the Relative Sea Level Rise effects, the change in fluxes within transitional areas and open-sea regions, the possibilities of detecting salt water intrusions) that are usually neglected at global scale. Based on these results, some indications will be drawn for the Coastal Zoning of hydrological hot spots, to be considered in the definition of the planning options envisaged in WP5.

Version:	Draft/Final 2.0	Date:	31 July 2020
Type:	Report		
Availability:	Public		
Responsible Partner:	CNR-ISMAR		
Editor:	Fabio Raicich		
Contributors:	Debora Bellafiore, Davide Bonaldo, Christian Marasmi, Roberto Montanari, Fabio Raicich, Antonio Ricchi, Ivica Vilibić, Mili Novak, Srećko Radnić, Jure Margeta, Dijana Vrdoljak, Jelena Borota		

CONTENTS

1. FOREWORD

This document has been produced in the framework of the INTERREG Italy – Croatia CHANGE WE CARE Project. CHANGE WE CARE fosters concerted and coordinated climate adaptation actions at transboundary level, tested in specific and representative pilot sites, exploring climate risks faced by coastal and transitional areas contributing to a better understanding of the impact of climate variability and change on water regimes, salt intrusion, tourism, biodiversity and agro-ecosystems affecting the cooperation area. The main goal of the Project is to deliver integrated, ecosystem-based and shared planning options for different problems related to climate change (CC), together with adaptation measures for vulnerable areas, to decision makers and coastal communities. Additional information and updates on the CHANGE WE CARE can be found at https://www.italy-croatia.eu/web/changewecare.

Chapter 5 “Applications at the Pilot Site scale” only includes the contribution by ISMAR about Po Delta and by RERA about Jadro River and Kaštela Bay. Originally, contributions were also planned about the Neretva River Delta, Vran Lake, and Banco della Mula di Muggia. Unfortunately, these tasks could not be accomplished due to disruptive consequences for the work organization of the COVID-19 pandemy.

2. INTRODUCTION

The Mediterranean region is affected by interactions between mid-latitude processes occurring in central Europe and the eastern Atlantic, and tropical processes taking place in northern Africa and the Middle East. Because it lies in a transition area between such different climates, the Mediterranean turns out to be very sensitive to even minor modifications of the general atmospheric circulation. As a consequence, the Mediterranean region is potentially highly vulnerable to climatic changes, and it has been identified as a "Hot-Spot" in future climate change projections.

The Mediterranean Sea is only connected to the Atlantic Ocean by the narrow Strait of Gibraltar and is mostly surrounded by the large continental masses of Eurasia and Africa. The basin depth is quite large, namely about 1500 m on average, but up to over 5000 m in the Ionian basin, however, large shallow areas can be found, as is the case of the northern Adriatic Sea and the Gulf of Gabés in Tunisia. These facts together with the complex orography of the Mediterranean coasts, that affects the surface atmospheric circulation on the basin, lead to complex ocean dynamics that is characterized by a strong mesoscale activity. Moreover, the Gulf of Lyons and the Adriatic Sea are also characterized by deep water formation, induced by large heat losses occurring during cold air bursts connected with Mistral and Bora, respectively.

Future climate projections indicate that the Mediterranean region will experience warmer and drier conditions over compared to the past century, with higher evaporation and lower precipitation, which will likely result in higher salinity and temperature. Important effects can be expected on the amount and location of the deep water formation, the mean sea level and the ecosystems.

The present report describes the activity performed in WP4 to address the effects of climate change on hydrological and hydrodynamic processes at the Adriatic basin scale and in Pilot Sites. This will be achieved by means of dedicated numerical modelling tools, calibrated on the data collected and shared in WP3 activities, and properly downscaled to the spatial resolution required for the describing the physical dynamics relevant for the Pilot Sites. Modelling efforts will be particularly focused at characterising the intensity and variability of storm events in terms of wave parameters and surge (Section 3), the modulation of freshwater runoff, and the implications of climate change for the main thermohaline dynamics of the basin (Chapter 4), with some focus on the evolution of the main quantities at the Pilot Sites. Chapter 5 on "Applications at the Pilot Site scale" provides a high-resolution numerical modelling study on the Po Delta.

3. WAVE AND STORM DYNAMICS IN A CLIMATE CHANGE SCENARIO

3.1. MULTI-DECADAL WAVE MODELLING (ISMAR)

Due to the strong anthropic pressure acting on coastal regions, these are often strongly exposed to the effects of climate change on the sea and on the meteo-oceanic dynamics. Modifications in the drivers of coastal processes and in their interactions can trigger irreversible changes, particularly in transitional environments, with a potentially severe loss of landscape and ecological diversity. Besides sea level rise, wave climate and its variations can play an important role in controlling coastal dynamics and possibly affecting the stability of the coasts and the safety of the infrastructures. Most of the available tools supporting coastal management and risk assessment are based on information on the wave climate, with variable resolution and coverage requirements depending on the scope of the study. In the perspective of a multidisciplinary approach to coastal evolution in climate change conditions, increasing efforts are undertaken in order to integrate the description of nearshore hydrodynamics with evidences or projections from geological analyses. Climate simulations for the characterization of marine dynamics are made possible by the increasing computational power and multi-decadal observational records availability, and wave climate projections are available, sometimes publicly, at the regional scale. Nonetheless, coastal processes and their spatial patterns in basins characterized by complex geography and orography may undergo significant modifications in response to long-term wind regime variations (Soomere et al., 2015). In this case, dedicated high-resolution modelling efforts can be necessary in order to properly account for the spatial variability of the processes and their drivers.

Regional scale climate projections in the Mediterranean area are generally in agreement in suggesting a northbound migration of the “storm belt” (Trenberth et al., 2003; Giorgi and Lionello, 2008) and a consequent reduction of the storminess in the basin (Marcos et al., 2011; Conte e Lionello, 2013), although with spatially variable implications in terms of wave and storm surge hazard. In the Adriatic Sea this tendency has been overall confirmed by wave model downscaling experiments (Benetazzo et al., 2012), but the lack of suitable atmospheric fields (that is, capable to reproduce the directional properties of wind regime in the region) when that study was carried out (Bellafiore et al., 2012) limited the capability of drawing conclusions about the spatial patterns of climate change impacts. In fact, the elongated shape of the basin and the presence of mountain ridges along the coasts pose some rather strict requirements on the quality and resolution of the atmospheric fields to be used as forcing for ocean modelling applications (Signell et al., 2005). In the Northern Adriatic, marine dynamics are generally controlled by a warm and humid southeasterly wind (locally known as “Sirocco”) and jets of northeasterly wind (called “Bora”) blowing from the orographic gaps in the mountains surrounding the eastern coast. While Sirocco storms in the Adriatic Sea are generally associated with the eastward transit of an atmospheric minimum across the Mediterranean basin (Lionello et al., 2012a), Bora events can occur with different characteristics and names in response to two different synoptic conditions. “Clear” Bora, so called due to the clear sky generally associated with this condition, takes place in the presence of an intense and persistent

anticyclone over central-eastern Europe and blows cold and dry gusts across the basin. “Dark” Bora, associated with cloudiness and sometimes intense precipitation, occurs in the presence of cyclonic conditions in the Mediterranean region, with Sirocco blowing along the southern and central Adriatic basin (Horvath et al., 2009).

Recent improvements in climate models capability to resolve relatively small-scale features governing metocean processes in the Adriatic Sea provide new opportunities for the investigation of climate impacts on this area at an unprecedented level of insight. In this section we present the result of a work aiming at an analysis of the wave regime along the Adriatic coast in a severe climate change scenario, focusing on the projections offshore of the CHANGE WE CARE Pilot Sites. The ground for this study was set in the framework of National (RITMARE National Flagship initiative, funded by the Italian Ministry of Education, University and Research - IV Phase, Line 5, “Coastal Erosion and Vulnerability”) and International (CEASELESS, UE H2020 programme, grant agreement No. 730030) projects and brought to full ripeness within CHANGE WE CARE, ending up in the publication of a paper on International Journal of Climatology (Bonaldo et al., 2020).

3.1.1. Model implementation

This work is based on the implementation of a couple of climatological runs in control (CTR run, 1971-2000) conditions and in a climate change scenario (SCE run 2071-2100) referred to the IPCC Representative Concentration Pathway 8.5. The former has been used for evaluating the model capability in reproducing the wave climatological features of the basin, whereas the latter provides some indications about the possible variations of the properties. To this aim, it is worth recalling a fundamental methodological difference between climate modelling and short-term forecast modelling (and, even more, hindcast analysis). Whilst short-term forecast model runs are strongly controlled by available data ingested as initial conditions and assimilated during the simulation, climate models in future scenarios are driven by global projections of atmospheric and ocean bulk properties, due to the obvious lack of observational data. In order to allow the evaluation of the model performances and assess the reliability of future projections, control runs are designed to be consistent with the scenario simulations, and are therefore driven by the same kind of input even if observed data are actually available. For this reason, control simulations should not be expected to precisely reproduce really occurred events or exhibit skills comparable with operational forecast or hindcast analyses, but their results should instead be considered in statistical terms.

The model simulations have been carried out by using the SWAN (Simulating Waves Nearshore, Booij et al., 1999) modelling system, with a curvilinear orthogonal structured grid domain discretization and a horizontal resolution ranging from approximately 2 km in the northwest to nearly 10 km in the southeastern end of the domain (Figure 3.1). This configuration is the result of a compromise between the competing needs for spatial detail and computational affordability. A finer resolution in the northern Adriatic Sea allows to maximize the outreach of the experiment in a region characterized by low-lying morphology and severe exposure to coastal erosion and flooding. SWAN provides a phase-averaged

description of the seas states by reproducing wave generation, evolution and dissipation in terms of wave action density spectra, from which bulk parameters such as significant wave height, wave periods, and wave directions are derived and produced as model output. In the present implementation, the frequency domain has been divided into 25 values, logarithmically distributed between 0.05 and 0.5 Hz, and 36

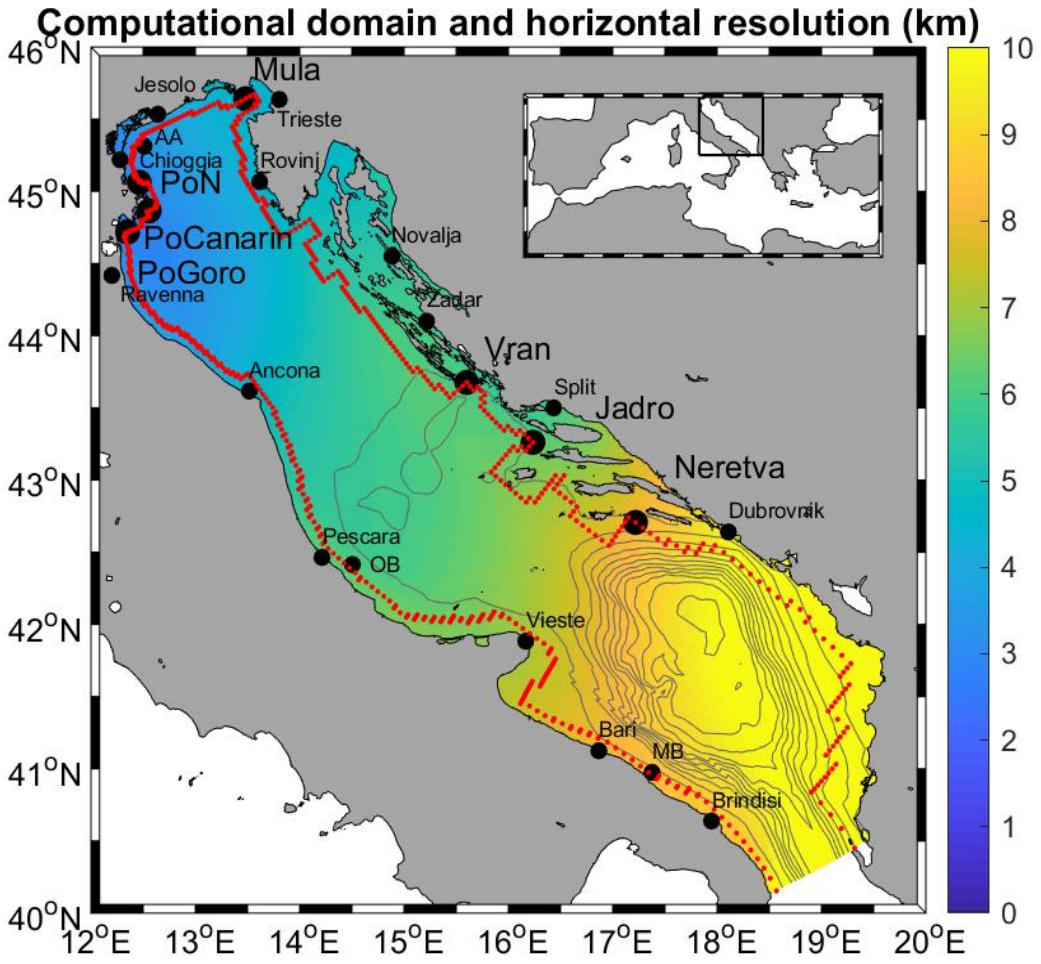

Figure 3.1: Geographical framework of the present study: Adriatic Sea and its position within the Mediterranean Basin. Contour lines represent 100-m spaced isobaths, colour pattern represents the dimension of the horizontal grid step, and red dots highlight the position of the points where spectra have been saved and nearshore wave statistics have been computed. Small black dots show the position of the main coastal cities as well as the observatories used for model validation, namely Acqua Alta oceanographic tower (AA), Ortona Buoy (OB), and Monopoli Buoy (MB), and large black dots represent the locations offshore of the pilot sites in which the wave parameters time series have been extracted and made available.

directional sectors. The bathymetry has been obtained by merging and resampling the available information, including large sectors of high-resolution multibeam data collected in the last decade. In order to take into account for the possible sea level rise in a RCP 8.5 climate change scenario, water depth

in SCE run has been uniformly enhanced by 0.70 m, based on the estimates provided by Antonioli et al. (2017) and on the argument that, due to the peculiar properties of the Mediterranean basin (evaporation basin characteristics, hydraulic control at Gibraltar Strait) relative sea level rise in this region should be smaller than the values envisaged by global estimates. The model simulations were forced by 6-hourly wind fields from a high-resolution implementation of the Regional Climate Model COSMO-CLM (Rockel et al., 2008; Bucchignani et al., 2016, the climate version of the operational weather forecast model COSMO-LM (Steppeler et al., 2003) with 8-km horizontal resolution over Italy and its marine regions. The wind fields, validated against observed data along the Italian Adriatic coast, have shown particularly good performances in the directional description of the wind regime (Bonaldo et al., 2017). The wave model has been provided at the same 6-hourly interval as the wind fields: this time resolution might be to some extent coarse for a detailed description of the storm peaks (particularly in the case of wind sea states), but seems nonetheless suitable for climatological considerations. In the absence of a wave modelling climate dataset at the Mediterranean scale forced by COSMO-CLM, no incoming waves have been prescribed at the southern boundary (Otranto strait), whereas outwards energy radiation is permitted. Given the importance of Sirocco in the wave climate of the Adriatic Sea, this assumption is acceptable outside of a buffer zone of approximately 100-200 km from the southern boundary, that is where the sea state becomes fully developed thus ceasing to be fetch-limited. Bulk parameters were extracted in all the grid points, whereas full spectra were saved on approximately 600 points along the coast, in order to have a more complete description of the wave climate impacting the littoral zone. The CTR simulation was validated against data from three observatories along the Italian coast, namely the Acqua Alta oceanographic tower (AA, 12.51 °E, 45.31 °N, Northern Adriatic), and the coastal buoys of Ortona (OB, 14.51 °E, 42.42 °N, Central Adriatic) and Monopoli (MB, 17.38 °E, 40.98 °N, Southern Adriatic). The latter is also particularly useful for controlling the impact of the assumptions concerning the boundary conditions. Available data from AA span a period longer than 30 years (1979-2017, see Pomaro et al., 2018), whereas data from OB and MB bracket respectively the periods 1989-1995 and 1989-2008. In order to compare time series referred to the same period and be consistent with the climatological framework, for each station only the data overlapping the period of the CTR simulations were considered, with the additional requirement of exhibiting a reasonable continuity throughout the year.

Time series of selected quantities offshore of the Pilot Sites are available from the Project Owncloud repository at https://owncloud.ve.ismar.cnr.it/owncloud/index.php/s/efj6wcDhi2Y9D4u, and other fields are available on request by contacting davide.bonaldo@ve.ismar.cnr.it

3.1.2. Wave model validation

Significant wave height (H_s) climatological statistics observed at AA (Figure 3.2) appear reasonably well reproduced in ordinary conditions (50th percentile) as well as in the case of moderate to severe sea states (90th percentile and beyond), in terms of both absolute bias and seasonal variability. The gap between model and measurements is generally smaller than 20 cm, mostly underestimating the values in the second half of the year, and only increases in the case of January and December intense storms (99th

percentile). This discrepancy is partially reverted at OB (Figure 3.1), where the model validation (although based on a shorter observation period) suggests a model overestimate of storm severity and a small underestimate in summer ordinary and intermediate conditions (50th and 75th percentiles). Apparently unexpectedly considering the relative proximity to the southern boundary, MB (Figure 3.2) exhibits a significant overestimate of H_s, rapidly increasing for significant wave height values exceeding 1 m. Some deeper insight on the possible reasons beneath the model shortcomings is provided, alongside an assessment of the directional skills of the model, by Figure 3.3. At AA, model results show a satisfactory statistical description of the Sirocco events, although missing the exceptional peaks (H_s greater than 5 m),

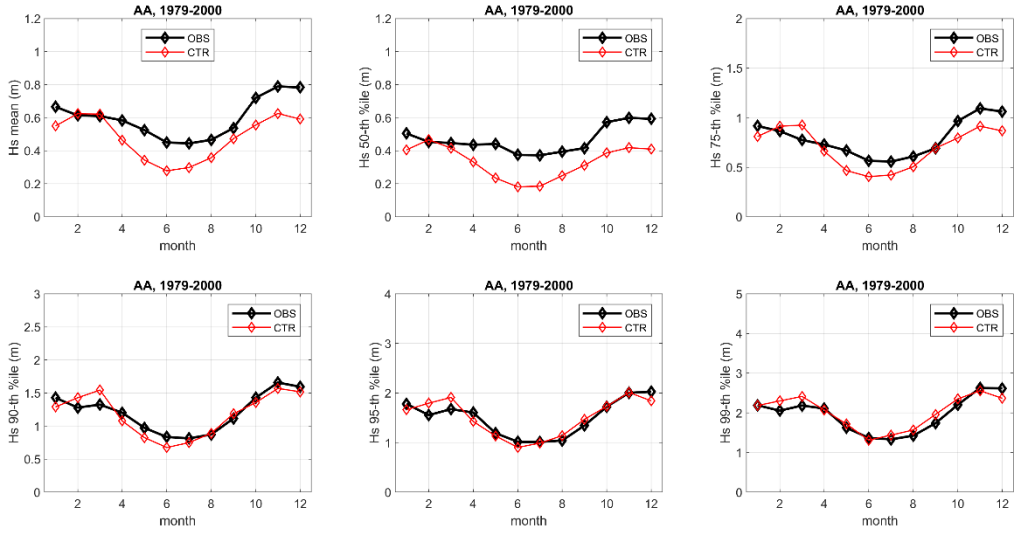

Figure 3.2: Observed (OBS) and modelled (CTR) significant wave height climatological mean and percentile distributions at Acqua Alta oceanographic tower (AA). Adapted from Bonaldo et al., 2020.

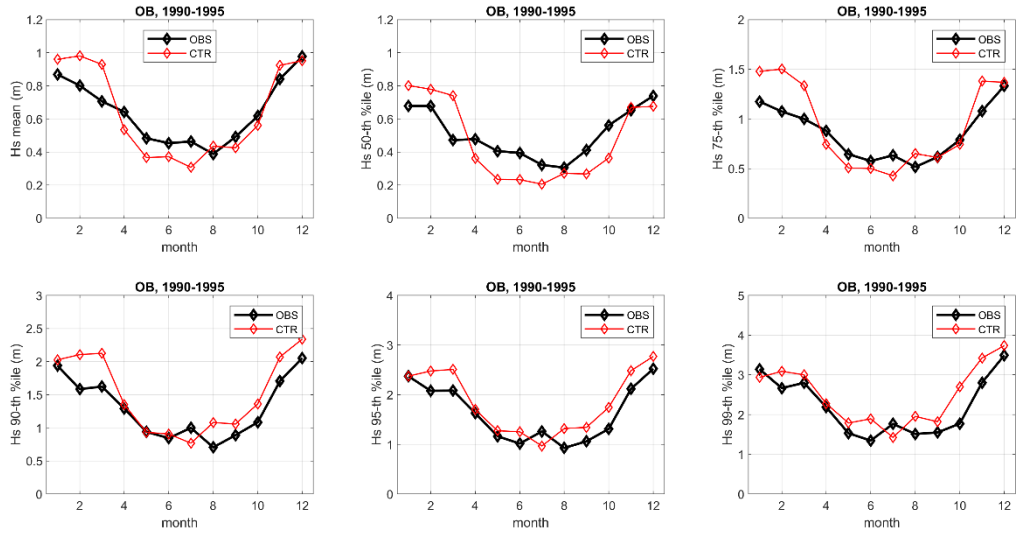

Figure 3.1: Observed (OBS) and modelled (CTR) significant wave height climatological mean and percentile distributions at Ortona Buoy (OB). Adapted from Bonaldo et al., 2020.

whereas Bora events with occurrence frequency around a few percent units seem only partially reproduced, probably explaining part of the underestimate found in Figure 3.2. Once again, the tendency is not particularly marked at OB, with the only exception of some H_s overestimate associated with sea states from the northerly sectors. At MB, the occurrence of storms with H_s greater than 1 m appears overestimated along most of the sectors. These evidences should be considered in the light of the known properties and limitations of the wind fields used as forcing for the wave model runs. In the analysis of

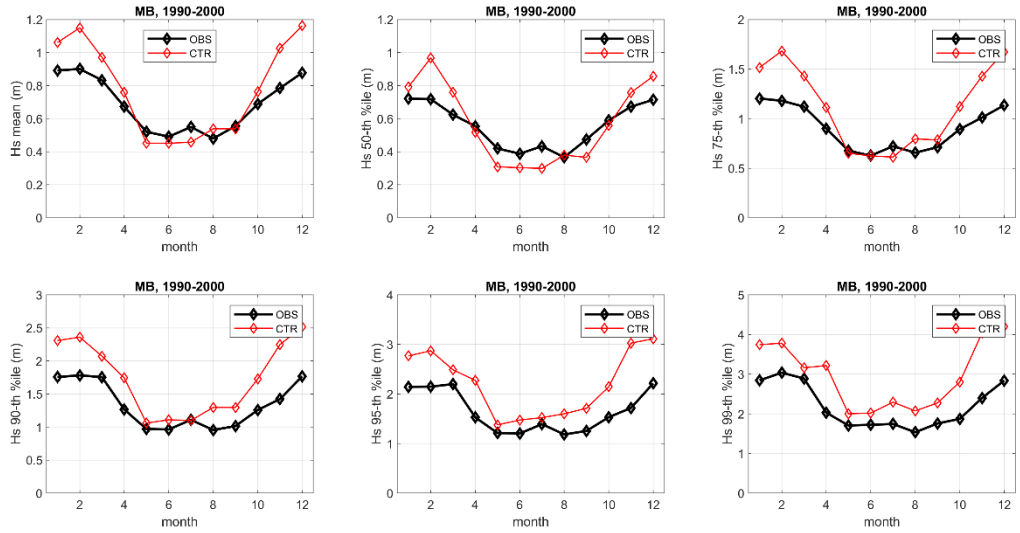

Figure 3.2: Observed (OBS) and modelled (CTR) significant wave height climatological mean and percentile distributions at Monopoli Buoy (MB). Adapted from Bonaldo et al., 2020.

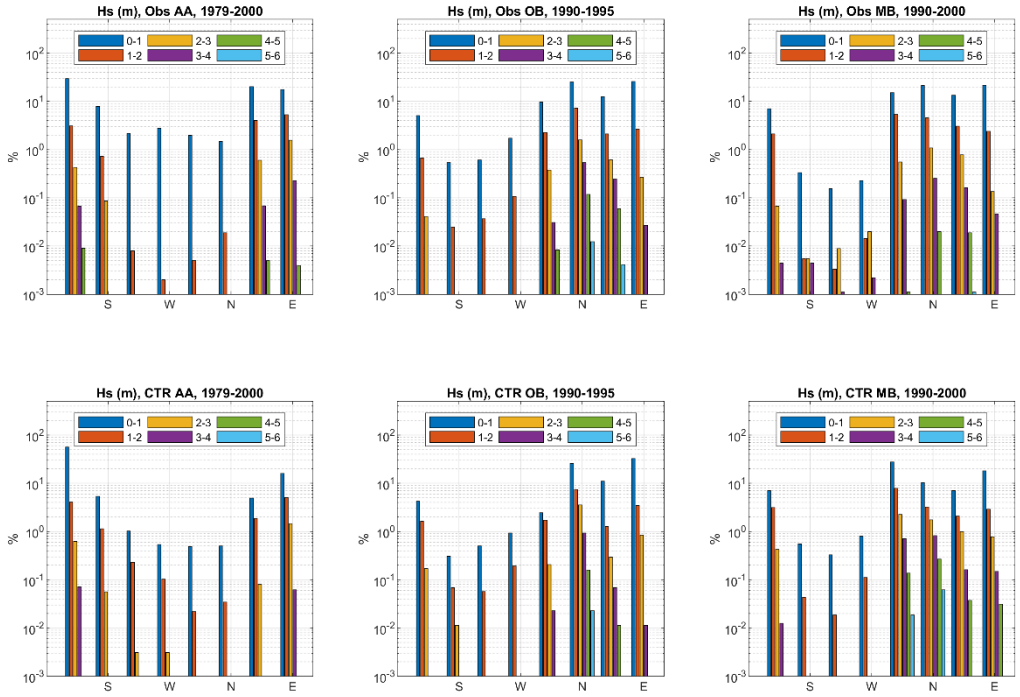

Figure 3.3: Observed (OBS) and modelled (CTR) directional distribution and frequency of significant wave heights (six classes) at Acqua Alta oceanographic tower (AA), Ortona Buoy (OB) and Monopoli Buoy (MB).

the wind fields produced by COSMO-CLM, Bonaldo et al. (2017) showed a generalized tendency toward an overall overestimate of the wind energy throughout the basin, most likely causing an artifact

intensification of sea states forced by dominant winds. In the case of the Northern Adriatic this can be partially masked, in the case of Sirocco and Bora wind seas, respectively by the prescriptions at the southern boundary and by the relatively long output time step and by an incomplete description of the orographic effects along the eastern coast. In turn, in the central and southern regions where northwesterly storms are more relevant and the fetch is long, this effect is completely visible.

3.1.3. Future Projections

3.1.3.1. Basin-scale picture

The basin-scale patterns of mean (Figure 3.4) and extreme (99 percentile, Figure 3.5) H_s as well as their variations in a RCP 8.5 climate change scenario exhibit a relevant directional modulation. Bora sea states (NE) will be on average characterized by a generalized and statistically significant decrease of mean and extreme H_s respectively on the order of 10 and 40 cm throughout the whole Adriatic Sea, and particularly along the axes of the wind jets. No significant variation is expected for mean Sirocco (SE) sea states,

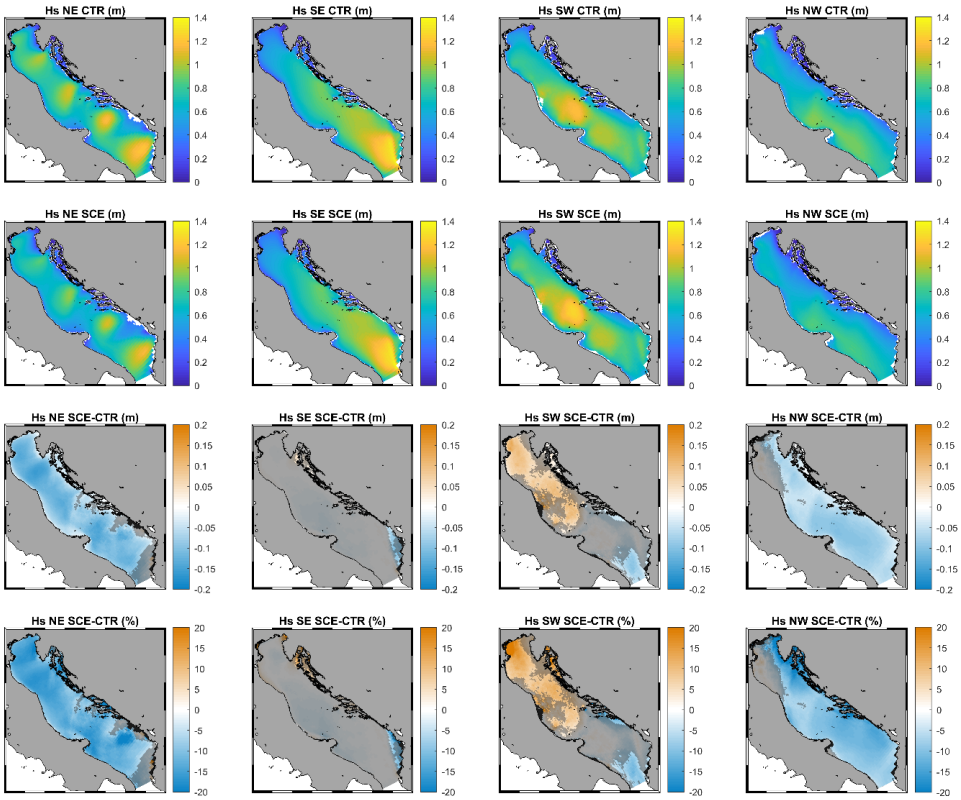

Figure 3.4: Mean directional H_s patterns in the Adriatic Sea and their projected absolute and relative variations. Areas with statistically non-significant variations are shaded in gray (adapted from Bonaldo et al., 2020).

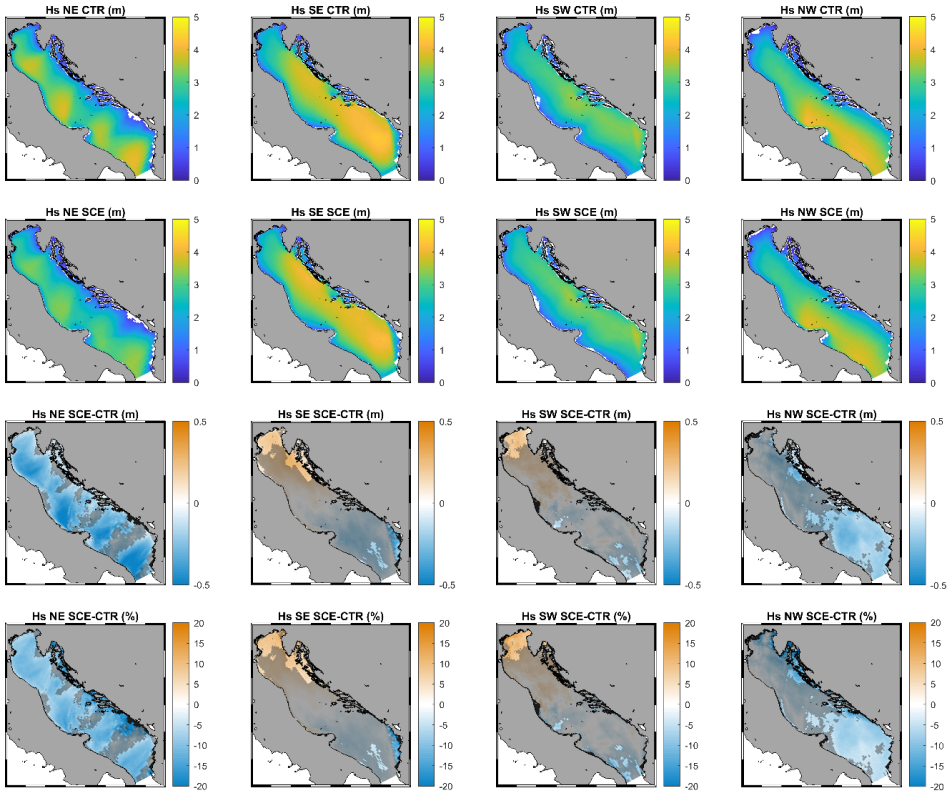

Figure 3.5: 99 percentile directional Hs patterns in the Adriatic Sea and their projected absolute and relative variations. Areas with statistically non-significant variations are shaded in gray (adapted from Bonaldo et al., 2020).

whereas the picture in the case of stormy conditions is more heterogeneous, with a 10% increase in the northern part of the basin (which means approximately 25 cm) and no statistically significant signal in the south. Predicted variations in H_s values associated with southwesterly winds blowing from the Italian peninsular mainland (quite uncommon, see Bonaldo et al., 2017) are subject to an along-axis gradient, with mean values tending to increase in the northern and central regions by approximately 10 cm (approximately 10 cm more in stormy conditions), and decrease by approximately the same quantity (although in this case with no statistical significance) in the south. Overall, projected H_s statistics envisage a generalized (although not uniform) decrease of mean, calm, and storm conditions throughout the basin, with the only exception of an increase in the extreme values along the northeastern coastal regions, associated with the variations in Sirocco wind regimes. This local effect, in countertrend compared to the remainder of the basin, is associated with a shift in the relative weight of Bora and Sirocco in the favour of the latter due to a tendency to a northbound migration of the Mediterranean cyclone tracks (see Bonaldo et al., 2020 for a deeper discussion).

3.1.3.2. Pilot sites statistics

Alongside an overview of the expected evolution at the basin scale, we focused on each Pilot Sites in order to provide local planners, stakeholders, and technicians with some operational information about projected wave climatology and extreme events. To this aim, for each Pilot Site we analyse the offshore model output (Figure 3.1) investigating monthly calm (50th percentile), mean, and stormy (99th percentile) conditions, as well as the yearly extremes for different directions and return periods, fitted following a Gumbel distribution. Statistical significance of the results has been checked by means of a Mann-Whitney test. It is important to notice that for some of the sites, particularly along the eastern coast, due to the complexity of the coastline and the presence of several islands limits the model results may not be fully representative of the wave climate affecting the coast proper. Nonetheless, the presented figures still provide useful information about the sea states undergoing the stronger modifications, and the dataset in the Project repository (https://owncloud.ve.ismar.cnr.it/owncloud/index.php/s/efj6wcDhi2Y9D4u can be used as a boundary condition for very high-resolution downscaling for local applications.

The region offshore the Neretva River delta (Figure 3.6) is mostly exposed to southeasterly sea states, with an expected tendency to a decrease in most of the wave statistics throughout the year, with statistically significant behaviour and a reduction of 20 to 40% in the summer months. Extreme events are not expected to undergo strong statistically significant variations.

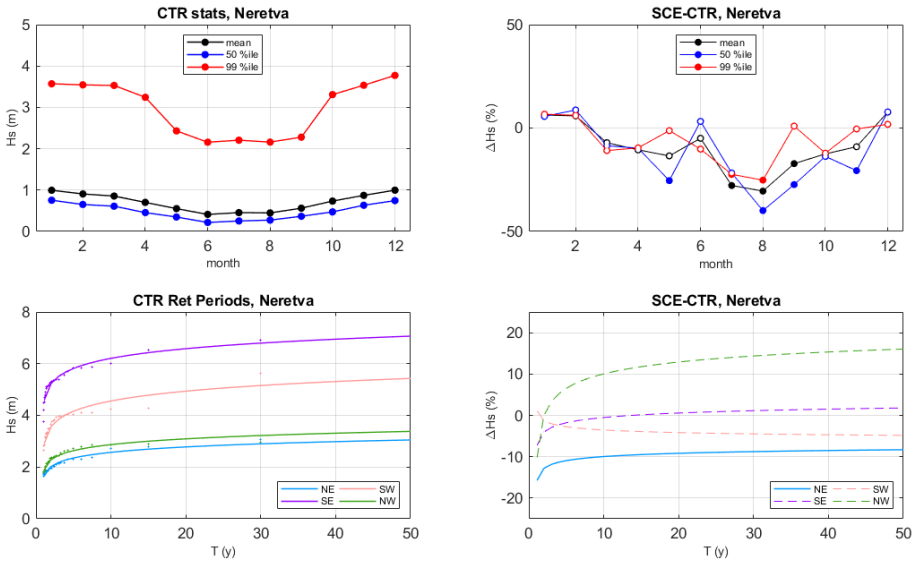

Figure 3.6: Neretva Delta Pilot Site (offshore) wave statistics. Top: H_s climatology (top left) and projected relative variations (top right, empty markers representing statistically non-significant information). Bottom: H_s from different quadrants and for different return periods (bottom left, dots representing modelled values and thick lines representing the fitting Gumbel distribution) and projected variations in climate change scenario (bottom right, dashed lines representing statistically non-significant trends).

Similar considerations hold for the region offshore Jadro River (Figure 3.7), with the only statistically significant trends affecting summerly statistics and northeasterly extreme events, not particularly relevant for the dynamics of this stretch of coast.

Offshore Vran Lake (Figure 3.8) the statistically significant climatological signal is a decrease in mild sea states statistics, whereas extreme events undergoing the stronger modifications are associated with northerly storms. In particular, significant wave height at the peak of northwesterly storms is expected to decrease relatively evenly by approximately 17%, while H_s associated with northeasterly storms is expected to decrease by up to 20% for return periods smaller than 5 years, and progressively increase by more than 15% for longer return periods.

At Banco della Mula di Muggia (Figure 3.9), the relatively shallow seabed and the partially sheltered position at the edge of the Gulf of Trieste tend to limit to some extent the severity of the wave storms impacting the coast. Nonetheless, it is worth noting that in this case a statistically significant increase of approximately 20 to 30% is actually expected in the autumn and winter months, alongside a reduction of H_s in the calmer summer conditions. The intensification of winter sea state severity is associated with an intensification of extreme southerly storms.

Given the peculiar shape of the Po delta, with two lobes directly facing Bora and Sirocco respectively, and to the presence of two focus sites in its southern lobe (that is, Sacca di Canarin and Sacca di Goro), for this Pilot Site three points were considered (Figure 3.1). The northern lobe (Figure 3.10) is most affected by Bora and, although no significant variations in seasonal statistics are expected (except for August calm and November storm conditions), wave extremes in this site will reflect the decrease of Bora storminess envisaged throughout the whole basin. In the southern lobe (Figures 3.Figure 3.11 and 3.Figure 3.12,

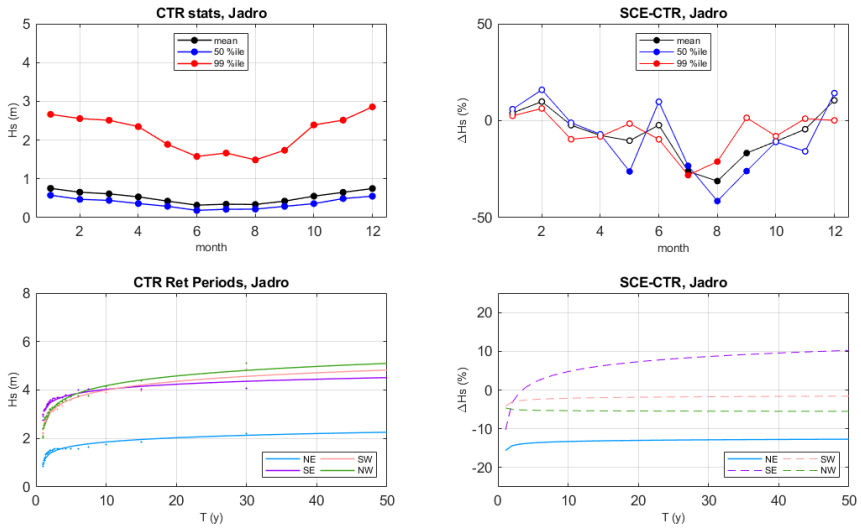

Figure 3.7: As Figure 3.8 but for Jadro River and Kaštela Bay Pilot Site (offshore).

respectively for Sacca di Canarin and Sacca di Goro) climatological trends are again rather weak and only involve calm conditions. A non-negligible and statistically significant decrease in the intensity of Bora extremes is nonetheless expected but it is not likely to reduce the maximum sea severity, since due to the coastline geometry this is instead associated with Sirocco.

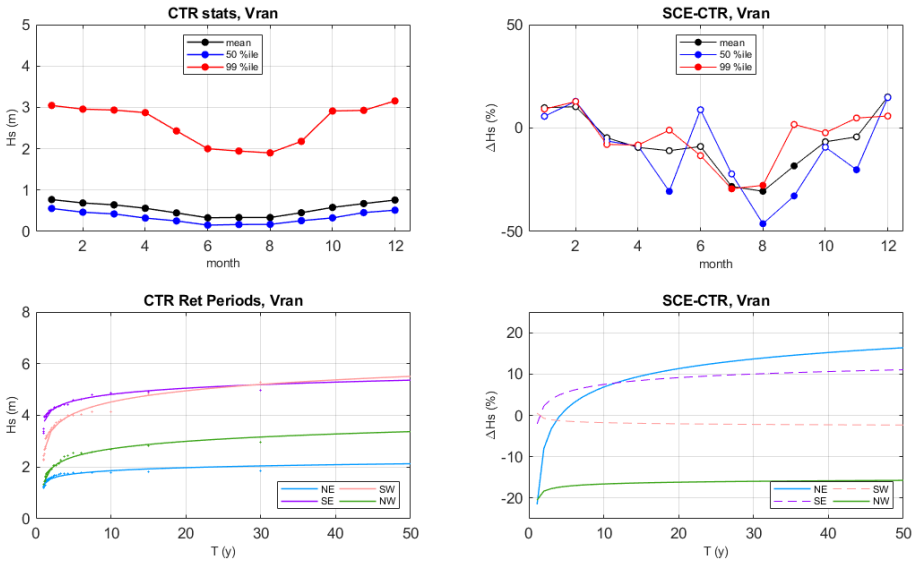

Figure 3.8: As Figure 3.8 but for Vran Lake Pilot Site (offshore).

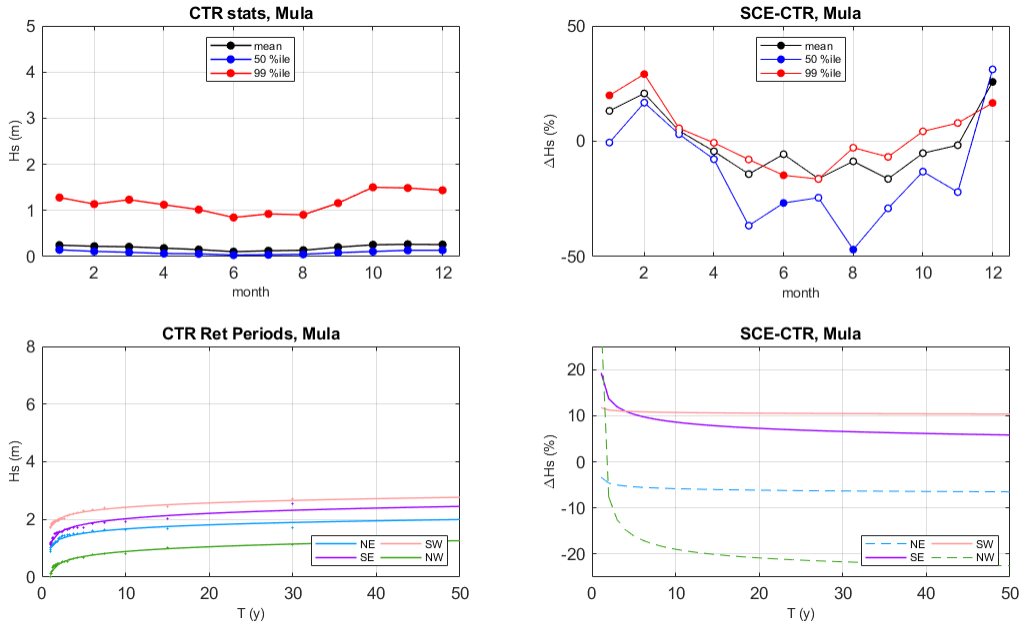

Figure 3.9: As Figure 3.8 but for Banco della Mula di Muggia Pilot Site (offshore).

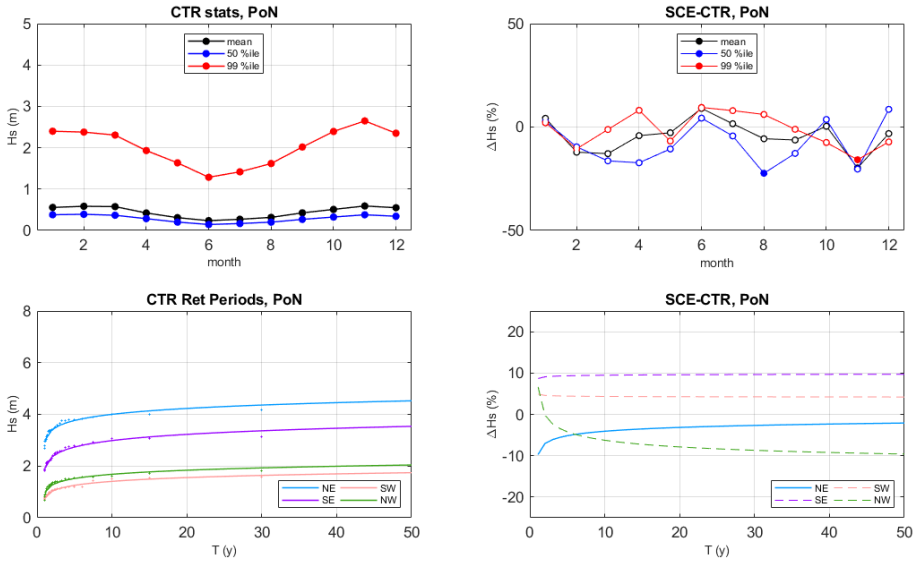

Figure 3.10: As Figure 3.8 but for Po Delta Pilot Site, Northern lobe (offshore).

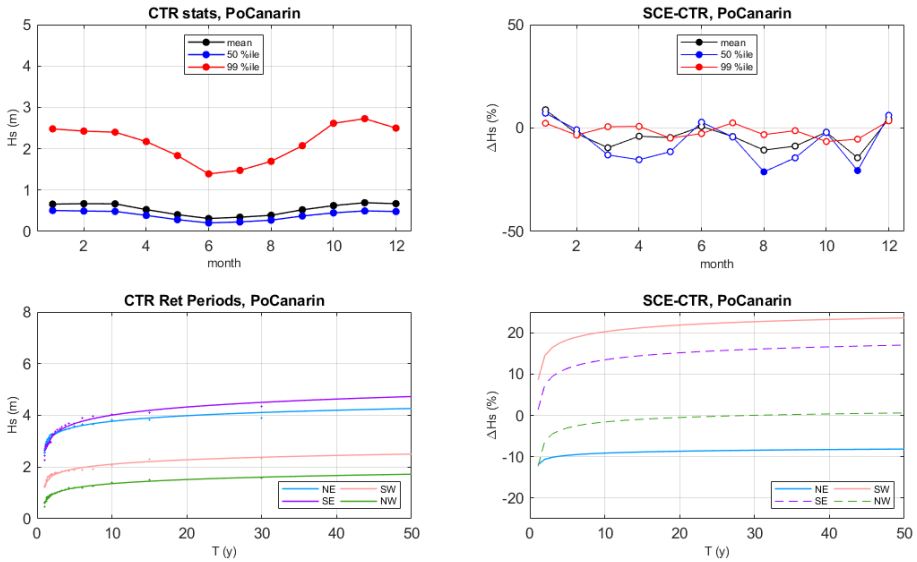

Figure 3.11: As Figure 3.8 but for Po Delta Pilot Site, Sacca di Canarin (offshore).

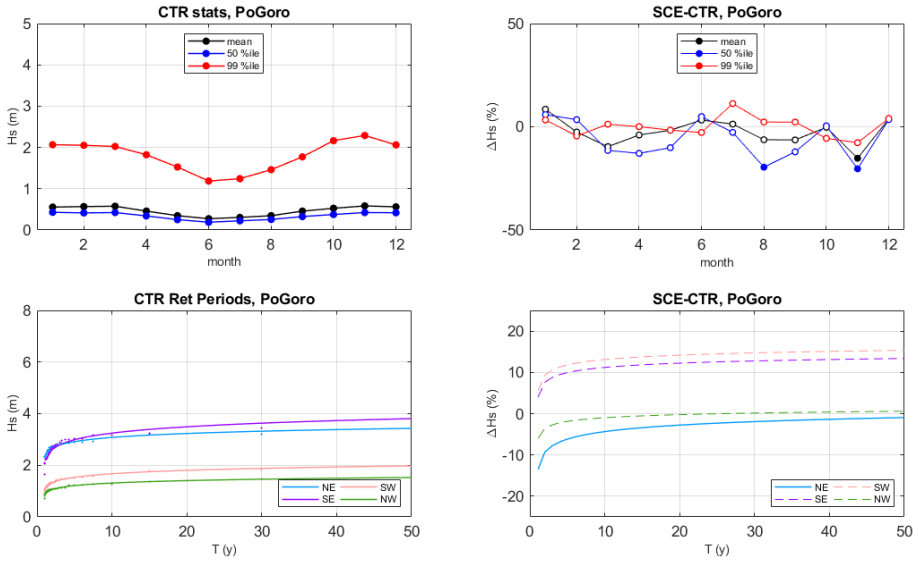

Figure 3.12: As Figure 3.8 but for Po Delta Pilot Site, Sacca di Goro (offshore) wave statistics.

3.2. FUTURE STORMS ANALYSIS WITH A PSEUDO-GLOBAL WARMING APPROACH (IOF)

In order to quantify changes of extreme storms over the Adriatic Sea in future climate, surrogate modelling approach has been used to assess changes of wind waves in RCP4.5 and RCP8.5 scenarios. This approach has been applied to severe sirocco and bora storms occurring in the last four decades. This report contains the description of the methodology and results on the basin scale. The material presented here is submitted to the peer-review journal Climate Dynamics.

3.2.1. The methodology and the data

3.2.1.1. The AdriSC model

The Adriatic Sea and Coast (AdriSC) modelling suite (Denamiel et al. 2019) has been recently developed with the aim to accurately represent the processes driving the atmospheric and oceanic circulation at different temporal and spatial scales over the Adriatic and northern Ionian Sea. In this spirit, the AdriSC modelling suite is based on two different modules: (1) a basic module which provides atmospheric and oceanic baroclinic circulation at the deep sea and coastal scales, and (2) a dedicated nearshore module which is used to better reproduce atmospherically-driven extreme events.

The basic module of the AdriSC suite rely on the use and development of the Coupled Ocean–Atmosphere–Wave–Sediment Transport (COAWST) modelling system (Warner et al. 2010). It is built

around the Model Coupling Toolkit (MCT) which exchanges data fields and dynamically couples the Weather Research and Forecasting (WRF) atmospheric model, the Regional Ocean Modeling System (ROMS), and the Simulating WAves Nearshore (SWAN) model. The basic module is set-up with (1) two different nested grids of 15-km and 3-km resolution used in the WRF model and covering respectively the central Mediterranean area and the Adriatic-Ionian region and (2) two different nested grids of 3-km and 1-km resolution used for both ROMS and SWAN models and covering respectively the Adriatic-Ionian region (similarly to the WRF 3-km grid) and the Adriatic Sea only.

In the nearshore module, the fully coupled ADCIRC-SWAN unstructured model (Dietrich et al. 2012) is forced every minute with the off-line atmospheric results of a dedicated high-resolution WRF 1.5-km grid. In more details, (1) the hourly results from the WRF 3-km grid obtained with the basic module are first downscaled to a WRF 1.5-km grid covering the Adriatic Sea and (2) the hourly sea surface elevation from the ROMS 1-km grid, the 10-min spectral wave results from the SWAN 1-km grid and finally the 1-min results from the WRF 1.5-km grid are then used to force the unstructured mesh of the ADCIRC-SWAN model.

The AdriSC modelling suite is installed and fully tested on the European Centre for Middle-range Weather Forecast (ECMWF) high-performance computing facilities. The operational component of the AdriSC modelling suite provides every day at midnight: (1) the next 48-h forecast results from the basic module and (2) the 15-min forecast results from the nearshore module for the next day. These results are published via an interactive interface at http://www.izor.hr/adrisc. More details on the AdriSC operational component set-up can be found in Denamiel et al. (2019).

In this study, in order to reproduce the strongest historical wave storms which took place in the Adriatic Sea during the 1979-2019 period and to assess their behavior under climate change projections (RCP 4.5 and RCP 8.5 scenarios), the SWAN model – originally unused in the AdriSC modelling suite, was set-up in both modules to be coupled with the ocean and atmosphere models (i.e. WRF, ROMS, ADCIRC). In the actual configuration, the third generation SWAN model is used with backward space and time propagation scheme, default initial condition, dissipation from whitecapping by Komen (1984) and Madsen bottom friction (Madsen et al. 1988). The wave model receives forcing from WRF 3-km (wind fields) and ROMS 3-km/1-km (ocean surface currents, sea level and friction) every 10 minutes in the basic module and from WRF 1.5-km (wind fields) and ADCIRC (ocean barotropic currents, sea level and friction) every minute in the nearshore module. In addition, the computation of the bottom stress of the ocean models (respectively ROMS and ADCIRC) was updated in order to take into account the spatial distribution of the sediment grain size at the bottom of the Adriatic Sea extracted from the Adriatic Seabed database (Jenkins et al. 2005) and the wave effects. For the evaluation runs during the 1979-2019 period, in order to reproduce the historical storms as accurately as possible, the basic module was set-up to run for three days – similarly to the operational component. Initial conditions and boundary forcing were provided by (1) the 6-hourly ERA-Interim re-analysis fields (Balsamo et al. 2015), (2) either the monthly or the daily re-analysis MEDSEA-Ocean fields (Pinardi et al. 2003), depending on whether the storm took place before or after the 1st of January 1987, and (3) either the 6-hourly ERA-Interim wave fields or the hourly MEDSEA-

Wave fields (Ravdas et al. 2018), depending on whether the storms took place before or after the 1st January 2006. The nearshore module, forced by the results of the basic module, was set-up to run for the last day and half of the basic module simulations.

Hereafter, only the last 24-h 1-min wave and sea level results of the nearshore module extracted from respectively the unstructured SWAN model (referred as AdriSC unSWAN in this study) and the ADCIRC model are analysed.

3.2.1.2. Documented historical extreme wave storms in the Adriatic Sea

In the Adriatic Sea, only two most frequent winds – bora and sirocco (Fig. 3.15.a), can produce fetches large enough to drive extreme wave storms (Pomaro et al. 2017). The bora is a cold east-northeast wind which flows through mountain passages along the Croatian coastline with a mean speed sometimes surpassing 30 m s^{-1} and gust reaching up to 70 m s^{-1} (e.g. Jiang and Doyle 2005; Kuzmić et al. 2005; Belušić and Klaić 2006; Gohm et al. 2008; Grisogono and Belušić 2009; Trošić 2015). Continuous gale force (> 15 m s^{-1}) bora winds are most common during the cold season (November through March) and have an average duration of 12 hours with rare events that can last up to two days. The sirocco is a warm southeast wind originating from North Africa, blowing over the Mediterranean Sea and sometimes affecting the Adriatic Sea, being channelled by the surrounding mountains, with gust reaching more than 30 m s^{-1} (e.g. Poje 1992; Jurčec et al. 1996; Penzar et al. 2001; Pasarić and Orlić 2004). Although sirocco winds are not as strong as the bora, continuous gale force events occur more frequently between October and March, usually lasting 10 to 12 hours – with rare occurrences as long as 36 hours, and often bring rain – sometimes mixed with Saharan dust (Cushman-Roisin et al. 2001). Both sirocco and bora episodes may differ between each other in intensity and spatial coverage, extending either over the whole Adriatic or just a part or being conjoined, with sirocco blowing in the southern and bora in the northern Adriatic. Finally, in terms of extreme conditions, as sirocco winds can produce extended fetch, contrarily to the bora winds which are fetch-limited, the largest wave heights were recorded in the northern Adriatic during extreme sirocco events (Leder et al. 1998; Bertotti et al. 2011; Pomaro et al. 2017), which can be associated with extreme storm surges in the Venice Lagoon, the Gulf of Trieste (Fig. 3.15.a) and the whole northern Adriatic (Lionello et al. 2012a; Međugorac et al. 2015).

In this study, in order to perform the evaluation of the AdriSC nearshore module, the choice of the studied extreme events was mostly driven by the available information and measurements recorded during the 1979-2019 period. For the sirocco events, the 14 selected storms (Fig. 3.15.b) were extracted from the long-term record of the Venice extreme flooding (https://www.comune.venezia.it/it/content/le-acque-alte-eccezionali).

For the bora events, only 22 of the most recent extreme storms were selected (Fig. 3.15.b) as more wave measurements became available in the Adriatic Sea at the end of the 20th century. The majority of the bora events peaked in the northern Adriatic, where bora wind is the strongest (Grisogono and Belušić 2009). The set of wave measurements (Table 3.1) – used to evaluate the skills of the AdriSC nearshore module to reproduce the 36 selected storms, spans between 1979 and 2019 and consists in 6 stations

along the Italian coast – Acqua Alta tower from Pomaro et al. (2018), Venice 1 (only for the significant wave height measurements) from the Copernicus Marine Environment Monitoring Service (ftp://my.cmems-du.eu/Core/INSITU_GLO_WAVE_REP_OBSERVATIONS_013_045/history/mooring/) and Venice 2, Ortona, Ancona, Monopoli from the Italian Data Buoy Network managed by ISPRA (Bencivenga et al. 2012), 4 stations along the Croatian coastline – Rovinj, Split, Ploče and Dubrovnik, from the Croatian Hydrographic Institute (Hrvatski hidrografski institut – HHI), and one station in the middle of the northern Adriatic shelf – IVANA-A also from HHI. From Table 3.1, it should be noted that storm coverage is about 5 times higher from the Italian than the Croatian measurements. In addition, concerning the extreme storm surges associated with the sirocco events, two long-term hourly sea level measurements extracted between 1979 and 2019 from tide gauges located respectively in the Venice Lagoon (at Punta Della Salute, 45.4310°N, 12.3364°E, maintained by ISPRA) and in the Gulf of Trieste (at 45.6544°N, 13.7561°E, maintained by ISMAR) were also used to evaluate the skill of the AdriSC nearshore module.

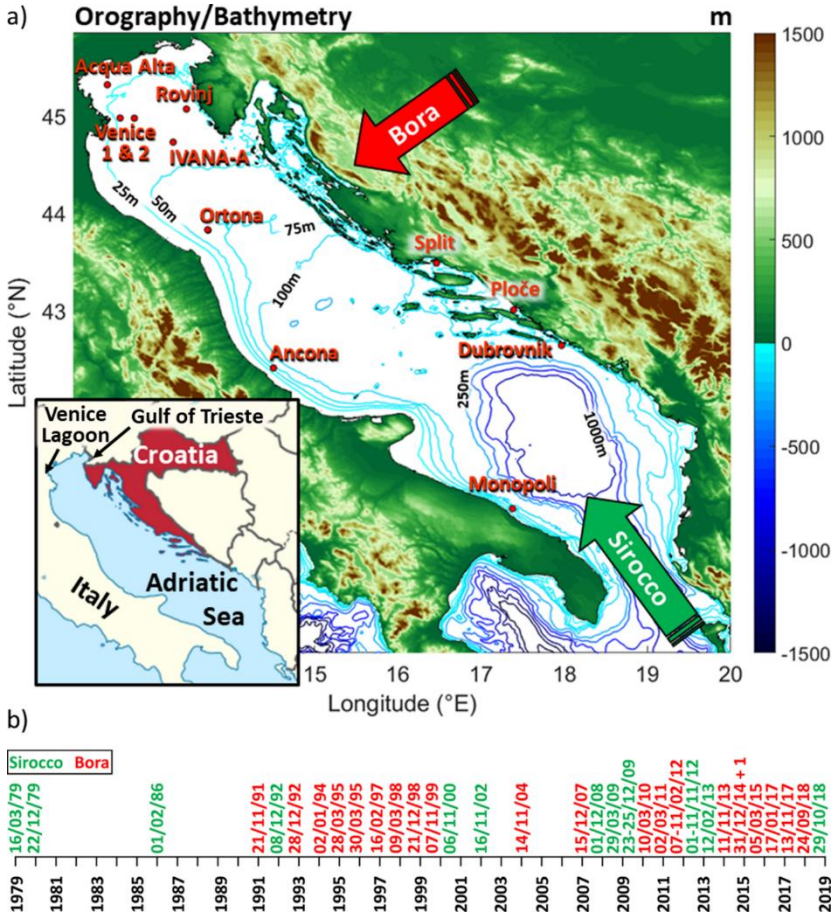

Figure 3.15. (a) Location of the different Adriatic Sea wave measurements along the Italian and Croatian coastline and (b) selected 36 one-day extreme wave events during the 1979-2019 period – depending on the wind conditions (bora or sirocco) schematized by arrows in the map, used for the SWAN model evaluation. The notation + 1 (panel b) means that the 01/01/2015 event is also selected.

Table 3.1. Adriatic Sea wave buoy data available along the Italian and Croatian coastlines between 1979 and 2019.

Name	Location	Period of measurements	Sampling	Events*
Acqua Alta	12.5088 °E, 45.3138 °N	01.01.1979 – 01.01.2018	3 h	33
Venice 1	12.6627 °E, 44.9735 °N	01.06.2013 – 01.01.2015	1 h	3
Venice 2	12.8330 °E, 44.9717 °N	01.06.2002 – 01.01.2015	1 h	9
Ortona	14.5056 °E, 42.4150 °N	01.07.1989 – 19.05.2011	1 h	17
Ancona	13.7144 °E, 43.8297 °N	10.03.1999 – 07.11.2014	1 h	13
Monopoli	17.3767 °E, 40.9750 °N	01.07.1989 – 01.01.2015	1 h	19
IVANA-A	13.2997 °E, 44.7262 °N	01.11.2007 – 13.05.2010	30 min	6
Rovinj	13.4599 °E, 45.0655 °N	11.05.2018 – 01.01.2019	30 min	1
Split	16.4650 °E, 43.4883 °N	29.10.2007 – 01.01.2019	30 min	5
Ploče	17.3913 °E, 43.0096 °N	09.12.2016 – 01.01.2019	30 min	4
Dubrovnik	17.9667 °E, 42.6460 °N	06.04.2017 – 01.01.2019	30 min	3

* number of the selected 36 storms covered by the measurements

3.2.1.3 Pseudo-global warming methodology

The two major challenges posed by performing ultra-high resolution climate projection simulations are (1) the relative slowness of the AdriSC modelling suite (a month of results produced per day with the basic module alone), and (2) the low temporal and spatial resolutions (only few vertical levels for daily or monthly data) of the coupled regional climate model (RCM) results available to provide boundary conditions to the WRF 15-km and ROMS 3-km models. To address these concerns, the projection of the extreme Adriatic Sea wave events for the RCP 4.5 and RCP 8.5 scenarios is performed, in this study, via a pseudo-global warming (PGW) method. The principle of the PGW simulations – as first introduced by Schär et al. (1996) and described in details by Rasmussen et al. (2011), Kröner et al. (2017) and Brogli et al. (2019a, 2019b), is to impose an additional climatological change (e.g. a temperature change representative of the increase in temperature between past and future climate) to the forcing used to produce the evaluation runs.

In the Mediterranean Sea, one of the specific aim of the Med-CORDEX experiment (https://www.medcordex.eu/) – part of the Coordinated Regional Climate Downscaling Experiment (CORDEX) initiative (https://esg-dn1.nsc.liu.se/search/cordex/) which coordinates the production of climate change projections at the regional scale (Giorgi et al. 2009; Giorgi and Gutowski 2015; Ruti et al. 2016), is to provide coupled ocean-atmosphere regional model results. However, at the time of this study, due to a reported issue with the CNRM-CM5 CMIP5 forcing for the historical run (that removes reliability of this product, https://www.medcordex.eu/warnings/Communication-Issue-Files_CNRM-CM5_historical_6hLev_en.pdf), the only coupled results publicly available – with high enough temporal and spatial resolutions for the historical period (1950-2005) and the two climate scenarios RCP 4.5 and RCP 8.5 (2006-2100), were those of the LMDZ4-NEMOMED8 model (Hourdin et al. 2006; Beuvier et al. 2010) forced by the Institut Pierre Simon Laplace (France) model, IPSL-CM5A-MR, simulations (r1i1p1). These results – defined as two continuous LMDZ4-NEMOMED8 simulations (1950-2100) extending the historical run with either the RCP 4.5 or the RCP 8.5 runs, are referred as SCEN 4.5 and SCEN 8.5, respectively, and used hereafter to force the PGW simulations. The PGW climatological changes derived from SCEN 4.5 and SCEN 8.5 between the 1979-2019 and the 2060-2100 periods are thus tested in this study.

Finally, the key development of this study is the extension of the PGW method – which had till now only been used in atmospheric models, to the ocean models and more particularly to the AdriSC modelling suite. For the atmosphere, as described in many previous studies (Pan et al. 2011; Kendon et al. 2014; Tolle et al. 2014; Argueso et al. 2014; Rasmussen et al. 2014; Ban et al. 2015; Prein et al. 2015; Fosser et al. 2016; Kendon et al. 2017), the ERA-Interim air temperature $\left(T^{ERAI}\right)$, relative humidity $\left(RH^{ERAI}\right)$ and horizontal wind velocities $\mathbf{V}^{ERAI}=\left(V_x^{ERAI},V_y^{ERAI}\right)$ defined on 37 atmospheric pressure levels $\left(p\right)$ are modified between 1000 hPa and 70 hPa with respectively $\Delta T\left(t_{\text{clim}},x,y,p\right)$, $\Delta RH\left(t_{\text{clim}},x,y,p\right)$ and $\Delta\mathbf{V}=\left(\Delta V_x\left(t_{\text{clim}},x,y,p\right),\Delta V_y\left(t_{\text{clim}},x,y,p\right)\right)$ derived from SCEN 4.5 and SCEN 8.5 atmospheric results to produce 6-hourly climatologic changes $\left(t_{\text{clim}}\right)$ for the 366 days of the year. The WRF 15-km boundary and initial conditions of the PGW simulations (T^{SCEN}, RH^{SCEN}, V_x^{SCEN} and V_y^{SCEN}) are thus given by:

$$
\begin{aligned}
T^{SCEN}\left(t,x,y,p\right)&=T^{ERAI}\left(t,x,y,p\right)+\Delta T\left(t_{\text{clim}},x,y,p\right)\\
RH^{SCEN}\left(t,x,y,p\right)&=RH^{ERAI}\left(t,x,y,p\right)+\Delta RH\left(t_{\text{clim}},x,y,p\right)\\
V_x^{SCEN}\left(t,x,y,p\right)&=V_x^{ERAI}\left(t,x,y,p\right)+\Delta V_x\left(t_{\text{clim}},x,y,p\right)\\
V_y^{SCEN}\left(t,x,y,p\right)&=V_y^{ERAI}\left(t,x,y,p\right)+\Delta V_y\left(t_{\text{clim}},x,y,p\right)
\end{aligned}
\qquad (1)
$$

In order to adjust the height of the surfaces of constant pressure to the temperature and relative humidity changes, the geopotential – depending on the virtual temperature T_v^{SCEN} and the ERA-Interim geopotential ϕ^{ERAI} at the reference pressure $p_{ref} = 1000hPa$, is recalculated as follow:

$$\phi^{SCEN}(t,x,y,p) = \phi^{ERAI}(t,x,y,p_{ref}) - \int_{p_{ref}}^{p} \frac{RT_v^{SCEN}}{p} dp \quad (2)$$

Finally, the 2-m air temperature change ΔT_S derived from SCEN 4.5 and SCEN 8.5 runs is used to adjust the ERA-Interim surface (ground and 2-m air) temperatures $\left(T_S^{ERAI}\right)$ such as:

$$T_S^{SCEN}(t,x,y) = T_S^{ERAI}(t,x,y) + \Delta T_S(t_{clim},x,y) \quad (3)$$

The developed methodology for the ocean follows the principles of the PGW for the atmosphere. In this study, the MEDSEA ocean temperature $\left(T^{MEDSEA}\right)$, salinity $\left(S^{MEDSEA}\right)$ and currents $\left(V_x^{MEDSEA}, V_y^{MEDSEA}\right)$ defined on 72 unevenly spaced vertical levels (z), are thus modified with respectively $\Delta T(t_{clim},x,y,z)$, $\Delta S(t_{clim},x,y,z)$ and $\Delta \mathbf{V} = \left(\Delta V_x(t_{clim},x,y,z), \Delta V_y(t_{clim},x,y,z)\right)$ derived from SCEN 4.5 and SCEN 8.5 ocean results to produce daily climatological changes (t_{clim}) for the 366 days of the year. The ROMS 3-km boundary and initial conditions of the PGW simulations (T^{SCEN} and S^{SCEN}) are thus given by:

$$\begin{aligned}
T^{SCEN}(t,x,y,z) &= T^{MEDSEA}(t,x,y,z) + \Delta T(t_{clim},x,y,z) \\
S^{SCEN}(t,x,y,z) &= S^{MEDSEA}(t,x,y,z) + \Delta S(t_{clim},x,y,z) \\
V_x^{SCEN}(t,x,y,z) &= V_x^{MEDSEA}(t,x,y,z) + \Delta V_x(t_{clim},x,y,z) \\
V_y^{SCEN}(t,x,y,z) &= V_y^{MEDSEA}(t,x,y,z) + \Delta V_y(t_{clim},x,y,z)
\end{aligned} \quad (4)$$

In the ocean, the static stability depends on the density (ρ) and the vertical variations of the local potential density (σ_n) such as:

$$E(x,y,z) = -\frac{1}{\rho(x,y,z)} \frac{\delta \sigma_n}{\delta z} \quad (5)$$

The stability of the ocean forcing (at the boundaries and for the initial condition) is thus ensured by imposing $E^{SCEN} \geq 0$ at all vertical levels.

The temperature changes (ΔT) imposed at the boundaries of both the ocean and atmosphere models are illustrated in Fig. 3.16. The vertical variations of the spatially- and time- averaged ΔT presented in Figure 3.16.b clearly show that, near the surface of the earth, the differences in temperature between scenarios RCP 4.5 and RCP 8.5 reach more than 1.5°C (for both the ocean and the atmosphere). For the ocean, no significant difference between the two scenarios is seen below depth of 1000 m. For the atmosphere, the difference only starts to decrease above 400 hPa and is minimized above 100 hPa. In addition, the time variations of the spatially-averaged ΔT for scenario RCP 8.5 (Fig. 3.16.c) highlights that the temperature change imposed to the atmosphere at 2 m height is, most of a year, at least 0.5°C higher than the one imposed to the sea surface temperature. Finally, Figs. 3.16.d and 3.16.e present the vertical variations of the temporally-averaged ΔT along the southern and western boundaries of both the atmosphere and ocean models and illustrate the importance of using spatially varying temperature changes for realistic climate simulations. In Fig. 3.17, the surface distribution of the temporally-averaged RCP 8.5 changes show that (1) for the atmosphere, the orography plays a major role in terms of the intensity of the changes (i.e. the strongest increase in temperature, decrease in relative humidity and change in wind speed are generally found at the highest altitudes), and (2) for the ocean, the changes imposed to the Adriatic and northern Ionian Seas (i.e. strongest increase in temperature and salinity) do not correspond to the changes imposed in the western side of the domain where the strongest changes in current speed occur. Concerning the sea surface elevation, the RCP 8.5 changes are mostly negative and only of the order of a few centimeters (with a maximum of 8 cm). Given that (1) the open boundary of the LMDZ4-NEMOMED8 model (similarly to all the Med-CORDEX simulations, Adloff et al. 2018) does not properly include the projected Atlantic sea level changes, but just takes into account the thermosteric

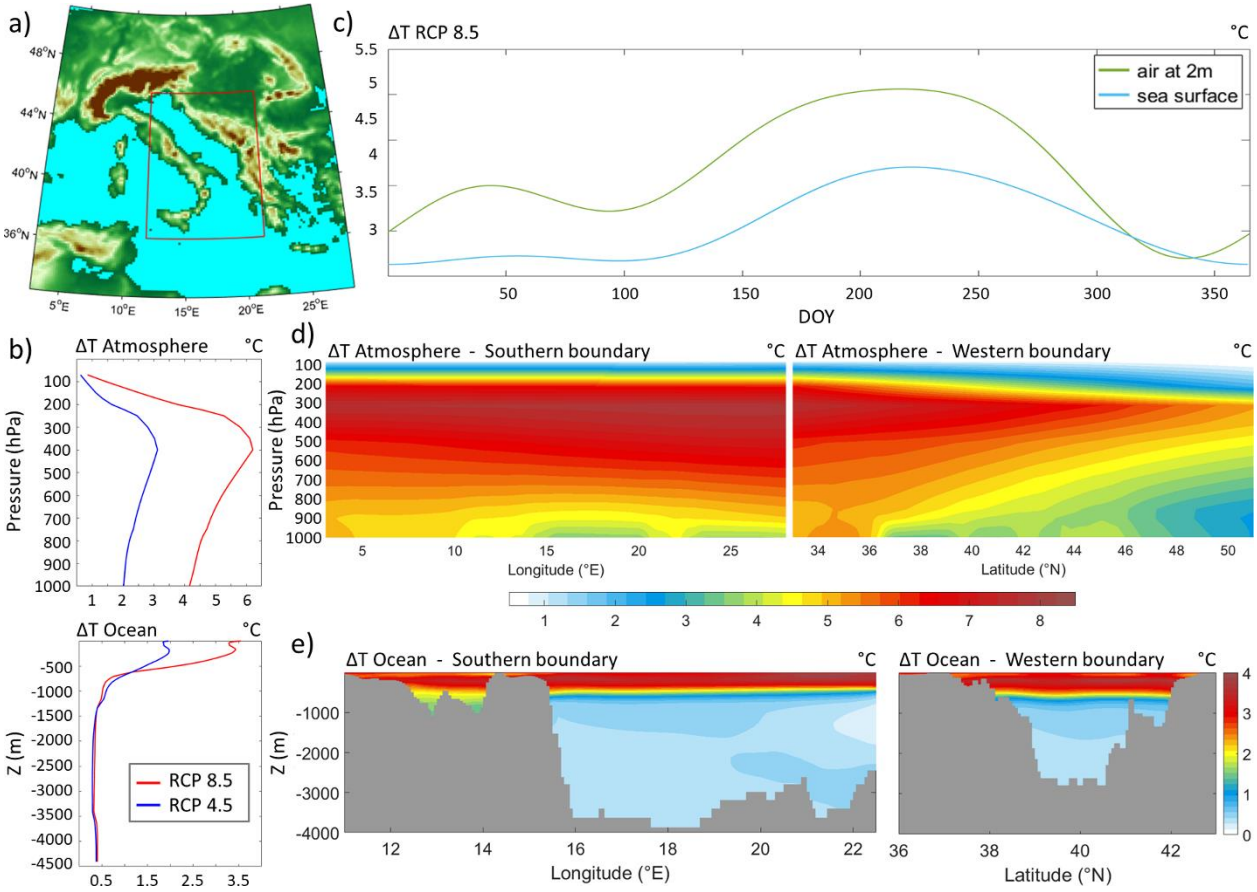

Figure 3.16. (a) Spatial domain and boundaries of the WRF 15-km model and the ROMS 3-km model. (b) Vertical variations of average temperature changes ΔT *for scenarios RCP 4.5 and RCP 8.5 following pressure level in the atmosphere and depth in the ocean. (c) Time evolution depending on the day of a year (DOY) of the spatially-averaged 2-m air (in green) and sea level (in blue) climatologic temperature changes* ΔT *for scenario RCP 8.5. Vertical structure of the temporally-averaged temperature changes* ΔT *(RCP 8.5) imposed at the southern and western boundaries of (d) the WRF 15-km model and (e) the ROMS 3-km model.*

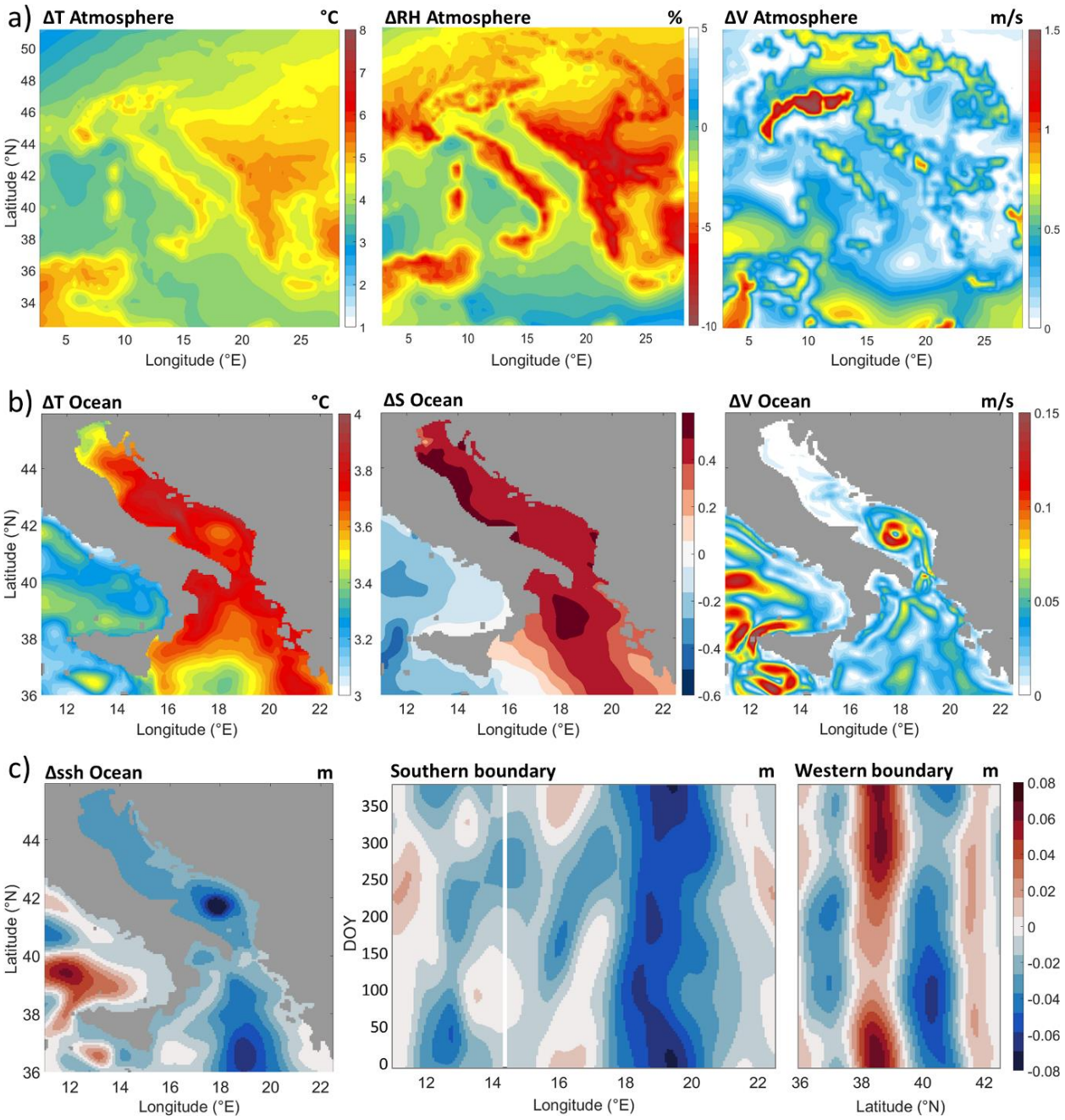

Figure 3.17. Surface distribution of the temporally-averaged RCP 8.5 changes of (a) temperature (ΔT), relative humidity (ΔRH) and wind speed (ΔV) in the atmosphere for the WRF 15-km domain and (b) temperature (ΔT), salinity (ΔS) and current speed (ΔV) in the ocean for the ROMS 3-km domain. The variations of the sea surface elevation (Δssh) RCP 8.5 changes are presented in panel (c) as temporally-averaged surface distributions and time-varying open boundary conditions.

effects and (2) the thermal stretching is balanced by the haline shrinking, these results are in accordance with the estimated -7 cm to 13 cm expected in the Mediterranean Sea (Tsimplis et al. 2008; Jordà and Gomis 2013; Gualdi et al. 2013). Thus, for realistic sea level projections, mass change-induced sea level increase – approximated to 50-60 cm in the Mediterranean till 2100 (Jordà and Gomis 2013), should be added to the presented PGW sea level estimates.

Finally, the sea surface elevation change Δssh derived from SCEN 4.5 and SCEN 8.5 runs is used to adjust the MEDSEA surface layer $\left(ssh^{MEDSEA}\right)$ such as:

$$ssh^{SCEN}\left(t,x,y\right)=ssh^{MEDSEA}\left(t,x,y\right)+\Delta ssh\left(t_{c\lim},x,y\right) \quad (6)$$

In addition to the changes imposed to the ERA-I and MEDSEA forcing presented in the previous paragraphs, (1) the volume mixing ratio of five atmospheric gases (carbon dioxide, methane, nitrous oxide and chlorofluorocarbons 11 and 12) used in the evaluation runs is modified in the scenario runs using projected values (Meehl et al. 2007; Bernstein et al. 2008) averaged between 2060 and 2100 (Table 3.2), and (2) the historical monthly Adriatic Sea river discharges are climatologically changed for the RCP 4.5 and RCP 8.5 scenarios (Fig. 3.18) following the study of Macias et al. (2018). Concerning the waves, the forcing used in the evaluation simulations were kept unchanged for the scenario runs as the required data needed to apply the PGW methodology to the waves was not available. However, since the open boundary of the ROMS 3-km grid is located at least 400-km south of the Strait of Otranto, the wave field within the Adriatic basin is not considered to be highly affected by the propagation of these forcing. Finally, as this study aims to estimate the impact of climate change on atmospherically-driven extreme events and not to forecast future storms, the tidal forcing imposed for the evaluation runs was also kept unchanged for the scenario runs.

To summarize, the set of 108 runs used in this study consists in 36 Adriatic Sea wave storm simulations (selected in Section 3.2.2) carried out with the AdriSC modelling suite (described in Section 3.2.1) – for 3 days within the general module (i.e. coupled WRF-ROMS-SWAN) and 1.5 day within the nearshore module (i.e. WRF 1.5-km and coupled ADCIRC-unSWAN), in evaluation mode first and then in climate change mode, for both RCP 4.5 and RCP 8.5 scenarios, imposing the PGW methodology (presented in Section 3.2.3).

Table 3.2. Atmospheric gas volume mixing ratios used for the evaluation and scenario runs

	carbon dioxide CO2 (ppmv*)	methane CH4 (ppbv**)	nitrous oxide N2O (ppbv**)	Chlorofluorocarbon	
				CFC-11 (pptv***)	CFC-12 (pptv***)
Evaluation	379	1774	319	251	538
RCP 4.5	528	1680	365	105	242
RCP 8.5	762	3470	408	99	231

* parts-per-million volume ** parts-per-billion volume *** parts-per-trillion volume

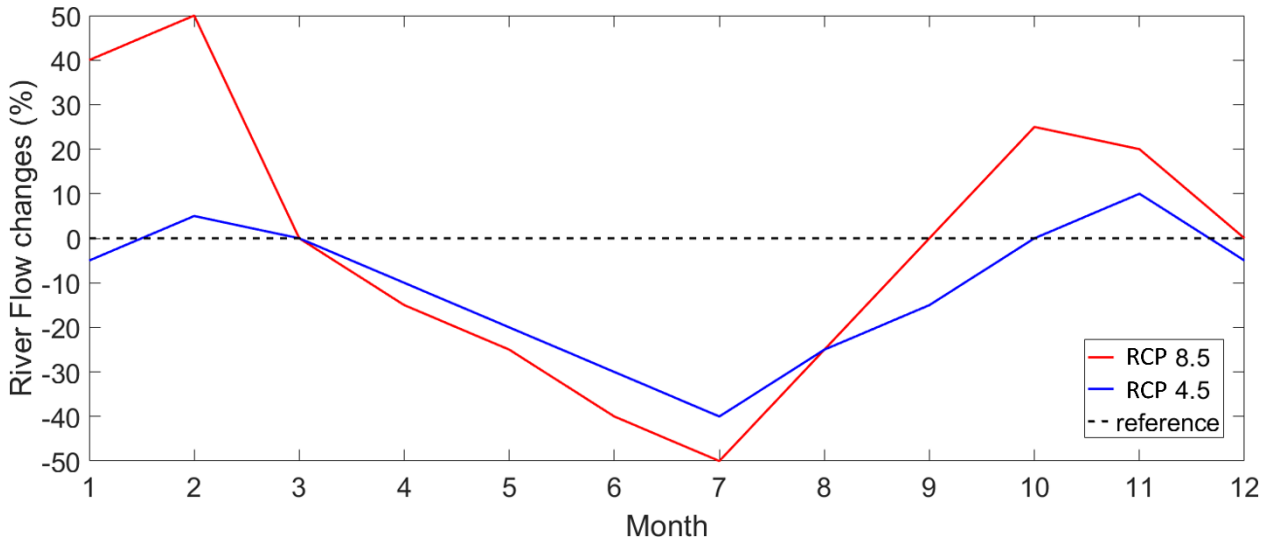

Figure 3.18. Monthly climatological changes (in percentage) imposed to the Adriatic Sea river discharges for scenario runs RCP 4.5 and RCP 8.5.

3.2.2 Model validation

To assess the skill of the AdriSC unSWAN model, the last 24-h of the 1-min significant wave height, peak wave period and mean wave direction results are extracted from the 36 simulations carried out in evaluation mode at the 11 locations of the wave stations presented in Section 3.2.2. The data are analysed in three steps (see Figs. 3.19, 3.20 and 3.21). First, the overall behavior of the model is presented as a scatter plot (Figs. 3.19.a, 3.20.a and 3.21.a) for the entire set of simulations and measurements. Then, the quantile-quantile distributions of the wave parameters are displayed separately for the Italian and Croatian wave stations (Figs. 3.19.b, 3.20.b and 3.21.b) and, finally, the performance of the unSWAN model wave distributions during bora and sirocco events (Figures 3.19.c, 3.20.c and 3.21.c) is showed with violin plots (Hintze and Nelson 1998).

On the whole (Figs. 3.19, 3.20 and 3.21), for the 36 studied storm events, the unSWAN model is in good agreement with the available wave measurements (significant height, peak period and mean direction): (1) in the scatter plots, the points with higher density (in red) are mostly located along the reference lines, (2) the quantile-quantile distributions for both the Croatian and Italian stations also follow the reference lines, except for the mean direction which is not well reproduced for the Croatian stations, and (3) the shapes of the violin plots for the unSWAN model results are similar to those obtained for the measurements during both bora and sirocco events.

However, in more details, some discrepancies between the measurements and the unSWAN model results can be noticed. For the significant wave height (Fig. 3.19), (1) the spread of the scatter plot (Fig. 3.19.a) increases from about 0.25 m up to 2 m when reaching the highest values, (2) the model slightly overestimates (up to 0.25 m) the values between 2 m and 4 m for both the Croatian and Italian stations and significantly overestimates (up to 1 m) the values above 4 m for the Croatian stations (Fig. 3.19.b),

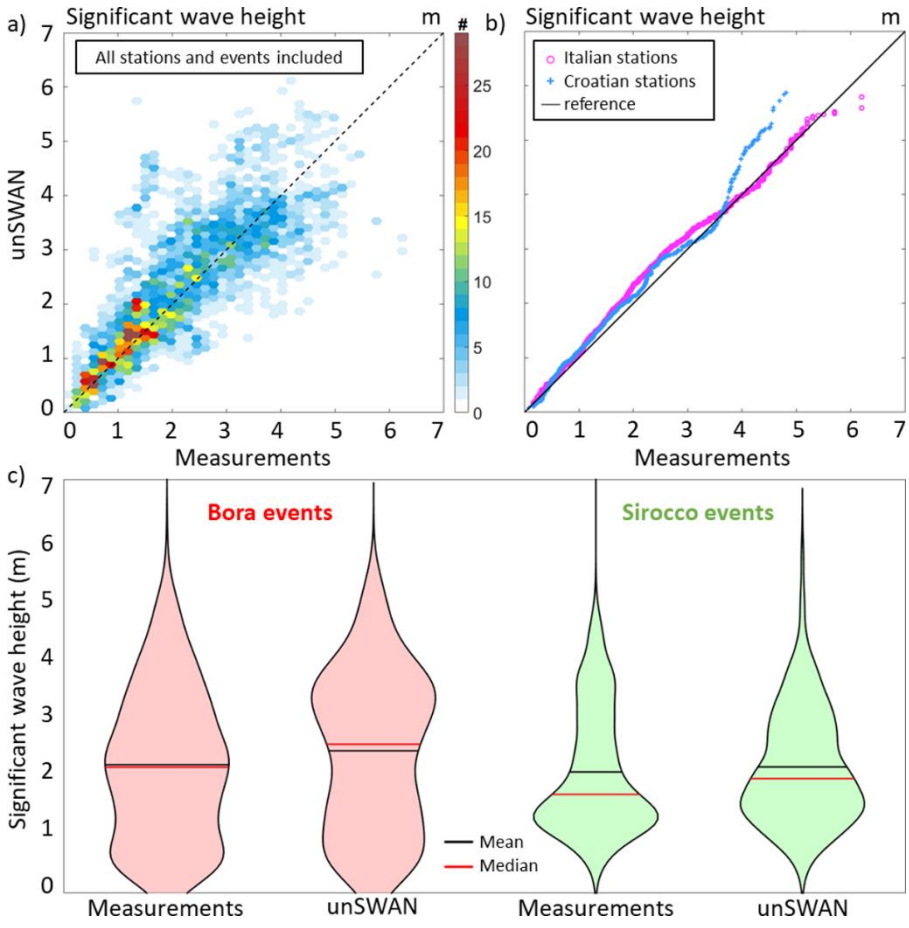

Figure 3.19. Evaluation of the AdriSC unSWAN significant wave height distributions against measurements (a) for all the available stations and selected storm events as a scatter plot showing the density (number of occurrences #) with hexagonal bins, (b) separately for the Italian and Croatian stations as a quantile-quantile plot, and (c) separately for the bora and sirocco events as violin plot distributions.

and (3) the mean and median of the model distributions (Fig. 3.19.c) are also overestimated for the bora (2.41 m vs. 2.17 m and 2.52 m vs. 2.13 m, respectively) and for the sirocco (2.13 m vs. 2.05 m and 1.94 m vs. 1.67 m, respectively) events.

For the peak wave period (Fig. 3.20), (1) similarly to the significant wave height, the spread of the scatter plot (Fig. 3.20.a) increases from about 1 s up to 6 s when reaching the highest values (to be noted: the discontinuities seen in the plot result from the fact that some measurements were provided as integer values), (2) the model slightly underestimates (up to 1 s) the values below 5 s and above 9 s for the Italian stations (Fig. 3.20.b), and (3) the mean and median of the model distribution for the bora events (Fig. 3.20.c) are overestimated (6.88 s vs. 6.61 s and 7.67 s vs. 7.10 s, respectively). Finally, for the mean wave

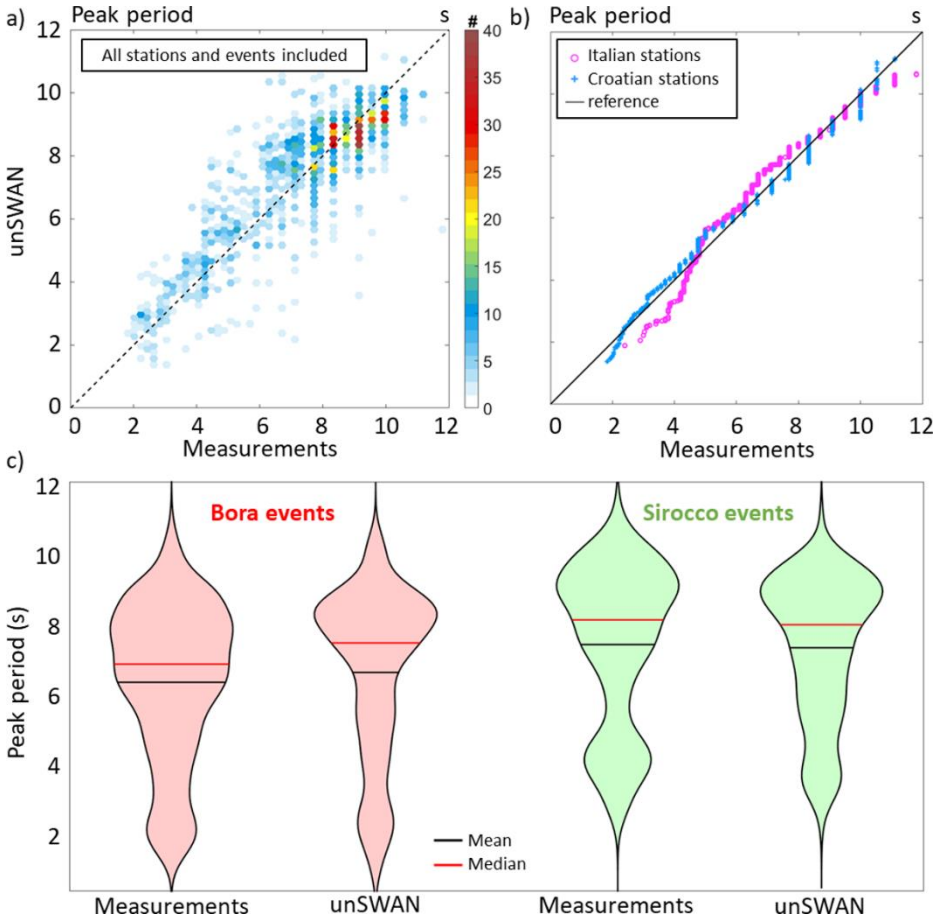

Figure 3.20. As in Fig. 3.19, but for the peak wave period.

direction, the major problem is the very large underestimation (up to 200°) of the values between 0° and 200° for the Croatian stations (Fig. 3.21.b).

In a nutshell, the unSWAN model seems (1) to have more difficulties to represent the wave conditions during bora events than during sirocco events, which means that the WRF 1.5-km model is most probably overestimating the intensity of the bora winds, (2) to be capable of reproducing the intensity of the extreme wave events (see quantile-quantile distributions) but not their timing (see spread of the scatter plots), and (3) to have better agreement with measurements along the Italian coast than along the Croatian coast. For the last point, the analysis of each Croatian station (not shown here), reveals that the mismatching of the model for the wave directions between 0° and 200° principally occurs at the IVANA-A and Dubrovnik locations which, as the model is in good agreement with the data for the other 9 stations, likely results from a problem with the measurements at these two locations. Beside these limitations, the evaluation of the unSWAN model has shown that the newly added wave component of the AdriSC modelling suite can be used to reproduce the historical Adriatic wave storms with a good level of accuracy.

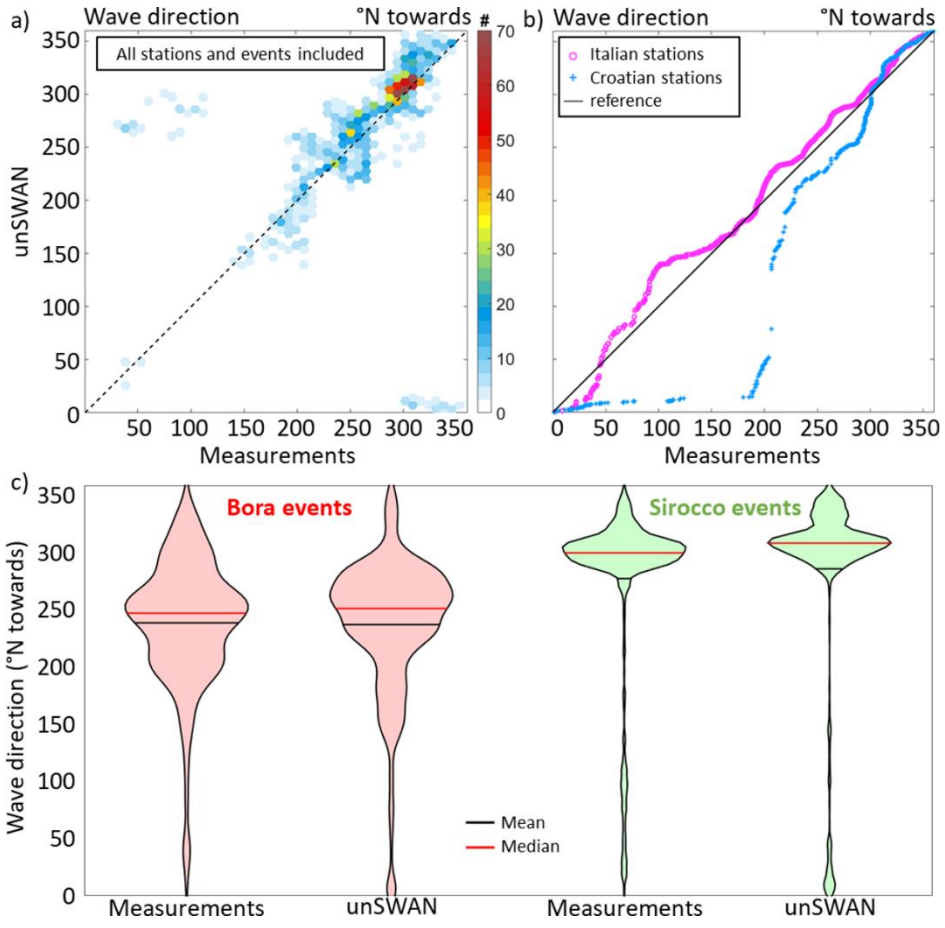

Figure 3.21. As in Fig. 3.19, but for the mean wave direction.

3.2.3 Future wave projections

With the aim to quantify the climate change impact on the Adriatic extreme wave events under both RCP 4.5 and RCP 8.5 projections for the 2060-2100 period, two kind of results are statistically analysed: (1) the spatial variations of the extreme wave conditions (Figs. 3.22 to 3.24), and (2) the temporal variations of the wave parameters at chosen locations along the Adriatic Sea (Figs. 3.25 to 3.28).

The spatial analysis of the extreme wave conditions consists first in defining the baseline conditions (Fig. 3.22), which are presented as the median over the ensembles of the 22 bora and the 14 sirocco storm simulations in evaluation (present climate) mode. The considered parameters are again the maximum significant wave heights, maximum peak wave periods and mean wave directions – calculated for each storm over the last 24-h results of the AdriSC nearshore module. Then, the climate change impact on the wave extremes is given by the differences (referred hereafter as biases) in maximum significant wave heights, maximum peak wave periods and mean wave directions between the climate change simulations (with the RCP 4.5 and RCP 8.5 scenarios treated separately) and the evaluation runs. Finally, the median and root-mean-square (RMS) of these biases are calculated for the ensembles of the 22 bora (Fig. 3.23) and the 14 sirocco (Fig. 3.24) events. The analysis of the baseline conditions (Fig. 3.22) shows that the typical significant wave heights and peak wave periods are above 3.5 m and 8 s, respectively. For the bora events, this particularly applies to the Italian coast between 42°N and 45°N of latitude, peaking between 44°N and 45°N latitude with the respective values of 5 m and 10 s. This is the result of the maximum in both bora speed and outreach, coming off the Croatian city of Senj at latitude 44.99°N (the Senj Jet, Grisogono and Belušić 2009). The typical wave propagation for analysed bora episodes is mostly towards

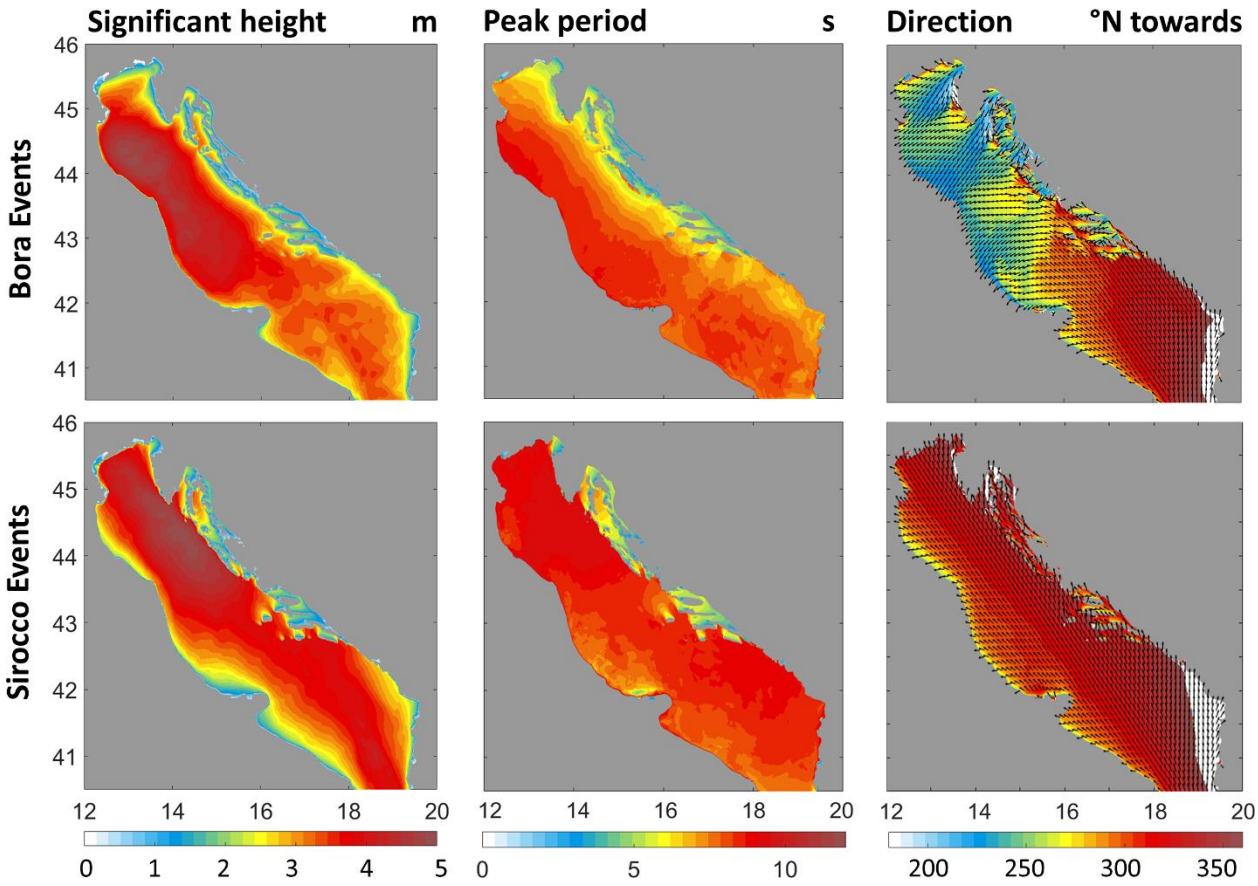

Figure 3.22. Baseline (present climate) plots defined as the median, over the entire Adriatic Sea, of the maximum significant wave heights, the maximum peak wave periods and the mean wave directions of the 22 bora (top panels) and 14 sirocco (bottom panels) events.

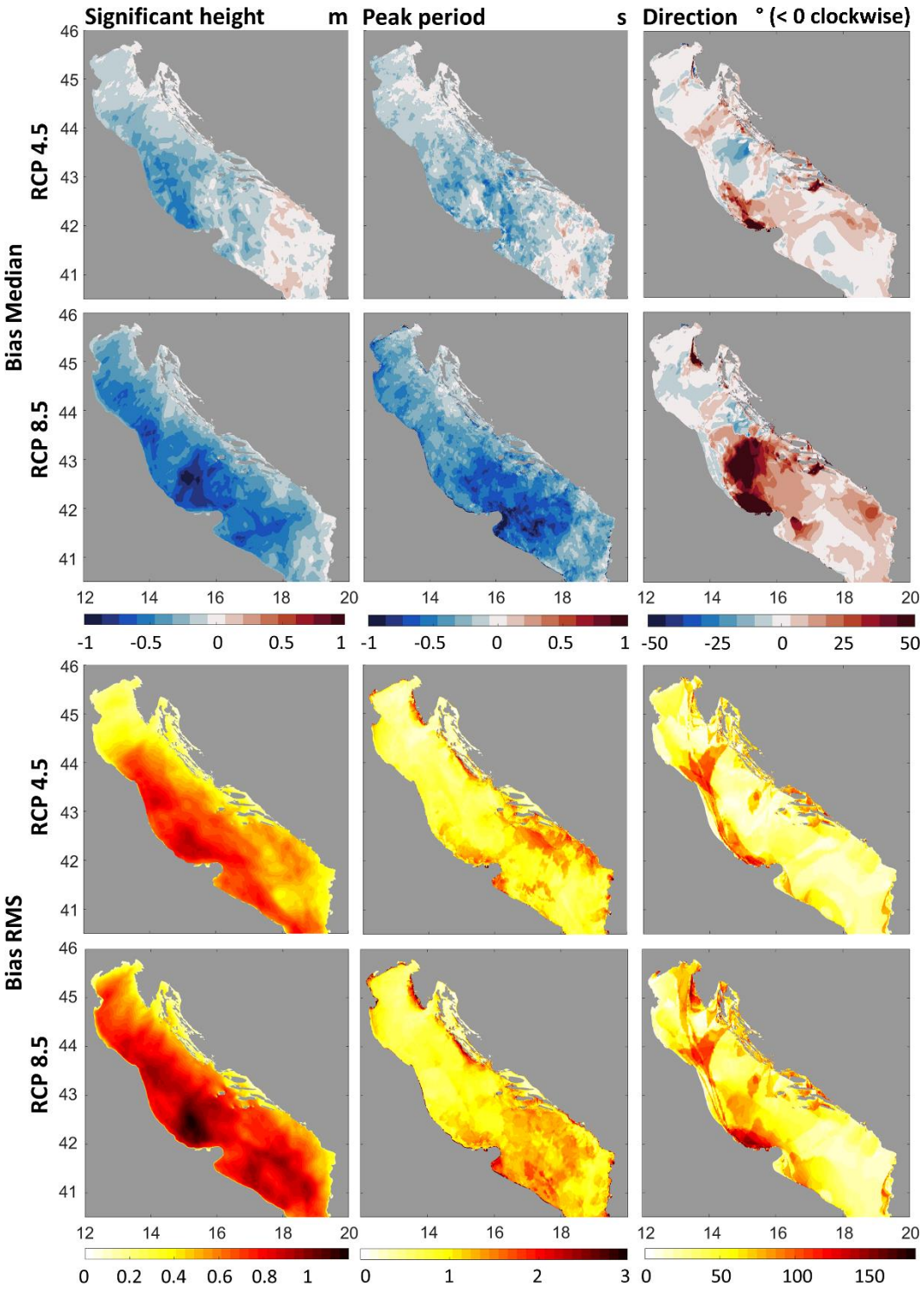

Figure 3.23. Climate change (RCP 4.5 and RCP 8.5) impact on the waves defined as the median and root-mean-square (RMS) of the bias (scenario minus evaluation results) of the maximum significant heights, the maximum peak periods and the mean wave directions of the 22 bora events.

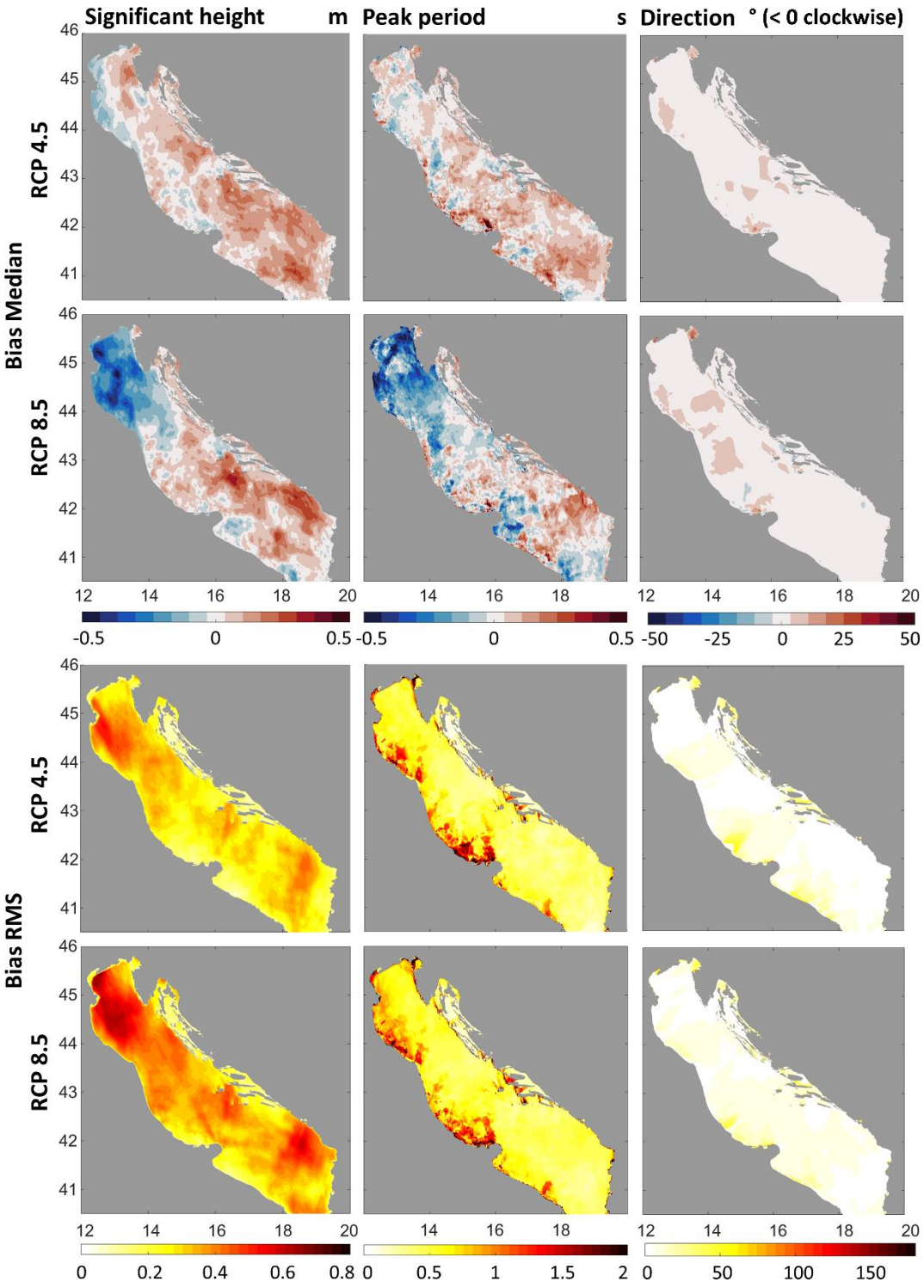

Figure 3.24. As Fig. 3.23, but for the 14 sirocco events.

south-west and west in the northern Adriatic and north-westward in the south. The latter indicate that majority of the selected severe bora events peaked in the northern Adriatic, while being mostly conjoined with sirocco conditions in the southern Adriatic. For the sirocco events, wave heights are substantial in the open Adriatic Sea for the entire domain (except close to the Italian shoreline and in the coastal Croatian area), peaking with values up to 6 m associated with wave periods of 10 s between 44°N and 45°N latitude off the Croatian islands and coast. The typical wave propagation for sirocco events is towards north and north-west.

Typical significant wave heights and peak wave periods are foreseen, in the future climate, to overall decrease during bora events (Fig. 3.23), for both RCP 4.5 and RCP 8.5 scenarios. Negative bias median is projected over the entire Adriatic domain, except at its southern part in the RCP 4.5 scenario. For the RCP 8.5 scenario, the negative bias median reaches up to 1 m in significant height and 1 s in peak period off the Italian coast between 41°N and 43°N latitude and is associated with larger bias variability between events (larger bias RMS) surpassing 0.8 m and 1 s, respectively. The direction of the bora winds is also affected over the entire domain (up to 50° change of direction for the RCP 8.5 scenario), but mostly along the Italian coastline between 42°N and 43°N latitude and regions where strong wind shear occur in the bora jets.

For the sirocco events (Fig. 3.24), the typical significant heights and peak periods are also mostly decreased in the northern Adriatic for both RCP 4.5 and RCP 8.5 scenarios (i.e. small or negative bias median) but increased (i.e. positive bias median) for the rest of the domain. For the RCP 8.5 scenario, the northern Adriatic decreases can reach up to 0.5 m in significant height and 0.8 s in peak period and are associated with large variabilities (i.e. bias RMS) above 0.6 m and 0.5 s, respectively. Furthermore, the direction of the sirocco waves seems to be totally unchanged (both bias median and bias RMS are low) for both RCP 4.5 and RCP 8.5 scenarios.

The analysis of the temporal variations of the wave parameters during the selected Adriatic wave storms is based on the 1-min unSWAN series extracted at 5 open Adriatic Sea locations (O_1 to O_5, Figs. 3.25 to 3.28). Then, a comparison between the distributions obtained in the evaluation and future climate (for RCP 4.5 and RCP 8.5 scenarios) simulations is performed, separately for the ensemble of the 22 bora and 14 sirocco events. The results are presented as a combination of scatter and probability density function (PDF) plots for the significant wave height and peak wave period parameters (Figs. 3.25 and 3.27), and polar histogram plots for the mean wave direction (Figs. 3.26 and 3.28).

For the bora events (Fig. 3.25 and 3.26), the scatter plots at the five chosen locations (Fig. 3.25) reveal that the overall distribution of the peak wave period vs. the significant wave height is not significantly modified under climate change projections and is presenting a strong linear trend at all locations (i.e. the peak periods tend to increase linearly with the significant wave heights), with a little spread in the northern Adriatic only (locations O_4 and O_5). However, the analysis of the PDF distributions confirms that both peak wave periods and significant wave heights during bora events are likely to decrease under climate change projections:

- concerning the significant wave height distributions, the values are consistently lowered in the future climate, with a minimum of 0.25 m at location O_5 (northern most part of the Adriatic Sea) for the RCP 4.5 scenario and a maximum of 2 m at location O_4 (where strongest bora wind are likely to blow) for the RCP 8.5 scenario; the tail is generally becoming less heavy under RCP 8.5 scenario at locations O_3, O_4 and O_5 (i.e. the probability of significant wave heights above 3 m is largely reduced), but does not significantly change in the southern Adriatic (locations O_1 and O_2), at locations under the sirocco influence, for both RCP 4.5 and RCP 8.5 scenarios;

- concerning the peak wave period distributions, the values are also lowered at locations O_2, O_3, O_4 and O_5, with a minimum of 0.5 s at location O_2 and a maximum of 1.5 s at location O_3, both obtained for the RCP 4.5 scenario; as for the significant wave height, the tail is generally becoming less heavy under RCP 8.5 scenario at all locations (i.e. the probability of the peak wave periods above 7 s is largely reduced), but does not present major changes for RCP 4.5 scenario, except at location O_5 (where the tail is clearly less heavy), and at location O_1 (where the tail is more heavy).

- Concerning the mean wave direction distributions (Fig. 3.26), the most significant changes appeared at location O_3 where the waves primarily propagated westward in the evaluation mode; they shift southward and south-eastward for both RCP 4.5 and RCP 8.5 scenarios. Such a shift indicates that the bora events, characterized here by a strong wind shear in the central Adriatic and encompassing mostly the northern Adriatic (Fig. 3.22), will expand towards the central and southern Adriatic in the future climate. This behavior can also be noticed, in a smaller measure, at locations O_2, O_4 and O_5 (Fig. 3.26), where however the main direction of propagation is unchanged. Finally, at location O_1, the most noticeable changes in direction occur for the RCP 4.5 scenario, where the south-westward waves are shifted to north-westward and south-eastward, but the main direction of propagation (i.e. north north-westward) is also unchanged.

For the sirocco events (Figs. 3.27 and 3.28), as for the bora events, the scatter plots at the five chosen locations (Fig. 3.27) reveal that the overall distribution of the peak wave period vs. the significant wave height is not substantially modified under climate change projections. However, these distributions do not present a strong linear trend in the northern Adriatic and show that, at locations O_3, O_4 and O_5, for peak periods above 7 s, significant wave heights can vary between 1 m and 7 m. The analysis of the PDF distributions reveals that, compared to the bora events, less dramatic changes are to be expected concerning the sirocco wave parameters under RCP 4.5 and RCP 8.5 scenarios:

- concerning the significant wave height distributions, the values are mostly unchanged, even though slightly (about 0.25 m in average) increased in the southern Adriatic Sea and decreased in the northern Adriatic Sea; the tail is however generally becoming less heavy under RCP 8.5 scenario in the northern Adriatic Sea at locations O_4 and O_5 (i.e. the probability of significant wave heights above 3 m is reduced) but slightly heavier or unchanged for the remaining locations under RCP 8.5 scenario and for all locations under RCP 4.5 scenario;

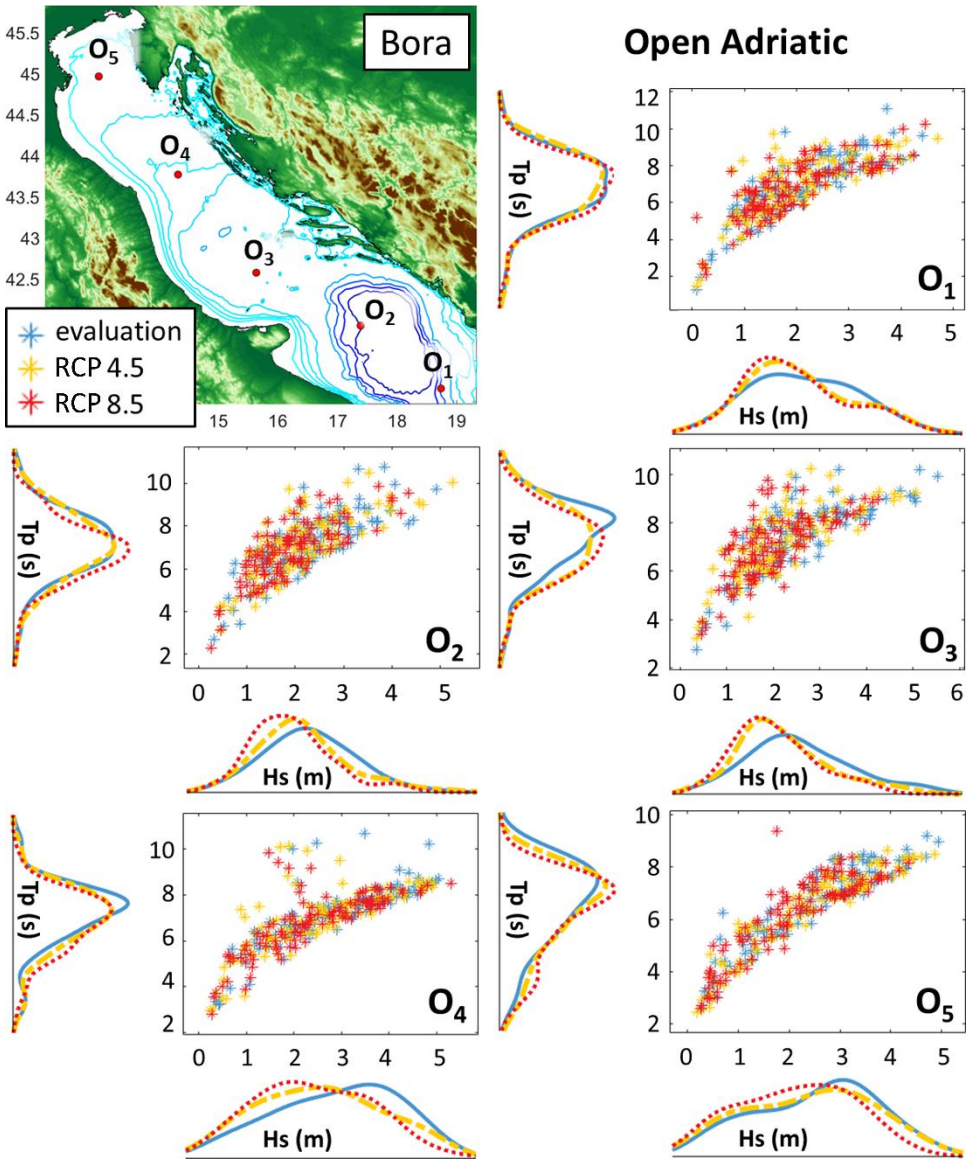

Figure 3.25. Peak wave period (Tp) vs. significant wave height (Hs) distributions derived from the 1-min AdriSC unSWAN evaluation and future climate projection (RCP 4.5 and RCP 8.5) results of the 22 bora events and extracted at 5 open Adriatic Sea locations (O_1 to O_5). The results are presented as a combination of scatter plots displaying the distributions of the peak period vs. the significant height.

- concerning the peak wave period distributions, the distributions are also mostly unchanged at all locations and for both climate change scenarios, but the respective probabilities are increased in the southern Adriatic (locations O_1, O_2 and O_3); as for the tail, it is generally becoming slightly less heavy under RCP 8.5 scenario in the northern Adriatic (i.e. the probability of the peak wave periods above 9 s is reduced) but does not present major changes for RCP 4.5 scenario.

Finally, the mean wave direction distributions (Fig. 3.28) show that the north-westward main direction of the waves in evaluation mode remains unchanged under both RCP 4.5 and RCP 8.5 scenarios.

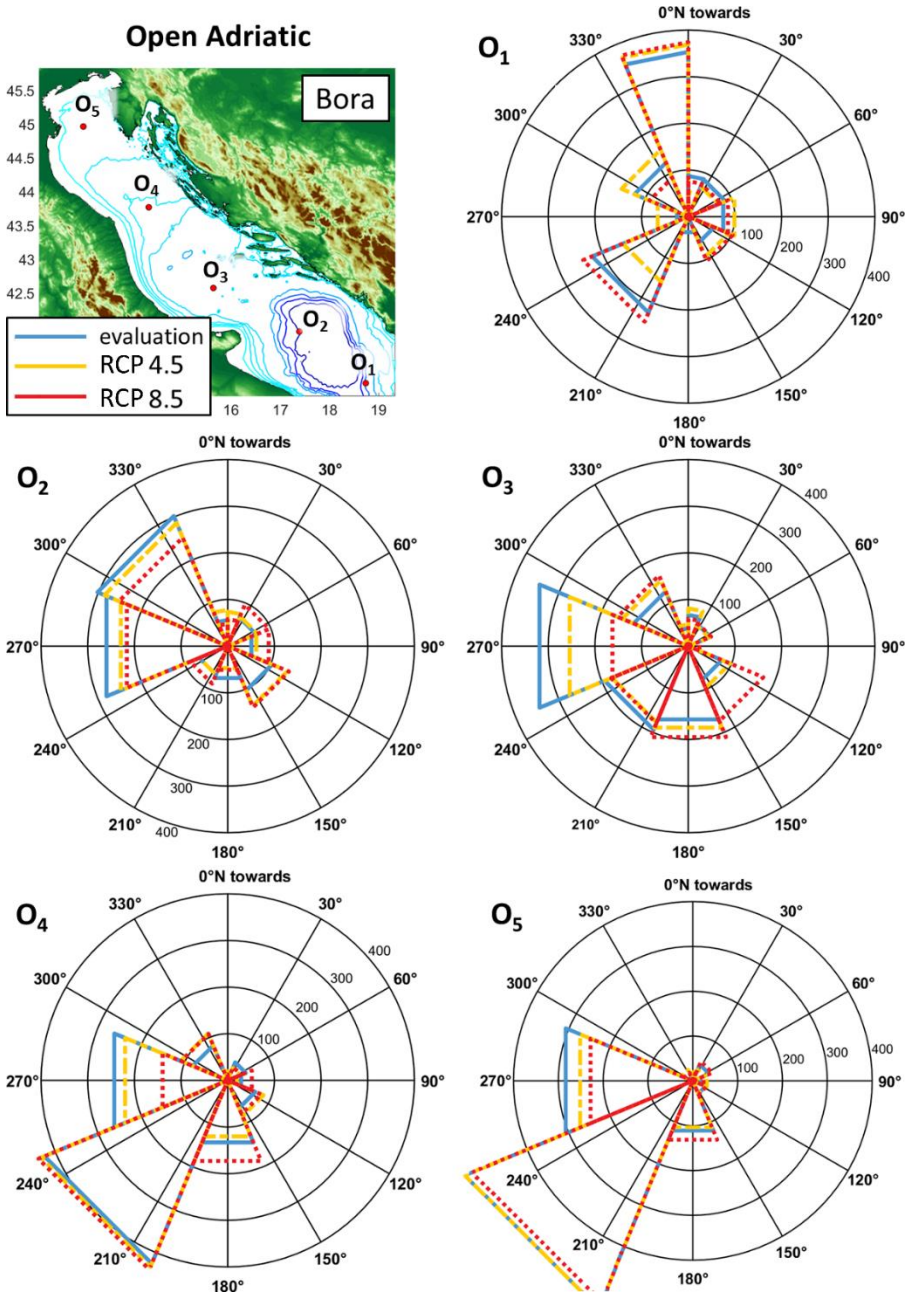

Figure 3.26. Mean wave direction distributions derived from the 1-min AdriSC unSWAN evaluation and climate projection (RCP 4.5 and RCP 8.5) results of the 22 bora events and presented as rose plots at 5 open Adriatic Sea locations (O_1 to O_5).

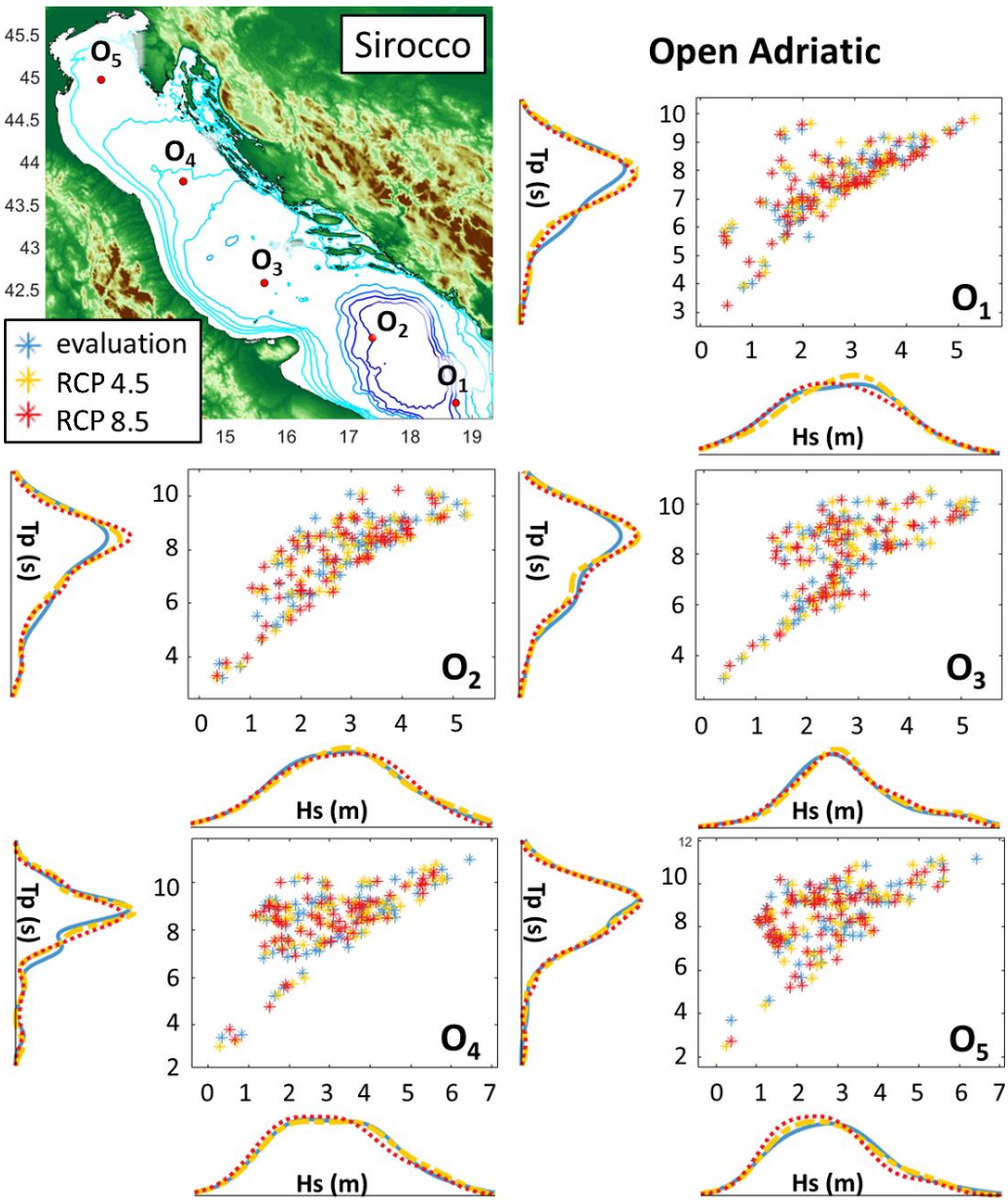

Figure 3.27. As in Fig. 3.25, but for the 14 sirocco events.

To summarize, the spatial variations of the extremes and the 1-min time series – extracted along the open Adriatic Sea, reveal that, under warming climate change (for both RCP 4.5 and RCP 8.5 scenarios), significant wave heights and peak wave periods are likely to strongly decrease over the entire domain, with a south-eastward shift of direction during the extreme bora events, and to decrease in the northern

Adriatic with no change in direction during the extreme sirocco events. These results are in good agreement with the study of Belušić Vozila et al. (2019) which estimated the possible future changes in wind speed over the Adriatic region, for the 2041-2070 period, from an ensemble of 19 high-resolution

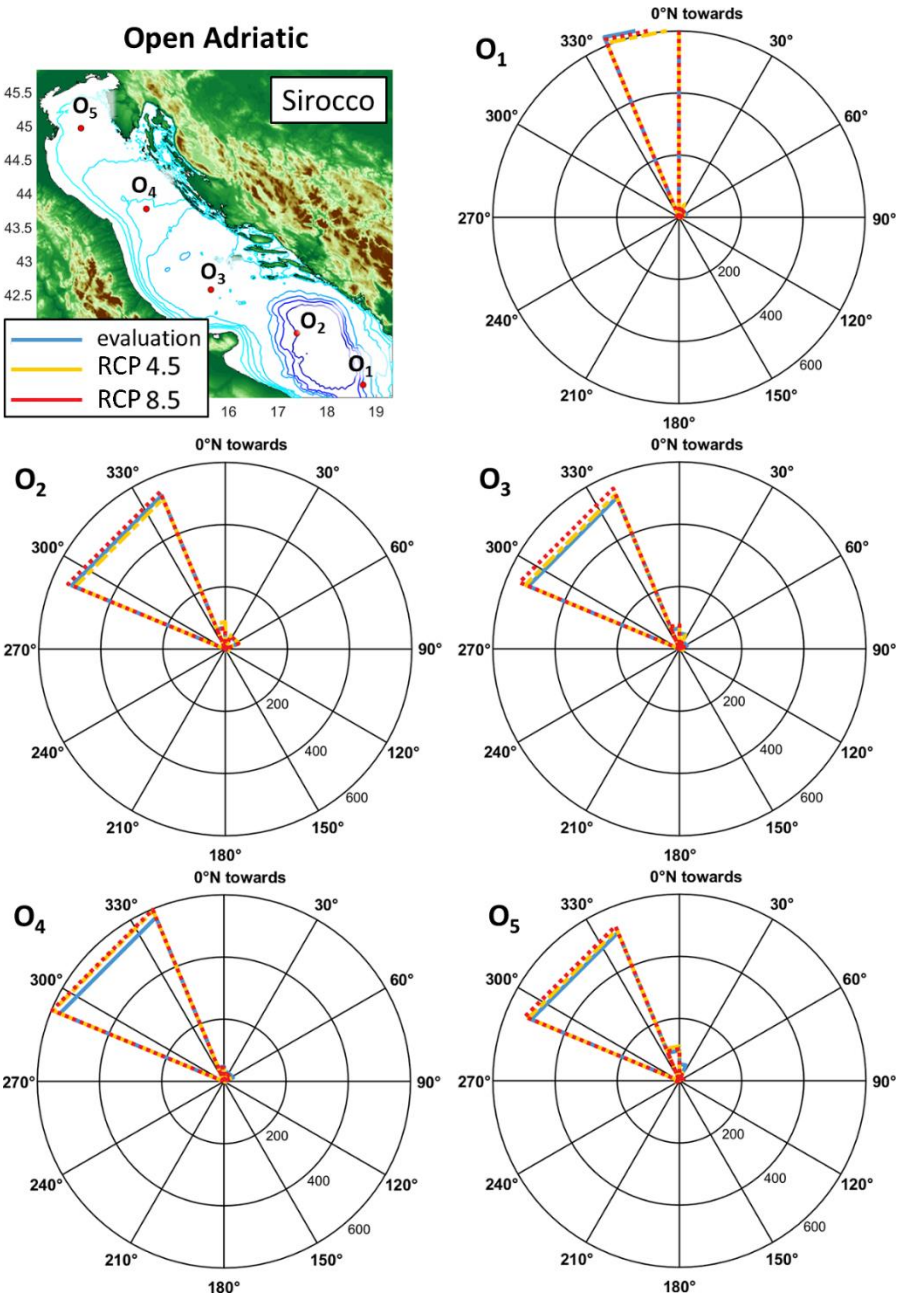

Figure 3.28. As in Fig. 3.26, but for the 14 sirocco events.

(0.11°) CORDEX simulations and found that overall the mean wind speed as well as the number of storms is reduced under the RCP 8.5 scenario for both bora and sirocco conditions. However, Belušić Vozila et al. (2019) also highlights an increase of the bora mean wind speed in the northern Adriatic, which is not in accordance with the presented results (Figs. 3.23 and 3.25). Although selection of bora events differs between the two studies, this result may indicate the limitation of the PGW methodology which can only be used to assess how past storms would behave under climate change. Additionally, the presented results are in good agreement with other wave climate studies, which all envisage a decrease of wave heights in the Adriatic Sea, in particular concerning sirocco events (Benetazzo et al. 2012; Lionello et al. 2012a; Bonaldo et al. 2017; Pomaro et al. 2017).

3.2.4 Future "acqua alta" projections

In terms of the climate change impact on storm surges, the flooding of the coastal cities along the Adriatic coast – and most particularly in the northern Adriatic, is known to be driven by extreme sirocco conditions (e.g. Robinson et al. 1973; Cavaleri 2000; Cavaleri et al. 2010; Raicich 2015; Međugorac et al. 2015), such as those selected in Section 3.2.2 which led to the highest water levels recorded in Venice lagoon between 1979 and 2019. The atmospherically- driven extreme sea level changes in the northern Adriatic under RCP 4.5 and RCP 8.5 scenarios and following the PGW methodology can thus be assessed in this study with the ensemble of the selected 14 sirocco events.

The AdriSC ADCIRC model capability to reproduce the storm surges in the northern Adriatic and more specifically in the Venice Lagoon and the Gulf of Trieste is first assessed with a sea level distribution quantile-quantile analysis (Fig. 3.29.a) of the available hourly measurements and the ADCIRC model results – extracted at the locations of the two tide gauges (Section 3.2.2) from the last 24-h results of the 14 sirocco simulations carried out in evaluation mode. To be noted, (1) as the bathymetry used in the ADCIRC model may be imprecise and may use a different vertical reference level than the tide gauges, the local mean sea levels of the model results at Venice and Trieste locations were adjusted by adding the difference between the measured and the modelled mean values calculated for the ensemble of the 14 sirocco events; (2) as tides play an important role on extreme storm surges, they were not removed from the sea level signals, and (3) as this study only aims to present the climate change impact on the sea level distributions during sirocco events in the northern Adriatic Sea and not to reproduce individual storm surges, the model evaluation can be performed with the presented quantile-quantile analysis.

Similarly to the analysis performed for the waves in Section 3.3.2, the impact of climate change for the 2060-2100 period on the northern Adriatic storm surges under both RCP 4.5 and RCP 8.5 projections, is then estimated via the statistical analysis of two kind of results: the spatial variations of the maximum sea-levels obtained for each storm (Figs. 3.29.b and 3.30) and the 1-min sea level temporal variations at both the Venice Lagoon and the Gulf of Trieste tide gauge locations (Figs. 3.29.c and 3.29.d).

For the spatial variations, the sea level baseline condition (Fig. 3.29.b) is defined as the median over the ensemble of the 14 selected storm simulations in evaluation mode and their maximum sea levels –

calculated for each storm over the last 24-h results of the AdriSC nearshore module. As in Section 3.3.2, the climate change impact on the storm surges is given by the differences (referred hereafter as biases)

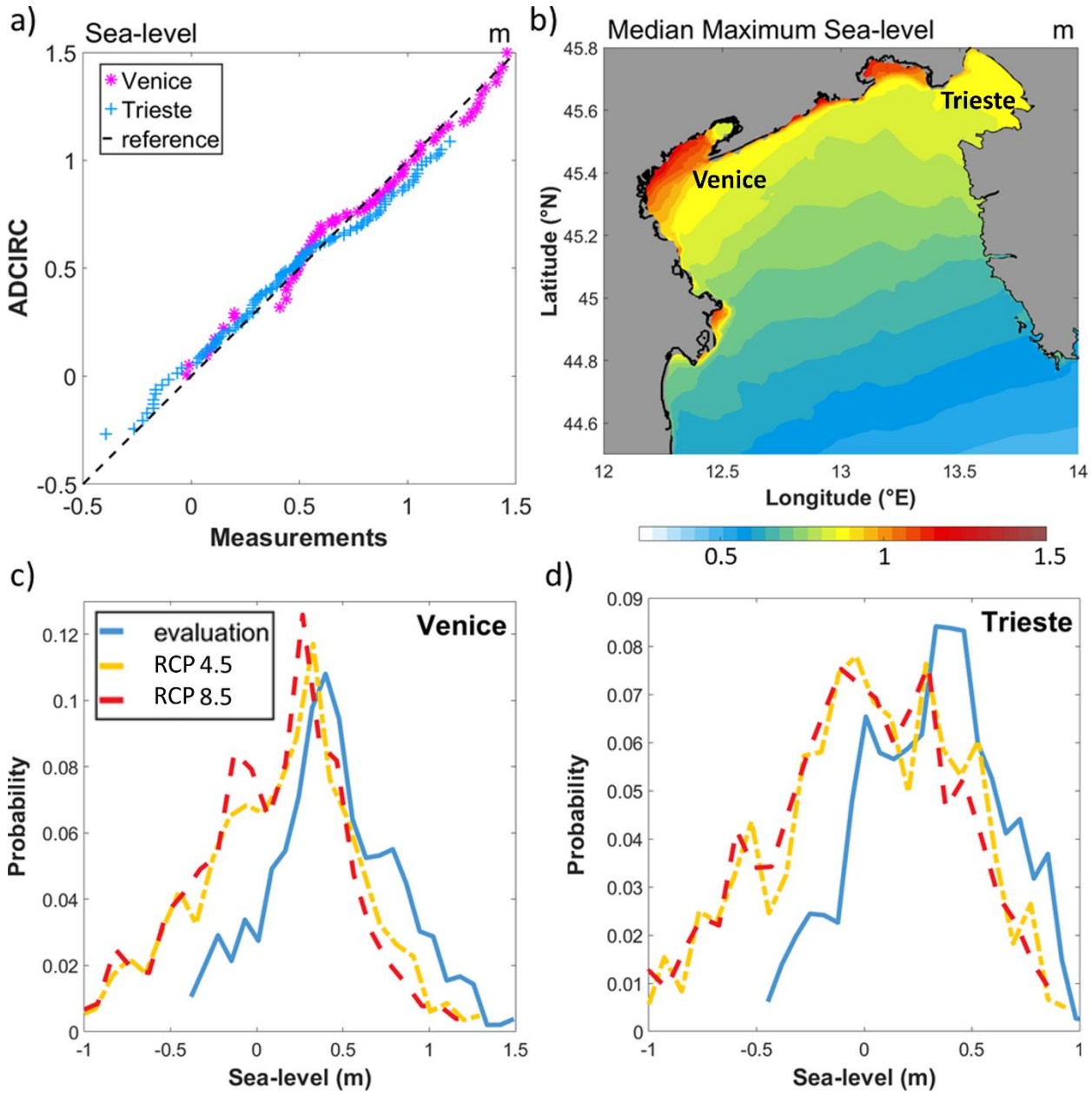

Figure 3.29. Analysis of the northern Adriatic storm surge distributions during the 14 sirocco events: a) quantile-quantile analysis of the AdriSC ADCIRC results and the measurements at Venice and Trieste tide-gauge stations, b) baseline sea level plot defined as the median of the maximum sea levels generated by each storm, c) and d) sea level distributions derived from the 1-min AdriSC ADCIRC evaluation and climate projection (RCP 4.5 and RCP 8.5) results and extracted respectively at Venice and Trieste tide gauge stations.

in maximum sea levels between the climate change simulations (with the RCP 4.5 and RCP 8.5 scenarios treated separately) and the evaluation runs and the median and root-mean-square (RMS) of these biases are calculated for the ensemble of 14 sirocco events (Fig. 3.30). In terms of the results, the baseline condition (Fig. 3.29.b) shows that typical storm surges during sirocco events reach 1.4 m in the Venice Lagoon and 0.9 m in the Gulf of Trieste and, under climate change conditions (Fig. 3.30), are decreased (i.e. negative bias median) by more than 0.25 m over the entire northern Adriatic domain for both RCP

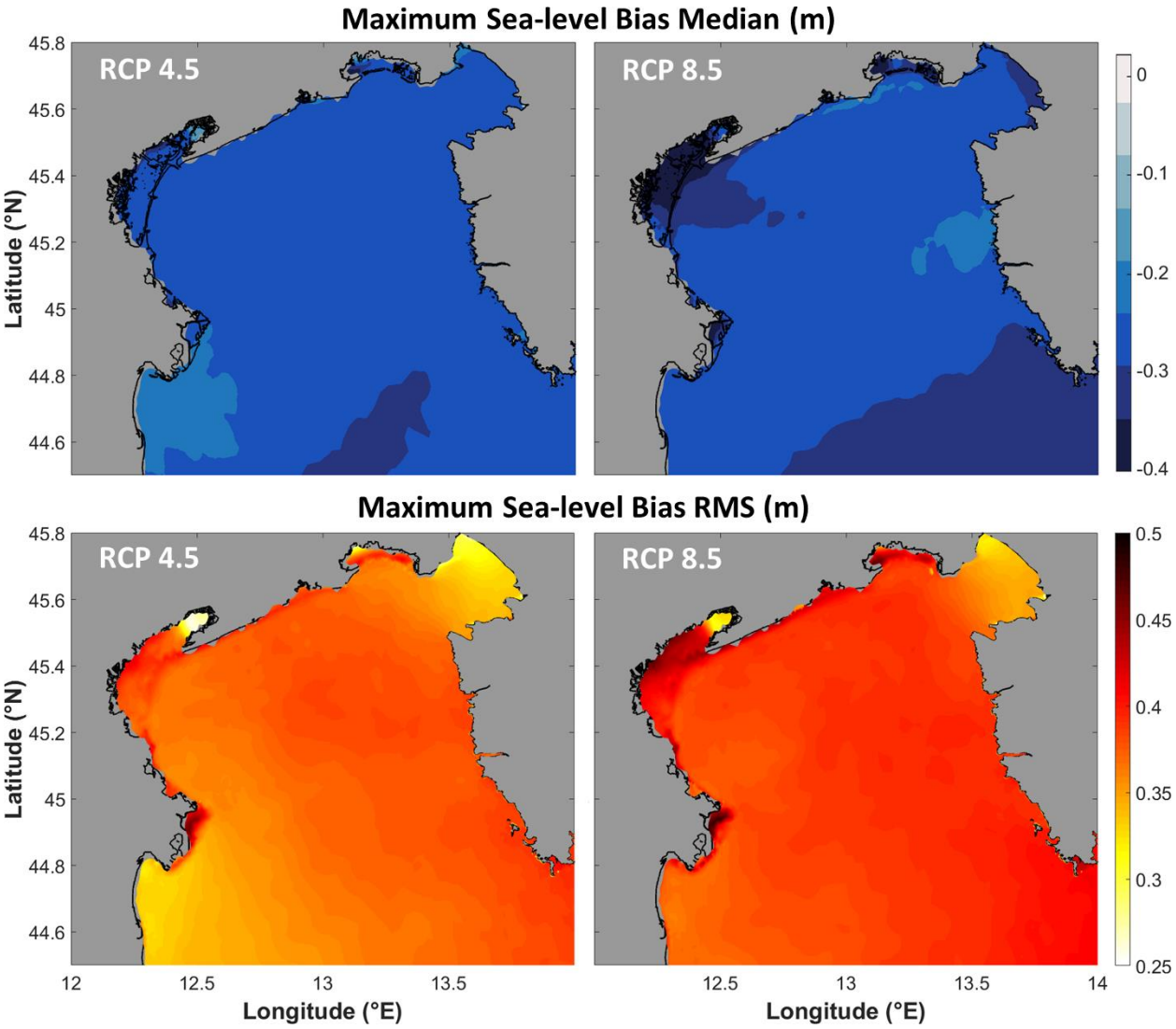

Figure 3.30. Climate change (RCP 4.5 and RCP 8.5) impact on the northern Adriatic extreme sea levels defined as the median and root-mean-square (RMS) of the bias (scenario minus evaluation results) of the maximum sea levels for the 14 sirocco events.

4.5 and RCP 8.5 scenarios, and more than 0.35 m in the Venice lagoon for the RCP 8.5 scenario. The decrease of the storm surges in the future climate is also associated with an important variability (i.e. bias RMS) of about 0.35 m in average for both RCP 4.5 and RCP 8.5 scenarios and reaching more than 0.45 m in the Venice Lagoon for RCP 8.5 scenario.

These results are confirmed by the temporal analysis of the sea level distributions (for the evaluation runs and the RCP 4.5 and RCP 8.5 projections) at Venice and Trieste tide gauge locations (Fig. 3.29.c and 3.29.d). It appears that, at both locations under RCP 4.5 and RCP 8.5 climate change, the modes of the sea level distributions are decreased by about 0.25 m, the tails of the distributions are less heavy (i.e. the probability of storm surges above 0.75 m is greatly decreased), the maximum surges are reduced by about 0.25 m and (4) the probability of sea-levels below -0.5 m (which was the minimum reached in evaluation mode) is largely increased. This last point reveals that, under the climate change projections, some of the strong sirocco events simulated in evaluation mode might take more time to develop (or never developed) as storms of lower intensity in the RCP 4.5 and RCP 8.5 simulations and thus, for these events, the wind-wave set-up – building up in the northern Adriatic during the 3 days of simulation in evaluation mode, was decreased as it built up over a smaller period with weaker winds (or did not built up at all).

To summarize, under climate change projections with imposed PGW methodology, the northern Adriatic sirocco storm surges are not only likely to decrease but also to be less frequent, which is in accordance with the analysis of the sirocco wind and storm surge projections (Lionello et al. 2012b; Androulidakis et al. 2015; Belušić Vozila et al. 2019). However, as the subsidence of the Venice Lagoon is not considered in this study, and the sea level change is imposed as a mean effect for the entire 2060-2100 period in the PGW methodology and the Atlantic global sea level rise is ignored, these results do not imply that flooding of the Venice city will be less likely in the future.

4. OCEAN DYNAMICS IN A CLIMATE CHANGE SCENARIO

4.1. MULTI-DECADAL OCEAN MODELLING (ISMAR)

For the present study the possible variations of oceanographic dynamics in the Adriatic Sea in a severe climate change scenario (RCP 8.5) have been investigated by implementing a ROMS (Regional Ocean Modeling System, Haidvogel et al., 2008) numerical simulation. In the present work we introduce the methodology underlying the model implementation, a validation of the results, and some preliminary conclusions in terms of future projections. As done for the wave modelling activity described in Section 3.1, selected time series and model fields are available in the Project Owncloud repository at https://owncloud.ve.ismar.cnr.it/owncloud/index.php/s/efj6wcDhi2Y9D4u, and other fields are available on request by contacting davide.bonaldo@ve.ismar.cnr.it.

4.1.1. Model implementation

Due to the long "memory" of the ocean thermohaline conditions, namely its strong dependency on its previous states, in this case future conditions could not be assessed by comparing a future scenario run with an independent (although carried out with the same model) control simulation, as done for instance in the wave modelling activity described in Section 3.1. On the contrary, it has been necessary to implement a single continuous multi-decadal experiment spanning from 1987 to 2099. Within this time range, three 30-year periods were identified and compared, namely:

- Control (CTR): 1987-2016;
- Mid-Term Scenario (MTS): 2020-2049;
- Long-Term Scenario (LTS): 2070-2099;

The horizontal domain discretization (Figure 4.1) is the same used in the wave modelling study, but here we highlight the position of the observing stations used for time series validation and of the transect conventionally used for delimiting the Northern and Southern parts of the basin (Artegiani et al., 1997). The water column is vertically discretised into 15 terrain-following "sigma" levels (that is, the level is not given in terms of its geodetic coordinate but of its relative position along the water column), progressively refining towards the surface, in order to better describe the processes controlled by heat and momentum exchanges between the sea and the atmosphere. The seabed bathymetry has been smoothed as described by Sikirić et al. (2009) in order to prevent sharp gradients to induce artifact numerical horizontal pressure gradients, thus altering the circulation fields.

Atmospheric forcing was provided by 6-hourly fields (total cloud fraction, relative humidity, air pressure at sea level, precipitation, solar short-wave radiation, near surface air temperature, 10-m wind speed) from the SMHI-RCA4 model run, with approximately 12 km horizontal resolution. Potential Temperature, Salinity, momentum and sea level were prescribed as monthly boundary conditions at Otranto Strait. The

baseline was given by the 30-year climatological values computed from the MFS 1/16° reanalysis (Simoncelli et al., 2019), with monthly temperature and salinity values modulated following the anomalies computed from CMCC-CM profiles. Both SMHI-RCA4 and CMCC-CM fields were collected from the EURO-CORDEX repository.

Fresh water input from rivers was prescribed as interannual modulations of the climatological values for 39 point sources throughout the Adriatic coast. The baseline was given by the estimates provided by Raicich (1994) and Janeković et al. (2014), plus the overall contribution from the Venice lagoon as estimated by Zuliani et al. (2005), whereas the modulation followed the interannual modulation of the precipitations reproduced by SMHI-RCA4 on the Adriatic watershed.

Model outputs were provided every three hours, in order to have a sufficient time resolution for a good description of sub-inertial oscillations within the basin (e.g. Bonaldo et al., 2018).

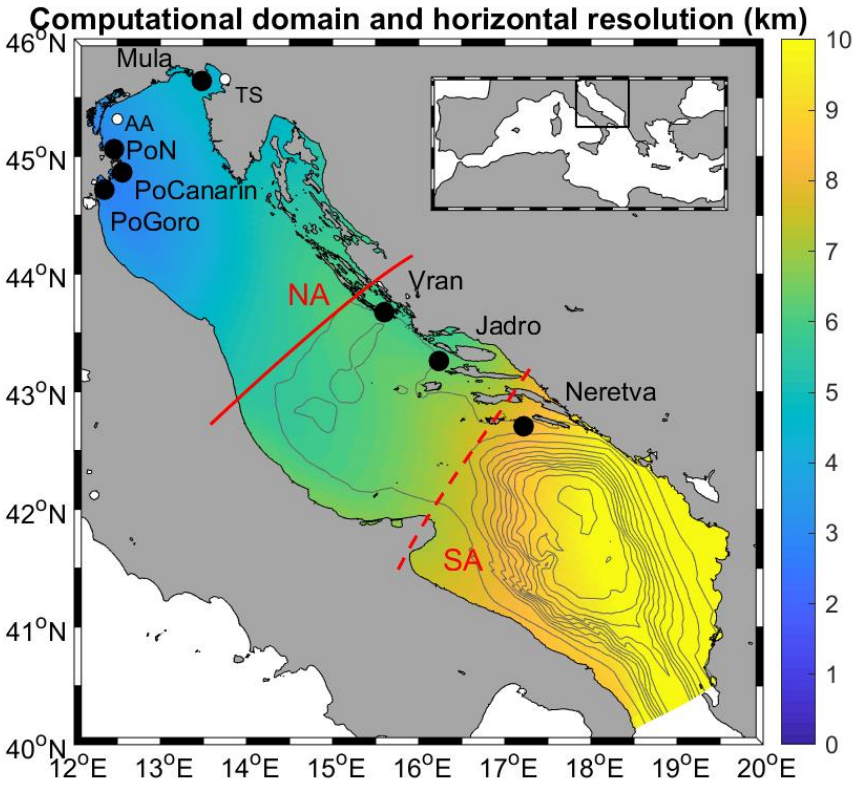

Figure 4.1: Geographical framework of the study: Adriatic Sea and its position within the Mediterranean Basin. Contour lines represent 100-m spaced isobaths, colour pattern represents the dimension of the horizontal grid step, and red solid and dashed lines represent the transects conventionally identify to delimit the Northern and Southern Adriatic respectively. Large black dots represent the locations offshore of the pilot sites in which the modelled time series have been extracted and made available. White dots represent the positions of the Acqua Alta oceanographic tower and Trieste observing station, considered in the model validation.

4.1.2. Model validation

The atmospheric forcing in CTR conditions was validated by comparing SMHI-RCA4 model field against multi-decadal wind speed and air temperature, respectively at Acqua Alta oceanographic tower (AA, 12.51 °E, 45.31 °N) and Trieste Station (TS, 13.75 °E, 45.64 °N), provided in the CHANGE WE CARE Deliverable 3.1.2 Dataset (https://owncloud.ve.ismar.cnr.it/owncloud/index.php/s/g4DVSdo58YTdgTK).

Figure provides a visualization of the daily-averaged wind roses for modelled (coloured bars) and observed (black bars) values at Acqua Alta oceanographic tower, unraveled along a linear axis in order to be superimposed for a direct comparison. Although with some overestimate in the milder easterly and southeasterly wind conditions, the model captures most of the directional features of wind climate in this site. Air temperatures ingested in ROMS as a forcing from SMHI-RCA4 (Figure) exhibit the same seasonal variability as observed in the measurements, but with a bias of approximately -2°. This mismatch could be related with local numerical effects due to the position of the grid point close to the land-sea interface, and should be further investigated by adding more points to the validation dataset.

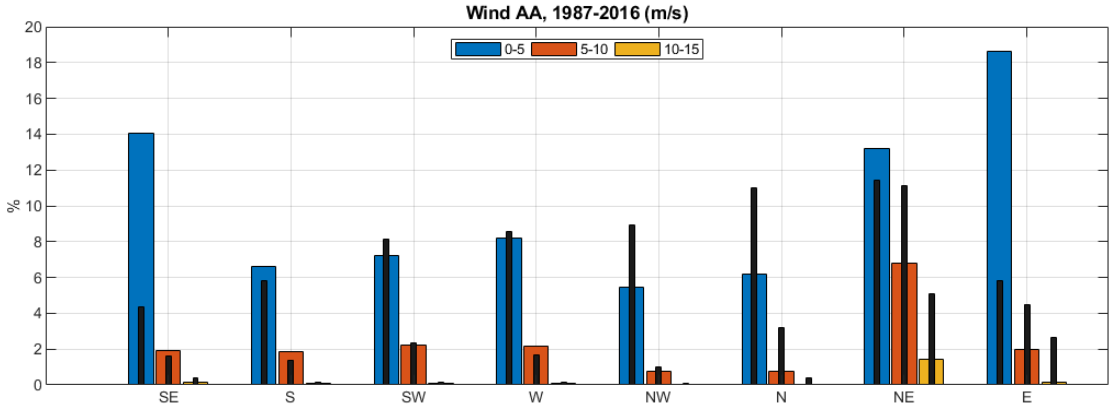

Figure 4.2: Directional validation of SMHI-RCA4 wind at Acqua Alta oceanographic tower (coloured bars) against observed data (black bars).

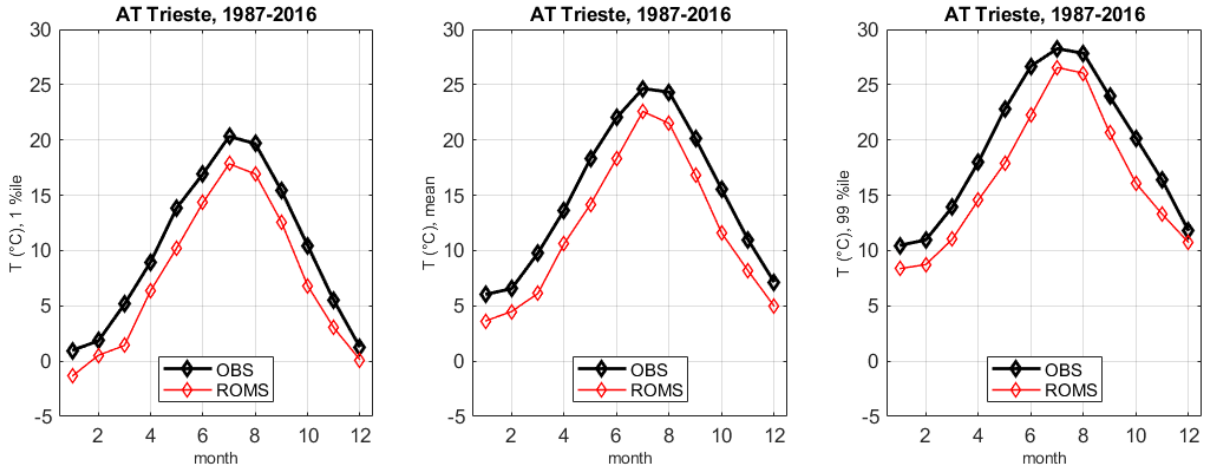

Figure 4.3: Air temperature climatology at Trieste, 1st percentile (left), monthly mean (middle), and 99th percentile (right).

In order to assess the model capability of reproducing the mean seasonal thermohaline properties of the Adriatic Sea and its northern and southern sub-basins (Figure 4.1), the modelled average vertical profiles of potential temperature, salinity and potential density were compared with the ones computed by Artegiani et al. (1997) based on a multi-decadal observational dataset. Consistently with that study, two extreme seasons were identified (namely Winter and Summer, respectively bracketing January to April and July to October), alongside two transitional ones (Spring, May-June, and Autumn, November-December).

In the Northern Adriatic Sea, winter and autumn are characterized by an overestimation of potential temperature (Figure) by 0.5-1 °C in the uppermost 40 m, whereas salinity profiles (Figure) in autumn are overestimated by up to 0.4, and in winter satisfactorily agree with Artegiani et al. (1997).

As a result, potential density anomaly profiles (Figure) in these seasons fit the observations with a mismatch generally smaller than 0.1 kg m^{-3}: this turns very relevant, for instance, in possible considerations about wintry dense water formation. In spring and summer, temperature appears underestimated by approximately 1 °C in the near-surface (0 to -20 m) zones, and overestimated by approximately the same amount deeper below. In the same seasons, salinity is overestimated by +1 or more in the near-surface levels, progressively reducing this mismatch while moving towards deeper regions: as a result, potential density anomaly is overestimated by 1 (2 in the summer) kg m^{-3} in the uppermost 20 m, while moving very close to the observations in the deeper zones.

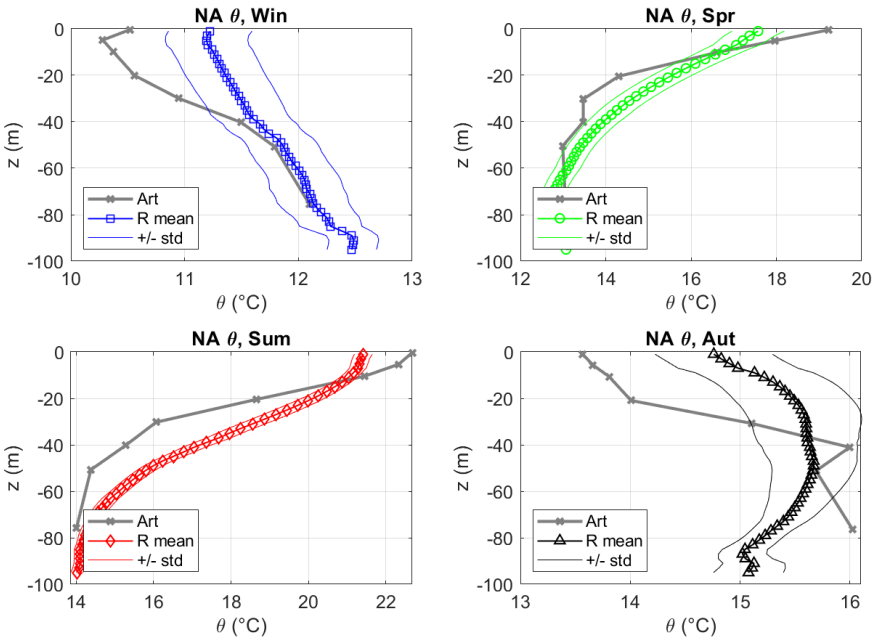

Figure 4.4: Seasonal potential temperature profiles in the Northern Adriatic basin: R(OMS) interannual mean and standard deviation (reference period 1987-1996) vs. Art(egiani et al., 1997) dataset.

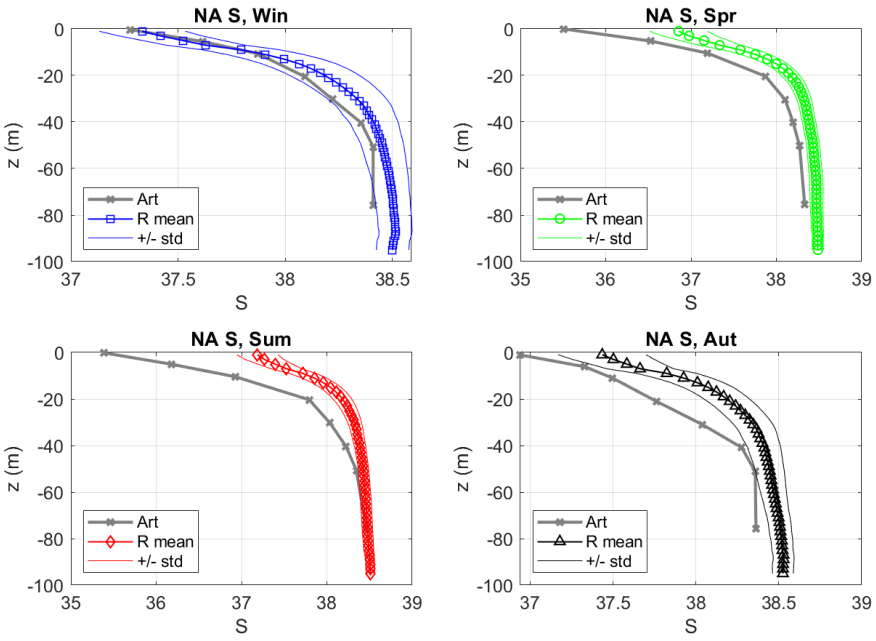

Figure 4.5: Seasonal salinity profiles in the Northern Adriatic basin: R(OMS) interannual mean and standard deviation (reference period 1987-1996) vs. Art(egiani et al., 1997) dataset.

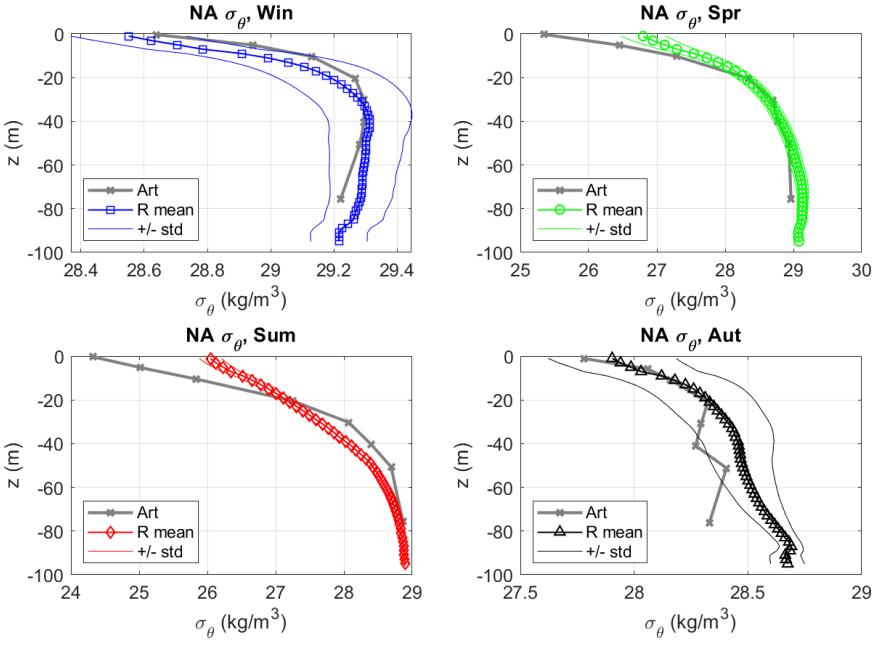

Figure 4.6: Seasonal potential density anomaly profiles in the Northern Adriatic basin: R(OMS) interannual mean and standard deviation (reference period 1987-1996) vs. Art(egiani et al., 1997) dataset.

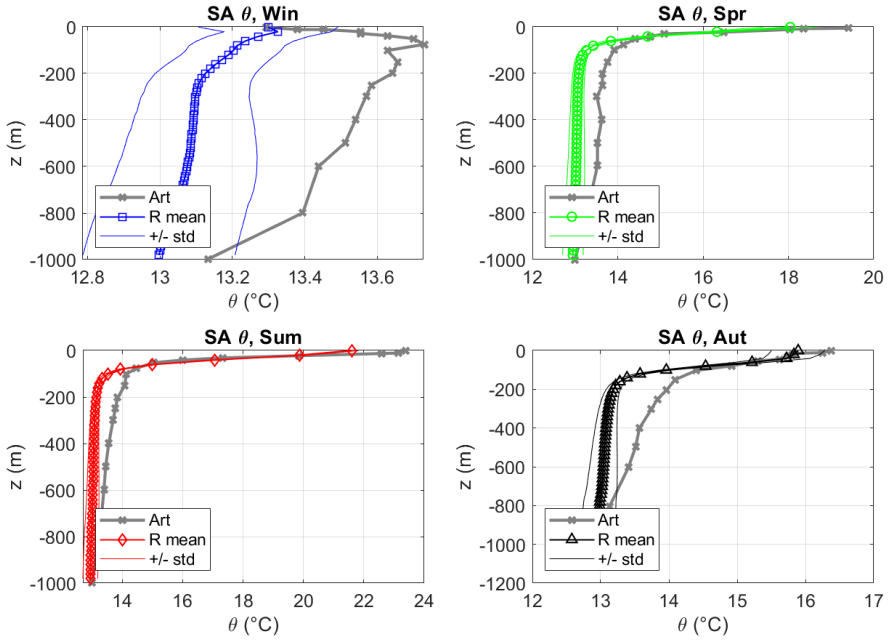

Figure 4.7: Seasonal potential temperature profiles in the Southern Adriatic basin: R(OMS) interannual mean and standard deviation (reference period 1987-1996) vs. Art(egiani et al., 1997) dataset.

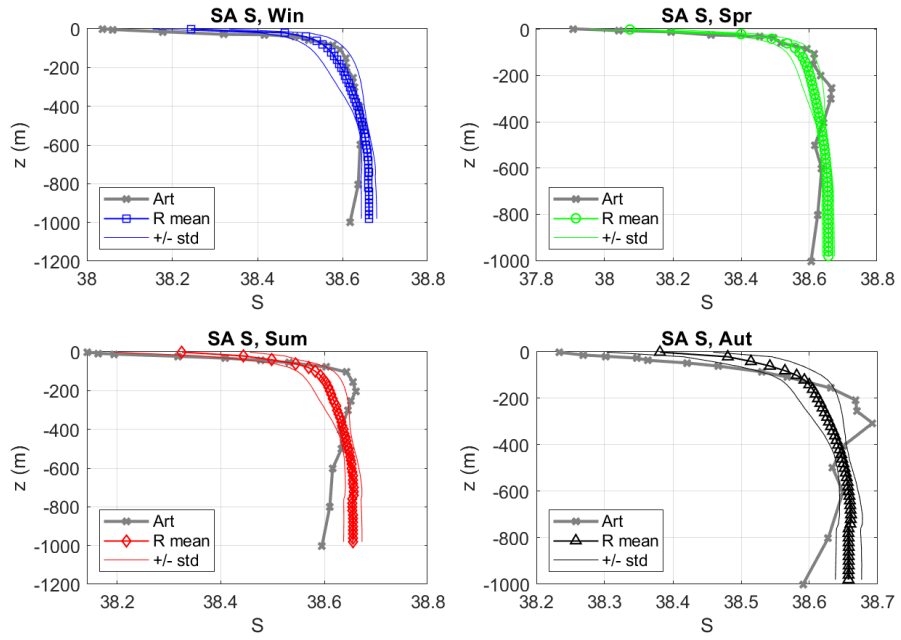

Figure 4.8: Seasonal salinity profiles in the Southern Adriatic basin: R(OMS) interannual mean and standard deviation (reference period 1987-1996) vs. Art(egiani et al., 1997) dataset.

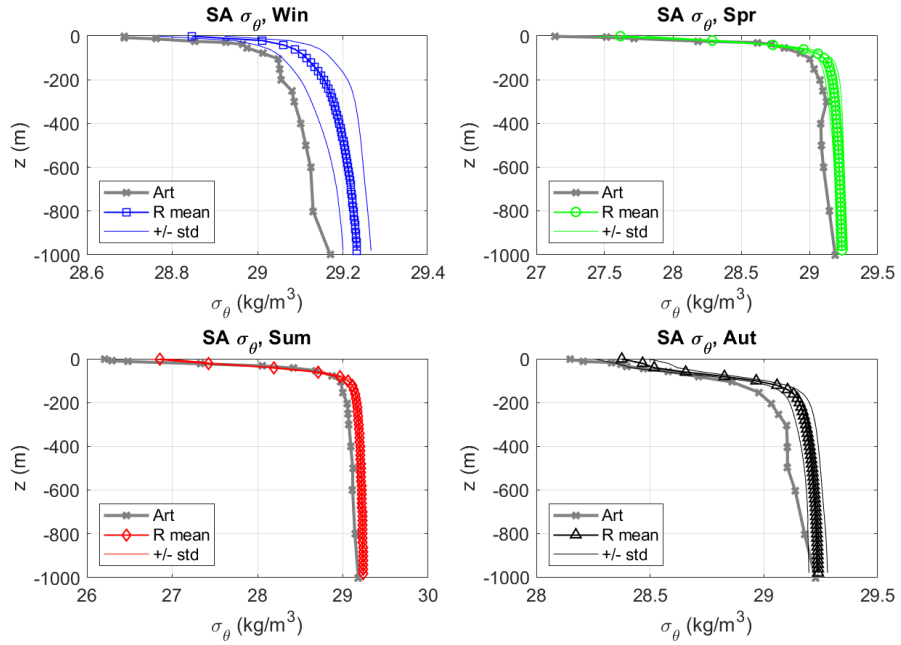

Figure 4.9: Seasonal potential density anomaly profiles in the Southern Adriatic basin: R(OMS) interannual mean and standard deviation (reference period 1987-1996) vs. Art(egiani et al., 1997) dataset.

In the Southern Adriatic Sea, modelled potential temperature (Figure) is characterized by a variable underestimate, with the largest mismatch in the intermediate zones between -200 and -800 m. In winter, spring and summer the maximum difference is around 0.5 °C, locally increasing up to 1 °C at approximately -200 m depth in autumn. In turn, modelled salinity profiles (Figure) are in good agreement with the estimates by Artegiani et al. (1997), with a slight underestimation (smaller than 0.1) between -200 and -400 m depth and an overestimate on the same entity for depth larger than -600 m. As a result, mostly in response to the temperature bias, potential density anomaly tends to a slight overestimate throughout all seasons, in any case never exceeding 0.1 kg m^{-3}.

Further indications about the model performances in reproducing seasonal variability in sea surface temperature (SST) can be drawn from the comparison against point-wise time series collected in Trieste (Raicich and Colucci, 2019) and from basin-wide statistics of satellite-retrieved SST from reprocessed Pathfinder V5.3 (PFV53) AVHRR data (available in CMEMS, Buongiorno Nardelli et al., 2013; Pisano et al., 2016). Data collected in Trieste (Figure) shows an overall satisfactory capability of reproducing seasonal variability, though with some limitations in terms of interannual variability, especially in late spring – early summer (that is, from June to August). In fact, modelled 1st and 99th temperatures in these months are respectively over- and under-estimated by up to 1.5 °C. At the basin scale (Figures 4.11-4.13), the mismatch between modelled and observed values is generally in the range of ±1°, with a relevant exception in spring and summer mean values and 99th percentiles, when SST is underestimated by 1° or more in the whole basin. It is nonetheless worth recalling that some attention should be paid when analysing these evidences. In fact, the comparison involves on the one hand the very uppermost layer of the water column, generally representative for a few millimeters close to the air-sea interface (as is the case of satellite-retrieved data), and on the other hand a discrete portion of the water column with thickness ranging between the order of 1 cm and 1 m (depending on the local water depth, as in the case of modelled values in the sigma-level vertical discretization).

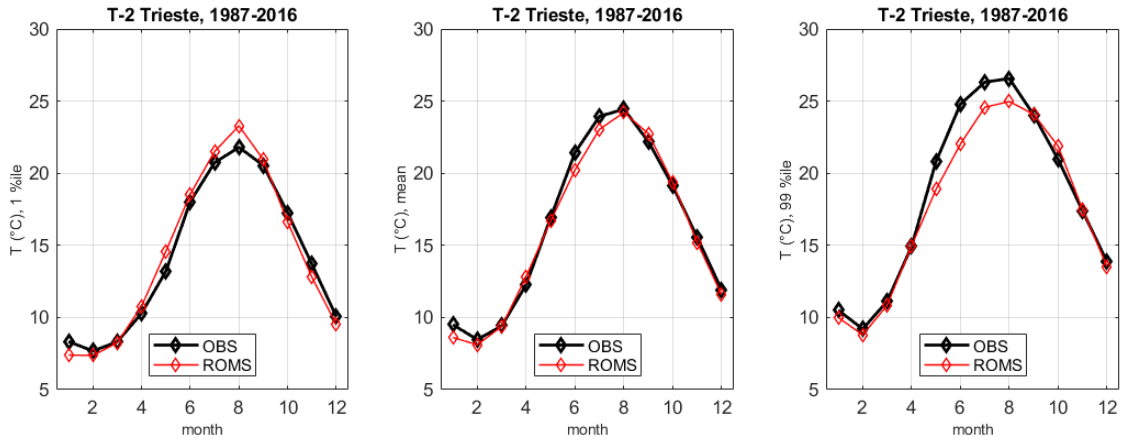

Figure 4.10: Climatological statistics of 2-m depth water temperature in Trieste harbour (see Figure 4.1) over the CTR period (1987-2016). Left: monthly 1st percentile; middle: monthly mean; right: monthly 99th percentile.

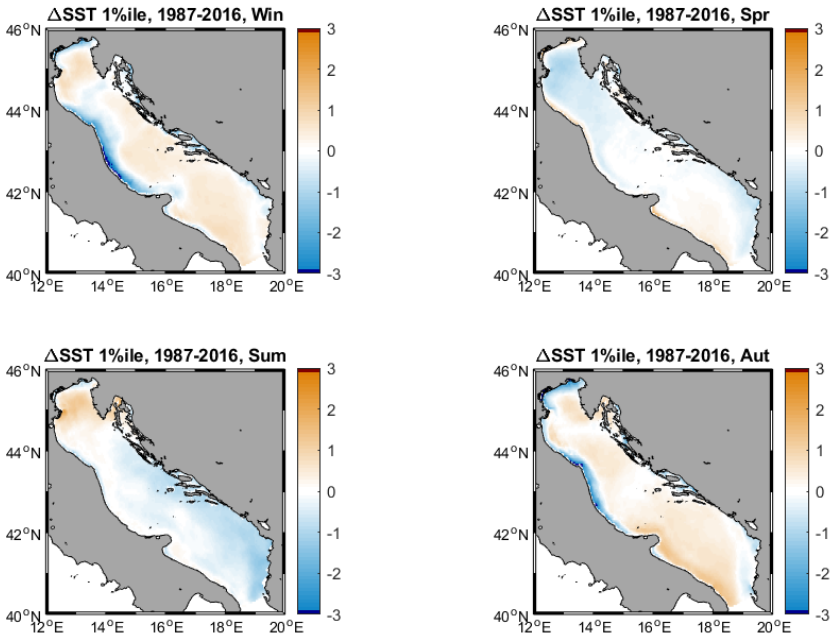

Figure 4.11: Difference between modelled and observed patterns of SST seasonal 1st percentile.

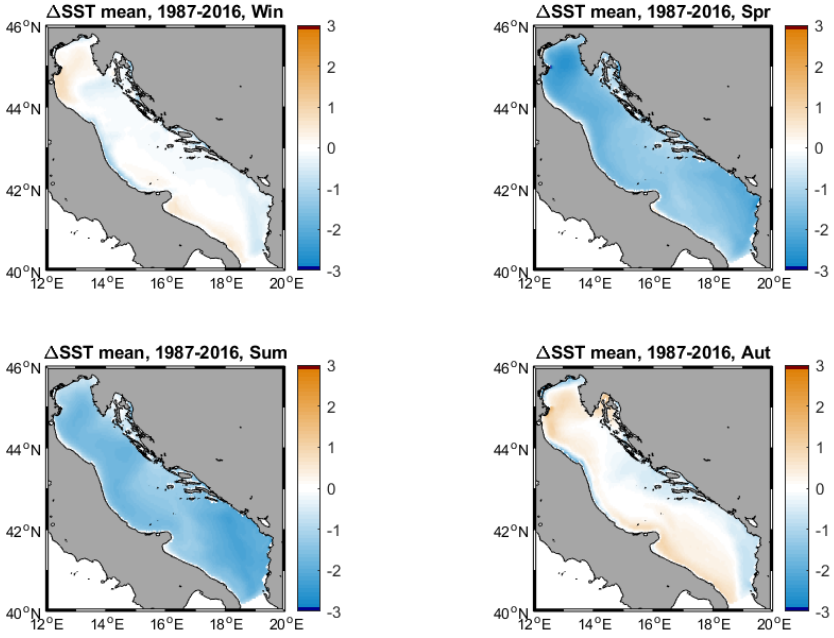

Figure 4.12: Difference between modelled and observed patterns of seasonal mean SST.

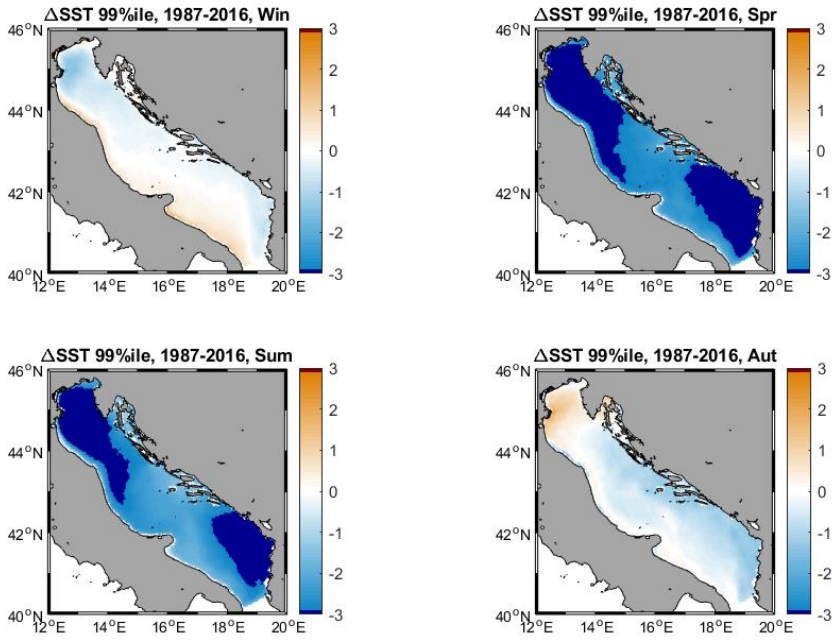

Figure 4.13: Difference between modelled and observed patterns of SST seasonal 99st percentile

4.1.3. Future Projections

4.1.3.1. Basin-scale picture

Mean and 1st and 99th percentile seasonal values of sea surface temperature (SST, Figures 4.14-4.16) and salinity (SSS, Figures 4.17-4.19) have been computed throughout the basin in control (CTR), mid-term (MTS) and long-term (LTS) scenarios. All the considered statistics tend to indicate a basin-wide increase in SST (by approximately 0.5-1.5 °C in MTS; up to 3 °C in LTS) and in SSS (mostly not greater than 0.5 °C in both MTS and LTS). The only exception to this SSS trend might take place in the northern basin, where a slight decrease has been modelled, although supported by statistical significance only within a narrow coastal region.

Considering the seasonal vertical structures of the water masses, the same statistics have been computed for potential temperature, salinity, and potential density spatially-averaged profiles in the northern (Figures 4.20-4.22) and southern (Figures 4.23-4.25) sub-basins, suggesting that the warming and salinization trend projected on the surface layers is actually a process involving the whole water column. From the dynamical point of view, potential density anomaly could face a decrease on the order of 0.1 kg m^{-3} in MTS and 0.3 kg m^{-3} in LTS in the NA, and slightly smaller in the SA. This is particularly important especially when referring to the deeper regions of the southern basin and wintry conditions,

that is where and when deep ventilation occurs with strong implications for benthic habitats and for the Mediterranean thermohaline circulation.

It is thus clear that, in order to investigate the expected dense water production regimes (and deep sea ventilation) in climate change conditions, the Northern Adriatic Dense Water (NAdDW) should be defined in dynamical terms, varying in time depending on the properties of the southern basin. Artegiani et al. (1997) suggest as a minimum threshold value for the NAdDW a potential density anomaly of 29.2 kg m^{-3}. This is in fact the maximum potential density anomaly in the Southern Adriatic Sea in recent past conditions (see Figure 4.9), and the value to be exceeded in order to permit dense water mass penetration in the deeper layers of the water column. Generalizing this concept, the yearly fluxes of NAdDW from the Northern Adriatic (that is, through the transect depicted in Figure 4.1), have been estimated considering the transport of water with potential density anomaly equal or greater than the current maximum sub-basin scale value computed in the SA. The emerging picture (Figure 13) seems to suggest a tendency towards a decrease in dense water export: this is not fully statistically significant over the Mid-Term perspective, but it is in LTS, and it might be a marker of a process to be more deeply investigated.

The overall variation of the Ocean Heat Content in different layers of the Adriatic Sea has also be computed as the vertically-integrated temperature change multiplied by the water density times the specific heat capacity. Three different regions have been considered, bracketing shallow (0-200 m depth), intermediate (200-800 m depth) and deep (800-1200] zones. Preliminary results (Figure 4.27) again suggest that, although not everywhere supported by evident statistical significance, the Adriatic Sea warming is impacting the whole water column.

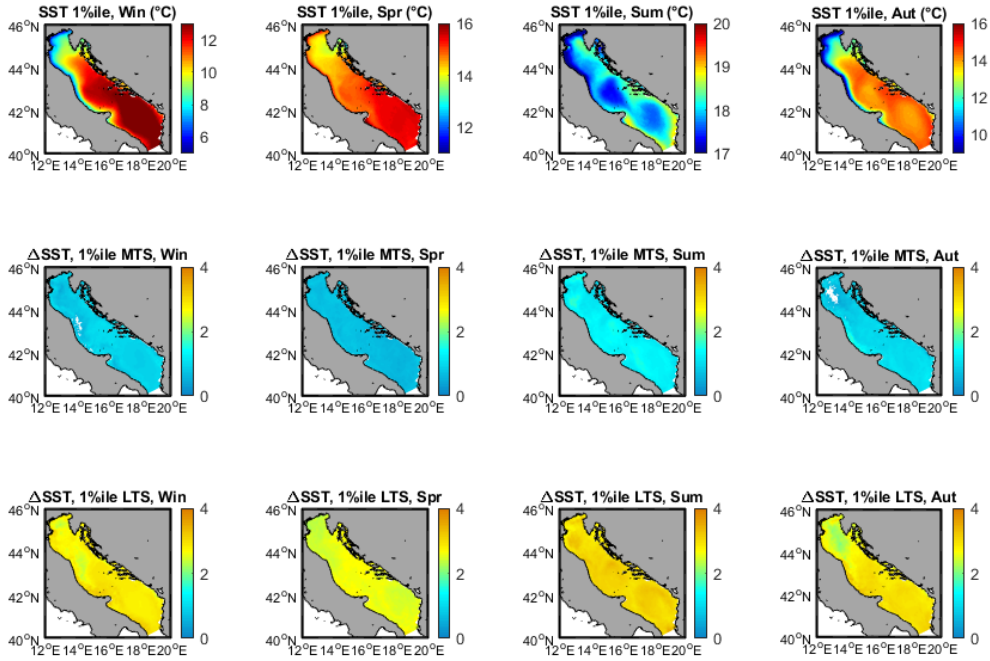

Figure 4.14: 1st percentile seasonal SST and expected variations in Mid-Term (MTS, 2020-2049) and Long-Term (LTS, 2070-2099) Scenarios. Statistically non-significant values are not represented.

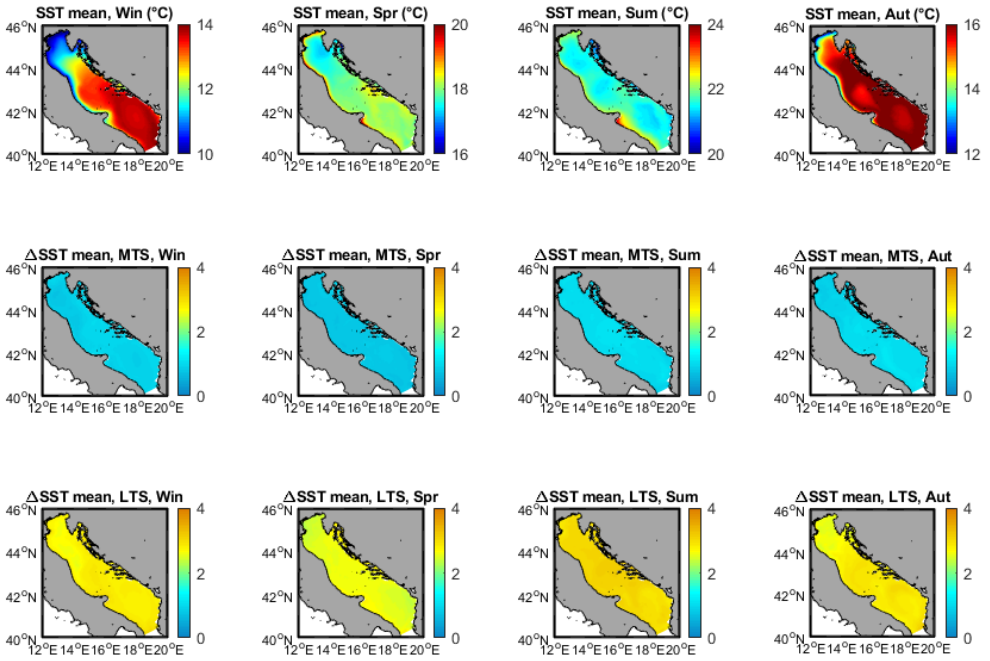

Figure 4.15: mean seasonal SST and expected variations in Mid-Term (MTS, 2020-2049) and Long-Term (LTS, 2070-2099) Scenarios. Statistically non-significant values are not represented.

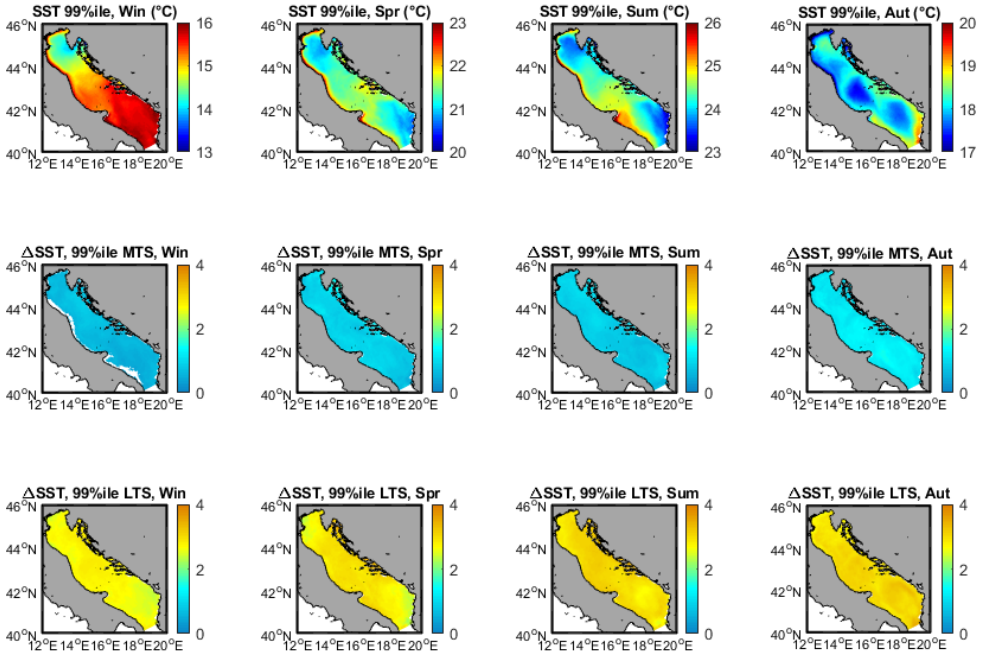

Figure 4.16: 99th percentile seasonal SST and expected variations Mid-Term (MTS, 2020-2049) and Long-Term (LTS, 2070-2099) Scenarios. Statistically non-significant values are not represented.

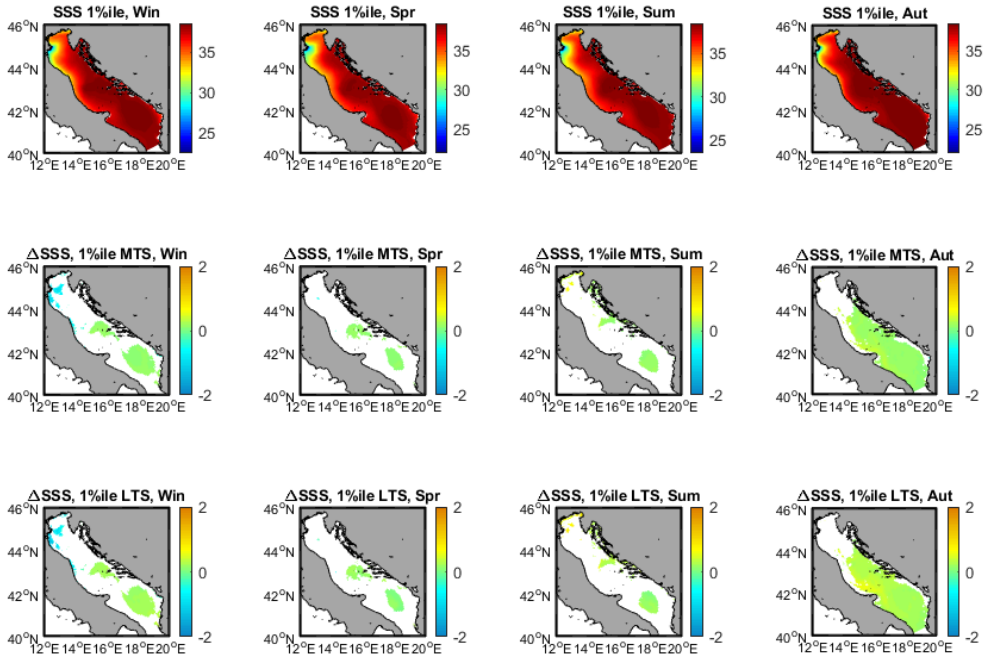

Figure 4.17: 1st percentile seasonal SSS and expected variations in Mid-Term (MTS, 2020-2049) and Long-Term (LTS, 2070-2099) Scenarios. Statistically non-significant values are not represented.

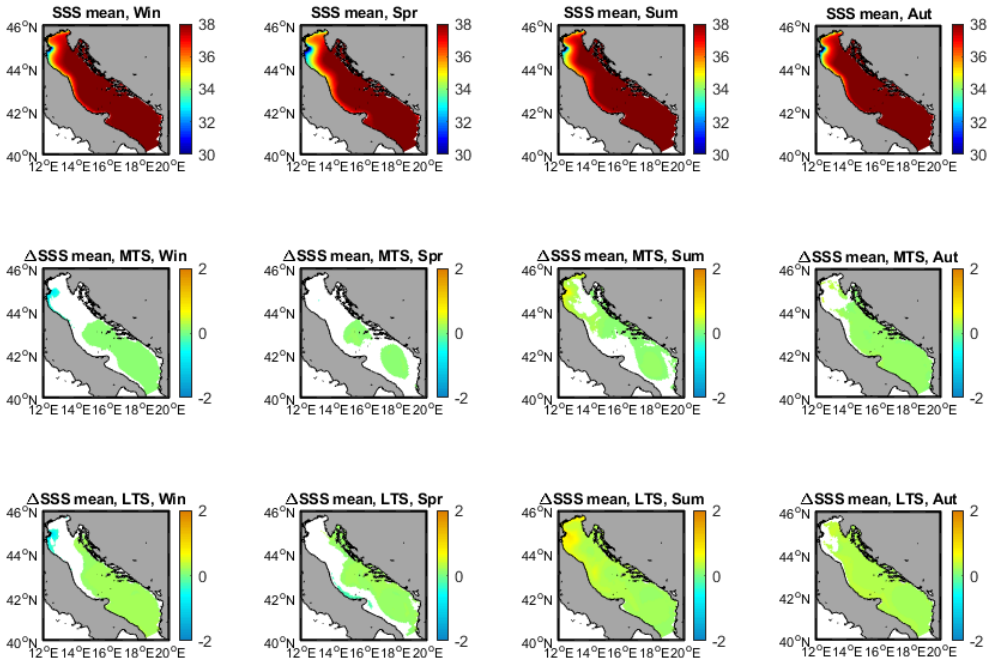

Figure 4.18: mean seasonal SSS and expected variations in Mid-Term (MTS, 2020-2049) and Long-Term (LTS, 2070-2099) Scenarios. Statistically non-significant values are not represented.

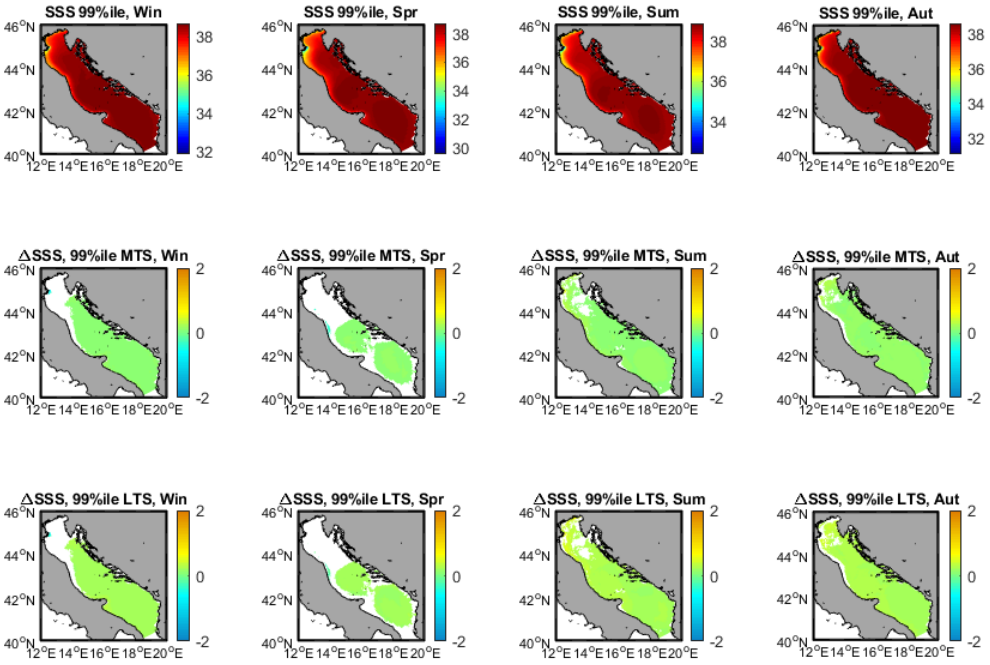

Figure 4.19: 99th percentile seasonal SSS and expected variations in Mid-Term (MTS, 2020-2049) and Long-Term (LTS, 2070-2099) Scenarios. Statistically non-significant values are not represented.

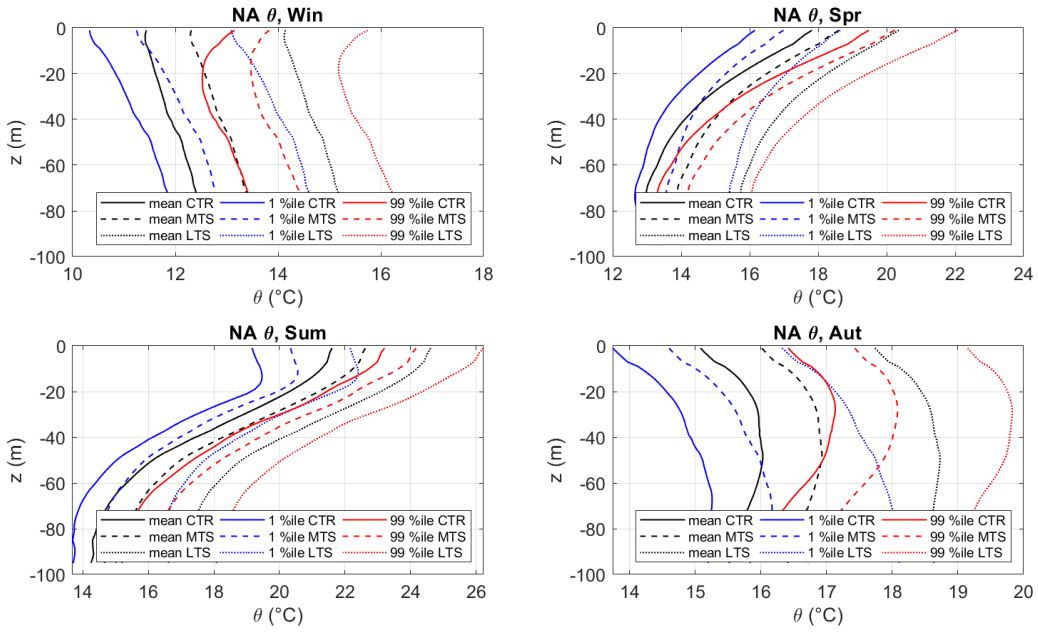

Figure 4.20: Seasonal potential temperature profile statistics in the Northern Adriatic Sea, under CTR (solid line), MTS (dashed line), and LTS (dotted line) conditions. Statistically non-significant projections are not shown.

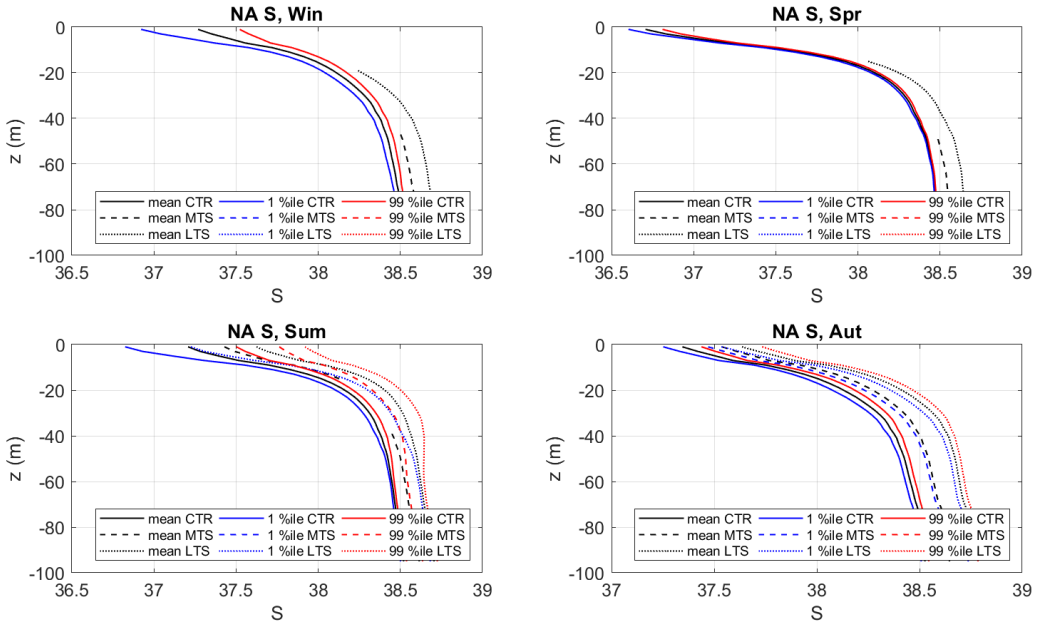

Figure 4.21: Seasonal salinity profile statistics in the Northern Adriatic Sea, under CTR (solid line), MTS (dashed line), and LTS (dotted line) conditions. Statistically non-significant projections are not shown.

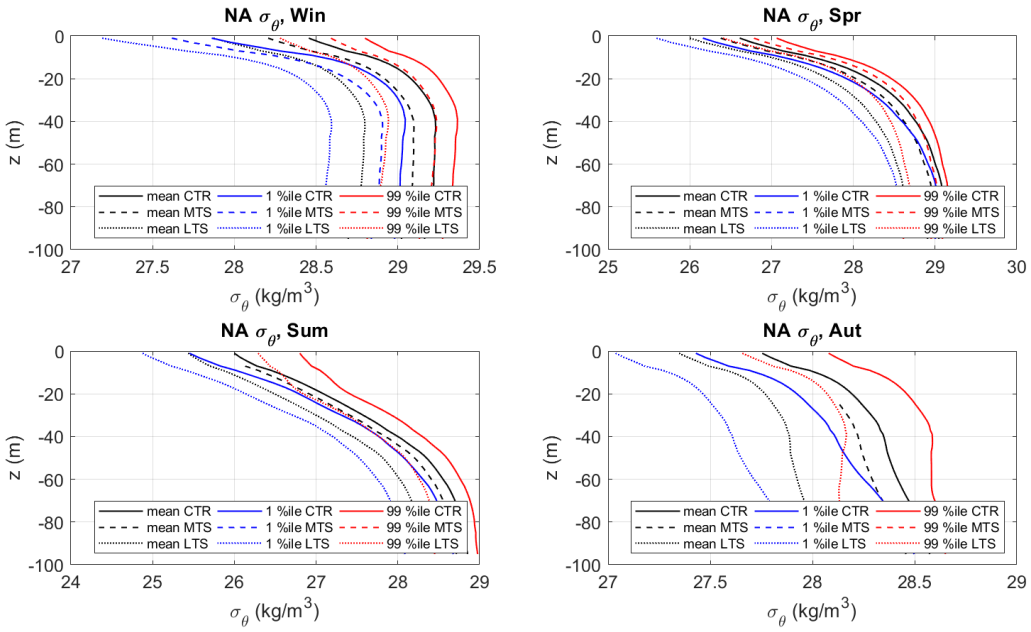

Figure 4.22: Seasonal potential density anomaly profile statistics in the Northern Adriatic Sea, under CTR (solid line), MTS (dashed line), and LTS (dotted line) conditions. Statistically non-significant projections are not shown.

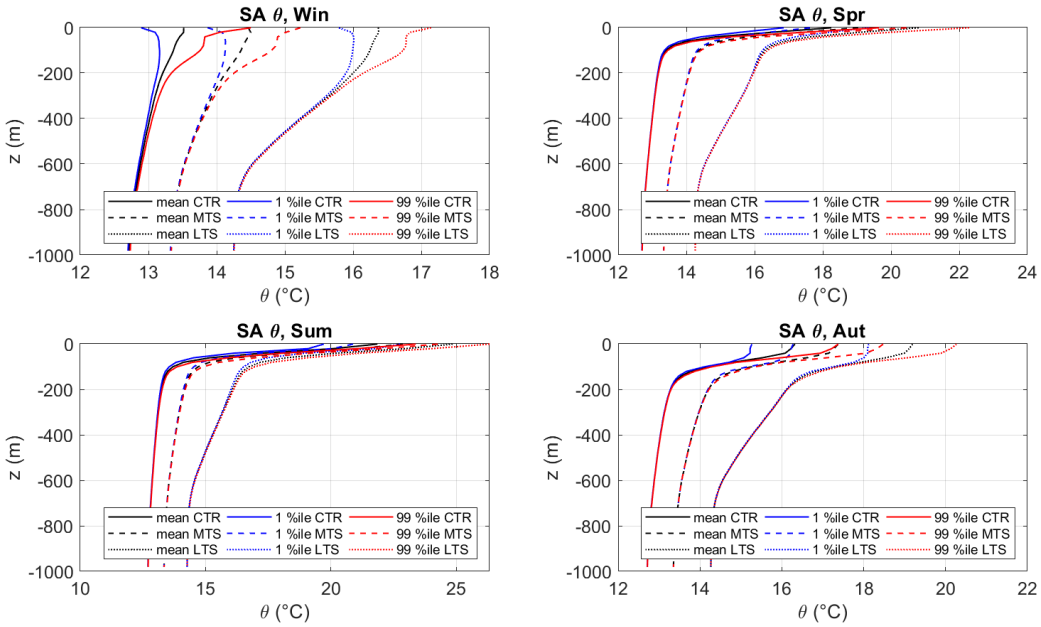

Figure 4.23: Seasonal potential temperature profile statistics in the Southern Adriatic Sea, under CTR (solid line), MTS (dashed line), and LTS (dotted line) conditions. Statistically non-significant projections are not shown.

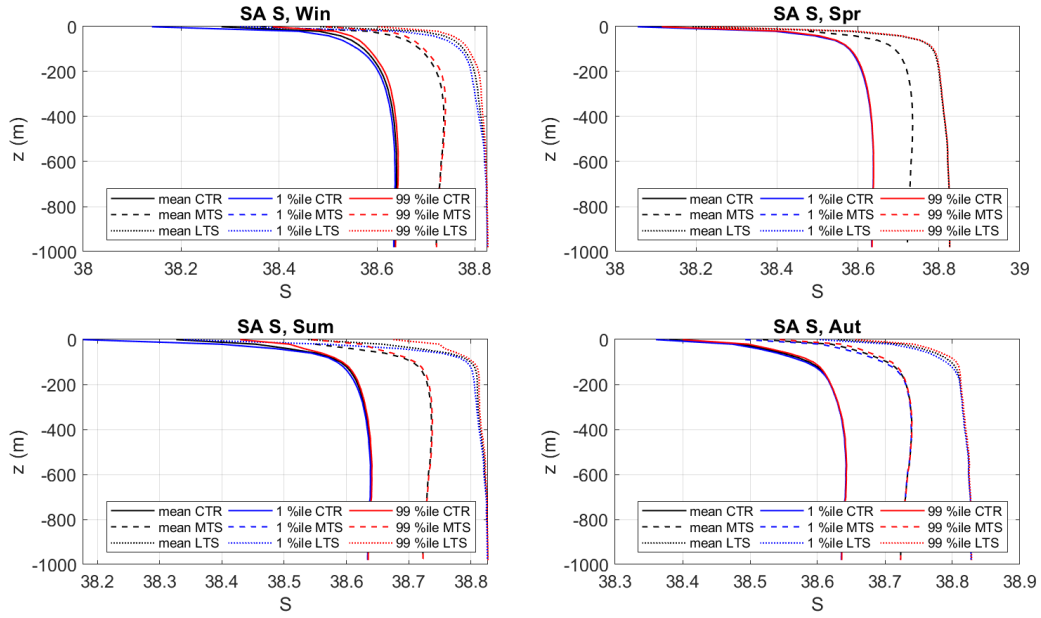

Figure 4.24: Seasonal salinity profile statistics in the Southern Adriatic Sea, under CTR (solid line), MTS (dashed line), and LTS (dotted line) conditions. Statistically non-significant projections are not shown.

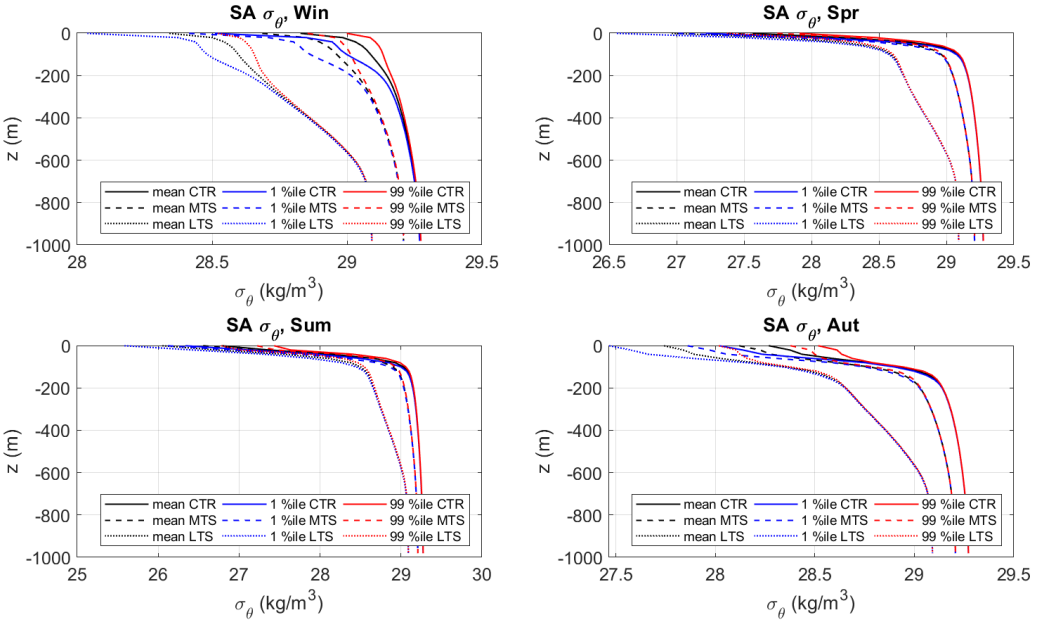

Figure 4.25: Seasonal potential density anomaly profile statistics in the Southern Adriatic Sea, under CTR (solid line), MTS (dashed line), and LTS (dotted line) conditions. Statistically non-significant projections are not shown.

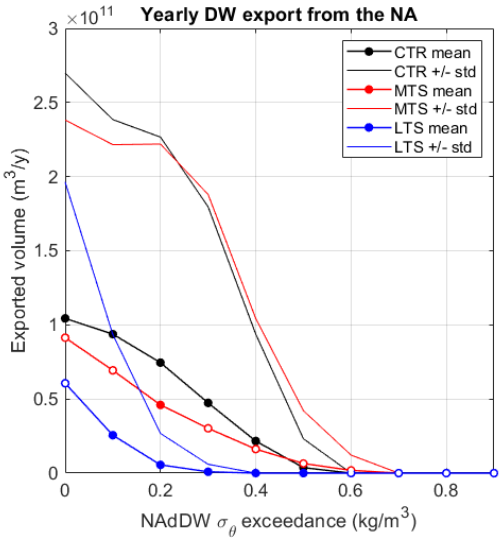

Figure 13: NAdDW export statistics under CTR, MTS and LTS conditions, expressed as exported volume of water with density exceeding the SA density threshold by different values. Thick lines represent mean values, whereas thin lines give an account of interannual variability by representing mean values plus the standard deviations. Mean values in MTS and LTS conditions for which the variation compared to CTR are statistically non-significant are marked with a white dot.

4.1.3.2. Pilot sites statistics

Offshore each of the Pilot Sites, at the locations depicted in Figure 4.1, the variations of key quantities such as potential temperature and salinity profiles have been computed in MTS and LTS conditions. Sea level statistics were also investigated, after removing the one-year moving average, in terms of monthly mean and 1st and 99th percentiles as well as yearly extremes fitted with a Gumbel distribution. Of course, due to the complex morphology and to the presence of several islands along the eastern coast, as mentioned in Section 4.1.1, information on these sites should be taken as indicative, and used as a preliminary assessment in the possible perspective of high-resolution model downscaling applications. Offshore of the Neretva River Delta (4.28), sea temperature warming in MTS involves the whole water column by approximately 1 °C and more, except in spring and early summer when values smaller than 1 °C are projected in the upper 50 m. In LST, the pattern is further enhanced by additional 1.5 °C. Salinity profiles seem to increase evenly (both in space and time) by 0.1 in MTS, although this value has no statistical significance at smaller depth in Winter-Spring, and by 0.3 in LTS. The pattern is similar off the Jadro River and Kaštela Bay area (Figure 4.29). Offshore of the Vran Lake Pilot Site (Figure 4.30) the sea water warming is slightly milder, and the salinity increase signal partially loses statistical significance. At the Banco della Mula di Muggia Pilot Site (Figure 4.31) all potential temperature statistics undergo a stronger increase in winter and summer (generally exceeding 1°C in MTS and 2.5 °C in LTS) and a more moderate one (between 0.5 and 0.7 °C in MTS, 1.9-2.3 °C in LTS) in spring. Mean and 1st percentile salinity is also expected to increase in summer months by 0.5 to 1, particularly in the uppermost layers. In other periods and throughout the whole year in the case of 99th percentile the signal is not likewise pronounced,

nor is it statistically significant, except for a near-surface decrease in mean and 1st percentile in March. Around the Po Delta Northern lobe (Figure 4.32) the situation is qualitatively similar, whereas the signal is enhanced in the Southern lobe (Figure 4.33, Figure 4.34).

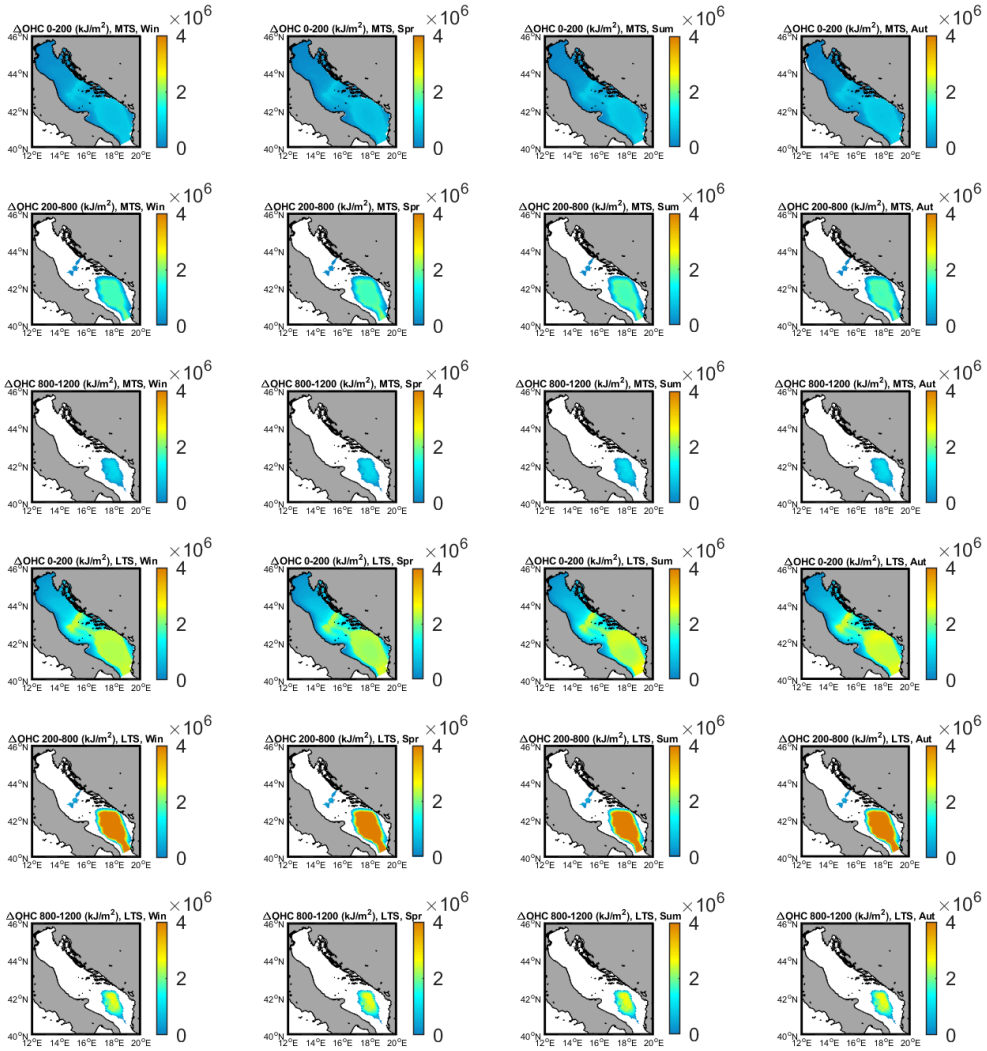

Figure 4.27: Ocean Heat Content variations in MTS and LTS conditions at different depth ranges. Statistically non-significant values are shaded in gray.

Statistically significant variations in sea level statistics are quite rare throughout all Pilot Sites. In any case it is important to point out that, due to the distance of the points from the coast, the sea level values considered in these figures are not completely representative of the surge actually impacting the littoral zone, as the estimate may be underestimated by a non-negligible extent.

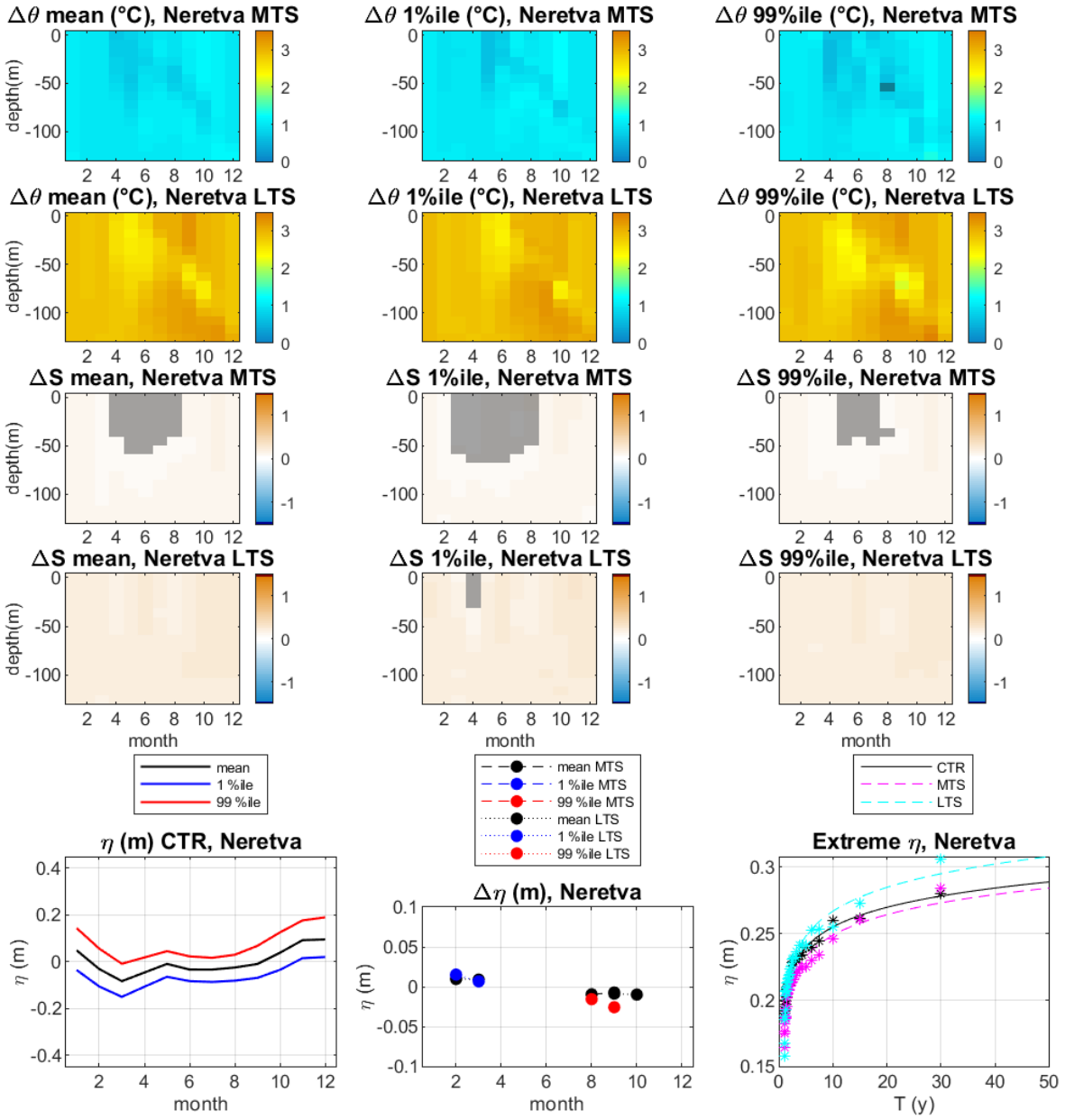

Figure 4.28: Neretva Delta Pilot Site (offshore) ocean statistics. Potential temperature (rows 1-2), salinity (rows 3-4), and sea level (bottom, computed net of the yearly moving average) variations in MTS (2020-2049) and LTS (2070-2099) scenarios with respect to CTR (1987-2016) conditions. Statistically non-significant quantities have been shaded in gray (temperature and salinity), not shown (climatological sea level variations), or depicted in dashed lines (bottom right).

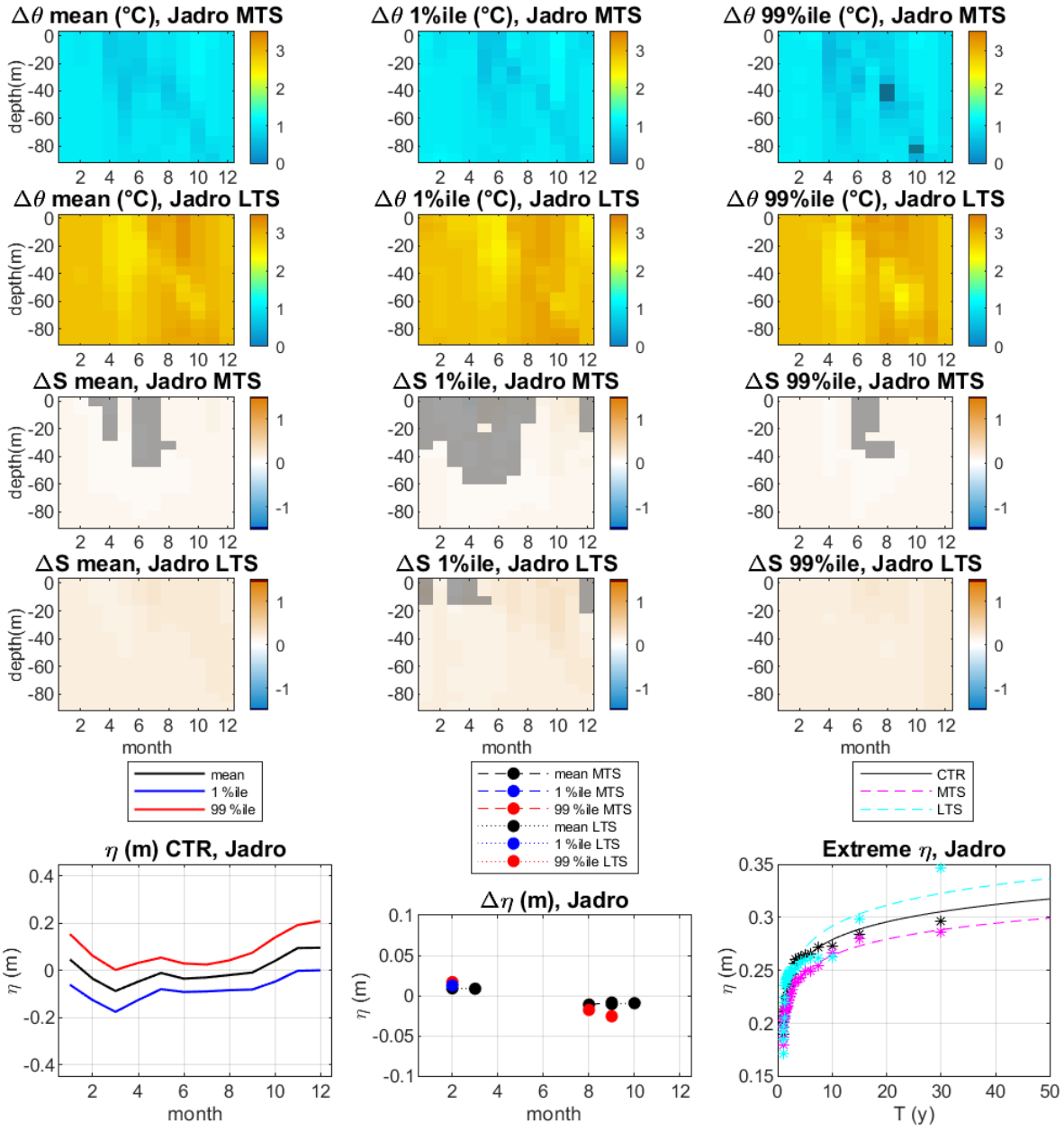

Figure 4.29: As Figure 4.28 but for Jadro River and Kaštela Bay (offshore).

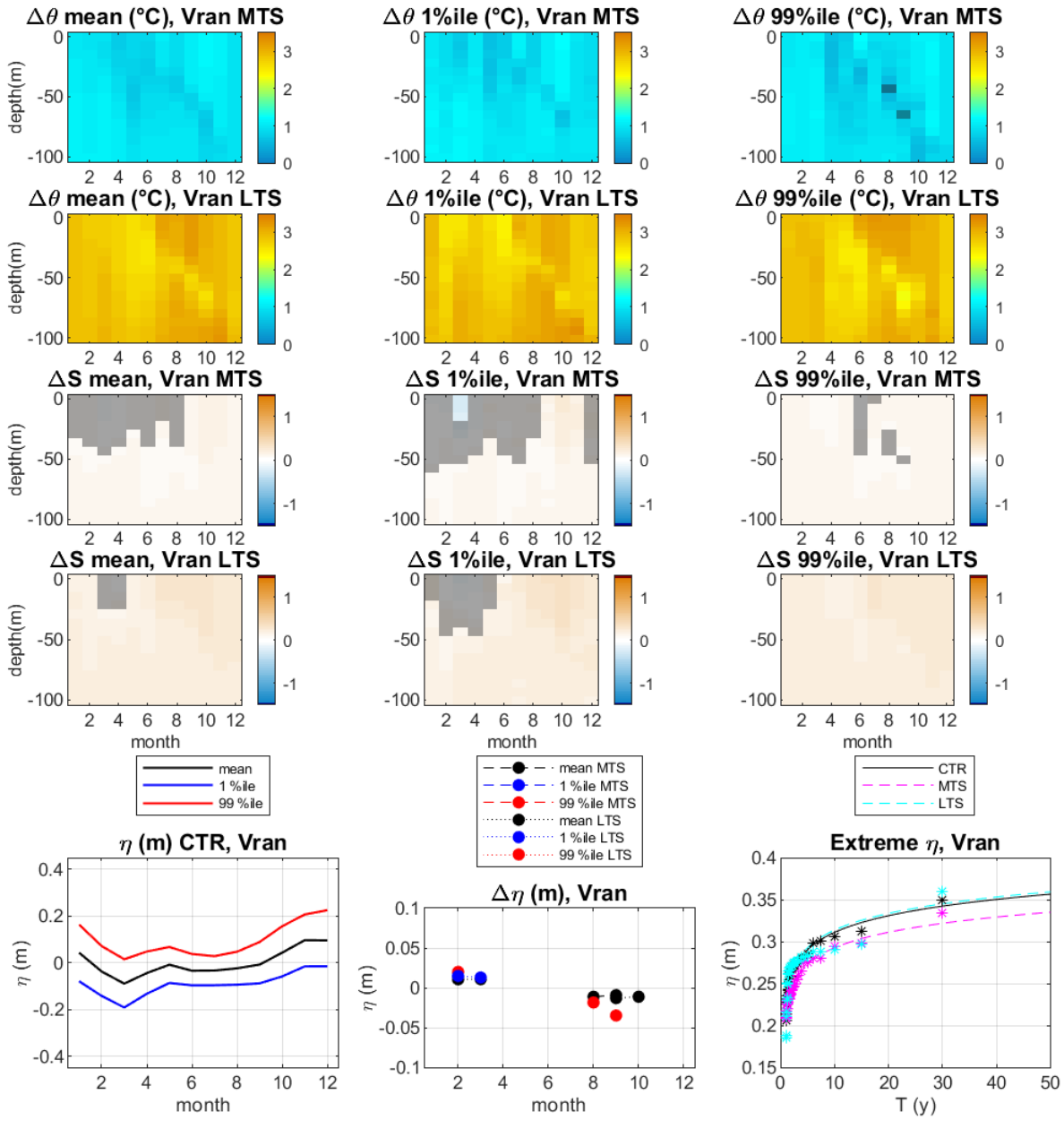

Figure 4.30: As Figure 4.28 but for Vran Lake Pilot Site (offshore)

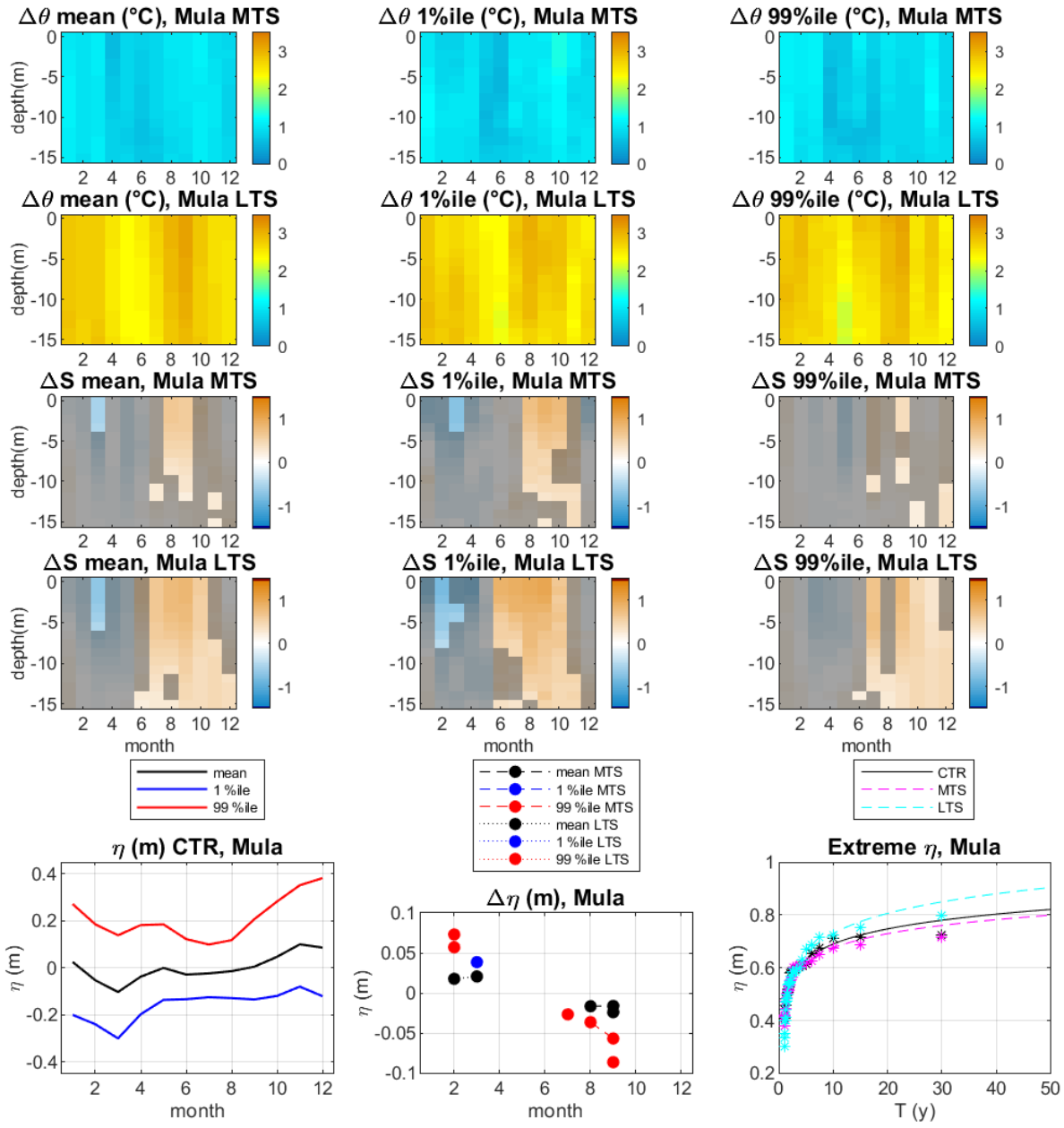

Figure 4.31: As Figure 4.28 but for Banco della Mula di Muggia Pilot Site (offshore).

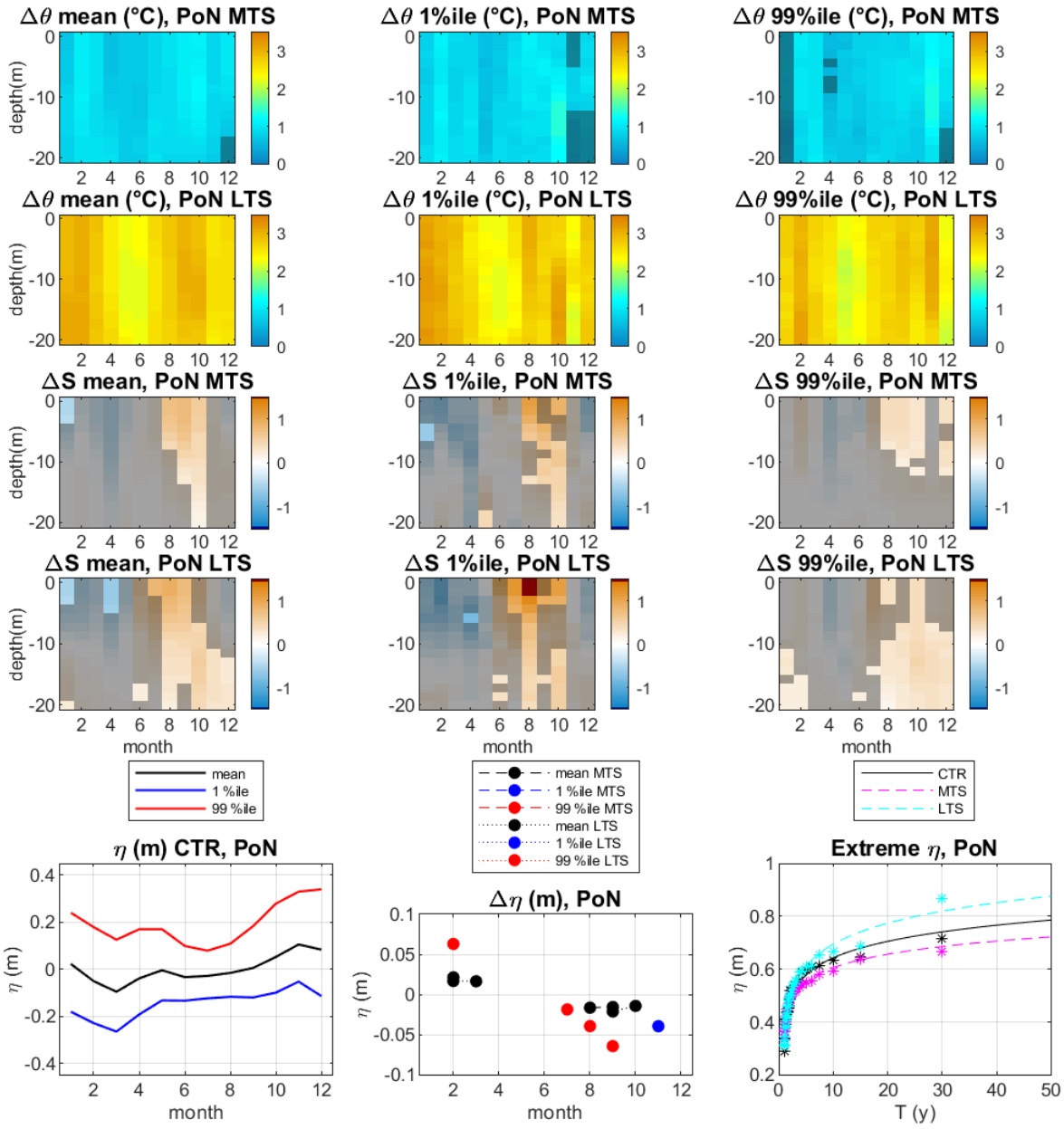

Figure 4.32: As Figure 4.28 but for Po Delta Pilot Site, Northern lobe (offshore).

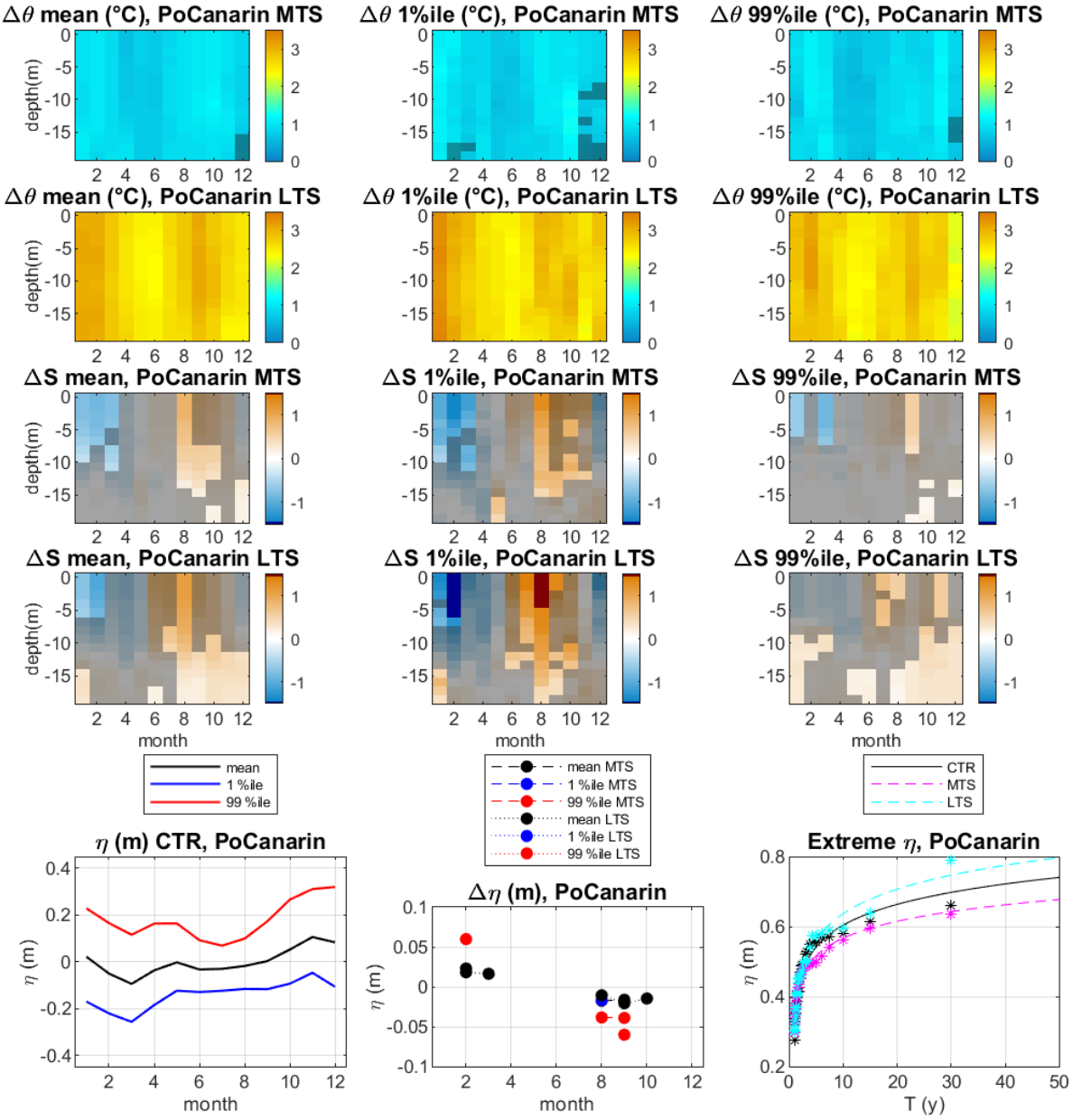

Figure 4.33: As Figure 4.28 but for Po Delta Pilot Site, Sacca di Canarin (offshore).

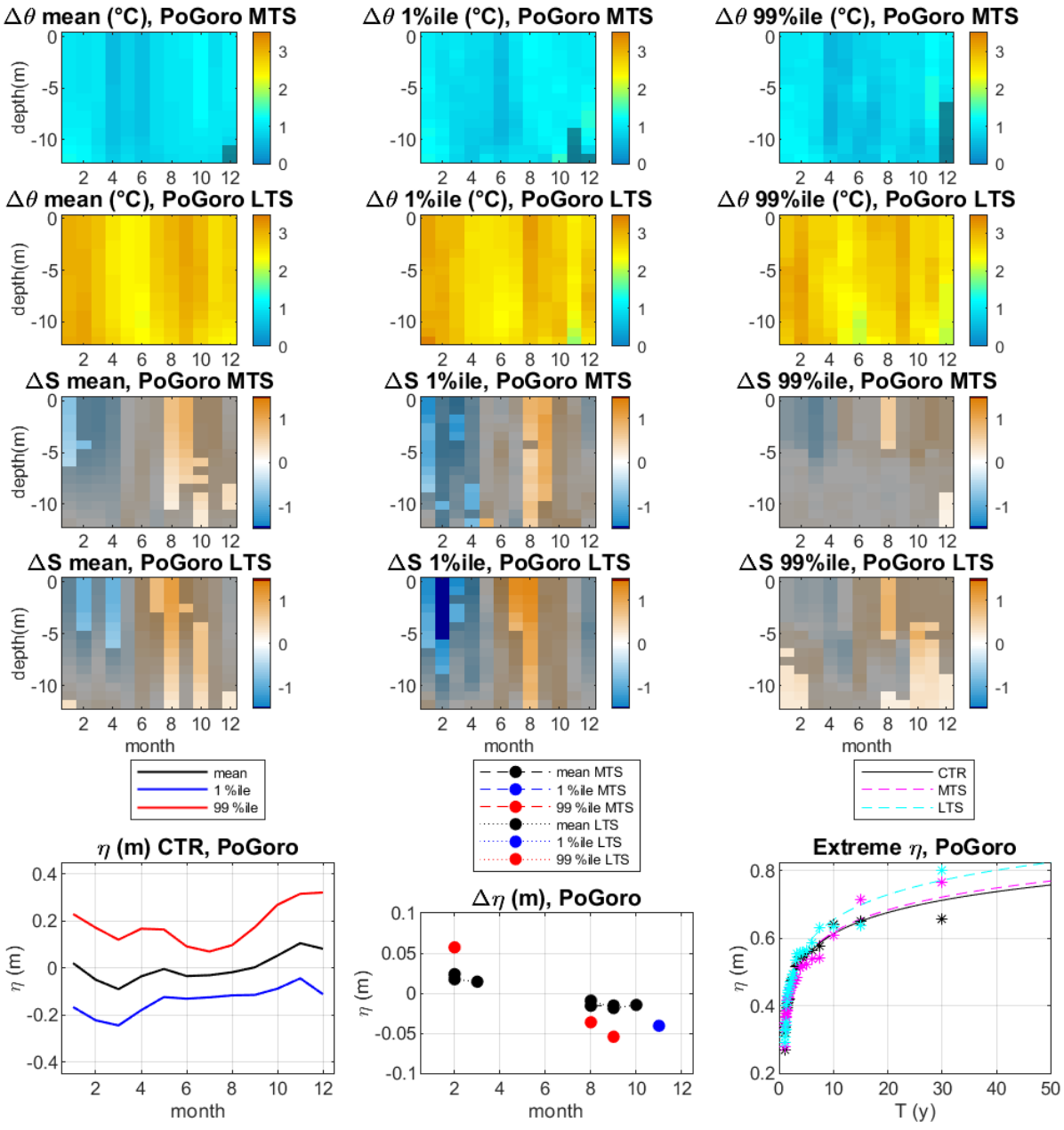

Figure 4.34: As Figure 4.28 but for Po Delta Pilot Site, Sacca di Goro (offshore).

4.2. REGIONAL OCEAN CLIMATE MODELLING: CNRM-RCSM4 SIMULATION (IOF)

4.2.1. The methodology

According to recent regional climate projections, the Mediterranean climate will become warmer and drier during the 21st century. However, the question is how climate change will affect the dynamics of the sea and, consequently, the changes in the thermohaline properties of the Mediterranean, since the influence of surface salinity on convective processes is unknown. Numerical studies to date indicate that by the end of the 21st century, the thermohaline circulation of the Mediterranean may weaken by up to 40% in the middle layers and as much as 80% in the deeper layers compared to the present climate, primarily due to a decrease in the intensity of dense water production process (Somot et al., 2006). Thermohaline properties and associated processes in the Adriatic in the future climate have not yet been sufficiently investigated, and the only hint of future properties in the Adriatic, based on the analysis of available long-term ocean data sets, indicates a weakening of the thermohaline circulation in the Adriatic over the last 70 years (Vilibić et al., 2013).

Therefore, in this chapter, three potential futures of the Adriatic climate in the 21st century are preliminary explored by analysing the fields of the oceanic regional climate model CNRM-RCSM4. The reason for choosing the CNRM-RCSM4 model is that the atmospheric and ocean models are coupled, and coupled models have a better ability to reproduce the Adriatic thermohaline circulation than non-coupled ones.

Model results were analysed for three different greenhouse gas emission scenarios: RCP8.5, RCP4.5 and RCP2.6. The boundary conditions given in the CNRM-RCSM4 are taken from the global climate model CNRSM - CM5, with an atmospheric component resolution of 50 km and oceanic resolution of 9 - 12 km. They do not reproduce the actual chronology of the thermohaline variability of the Mediterranean Sea (Darmaraki et al., 2019), but rather the statistical characteristics of individual climatic periods (e.g. mean values, variability). For the purposes of this paper, the following 30-year model projection periods are defined:

- The near future (2011-2040)
- The middle future (2041-2070),
- The far future (period 2071-2100)

The two-dimensional CNRM-RCSM4 model variables used in the analyses are values at the first layer of the model located at 6 m depth, except for the maximum mixing depth that was calculated from the three-dimensional temperature and salinity fields. To control the quality of the simulations of all the scenarios, a control simulation (CTRL) was used, which was forced by surface heat and water fluxes and of the current climate, taken from the period 1950 – 1979. The mid-emission scenario, and RCP2.6 - the low-emission scenario) were compared to the last 30 years of historical simulation (HIST, 1976-2005), which represents the reference period.

To extract the climate signal from the natural interannual variability contained in the historical simulation, an estimation of the confidence interval (IP) was made for 30-year historical simulation series (1976-2005). The confidence interval (IP) was calculated using the following expression:

$$IP = z \cdot \left(\frac{std(time\ series)}{\sqrt{N}} \right),$$

where N = 30 (length of time series) and z = 2.0452 (value corresponding to 95% significance for strings of length 30). In further analyses, all spatial distributions of deviations (anomalies) are presented only for those values that were outside the confidence interval, that is, beyond the [-IP, + IP] interval.

4.2.2. Projections of sea surface temperature

The change in surface temperature in different greenhouse gas emission scenarios in the 21st century has been compared to the reference period. As the linear temperature trend in the control simulation is very low and insignificant (0.005 °C /100 yrs, which is not statistically significant at the 95% level), we can assume that the projections do not contain initial deviations, but only a signal given by climate change.

Table 2 shows the sea surface temperatures averaged over the entire Adriatic (up to the transect in the Otranto Strait, 40° N) for the historical simulation period (HIST), and for three scenarios (RCP2.6, RCP4.5 and RCP8.5) in the near, middle and far future. As expected, the average surface temperature of the Adriatic is increasing in all projections. Already for the low-emission scenario (RCP2.6), the average surface temperature would increase by more than 1 °C at the end of the 21st century relative to the reference period (HIST, 1976-2005), while the RCP4.5 scenario gives an increase of 1.7 °C and RCP8.5 gives an increase of 2.7 °C. It is interesting to note the change in surface temperature in the Adriatic in scenario

Table 4.1. Average values of surface temperature in the Adriatic, for historical simulation (HIST) in the period 1976-2005 and for three scenarios (RCP2.6, RCP4.5 and RCP8.5) in the near, middle and far future period.

SIMULATION	HIST	RCP2.6			RCP4.5			RCP8.5		
period	1976-2005	2011-2040	2041-2070	2071-2100	2011-2040	2041-2070	2071-2100	2011-2040	2041-2070	2071-2100
SST (°C)	17.31	18.07	18.43	18.38	17.94	18.53	19.02	18.04	18.99	20.05

RCP2.6. By the end of 2040, the surface temperature in the Adriatic is rising, after which only interannual variability dominates, and after 2070 the temperature slowly decreases towards the end of the simulation period (Figure 4.34).

The average spatial temperature distribution for the reference period (HIST, Figure 4.35) indicates that the model correctly reproduces the basic properties in the Adriatic: the minimum temperature in the northern Adriatic, the maximum temperature along the eastern coast of the southern Adriatic indicating the northwestern current along the eastern coast Adriatic, and the minimum temperature in the central part of the southern Adriatic, as an indicator of a cyclonic vortex.

Changes in surface temperature in the Adriatic Sea in the future climate are positive and spatially homogeneous in all periods and in all scenarios (Figure 4.36). In the near future (2011 - 2040), the rise in sea surface temperature is similar in all scenarios, ranging between 0.6 - 0.7 °C, while in other periods (middle and far future) changes become more pronounced for medium- and high-emission scenarios (RCP4.5 and RCP8.5). The highest rise in sea surface temperature at the end of the 21st century in the entire Adriatic is expected in RCP8.5, i.e. in a scenario that assumes an instantaneous increase in atmospheric greenhouse gases (the so-called "business-as-usual" scenario).

The analysis of changes in sea surface temperature in the future climate in relation to the temperature of the reference period (HIST, 1976-2005) was made using QQ-graphs and histograms. The lowest increase in low temperatures (up to 13 °C), common for the winter, was found in the near future (2011-2040) of the RCP8.5 scenario (Figure 4.37a). Other projections (RCP4.5 and RCP2.6) have slightly lower winter temperatures in the near future compared to the reference period. Other temperature values show an increase over the reference period in all scenarios. This means that in the near future, winter cooling of the sea surface will continue to be as strong (or stronger) as it was in the historic period (1976-2005). In later periods (middle and distant future), all projections predict a year-over-year increase in temperature, i.e. across all percentiles of temperature. Moreover, after 2040, all projections show a monotonous rise in sea surface temperature. A similar conclusion can be drawn from the distribution of surface temperature histograms (Fig. 4.37b), which show an increase in winter (from about 10 °C to about 15 °C) and summer temperatures (from about 20 °C to about 25 °C).

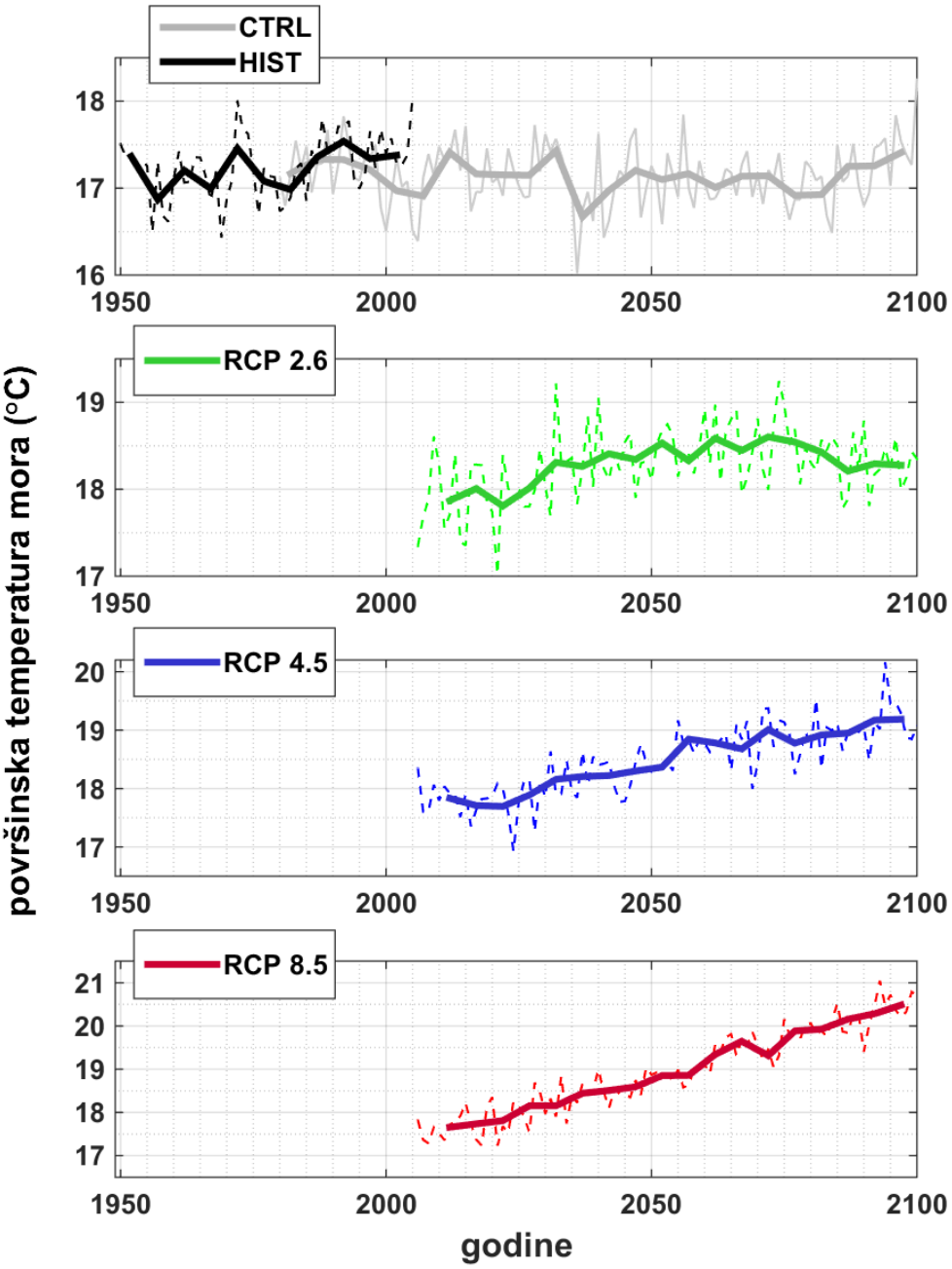

Figure 4.34. Time series of sea surface temperature in the Adriatic for historical simulation (HIST) and for three scenarios (RCP2.6, RCP4.5 and RCP8.5). The figure also shows the time series of the control simulation (CTRL). There are different scales on the y-axis.

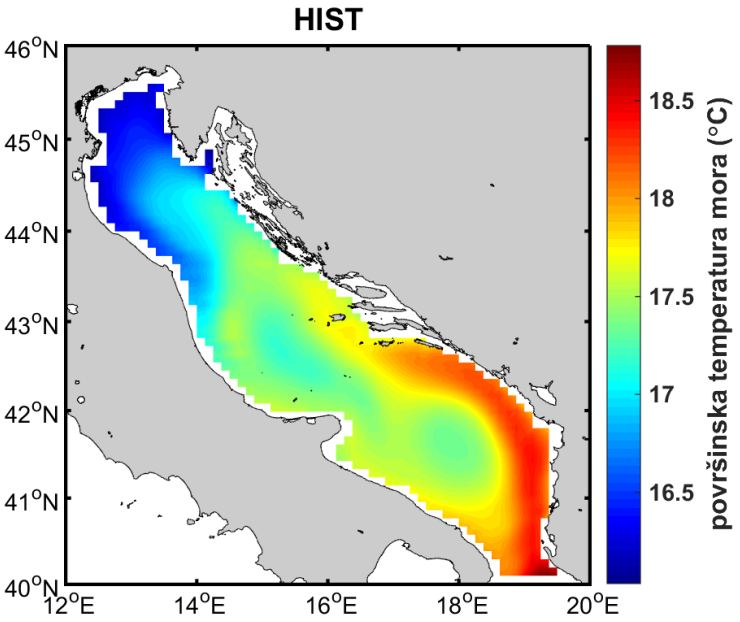

Figure 4.35. Average spatial distribution of surface temperature in the Adriatic for the reference period of historical simulation (1976-2005, HIST).

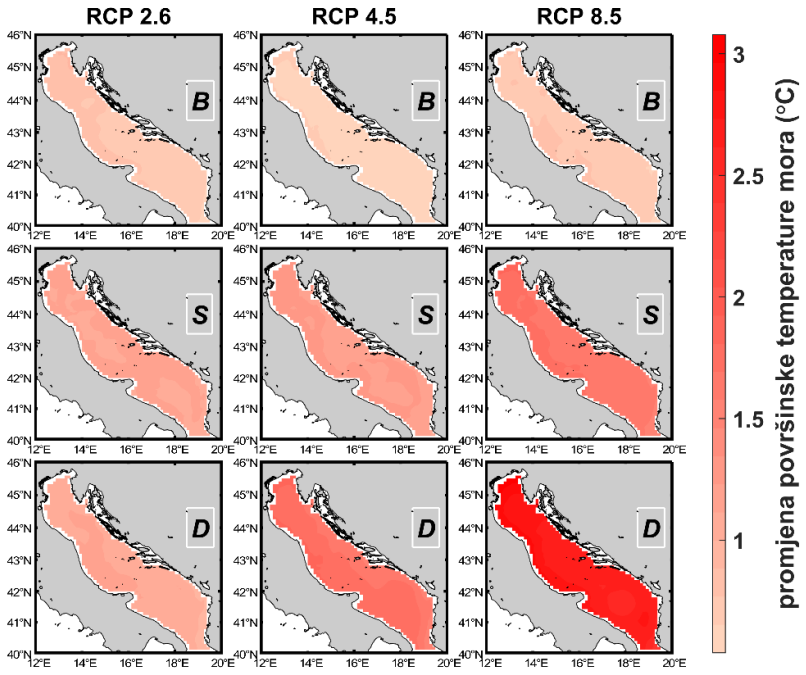

Figure 4.36. Changes in surface temperature in the Adriatic for three defined periods (near future - B, middle future - S and far future - D) and for three scenarios (RCP2.6, RCP4.5 and RCP8.5) relative to the reference period (1976-2005, HIST). Only values beyond the IP confidence interval are shown in the figure.

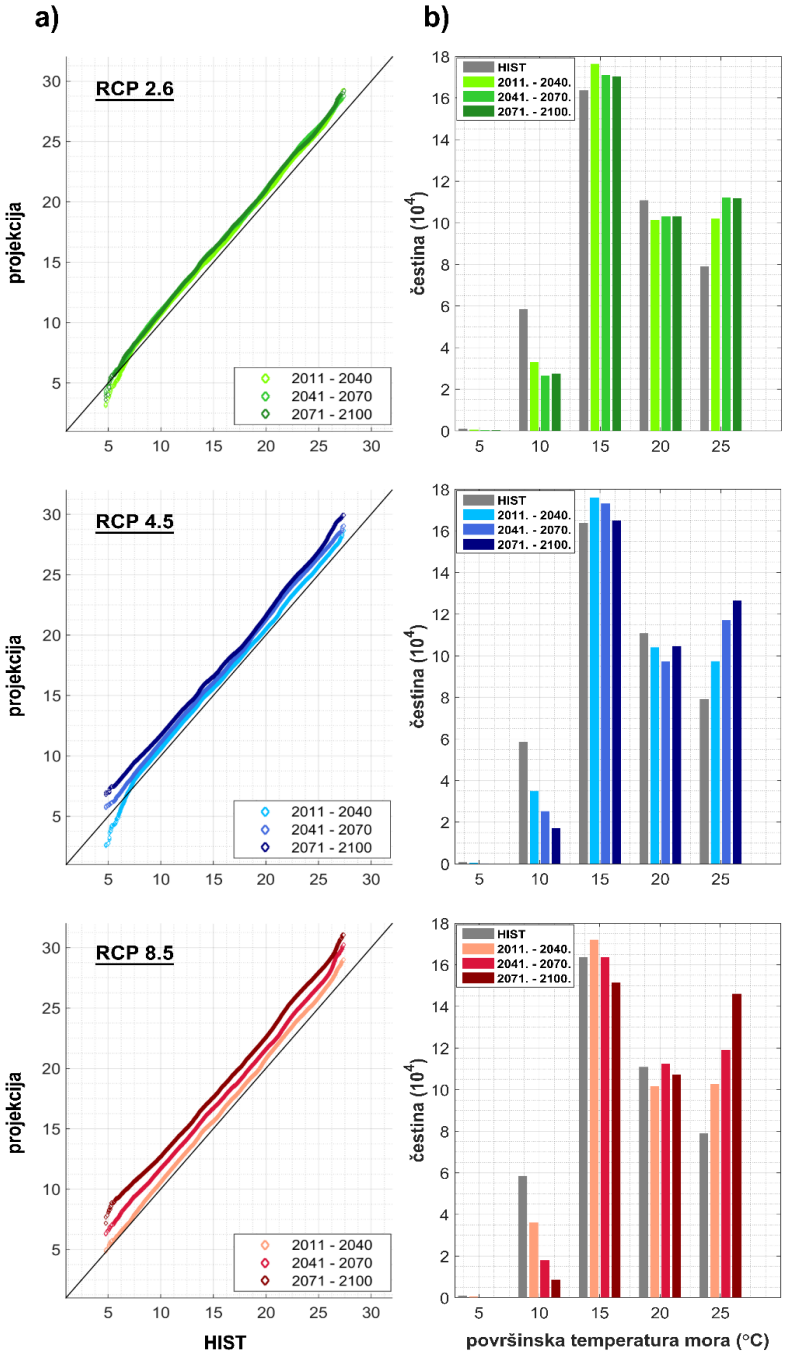

Figure 4.37. a) QQ-graphs of surface temperature in the Adriatic Sea projected for three scenarios (RCP2.6, RCP4.5 and RCP8.5) versus the reference period (HIST, 1976-2005), for three divisions, and b) associated histograms. The temperature values in the histograms are divided into classes of width 5, whose centers are indicated on the x-axis.

4.2.3. Projections of sea surface salinity

Similar to surface sea temperature, the trend of average surface salinity in the Adriatic Sea over the entire control simulation period is low (-0.05 / 100 yr) and not statistically significant. This further confirms the stability of the CNRM-RCSM4 model, and the plausibility of reproducing the climate signal in the three scenarios (RCP8.5, RCP4.5 and RCP2.6).

Compared to the reference period, the average surface salinity of the Adriatic shows an increase in the 21st century, recorded in all three projections (Table 3). The highest increase at the end of the 21st century (the period of the distant future) was found in scenario RCP8.5 (salinity higher by 0.71). A slightly lower increase was recorded in the RCP4.5 scenario (by 0.38), while the lowest increase was recorded in the RCP2.6 scenario (by 0.27). The rise in surface salinity is consistent with the analysis of projections for the entire Mediterranean (Somot et al., 2006). The RCP2.6 and RCP4.5 scenarios give the largest increases in surface salinity in the mid-term (2041 - 2070, an increase of 0.64 for RCP2.6 and 0.58 for RCP4.5), after which the average surface salinity in the Adriatic in these scenarios decreases.

Unlike changes in sea surface temperature, the impact of climate change on surface salinity is not so noticeable, due to the strong natural signal of interannual and decadal variability contained in all simulations, and therefore in the control simulation (Figure 4.38). The only simulation that shows a relatively clear picture of surface salinity growth by period is RCP8.5, although strong variability is also evident in this simulation. The reason is that the surface salinity in the Adriatic is conditioned by the inflow of rivers, and is influenced by the BiOS (Gačić et al., 2010), which by joint action "define" its strong interannual and decadal variability in the Adriatic. Therefore, to properly assess the impact of climate change on surface salinity in the Adriatic, an analysis of changes in surface salinity in the future climate relative to the historical climate was made, only with values that came out of the confidence interval estimated from the historical simulation.

Table 4.2. Average values of surface salinity in the Adriatic, for historical simulation (HIST) in the period from 1976 to 2005 and for three scenarios (RCP2.6, RCP4.5 and RCP8.5) in the near, middle and far future.

SIMULATION	HIST	RCP2.6			RCP4.5			RCP8.5		
period	1976-2005	2011-2040	2041-2070	2071-2100	2011-2040	2041-2070	2071-2100	2011-2040	2041-2070	2071-2100
SSS	36.59	37.13	37.23	36.86	36.90	37.17	36.97	36.9	37.07	37.30

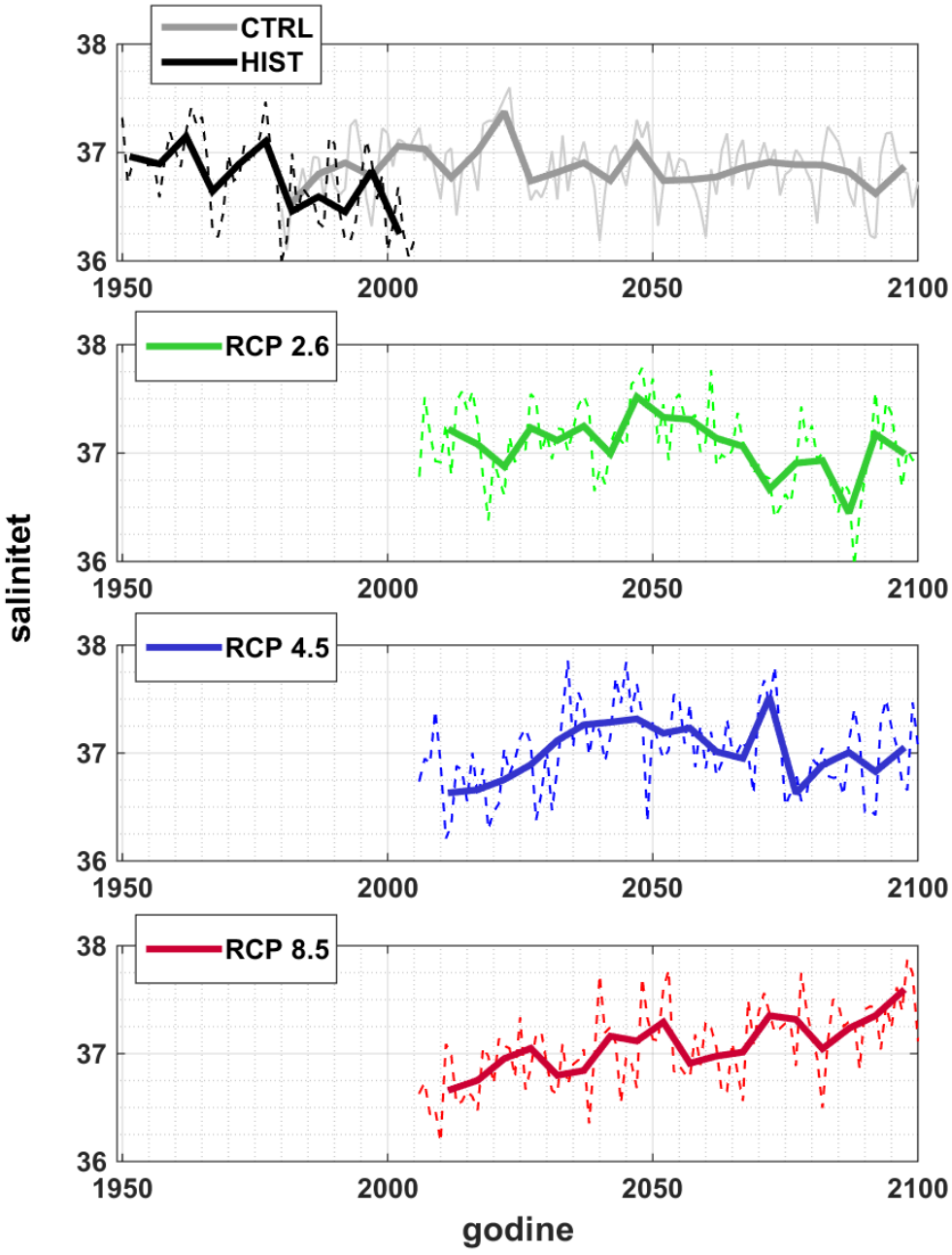

Figure 4.38. Time series of surface salinity in the Adriatic for historical simulation (HIST) and for three scenarios (RCP2.6, RCP4.5 and RCP8.5). The figure also shows the time series of the control simulation (CTRL).

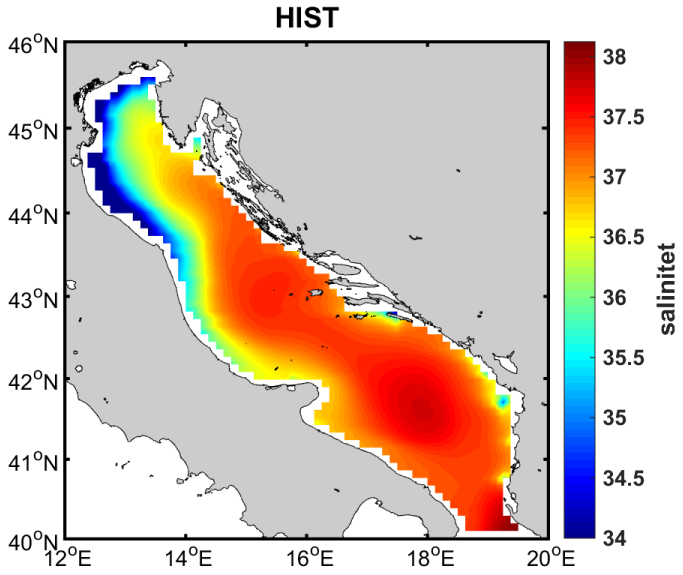

Figure 4.39. Average spatial distribution of surface salinity in the Adriatic for the reference period of historical simulation (1976-2005, HIST).

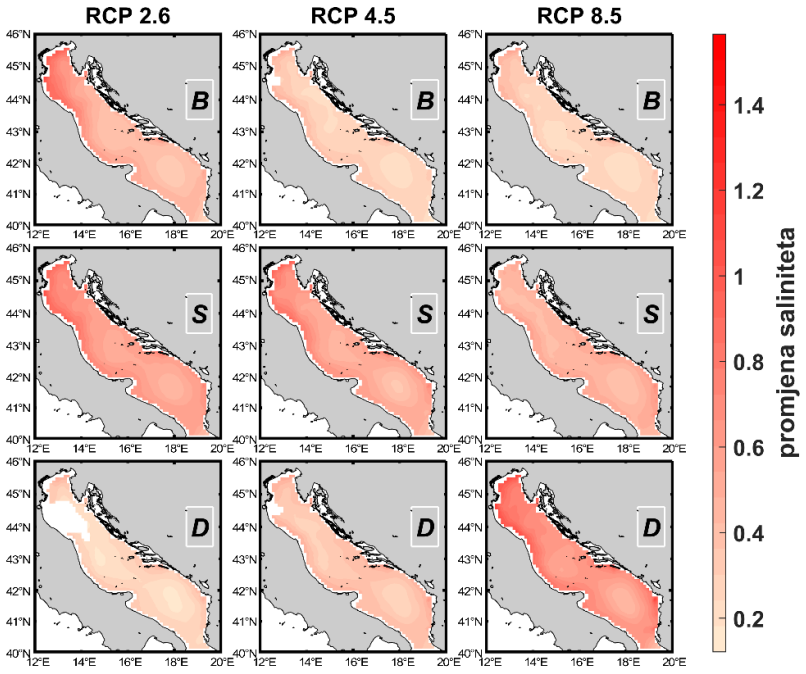

Figure 4.40. Changes in surface salinity in the Adriatic for three defined periods (near future - B, middle future - S and far future - D) and for three scenarios (RCP2.6, RCP4.5 and RCP8.5) relative to the reference period (1976-2005, HIST). Only values beyond the IP confidence interval are shown in the figure.

The spatial distribution of the surface salinity of the historical simulation for the period 1976-2005 (Figure 4.39) is in agreement with the documented distributions in the current climate. The model reproduces salinity minima in the coastal area of the northern and western Adriatic, influenced by the northern Adriatic rivers, the western Adriatic coastal current as far as Cape Gargano, and maximum values in the central part of the central and southern Adriatic (Artegiani et al., 1997; Lipizer et al., 2014). In almost all areas of the Adriatic, and for all projections, there is an increase in salinity relative to the reference period (HIST, 1976-2005, Figure 4.40), with a larger increase in coastal areas characterized by low salinity (Figure 4.41b). In scenario RCP2.6, a stronger increase in salinity was observed in the areas influenced by the northern Adriatic rivers (Figure 4.40 and Figure 4.41b), which may indicate a decrease in river flows in the near and medium term (until 2070). The far future (2071 - 2100) in the RCP2.6 scenario is characterized by a lower increase in surface salinity compared to the mean future (2041 - 2070), but also by stronger decadal oscillations (Figure 4.38), which may indicate a strengthening of BiOS. Similar changes are expected with the RCP4.5 scenario, but with a higher increase in surface salinity. The strongest impact of climate change is predicted by the RCP8.5 scenario, whose simulation shows a significant increase in surface salinity in the Adriatic, sometimes over 1.45 (in some coastal areas of the Adriatic, Figure 4.41a).

4.2.1. Projections of mixed-layer depth

Time series of annual maximum mixed-layer depth in the southern Adriatic (the area shown in Figure 53) are shown in Figure 4.42. The maximum mixed-layer depth is extracted from the daily mixed-layer depth values for February, when it reaches its maximum values, during deep convection. In the near and middle future term, the RCP2.6 and RCP4.5 scenarios predict more pronounced variability and stronger convection compared to the reference period, while in the far future convective processes weaken. In the RCP8.5 scenario, no event of more pronounced deep convection was recorded, with a maximum mixing depth of up to 400 m.

For the historical simulation (1976-2005), the average spatial distribution of the maximum mixed-layer depth in February is shown in Figure 4.43. The area of stronger winter convection is located on the southern edge of the South Adriatic, while slightly weaker convection is visible in its deepest central part (Figure 4.44). Other scenarios show visible changes in the middle future (2041 - 2070), with the largest increase in maximum mixed-layer depth in the southern boundary, and slightly weaker in the centre. In other periods, the impact of climate change could not be discerned, given the strong natural variability of the convection process in the southern Adriatic.

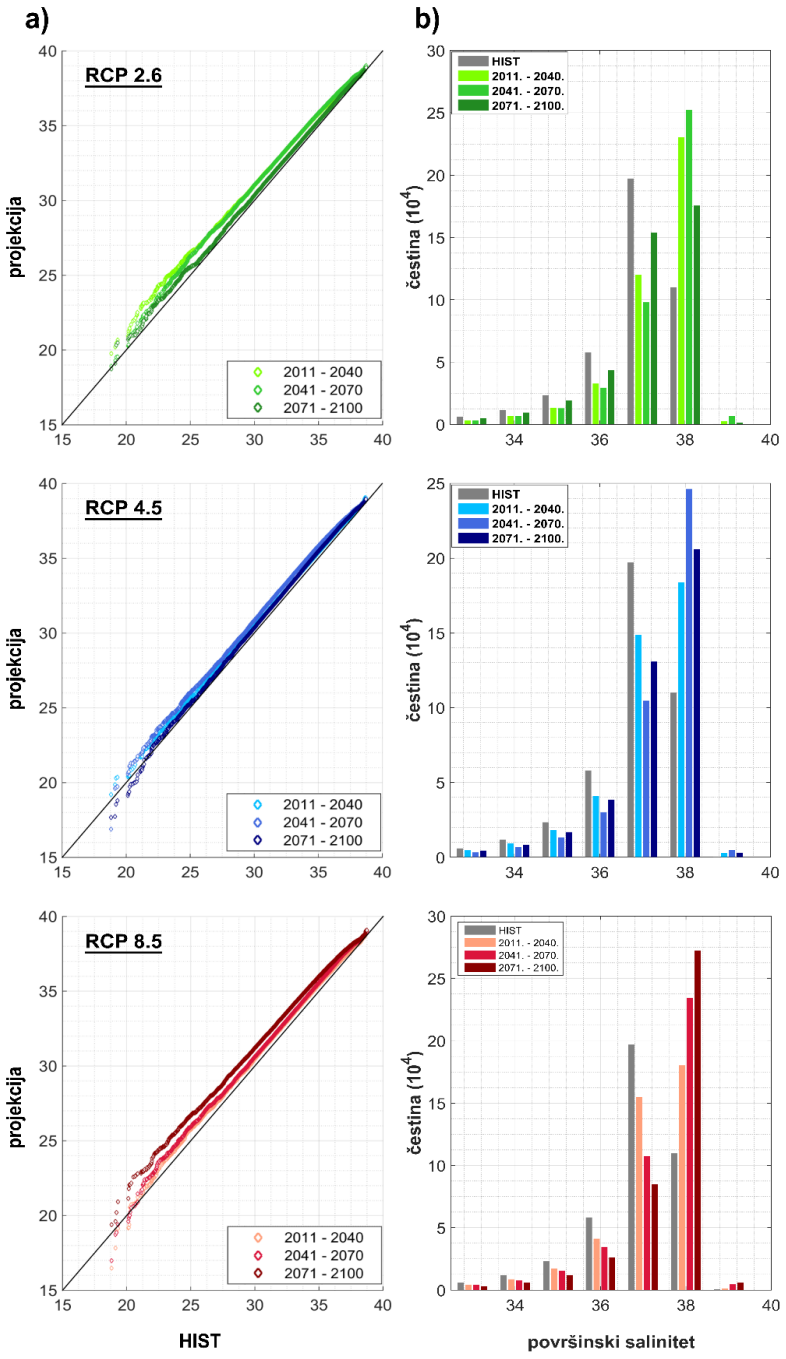

Figure 4.41 a) Q-Q graphs of surface salinity in the Adriatic Sea projected for three scenarios (RCP2.6, RCP4.5 and RCP8.5) versus the reference period (HIST, 1976-2005), for three periods (close, medium and the distant future) and b) the corresponding histograms. The salinity values in the histograms are divided into classes of width 1, the centres of which are indicated on the x-axis.

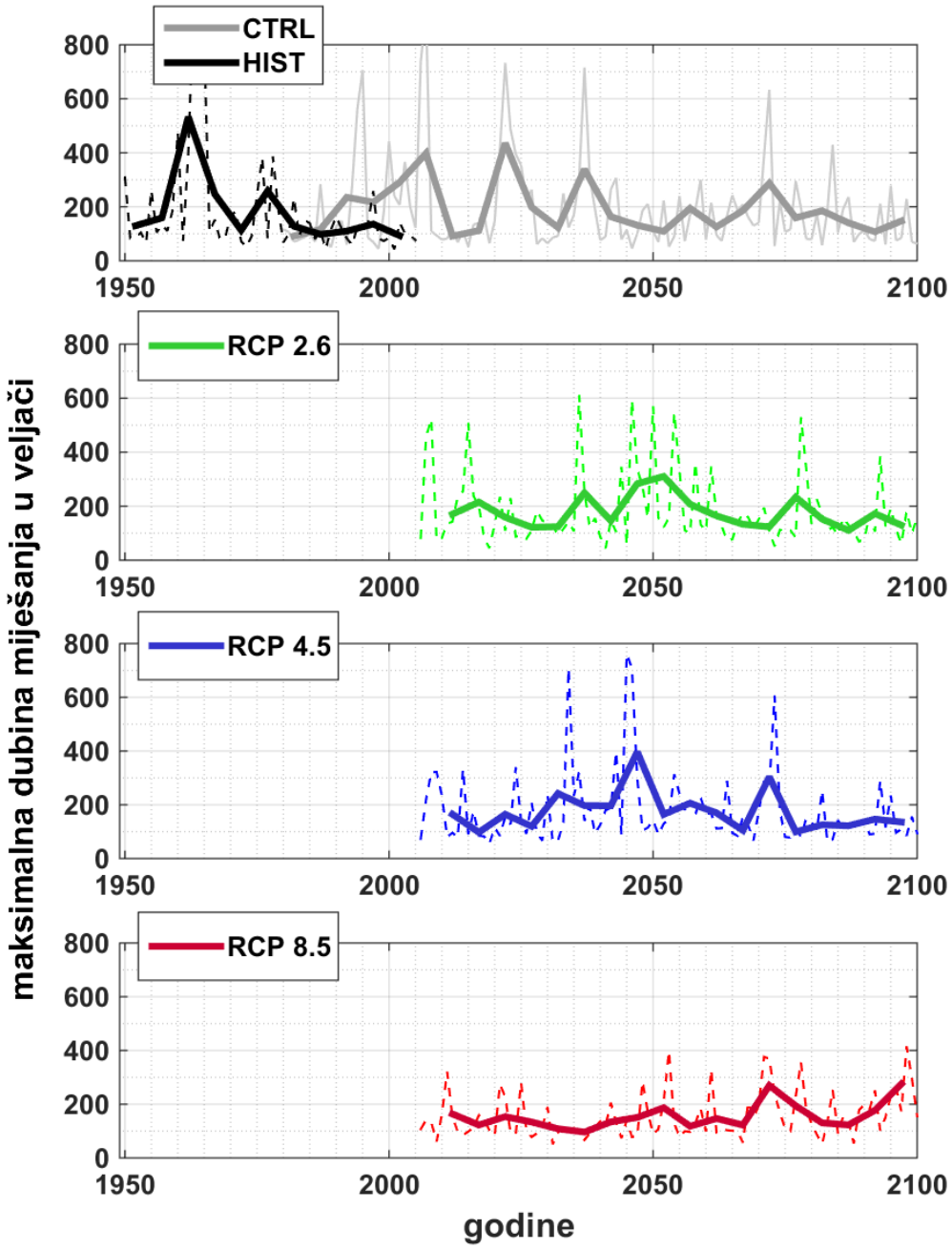

Figure 4.42. Time series of the maximum mixed-layer depth in February in the southern Adriatic for historical simulation (HIST) and for three scenarios (RCP2.6, RCP4.5 and RCP8.5). The figure also shows the time series of the control simulation (CTRL).

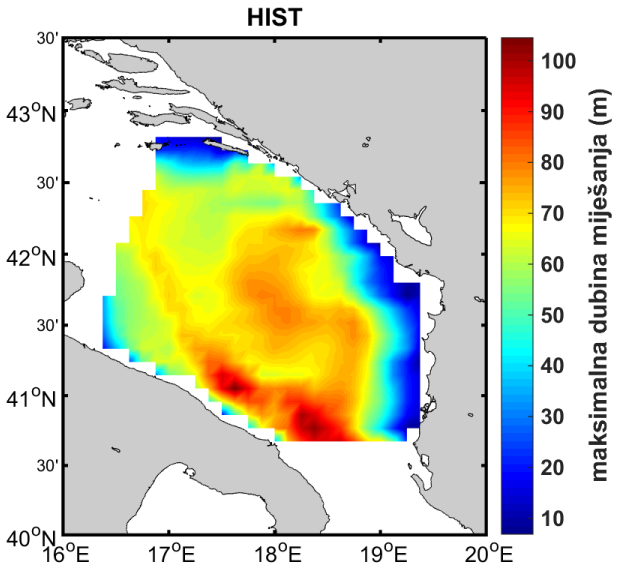

Figure 4.43. Average spatial distribution of maximum mixed-layer depth in February in the Adriatic for the reference period of historical simulation (1976-2005, HIST).

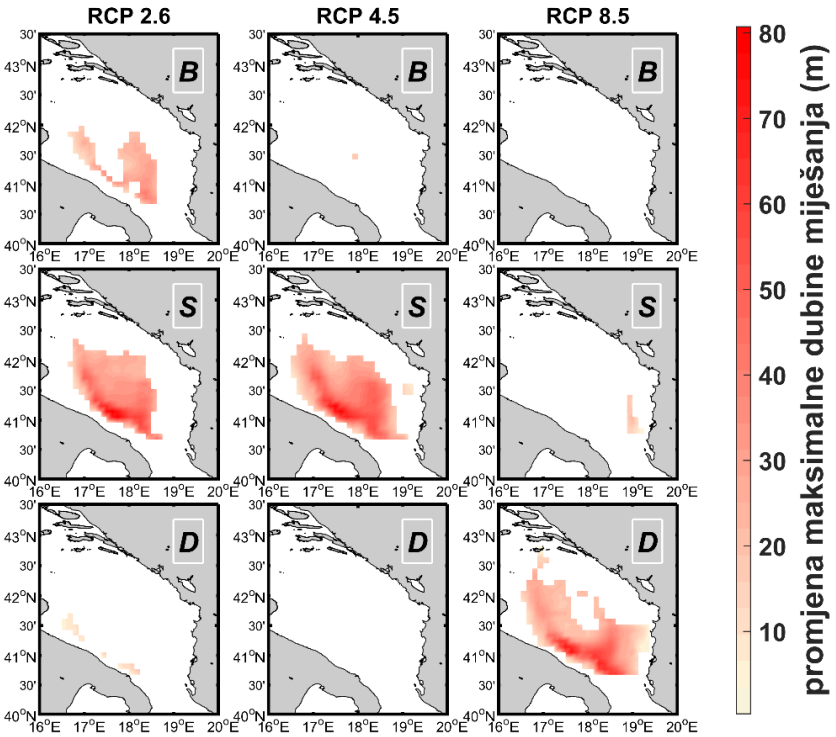

Figure 4.44. Changes in the maximum mixed-layer depth in the southern Adriatic in February for three defined periods (near future - B, middle future - S and far future - D) and for three scenarios (RCP2.6, RCP4.5 and RCP8.5) in relative to the reference period (1976-2005, HIST). Only values beyond the IP confidence interval are shown in the figure.

4.2.5 Projections of BiOS

The behaviour of the Adriatic-Ionian Bimodal Oscillating System (BiOS) in the future climate was analysed using a simplified BiOS index (the difference in sea level height between the centre and the perimeter of the Northern Ionian Gyre; Gačić et al., 2010). The control simulation records a very weak and insignificant positive trend of the BiOS index (0.02 cm / 100 yrs).

The oscillations of the time series of the BiOS index are random in nature, and the differences between periods cannot be clearly understood (Figure 4.45). However, the RCP4.5 scenario visibly predicts an increase in the index towards the end of the 21st century, suggesting a more frequent occurrence of anticyclonic circulation in the northern Ionian Sea and greater advection of less saline waters from the western Mediterranean to the Adriatic. The variability of the BiOS index is increasing in the RCP8.5 scenario towards the end of the 21st century, while the variability of the index is the lowest in the RCP2.6 scenario.

The QQ graph of all BiOS index values in the RCP4.5 and RCP2.6 scenarios and the corresponding histograms (Figure 4.46a) indicate a shift of the BiOS index towards the anticyclonic circulation (more frequent positive BiOS index values), especially in the far future. This would imply that the advection of lower salinity water masses from the western Mediterranean to the Adriatic would be stronger and more frequent in the future than advection of the Levantine Intermediate Water. The RCP8.5 scenario predicts similar behaviour of the BiOS index in the near and medium term. However, in the far future (2071-2100) there is a marked increase in the anticyclonic circulation of BiOS, with a slight increase in the cyclonic circulation too. The increase of the BiOS index and the frequency of occurrence of positive values are also seen on the histograms (Figure 4.46b), especially in the far future in all scenarios.

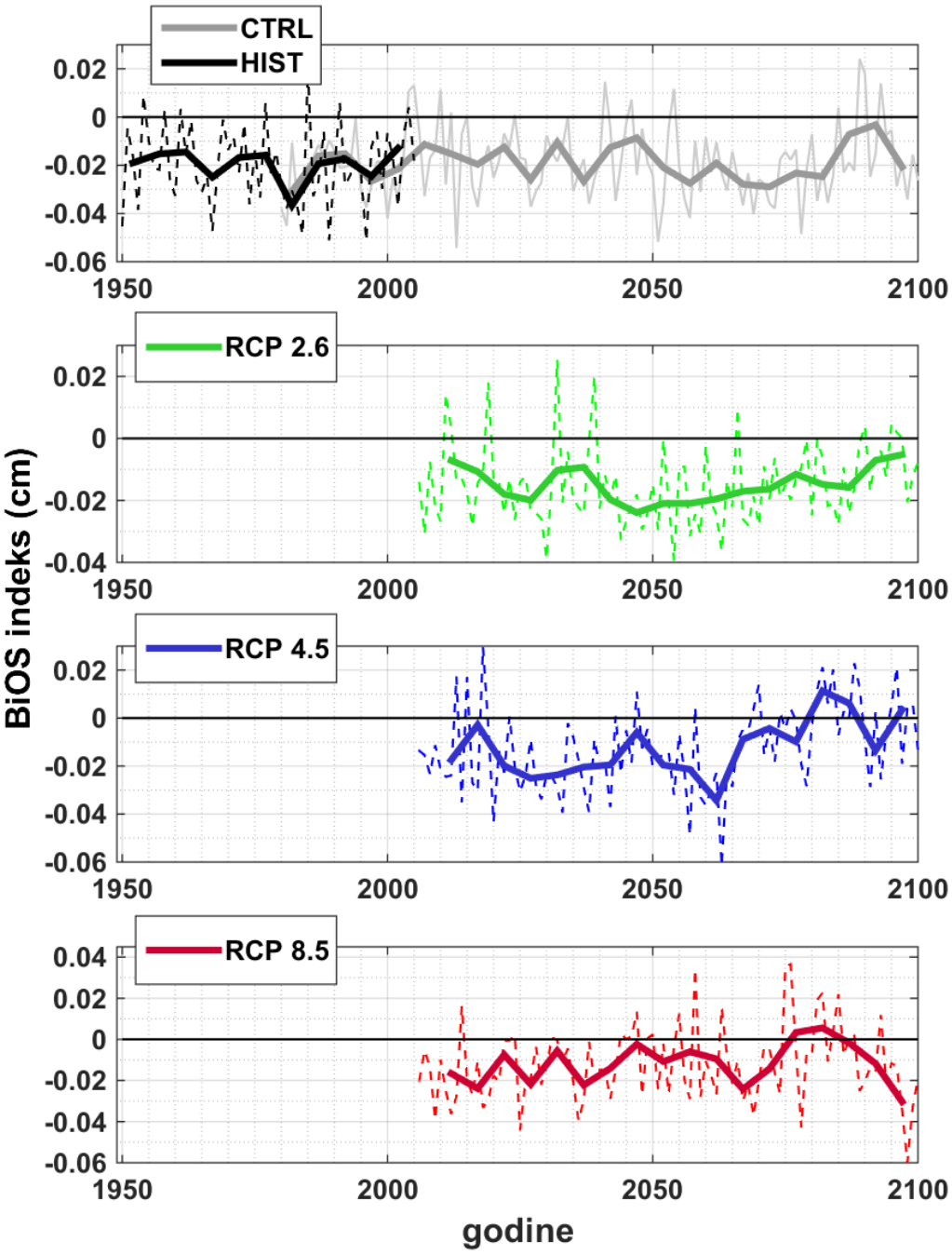

Figure 4.45. Time series of the annual averaged BiOS index for historical simulation (HIST), and for the three scenarios (RCP2.6, RCP4.5, and RCP8.5). The figure also shows the time series of the control simulation (CTRL).

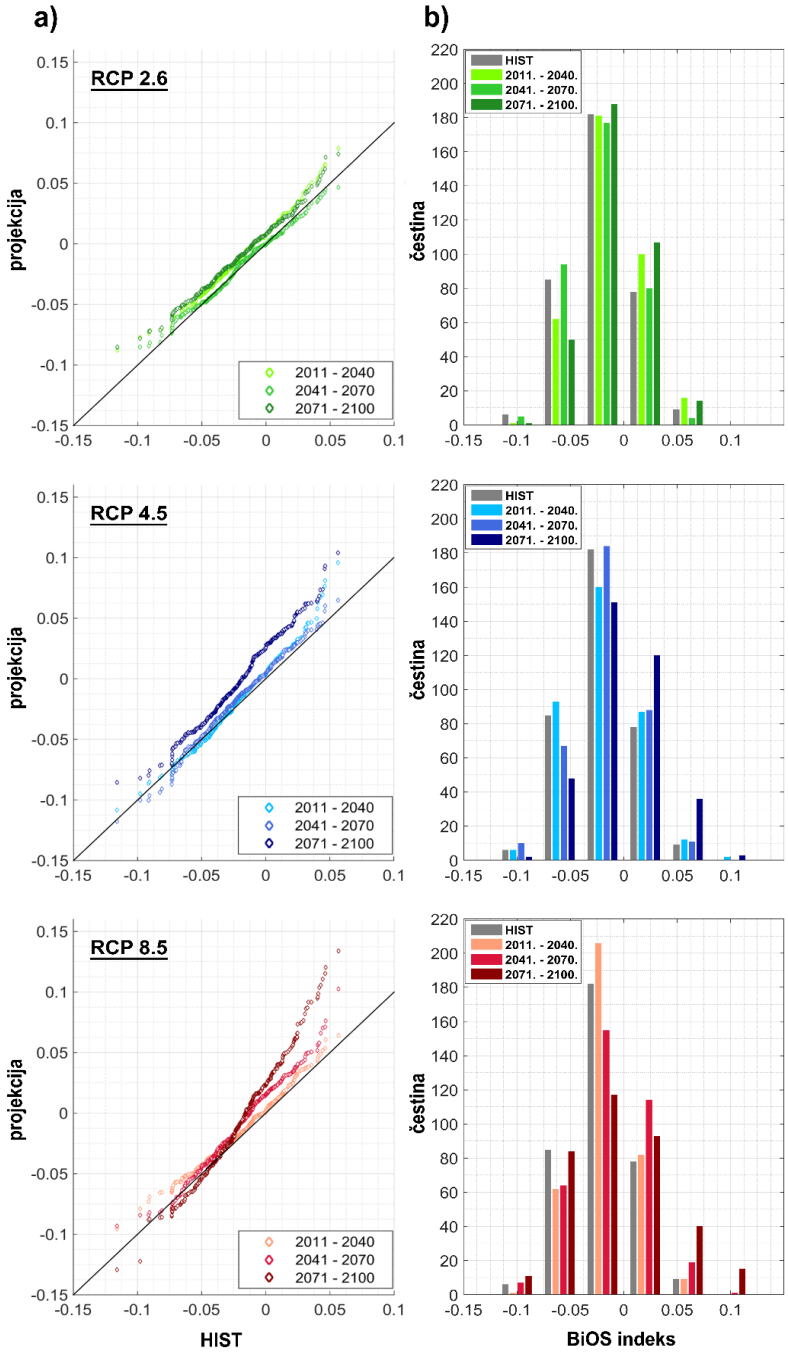

Figure 4.46. a) Q-Q graphs of the BIOS index projected for three scenarios (RCP2.6, RCP4.5 and RCP8.5) versus the reference period (HIST, 1976-2005), for three periods (near, middle and far future), and b) corresponding histograms. The index values in the histograms are divided into classes of width 0.04, whose centres are indicated on the x-axis.

5. APPLICATIONS AT THE PILOT SITE SCALE

5.1. PO DELTA (ISMAR, RER)

In order to investigate future changes through modelling activities, a scenario was defined. In the general approach needed to make use of these results within an adaptation plan, it is important to note that the future scenario can be set according to specific requests. The present implementation took into account the worst case available from IPCC (RCP8.5, https://ar5-syr.ipcc.ch/topic_futurechanges.php) and evaluated the change trend corresponding to the last period simulated (2080-2100), to make clear the rate of change. In future, short or medium term changes can be considered, being aware that the relative uncertainties embedded in future scenarios will be more evident, given the more limited rate of change.

The model implemented is SHYFEM (Shallow Water Hydrodynamic Finite Element Model). Full description of the modelling tool can be found in Umgiesser et al. (2014) and the code is open source and freely downloadable at www.ismar.cnr.it/shyfem.

In the following, the CLIMATE CHANGE RCP8.5 SCENARIO setup is described.

5.1.1. Model Setup

The finite element grid and the bathymetric information were kept as for the Present State simulation (described in Deliverable 3.3. and here re-proposed in Fig. 5.1) in order to allow clear comparisons. It is clear that in 100 years some morphological changes will be in place and, in future works, the adaptation of the bathymetric information and the more general morpho-dynamic asset will be needed, if data available.

The period modelled covers 2 years (namely 2080-2081), being a synthetic reproduction of the conditions of the years 2010-2011 with forcing adapted imposing the CC rate of change of a scenario in the time period 2080-2100.

The general approach adopted for the climate change scenario implies the imposition of the percentage rate of changes to the realistic time-series used to force the Present State simulation (in Deliverable 3.3). This allows keeping the same level of variability along the years, avoiding too weak hypothesis for the Future Scenario.

At the river boundary, both for the Adige and the Po Pontelagoscuro discharge and temperature inputs, the monthly rate of change in percentage is imposed, obtained from http://swicca.climate.copernicus.eu/wp-content/uploads/Metadata_RiverFlow_lisflood.pdf and from http://swicca.climate.copernicus.eu/wp-content/uploads/2016/10/Metadata_WaterTemperature_catchment.pdf.

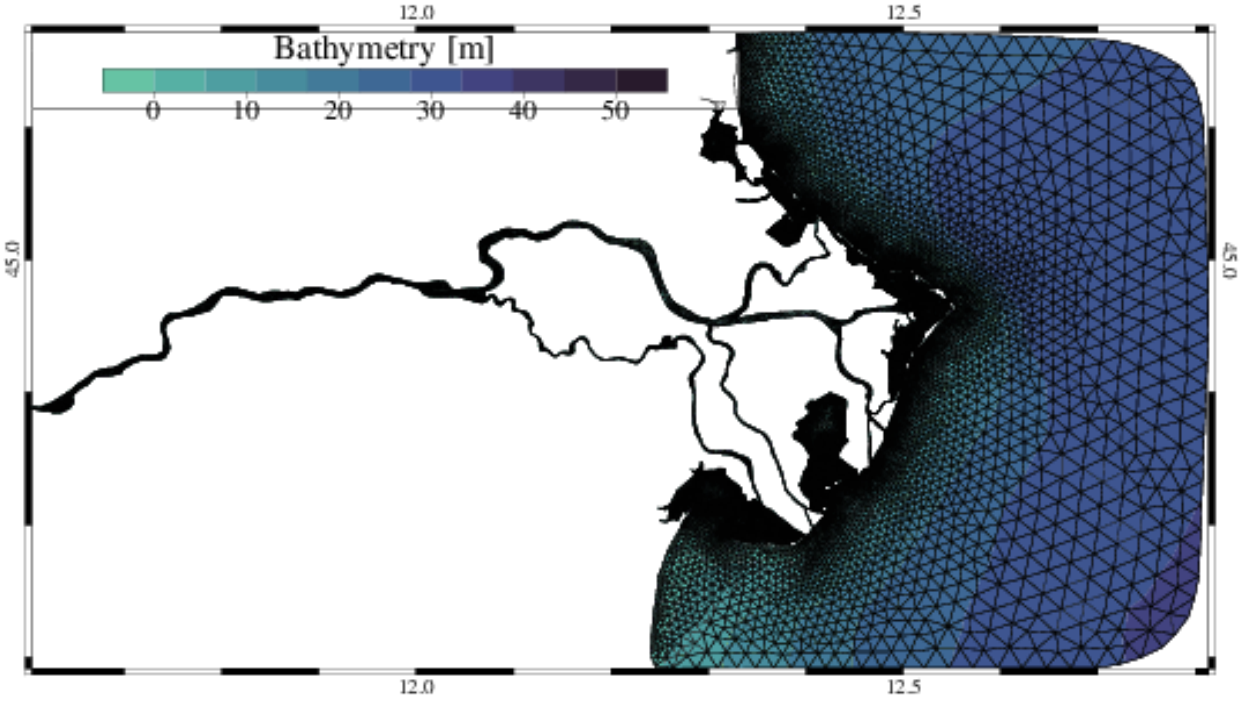

Figure 5.1: Finite element grid and bathymetry adopted for the Climate Change Scenario simulation with SHYFEM. The grid and bathymetry is the same used for the Present State simulation.

As evident also from Table 5.1, which summarizes the rate of change for the different variables used to force the simulation, river discharge variations along the year are positive during winter-spring time, while are negative during the summer season, compared to the present conditions.

For Po di Levante open boundary, the extracted flow from Present State simulation was modified applying the monthly rate of change, as for Adige and Po Pontelagoscuro. Given the absence of more temporally resolved data, for Po di Volano the average rate of change of discharge at the annual basis was adopted.

At the sea open boundary, +0.63 m was added to water level timeseries and, since no information on the rate of change of currents was available, nudging with present state velocity over the water column was done. 3D Salinity and Temperature monthly rate of change is applied to nodes timeseries along the open boundary at sea (RCP8.5).

Meteo-marine forcings are imposed, keeping the wind and atmospheric pressure as the Present State simulation (for helping in understanding dynamics, refer to monthly wind roses for the two years shown in Deliverable 3.3), arguing on the high uncertainty of these specific variables in climate change scenarios on the small spatial scale. Precipitation and air temperature were modified applying a monthly rate of change (RCP8.5, Table 5.1).

Table 5.1: IPCC RCP8.5 scenario, rate of changes imposed, at the monthly and annual basys, for the different forcings.

RCP8.5	Air Temperature [%]	Precipitation [%]	Salinity [%]	Water Level [m]	Water Temp [%]	River Discharge [%]	River Temperature [%]
Abs Var				+0.63			
January	49.42	18.71	1.65		32.86	41	39.66
February	50.45	18.09	1.51		38.61	43	42.80
March	42.37	5.51	1.56		38.81	41	44.02
April	30.78	-14.6	1.64		33.52	12	38.26
May	23.04	-4.57	1.72		25.82	-12	43.76
June	20.18	-17.97	1.81		20.36	-33	53.52
July	20.14	-32.41	1.88		18.58	-38	70.33
August	22.83	-31.31	1.91		19.03	-26	73.91
September	22.61	-12.95	1.92		18.91	-27	47.72
October	23.39	6.41	1.94		19.19	-8	38.62
November	30.93	11.94	1.92		21.66	15	35.12
December	39.07	17.18	1.84		26.21	11	35.23

What concerns the dewatering pumps introduced in the Present State simulation, since it was not possible to do hypothesis on their discharge changes in the future, they were kept as in the present state. The hypothesis, given the lack of data on scenarios, is that there is no change in the land use and anthropic water use. In order to evaluate also this aspect in future scenarios, a full model chain, considering the future plans on land water use and applying drainage basin models coupled to the river-sea model, is suggested.

For reference on the Present State simulation and the full description of the setup, see Deliverable 3.3.

The model implementation produced data, following the unstructured grid resolution, for the area of the Po Delta and its coastal shelf, for the following variables: water temperature, salinity, water level and currents. For the Po Delta Lagoons also the Water Residence Time (WRT) is computed.

5.1.2. Model Results

In the following, surface maps of the above mentioned variables are discussed (water temperature, salinity and currents). Here we discuss results for the surface since more relevant, particularly for the Po Delta system and its transitional areas. Water level maps are not shown, even though data are produced and made available, since no significant changes, in terms of monthly or seasonal mean, are detected, except the obvious shift of 0.63 m (all monthly variations are connected to annual variability driven by wind and atmospheric pressure that, as said, are imposed as in the Present State simulation). Monthly

and seasonal means are shown for all variables and for WRT, as well as maps of climate change vs present condition differences.

5.1.2.1. Monthly averages

In Figs. 5.2, 5.3, 5.4 and 5.5 monthly averages of surface salinity and temperature are presented for the two simulated years. These variables were computed in 3D and data are available not only for surface but for the whole water column, in NetCDF format and stored by the project.

Figs. 5.2 and 5.3 show how the ROFI (Region of Freshwater Influence) is evolving in the different months, following the higher/lower inflow of freshwater from the river. For the first year, the trend is similar to the one registered in the Present State simulation, with higher freshwater contribution of the river in late winter and spring 2080 (March, April, May, June) and in November. August and September 2080 are characterized particularly by higher surface salinity, compared to the rest of the year, while, generally, 2081 is generally saltier. The highest rate of change (increase) in salinity, compared to the Present State simulation, is registered in the summer season, even thou with different absolute values for the two years. It has to be mentioned that the changes registered for the first year of the scenario are not representative of the full period and the second year can give the flavor of the inter-annual variability that occurs in any case (even though longer simulations reproducing decades are needed to properly describe the inter-annual variability). At least it is possible to evaluate if the change induced by the climate change is abrupt or comparable with shorter scale variations due to normal weather evolution.

As evidenced in the present day simulation, the second simulated year seems characterized by lower freshwater input, compared to the first. This trend is evident also in the Present State simulation, understanding how the rate of change induced by climate change is less effective on salinity than the normal variability among years (Figs. 5.2 and 5.3 and see figures in Deliverable 3.3). The surface salinity patterns during the second year seem more homogeneous, with larger bands of fresher water along the coast in January, February and March 2081, with a slight increase also in June 2081 (due to the discharge peaks present in the measured data and just multiplied for a rate of change in the climate change simulation and imposed as boundary condition). The shelf is always characterized by salinity higher than 38, except for September 2081 when values are around 34-36.

Monthly average surface temperatures are generally higher if compared to the corresponding ones of the Present State simulation (Figs. 5.4 and 5.5). This is not surprising; however, the patterns and the horizontal gradients are slightly changed. January 2080 and 2081 show surface lower temperature within the delta system, in the inner parts of Goro, Scardovari and Vallona Lagoons (4°C), while a large coastal band shows values around 8°C, then increasing offshore up to 12°C in 2080. The offshore thermal condition of January 2081 is more homogeneous, being everywhere colder (8°C). The same gradients, from lower inland temperature to higher offshore temperature are seen in February and December 2080, early winter 2081 and October, November and December 2081, while more homogeneous situation, with

almost no horizontal thermal gradients, is seen in March 2080 (around 11-12°C) and September 2081 (28°C). June 2080 is also thermally homogeneous, around 28°C in the whole system. April 2080 is characterized by a clear thermal detachment between the delta system (warmer in the branches and in the lagoons, 20°C) and the full coastal and shelf area, which is colder (16°C). The same configuration of horizontal thermal gradients is present in April 2081. Interestingly, May 2080 shows a narrow colder surface band following the coastline (around 20°C), quite limited in space and originated by the river, indicating a limited ROFI (Region of Freshwater Influence) in this month. The rest of the system offshore has higher temperatures (24°C). July and August 2080 and 2081 present higher temperatures, around 32°C and 30°C respectively, in the majority of the system. In October 2080 and 2081 freshwater flows offshore at the same temperature of more offshore sea portions (24°C): while in 2080 narrow coastal bands of colder waters are seen (20°C), characterizing also the lagoons' system, in 2081 the full coastal and open sea area is constant at 24°C, with lagoons around 20°C. River water, warmer than the sea one, flows in the main basin in November 2080 (river-sea difference around 2-3°C). In November 2081 warmer waters seems just limited to the upper river branches, not reaching the sea.

In order to make evident the changes compared to the present conditions, the difference in absolute values for surface salinity (Figs. 5.6 and 5.7) and temperature (Figs. 5.8 and 5.9) are presented. As shown in Table 1, the open sea salinity increases of around 1.5% in winter (February) and less than 2% in the summer months. Therefore, no large changes are evident in the open sea. However, the different amount of freshwater from the river, with percentage increases of around +40% in the winter months (January, February) and corresponding decreases in summer (around -40% in July), mainly drive the local response in term of salinity change. Fig. 5.6 shows how January, February and March 2080 experience almost no changes in surface salinity in the shelf, while the deltaic system and specifically the lagoons are fresher, with a salt decrease of about 2-3, compared to present conditions. Quite similar is the situation in the early winter in 2081 (Fig. 5.7).

April, November and December 2080 show differences just within the Po Delta system and in the near coast, largely within the ROFI, with fresher environments in the transitional zones (-[2 3]) and saltier ones along the coast (+[2 3]). In the other months, both for the first and the second year of simulation, the full system seems saltier in the surface (+[5 6] in the innermost Canarin Lagoon and in the Tolle and Gnocca mouths, +[2 3] along the coastal areas), with the almost constant exception of Basson Lagoon, directly influenced by the Pila branch, that keeps always fresher water in it, compared to the present conditions. These conditions, even if similar in the two years, are enhanced in 2081.

If looking at the Goro Lagoon, it is saltier than the present condition from May to October in both years, with peaks just behind the sand bar detaching the lagoon from sea. On the other hand, in the other months of 2080 the salinity seems not to change significantly in the whole lagoon, compared to present condition, except for the confined area close to the sand bar that becomes fresher. Fresher conditions compared to the present condition are seen in January and February 2081, characterizing also the southernmost coastal band along the Emilia Romagna coastline. Therefore, the localized area within Goro

Lagoon seems to be dependent from the freshwater discharge inputs and from the excesses in evaporation during summer (as also evident from Figs. 5.8 and 5.9, relative to temperature difference).

What concerns the inner zones of Canarin Lagoon, interestingly they always experience saltier surface environments compared to the present conditions, no matter if in months with more or less river discharge. These aspects and more generally the behavior of other lagoons suggest that the salinity variations are not driven just by the changes in the river discharge, since they are more reactive to evaporative/precipitation processes and give more immediate feedbacks to the general increase in air temperature and, therefore, heat fluxes.

Fig. 5.8 clarifies how the full system experiences surface temperature increase, from 2°C in January 2080, to 5-6°C in June, July and August 2080 (Fig. 5.8). In 2081 the surface thermal range is from 2-3°C in January and February to +6°C in a large coastal area in July, August and September. The highest rate of change is registered always within the ROFI, and is the product, in certain months, of the combined effect of air temperature increase and river temperature increase (e.g. July and August, for both years, when the river water is around +70% warmer than present conditions, Table 5.1).

Concerning surface water currents, monthly maps are shown in Figs. 5.10 and 5.11. Monthly means filter out the major tidal signals and give indications about the mean currents induced by the other forcings (e.g. wind regimes, river discharge, thermal gradients). As expected, there are months when the coastal dynamics is stronger, due to the higher inflow coming from Po River branches. Clear plumes, with surface velocities above 20 cm s^{-1} are recognized outside Pila, Tolle, Goro and Gnocca branches, flowing southward in January, February, November and December 2080 and, even stronger in January, February and March 2081, particularly in the southern part of the delta. The strongest signals are registered in late fall 2080 and winter 2081. Tolle, Gnocca and Goro branches inject more energetic flows into the system, compared to Pila and Maistra and flows are still above 30 cm s^{-1} in March, September and October 2080. Really weak surface circulation is detected in July 2080 and September 2081, probably due to weak/absent wind regimes (large majority of events in the summer months of 2081, see wind roses in Deliverable 3.3) and low river discharge.

Wind regimes play surely a role in explaining the wide range of direction of surface currents, with plumes more detached offshore for Pila, like in May 2080, when probably winds blowing from South-West prevail. Some months show the classical geostrophic patterns of current, flowing along the coast from North to South. This is the case for early winter and late fall 2080 months (October), spring 2081 and October 2081 (Fig. 5.10). However, these evaluations on wind regimes are not providing insights on climate change effects, since they were not changed compared to Present State situation. They just express the rate of variability of currents in a climate change perspective, given certain wind regimes. Also, some local effects are evident, with closed anticyclonic cells forming in the northern part of the delta, like in July and August 2080 and late spring/summer 2081. Along the northern part of the delta also northward surface currents are seen in February and March 2080 and February, March and April 2081, with the Maistra plume spreading in a more radial way perpendicularly to the coast. A constant recirculation cell, more or less

energetic in correspondence of the intensity of river discharge is in the majority of months present just South of Pila branch, in front of the Basson and Canarin lagoons, particularly in 2081.

As expected, the internal circulation of lagoons is weak, always around 5-10 cm s^{-1}; if looking at Goro Lagoon, one of the more extensive and connected to the open sea ones, we notice that the surface current patterns, in its innermost area, are constant, with slight variations just in correspondence to the sand bar that detaches it from the main basin (Figs. 5.10 and 5.11).

Figures 5.12 and 5.13 provide interesting insight on the rate of change in surface current speed, comparing the Climate Change scenario to the present conditions. The river flow inside the river branches seems to be increased in winter and late fall periods (about +10 cm s^{-1}), while it is lowered in the summer months. Equally, during summer the river plumes seem to be weaker, from less than -12 cm s^{-1} at the river mouths to -8 cm s^{-1} few kilometers offshore. This result is explicable if we think that in the summer season the river discharge is up to 38% lower than in the present conditions (July, see Table 5.1). Looking at the rate of change of the boundary conditions it is evident that in the summer season the rate of change of river temperature is higher than the one of the open sea water. In fact, if the river is warming from +50 to +70%, the sea water warms of about +18-20% (Table 5.1) in June, July and August of the Climate Change scenario. Therefore, the horizontal thermal gradient is increasing. However, it has to be noted that this thermal gradient does not affect the surface speed as much as the discharge variation. Few areas where surface speed is empowered can be detected just at the border of river plumes, for example in February and March 2080 and February and March 2081, along the whole coastal belt (February 2080 and 2081) and particularly in the southern part of the delta (March and slightly in April 2080, March 2081). A more varied situation can be seen in the northern part of the delta, where months with speed decrease (January, March, April, May, June, July, October 2080) alternate with more patchy months like August and September 2080 and the majority of months in 2081. Here we have to consider the combined effect of discharge decrease and the lowest thermal gradients between river and sea waters. In the same area, the rate of change is almost zero in November and December 2080, which are months with quite low change in river discharge (-8% and +15%, respectively) and quite weak thermal gradients (19 and 13% respectively), which are not the lowest gradient but are weak compared to the summer ones (almost 50%).

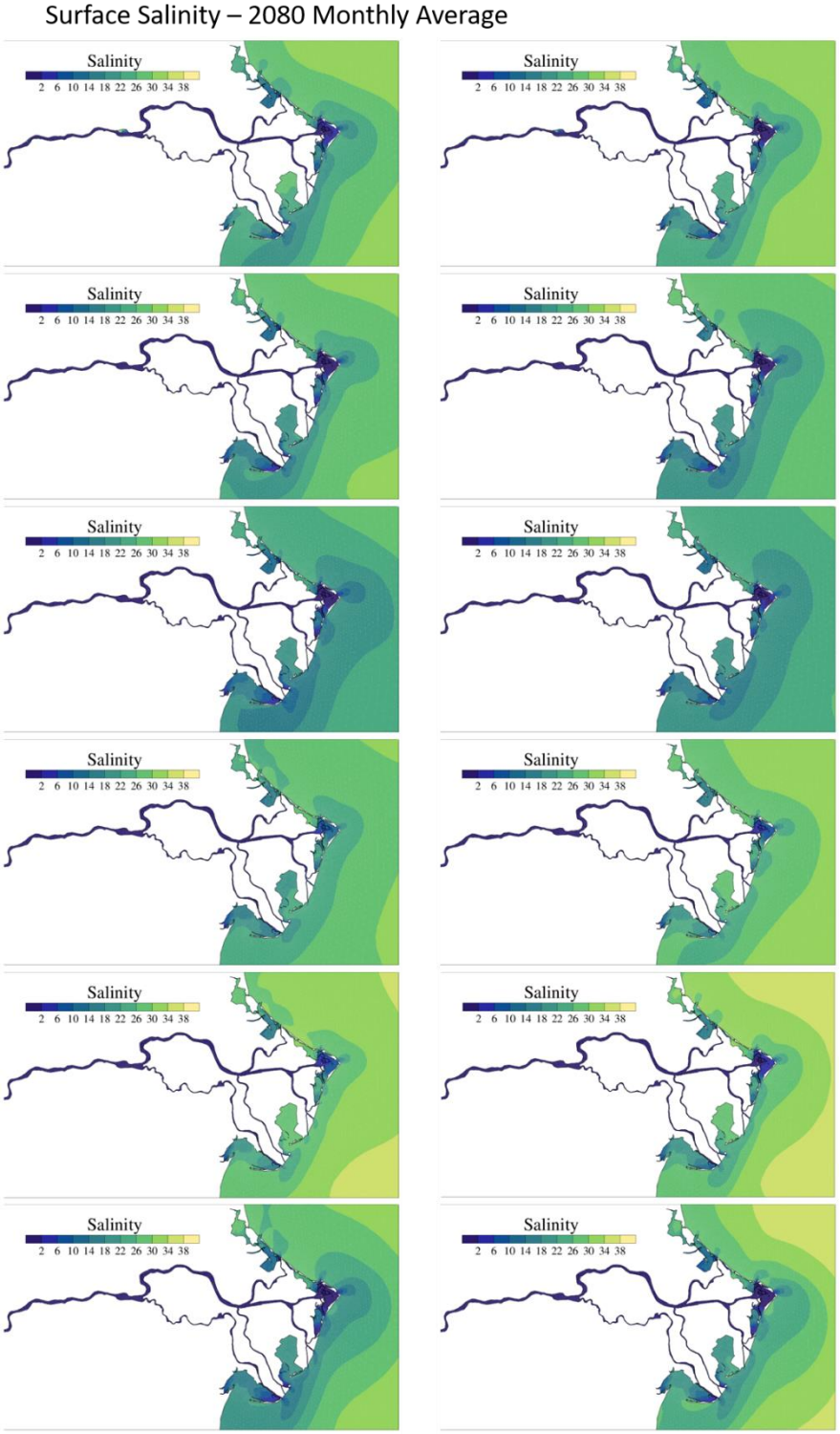

Figure 5.2: Monthly average of surface salinity for the Po River Delta and its shelf, for first year of simulation.

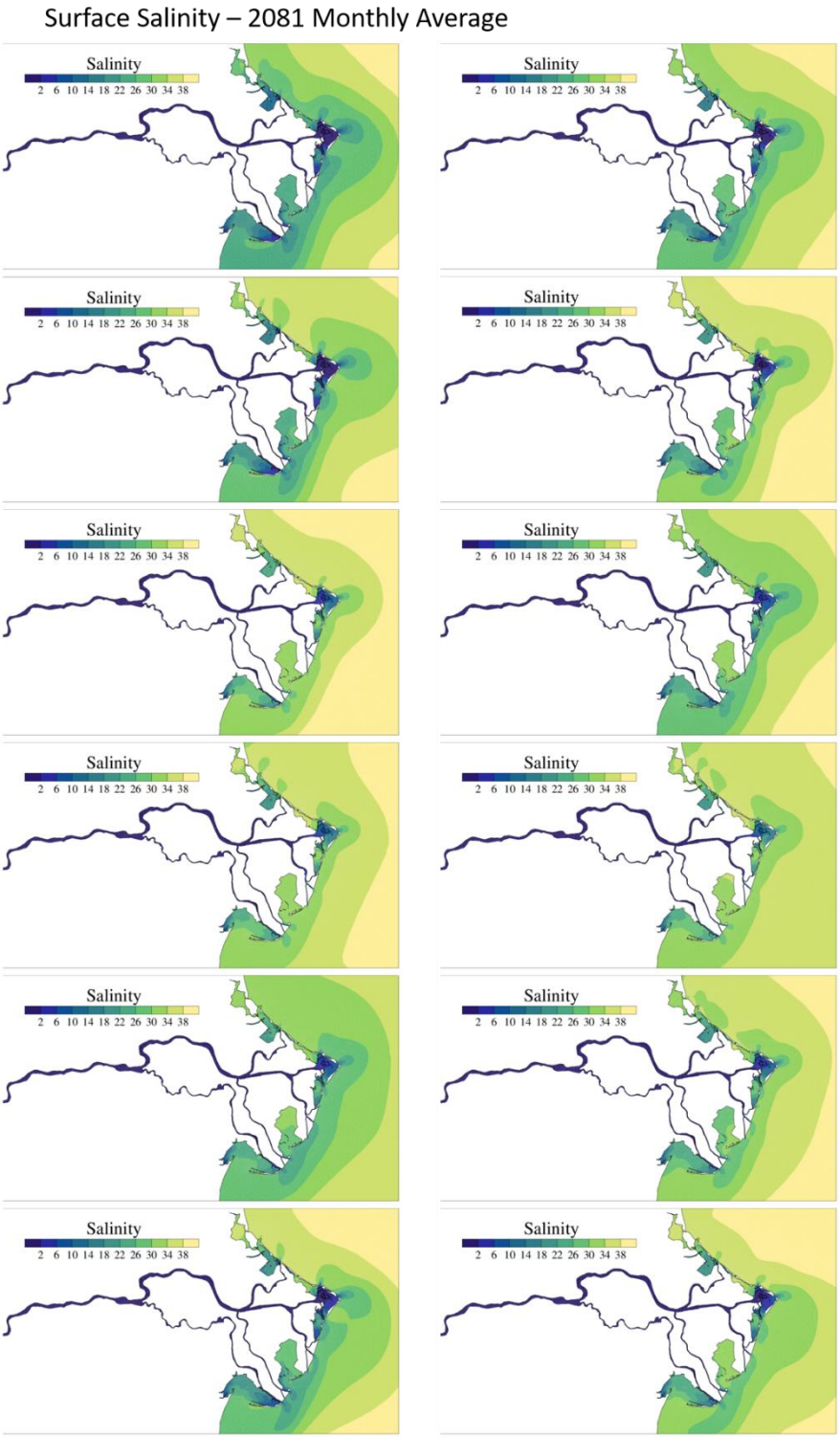

Figure 5.3: Monthly average of surface salinity for the Po River Delta and its shelf, for second year of simulation.

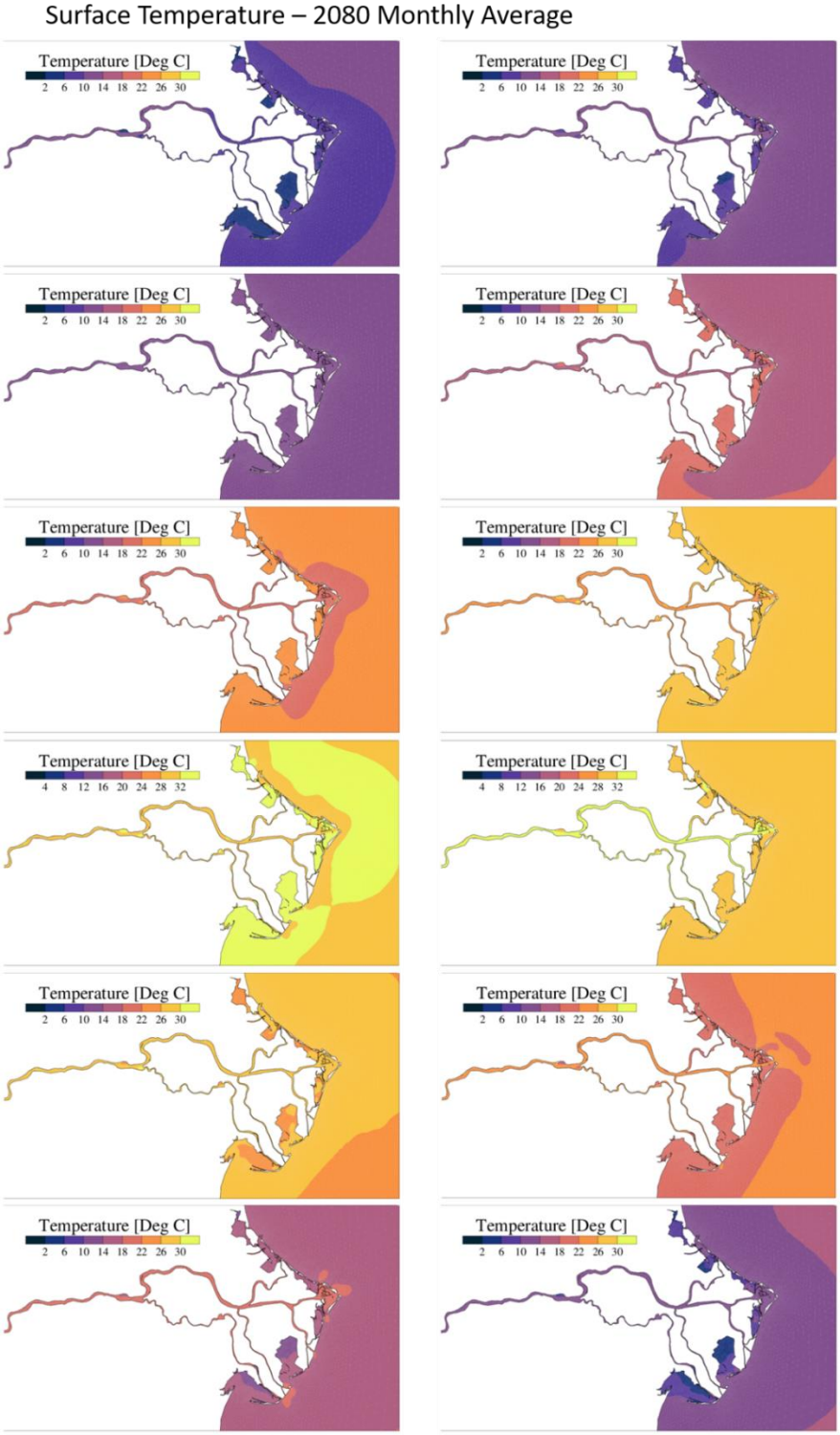

Figure 5.4: Monthly average of surface temperature for the Po River Delta and its shelf, for first year of simulation. Note that the temperature palette is the same for all months, except for July and August, which needed a palette covering higher temperature values.

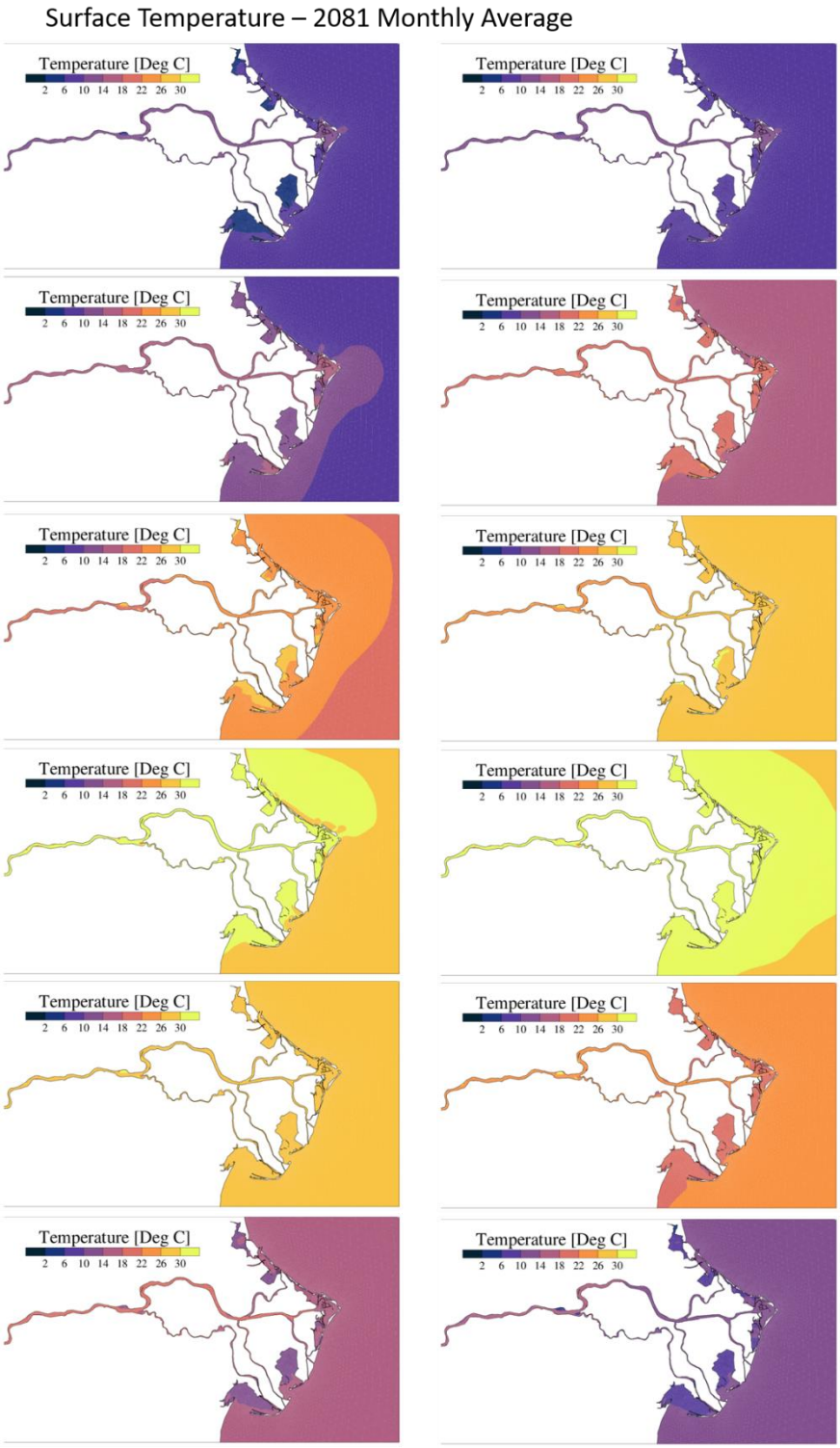

Figure 5.5: Monthly average of surface temperature for the Po River Delta and its shelf, for second year of simulation.

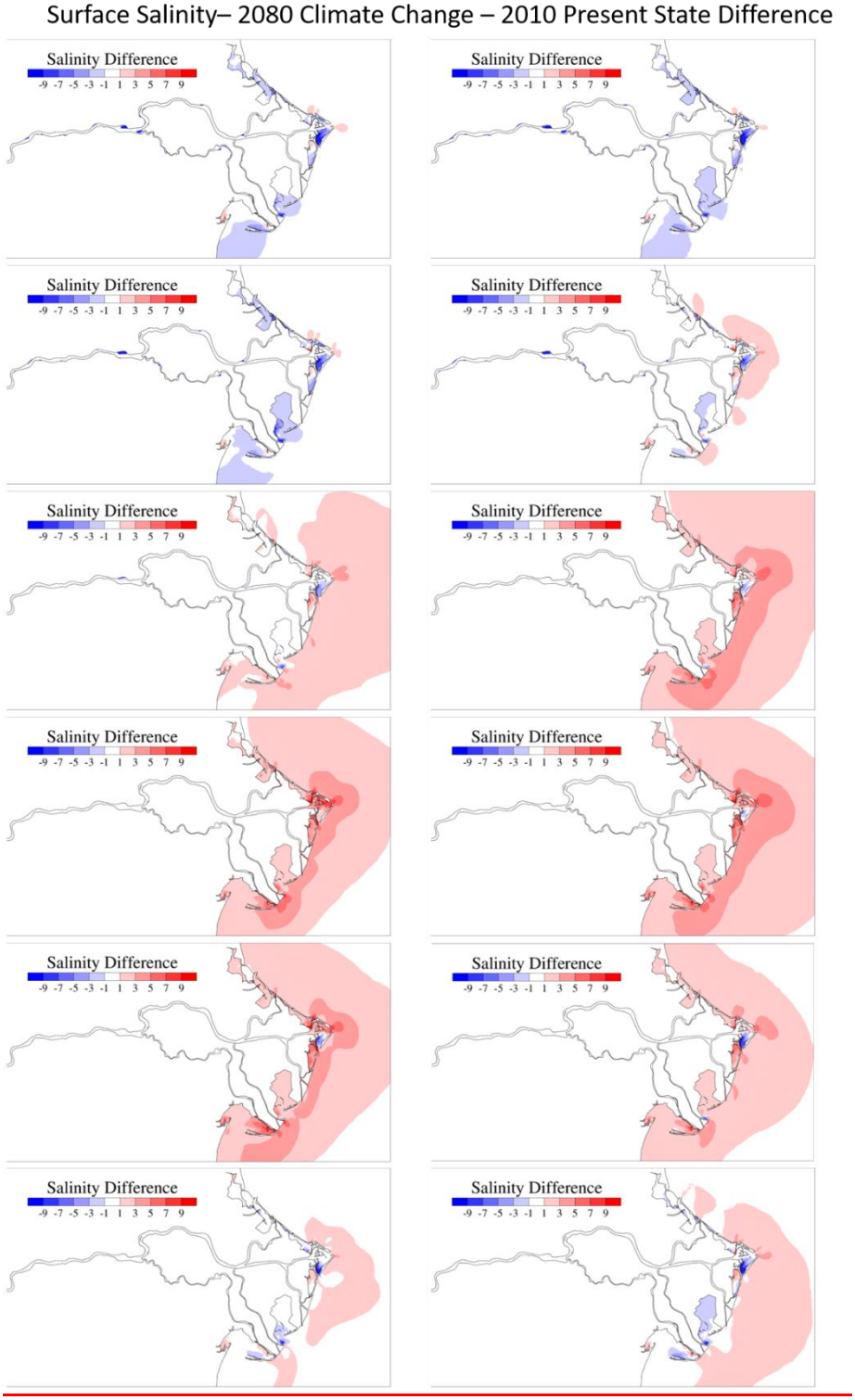

Figure 5.6: Surface Salinity Monthly Differences within the Po River Delta between the Climate Change Scenario 2080 and the Present State 2010. Computation for each month.

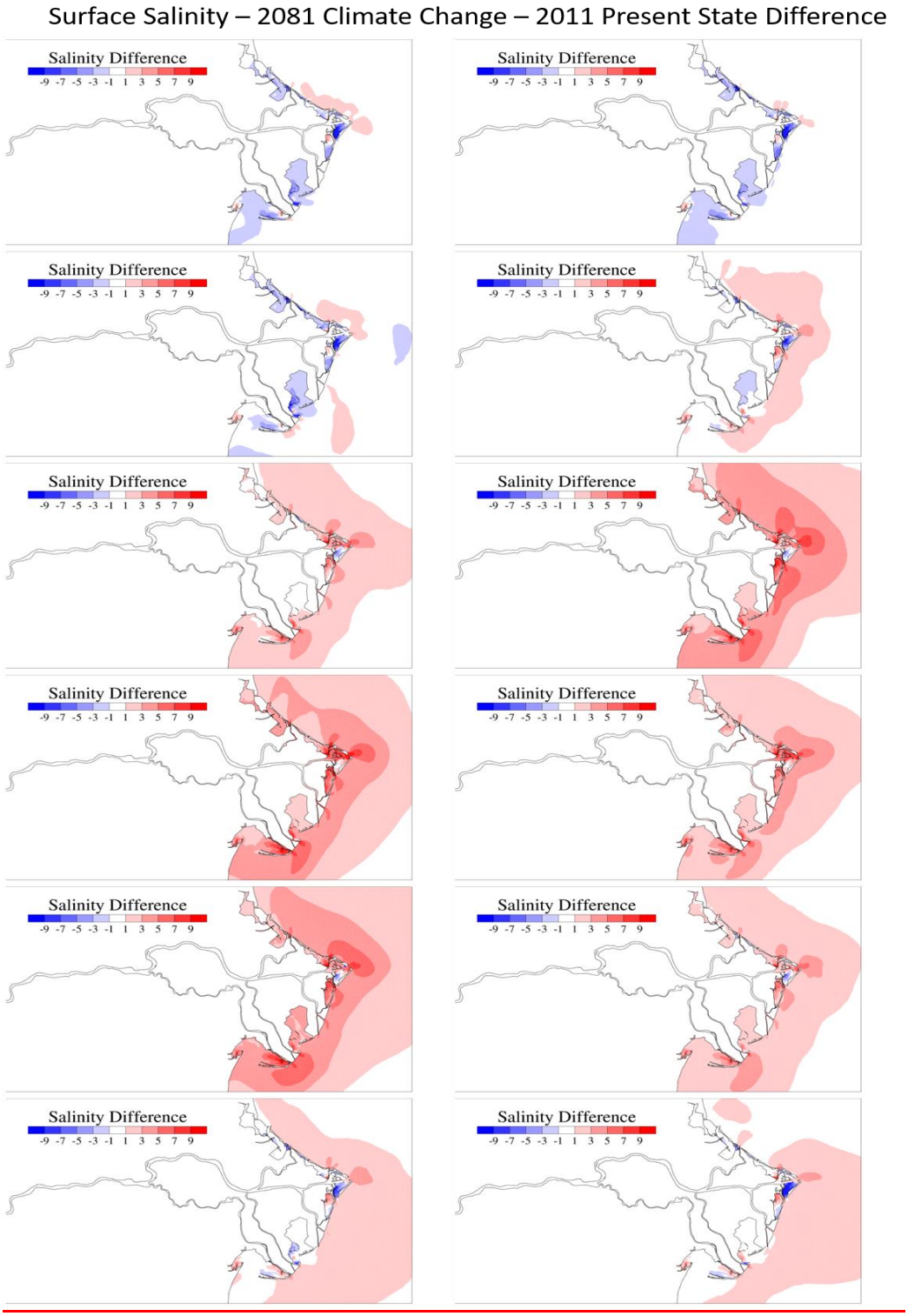

Figure 5.7: Surface Salinity Monthly Differences within the Po River Delta between the Climate Change Scenario 2081 and the Present State 2011. Computation for each month.

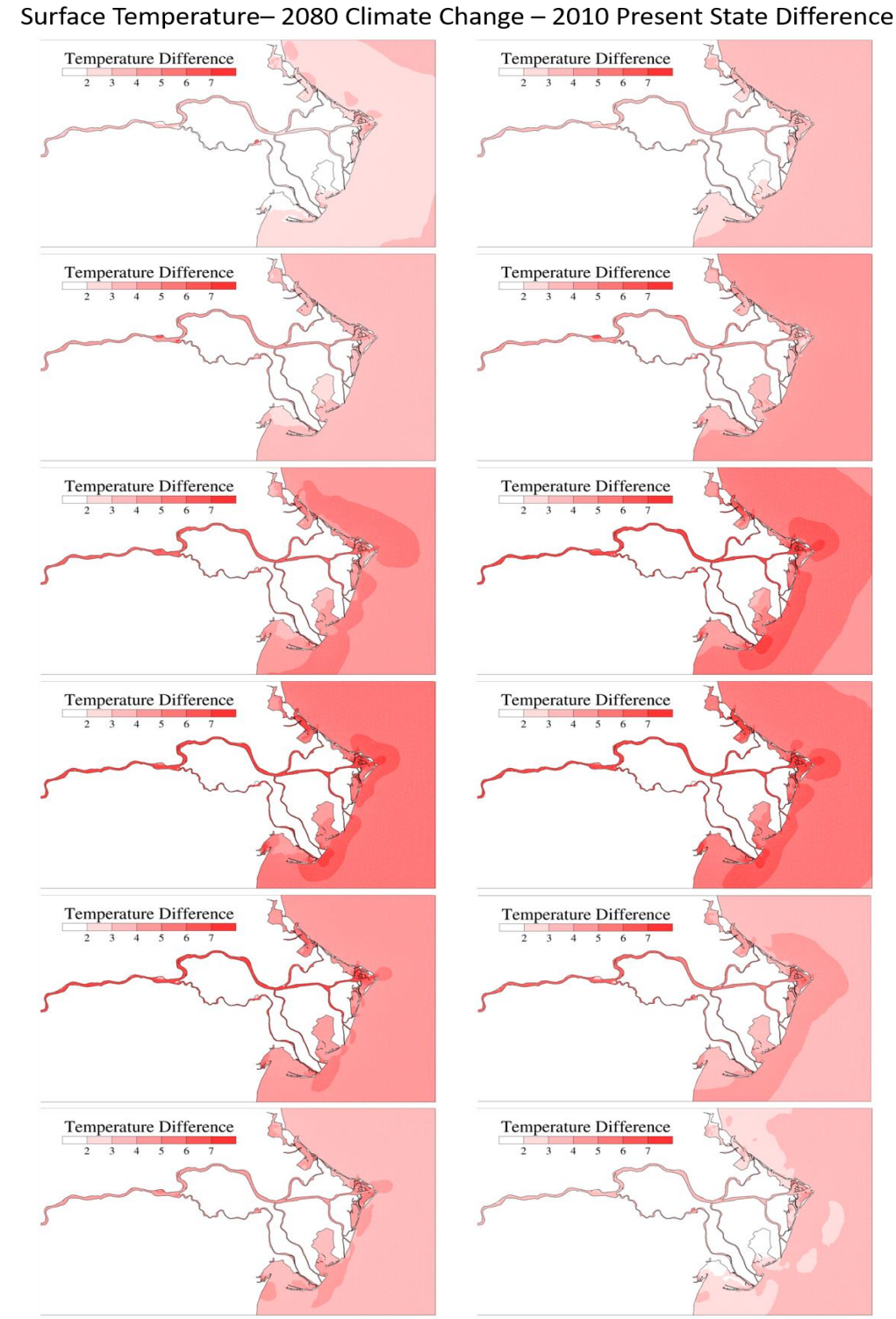

Figure 5.8: Surface Temperature Monthly Differences within the Po River Delta between the Climate Change Scenario 2080 and the Present State 2010. Computation for each month.

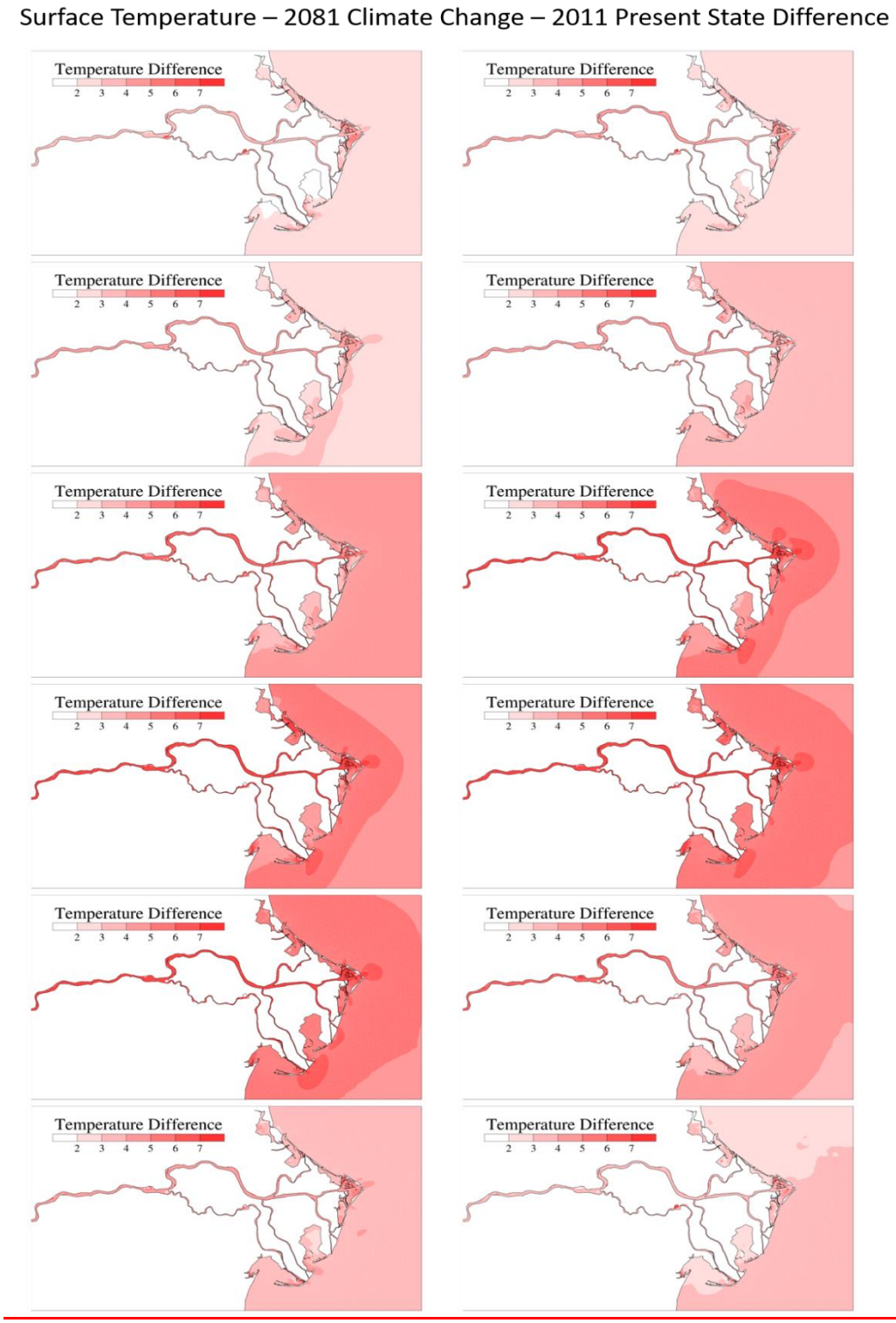

Figure 5.9: Surface Temperature Monthly Differences within the Po River Delta between the Climate Change Scenario 2081 and the Present State 2011. Computation for each month.

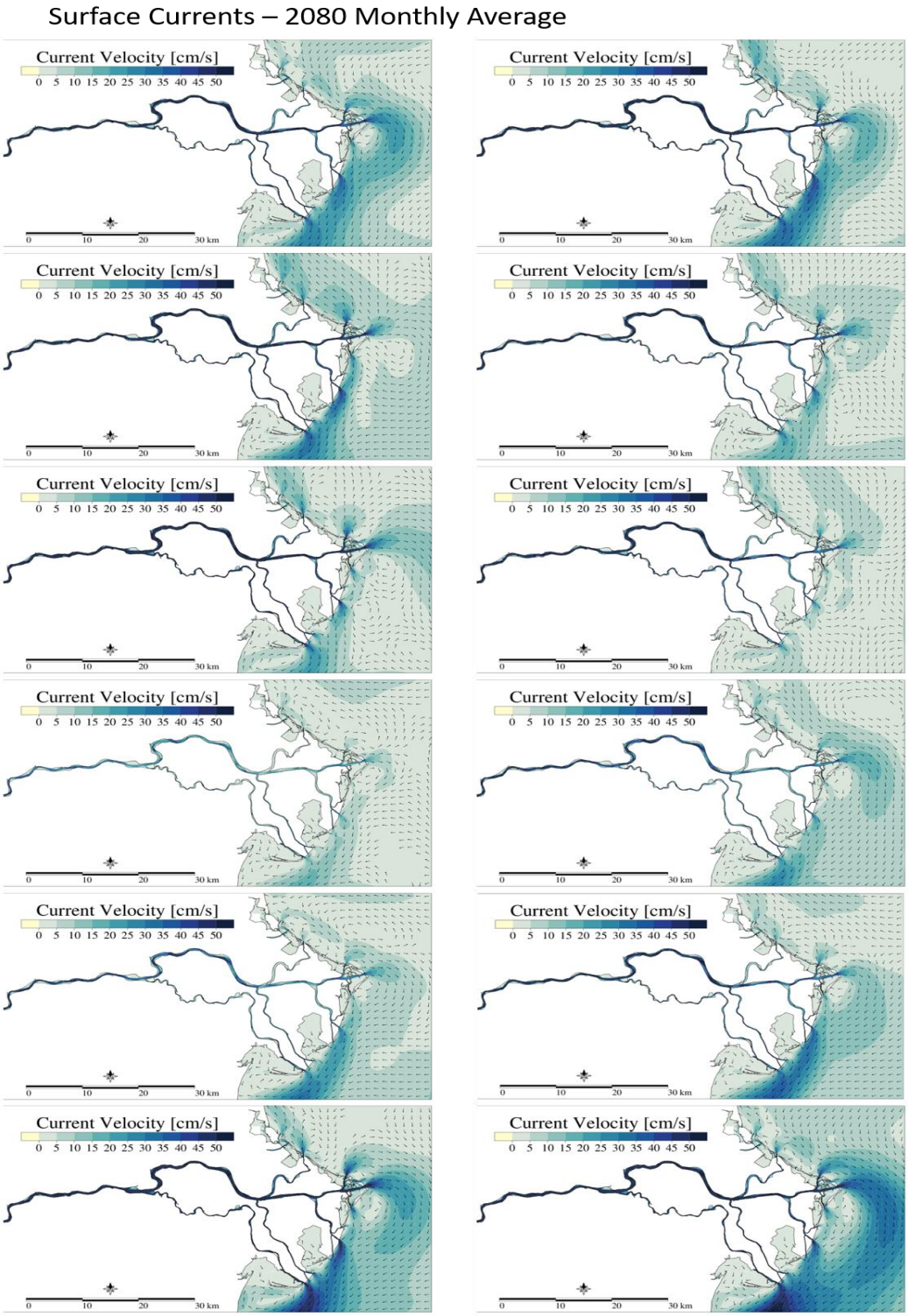

Figure 5.10: Monthly average of surface currents for the Po River Delta and its shelf, for first year of simulation.

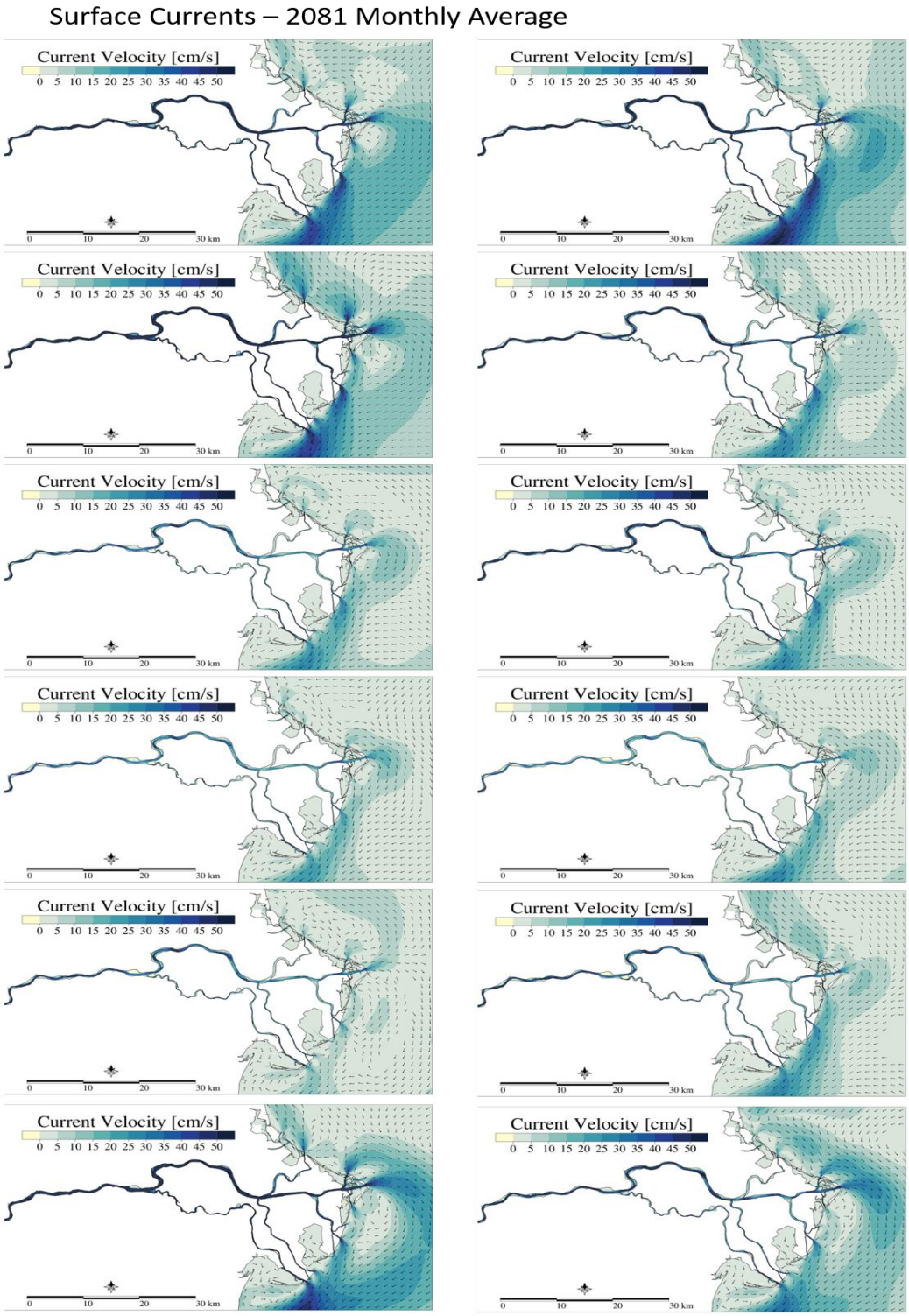

Figure 5.11: Monthly average of surface currents for the Po River Delta and its shelf, for second year of simulation.

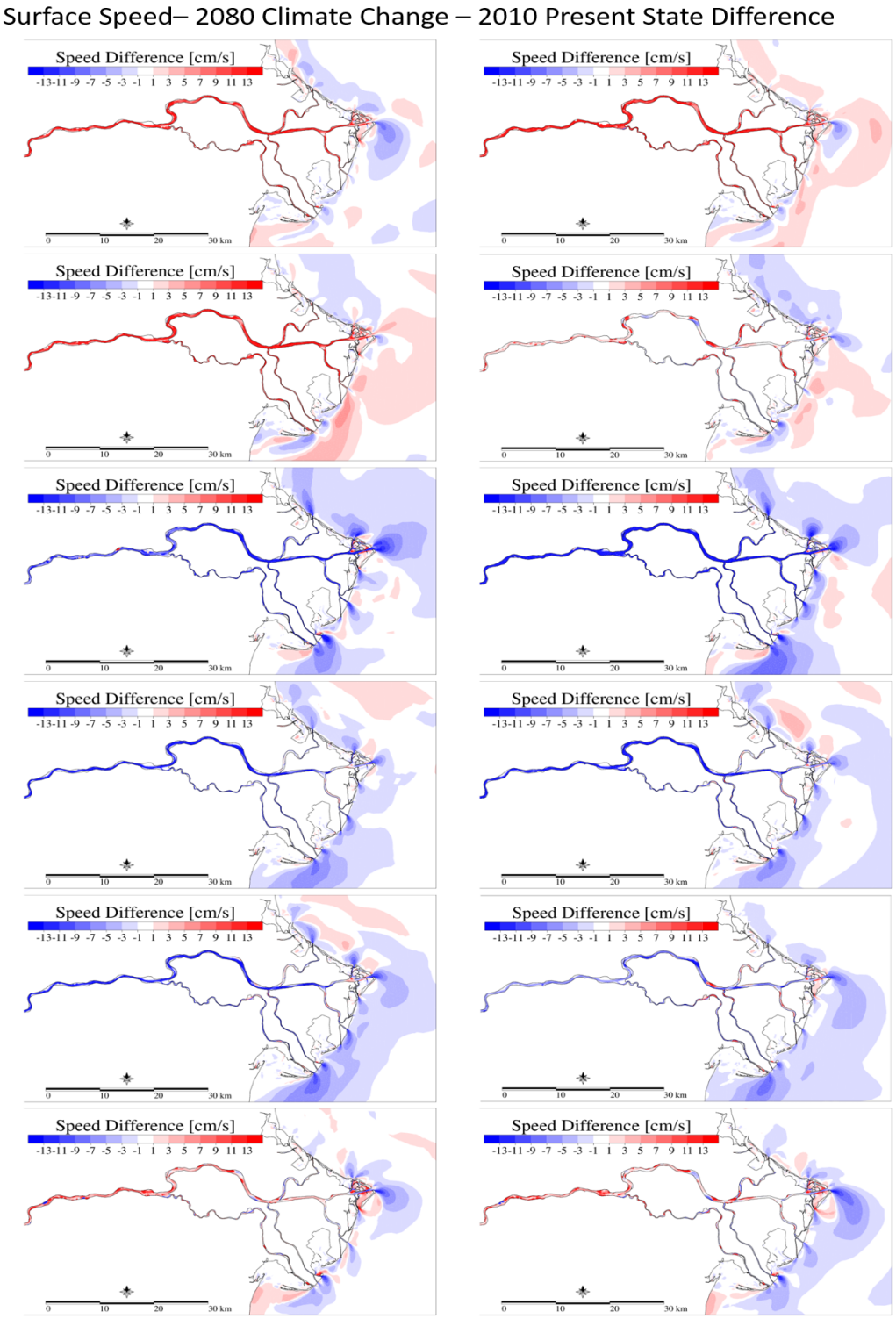

Figure 5.12: Surface Current Speed Monthly Differences within the Po River Delta between the Climate Change Scenario 2080 and the Present State 2010. Computation for each month.

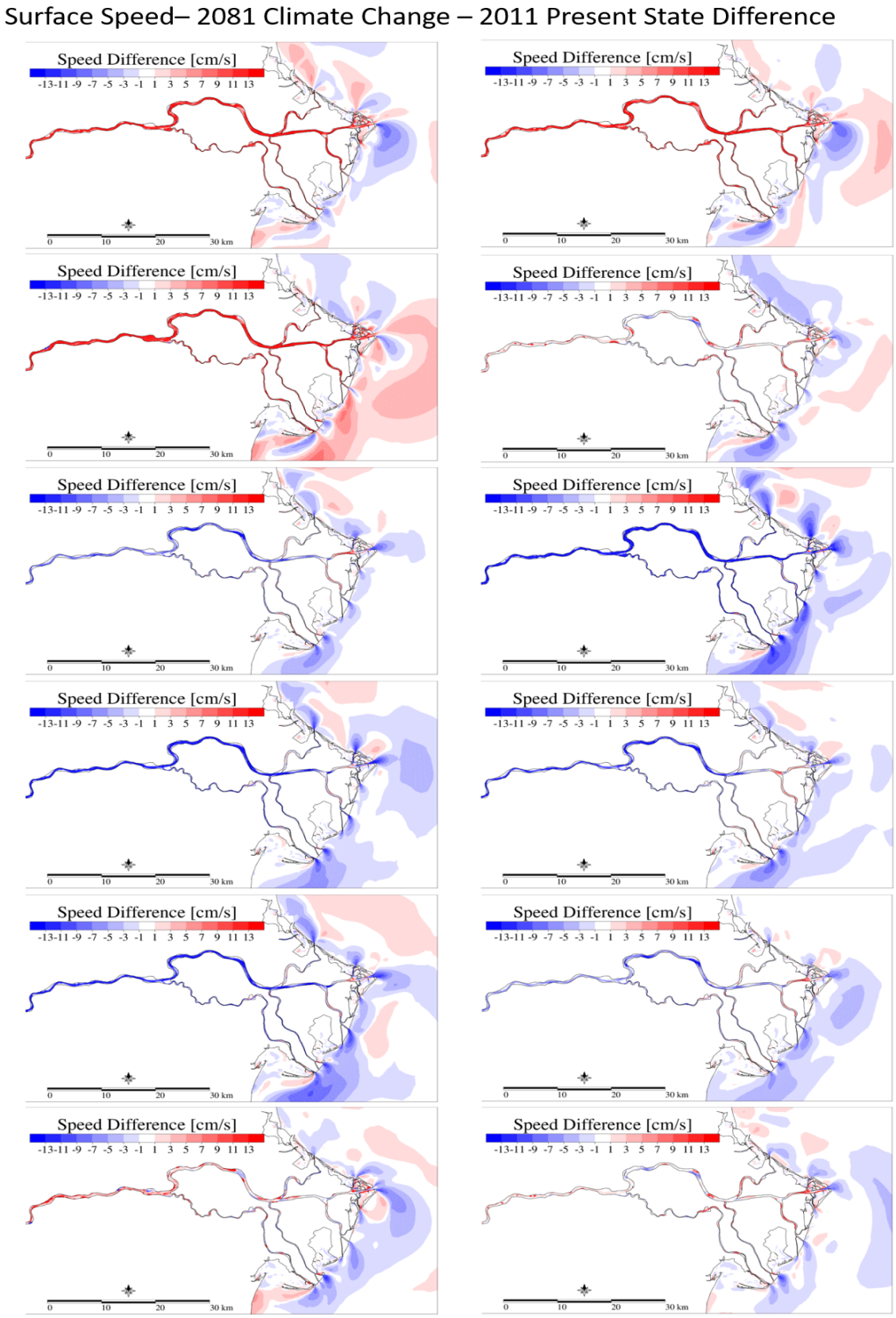

Figure 5.13: Surface Current Speed Monthly Differences within the Po River Delta between the Climate Change Scenario 2081 and the Present State 2011. Computation for each month.

5.1.2.2. Seasonal Averages

Seasonal averages where computed considering the internal division as: January, February and March (Winter); April, May and June (Spring); July, August and September (summer); and October, November and December (Fall).

Observing the seasonal variations of surface salinity and temperature (Figs. 5.14 and 5.15), we notice that the surface salinity pattern is kept in winter, summer and fall 2080, with values in the shelf around 34-36 and bands of fresher water, particularly South of Pila branch, around 24. In 2080 The higher discharge characterizing spring time enlarges the ROFI and surface waters, fresher than the open sea ones, can be detected also several kilometers offshore (salinity around 26-28). Freshwater bulges more pronounced just outside Pila and Gnocca are detected (Fig. 5.14 top). Seasonal averages for 2081 show saltier surface waters in all seasons, as expected. The major difference between same seasons is seen for spring, fresher in 2080 and saltier in 2081, as well as in fall, with a larger fresher area in 2080, fully dependent by the different river freshwater supply due to specific flood events.

What concerns surface temperature, in winter 2080 the full system seems homogeneous around 10-12°C and the peaks of colder waters are detected in the lagoons (8°C). The corresponding season the year after is colder, around 6°C. Totally opposite situation is shown in summer 2080, when the river branches and lagoons are characterized by warmer water, above 30°C, while the coastal and open sea is around 26-28°C. This feature is evident also in 2081 (Fig. 5.15 bottom). Fall 2080 shows a large coastal and inner part between 14 and 18°C, with gradients quite offshore with the open sea waters (20°C), while in 2081 the warmer sea area seems larger (around 20°C). Spring is more homogeneous in 2080, with no relevant surface gradients (24°C) while in 2081 the offshore sea seems colder (around 20°C).

Concerning seasonal averages of surface currents, the most dynamic seasons result to be fall 2080 and winter 2081 with energetic plumes, well above 30 cm s^{-1} flowing southward (Fig. 5.16). Goro and Tolle branches are those more contributing to the coastal surface speed and the southern part of the delta is characterized by a southward flow, while the northern part shows small scale recirculation cells, probably due to the local main wind regimes. Spring 2080 and summer 2081 show the less energetic surface dynamics, with more uniform, rounded river bulges and coastal flows around 5 cm s^{-1}. In spring 2080 two recirculation cells, a kind of dipole with the anticyclonic one northward and the cyclonic one southward, are seen South of the Pila branch. Another anticyclonic cell is detected in front of Goro Lagoon. The northern part of the delta is characterized by northward surface currents. In this area northward currents are seen also in winter 2080 and 2081, while small cells are present in summer 2080 and 2081. For both these seasons, the southern part of the delta shows southward currents, stronger in winter (about 25-30 cm s^{-1} in the plumes, 15 cm s^{-1} along the coast) than in summer (about 20 cm s^{-1} in the plumes, 10-15 cm s^{-1} along the coast).

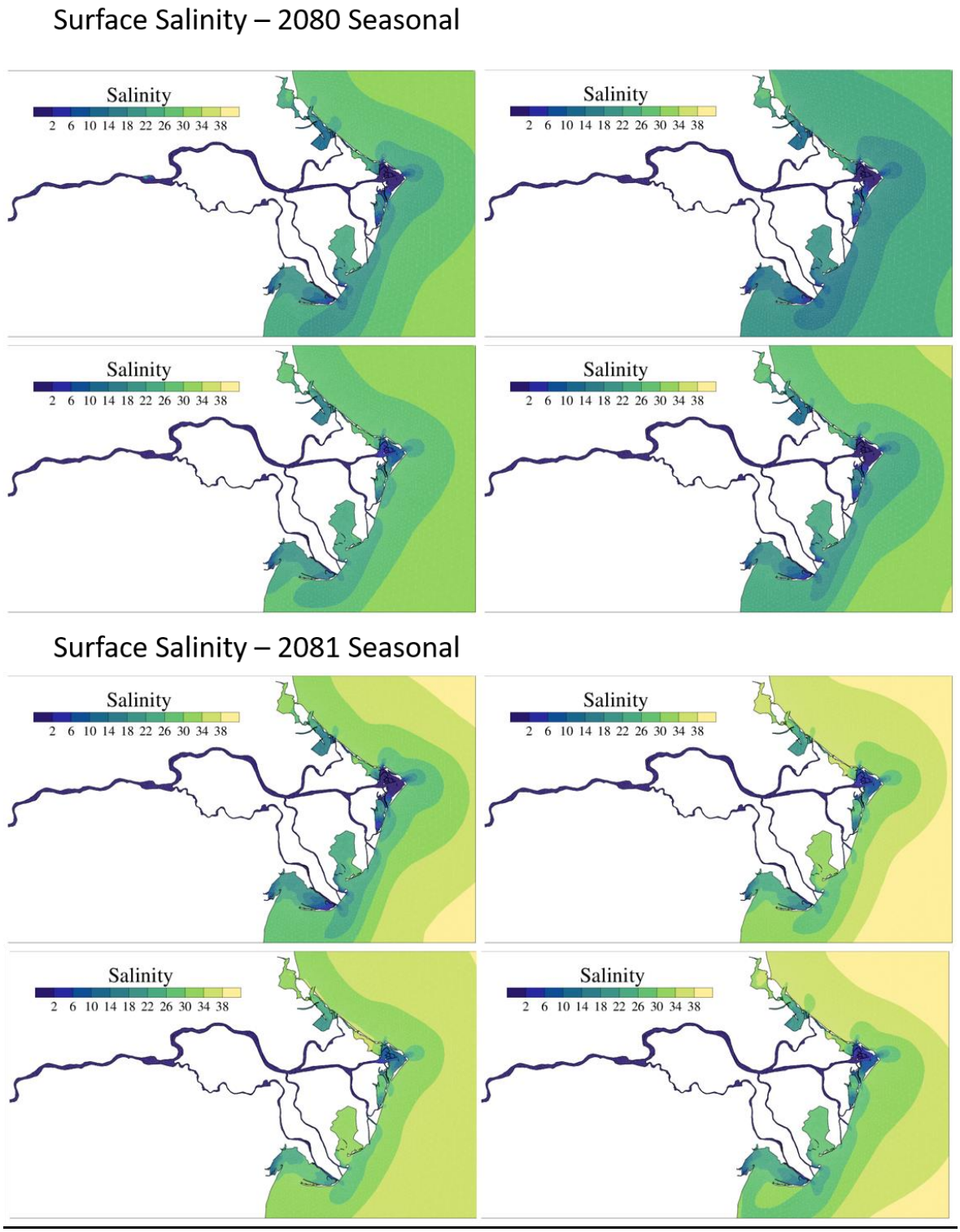

Figure 5.14: Seasonal average of surface salinity for the Po River Delta and its shelf, for the two years of simulation. Top) 2080, bottom) 2081. Winter (top left), Spring (top right), Summer (bottom left), Fall bottom right).

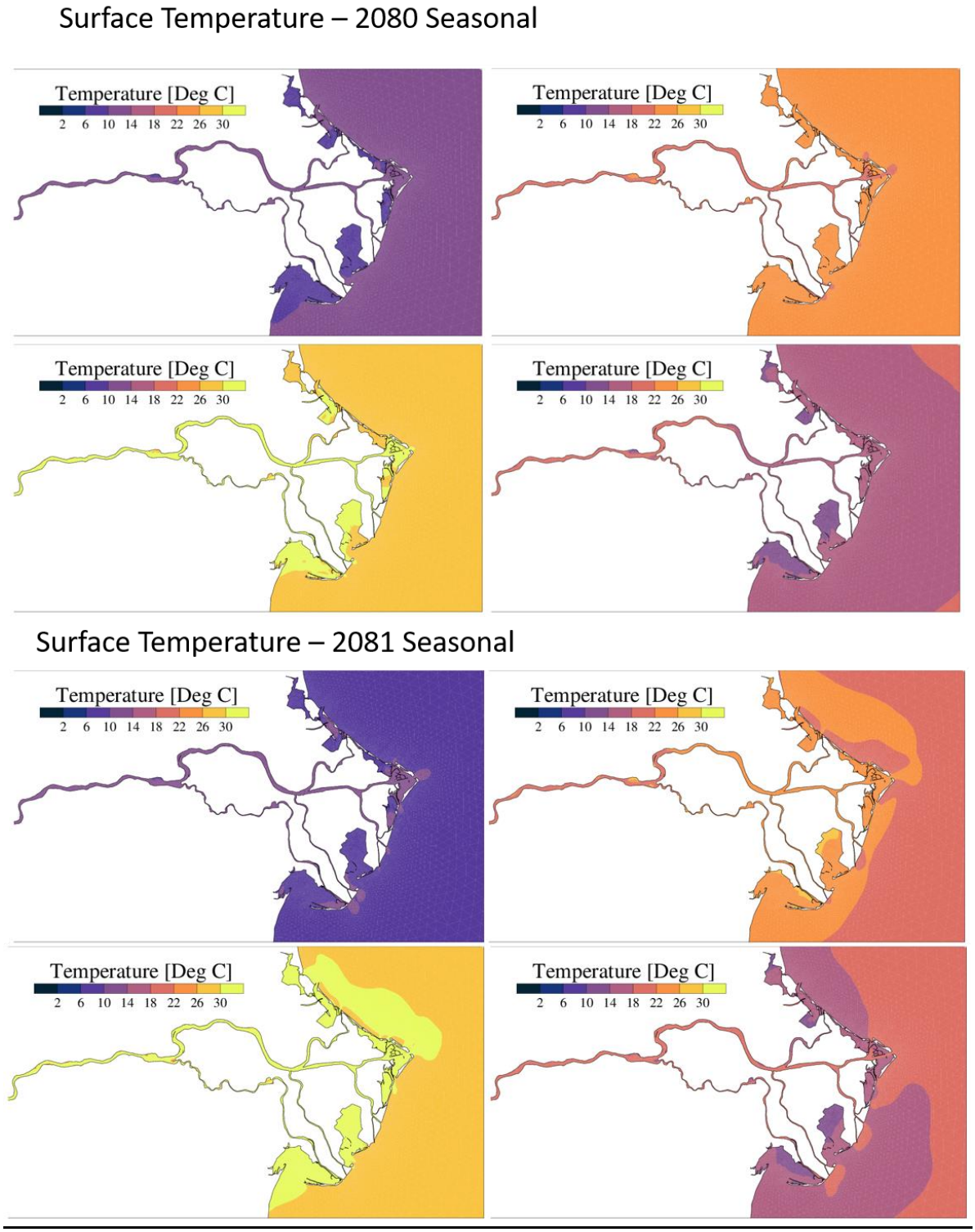

Figure 5.15: Seasonal average of surface temperature for the Po River Delta and its shelf, for the two years of simulation. Top) 2080, bottom) 2081. Winter (top left), Spring (top right), Summer (bottom left), Fall (bottom right).

Surface Currents – 2080 Seasonal

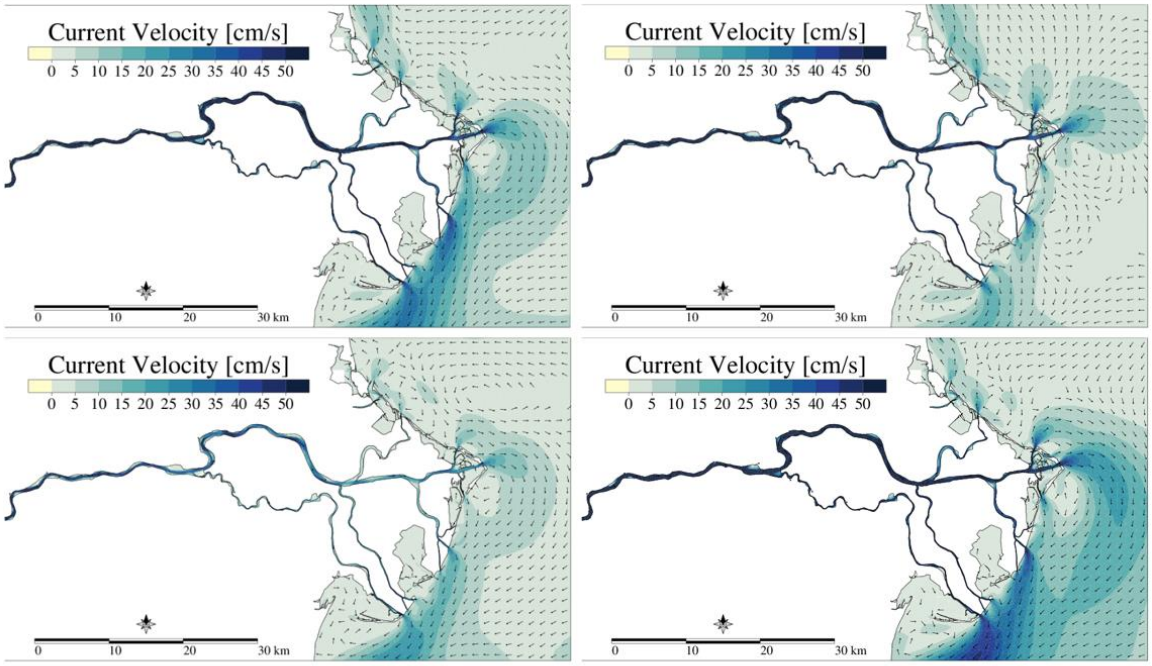

Surface Currents– 2081 Seasonal

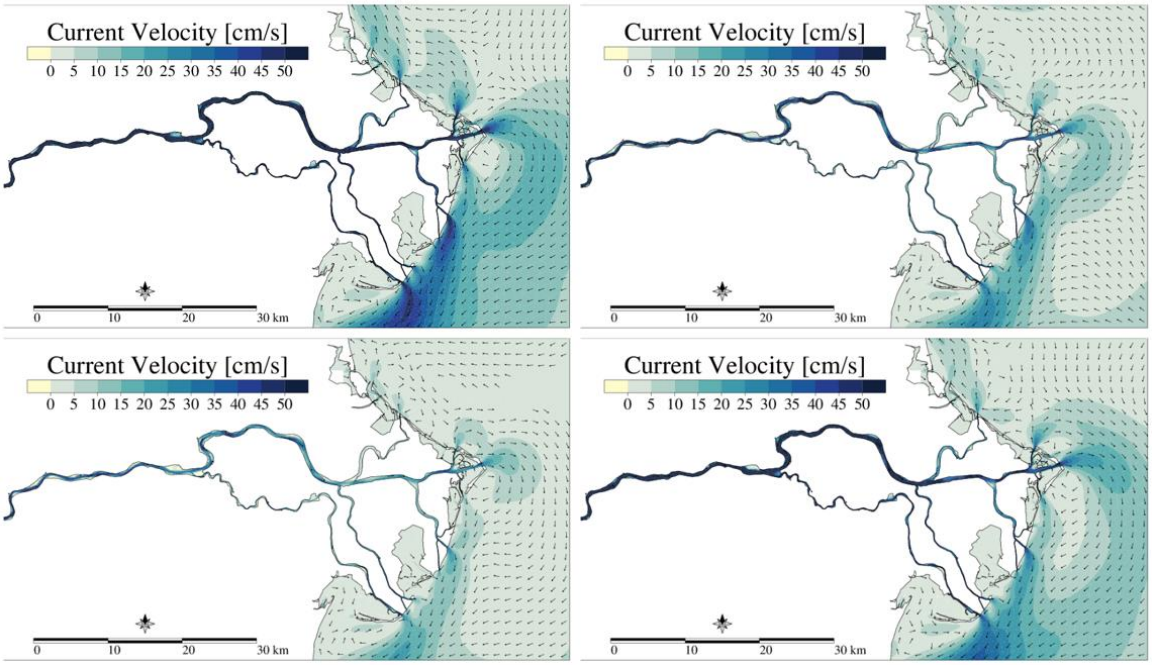

Figure 5.16: Seasonal average of surface currents for the Po River Delta and its shelf, for the two years of simulation. Top) 2080, bottom) 2081. Winter (top left), Spring (top right), Summer (bottom left), Fall (bottom right).

5.1.2.3. Po River Lagoons – Water Residence Time

If we focus on the hydrodynamic behavior in the Po Delta Lagoons, WRT allows infer on the capability of these transitional systems to keep the internal dynamics and exchange water with the main basin. Through the first year of simulation we note an increase of the portion of the Scardovari Lagoon characterized by high WRT (> 20 days), covering 2/3 of the area particularly in July, August. In 2081 the extent of the Scardovari area with high WRT seems generally a little bit smaller (except for November 2081), indicating better reflushing capability. Also Goro seems to increase, in its inner part, the WRT, particularly in the period May-September 2080. For 2081 the highest WRTs for Goro are seen in the summer months as well. Flushing is kept efficient in those lagoons more influenced by the river branches, as Basson, Canarin, Barbamarco, even thou in the summer months they reach 5 days of WRT, while in the Present State case (D.3.3) they are around 3 days. Also in the northern, more detached parts of Marinetta-Vallona Lagoon, in the period May-September the WRT increases from 7 days of the Present State simulation to 12 days. As expected, in all months the most complex areas to be flushed are the inner ones (Figs. 17 and 18).

To evidence the change, Figs. 19 and 20 show the absolute difference in surface WRT between the Climate Change and the Present State simulations. As said, the area that generally experience the highest increase in surface WRT is the inner Scardovari Lagoon (along the years, in February, May, August, 2080 and March, from June to November 2081 with +7 days). The same change is registered in Goro Lagoon, in the area behind the sand bar, more influenced by the river and more detached from the sea (where, therefore, a decrease in discharge would lead to a decrease in the flushing capability of the sub-system). If we look to Canarin Lagoon, it seems that surface WRT is not changing for the winter, early spring and late fall months, while a slight increase, of 2-3 days can be seen in the inner border areas during the late spring and summer months (Figs. 5.19 and 5.20). Therefore, this lagoon seems less prone to climate changes effects on the internal dynamics, compared to others.

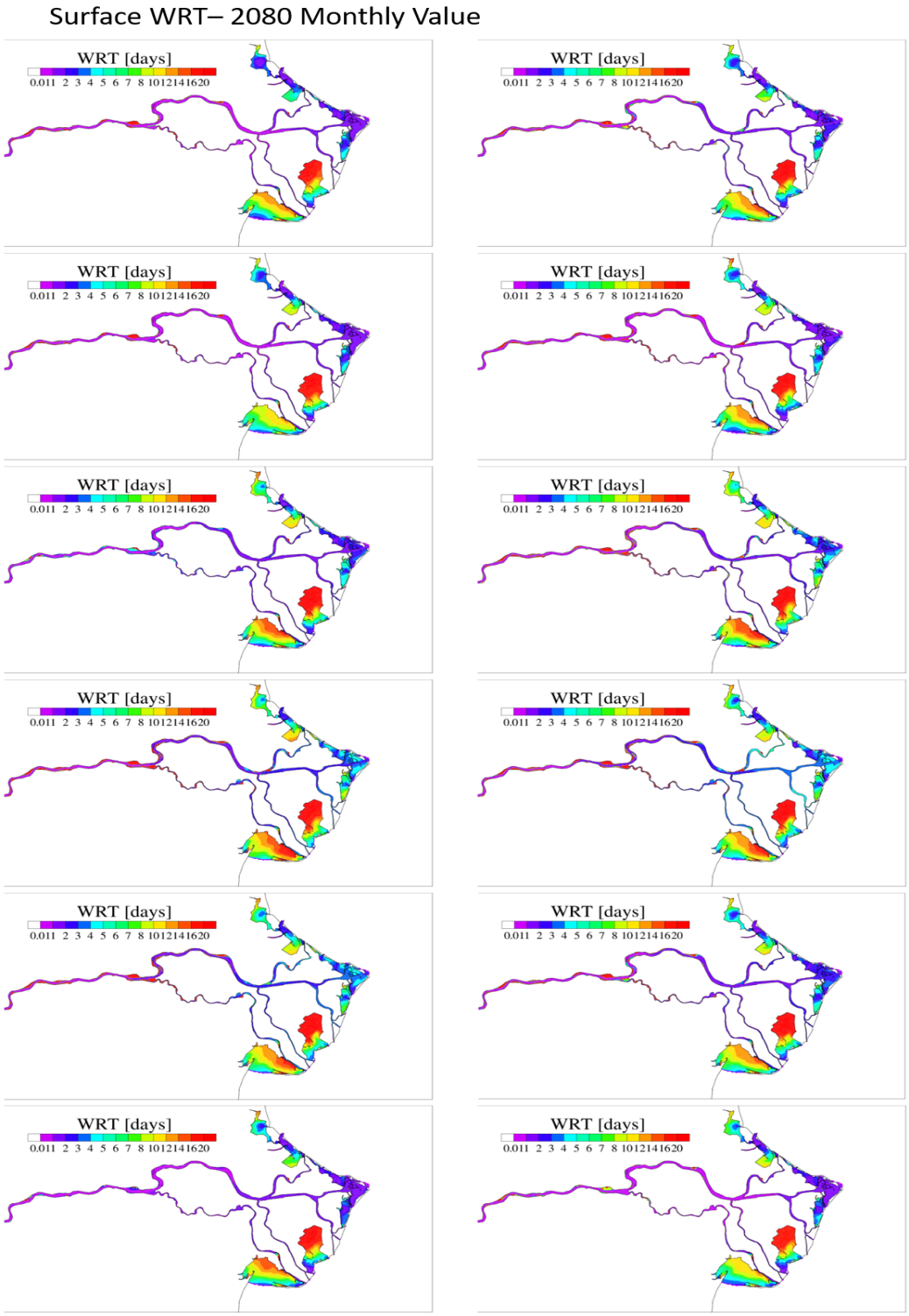

Figure 5.17: Surface Water Residence Time within the Po River Delta for the first year of simulation. Computation for each month.

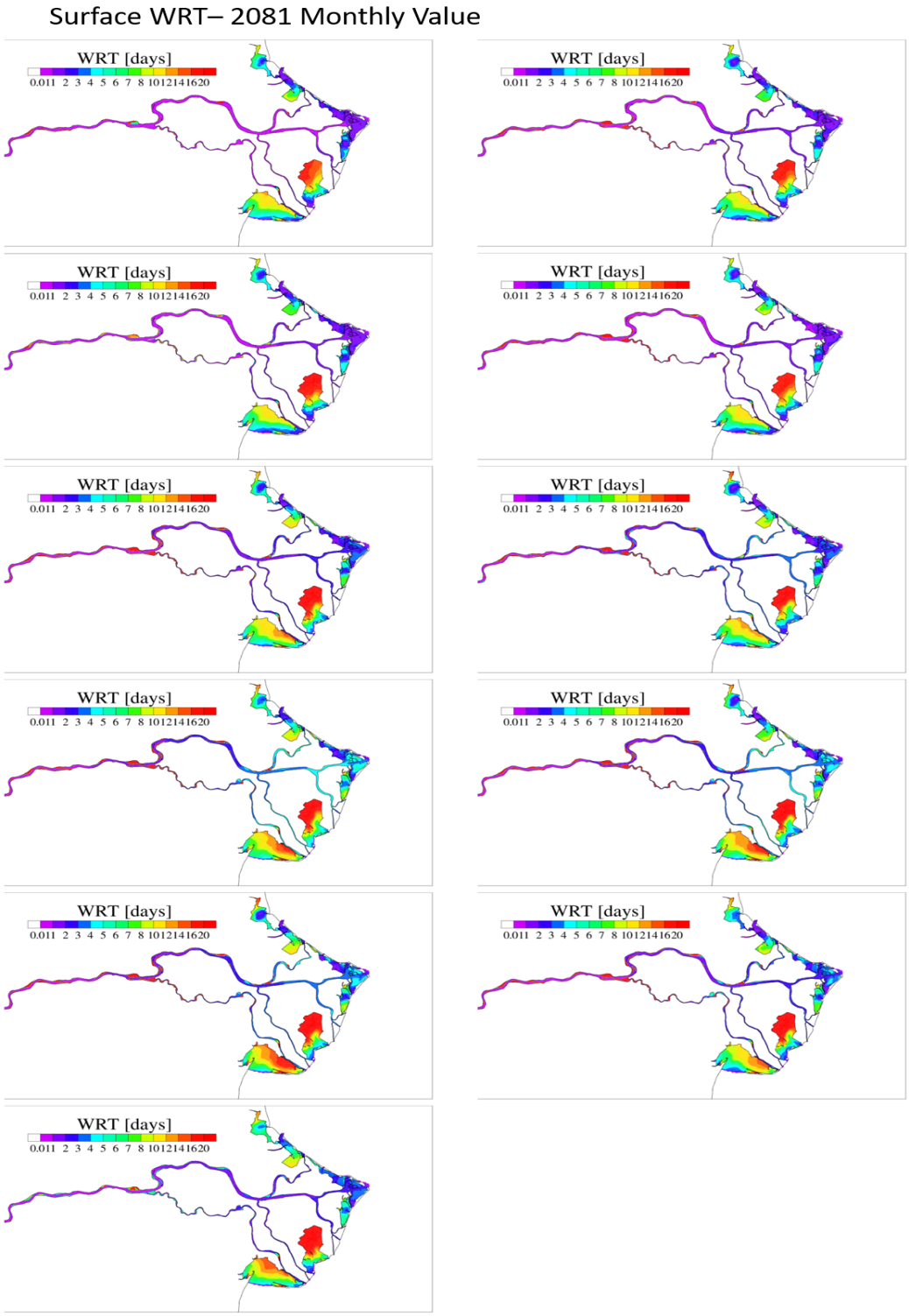

Figure 5.18: Surface Water Residence Time within the Po River Delta for the second year of simulation. Computation for each month.

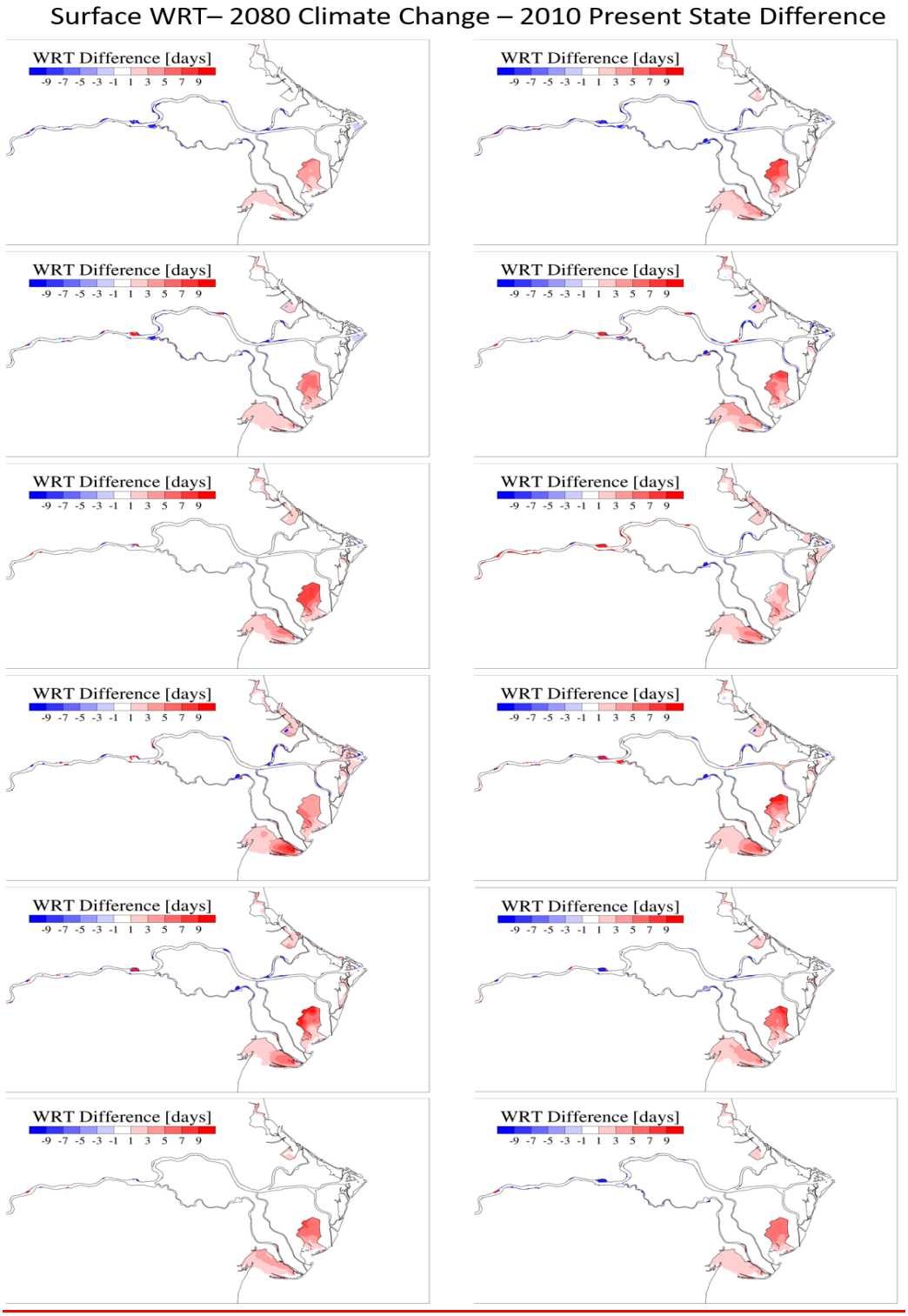

Figure 5.19: Surface Water Residence Time Differences within the Po River Delta between the Climate Change Scenario and the Present State case. Computation for each month.

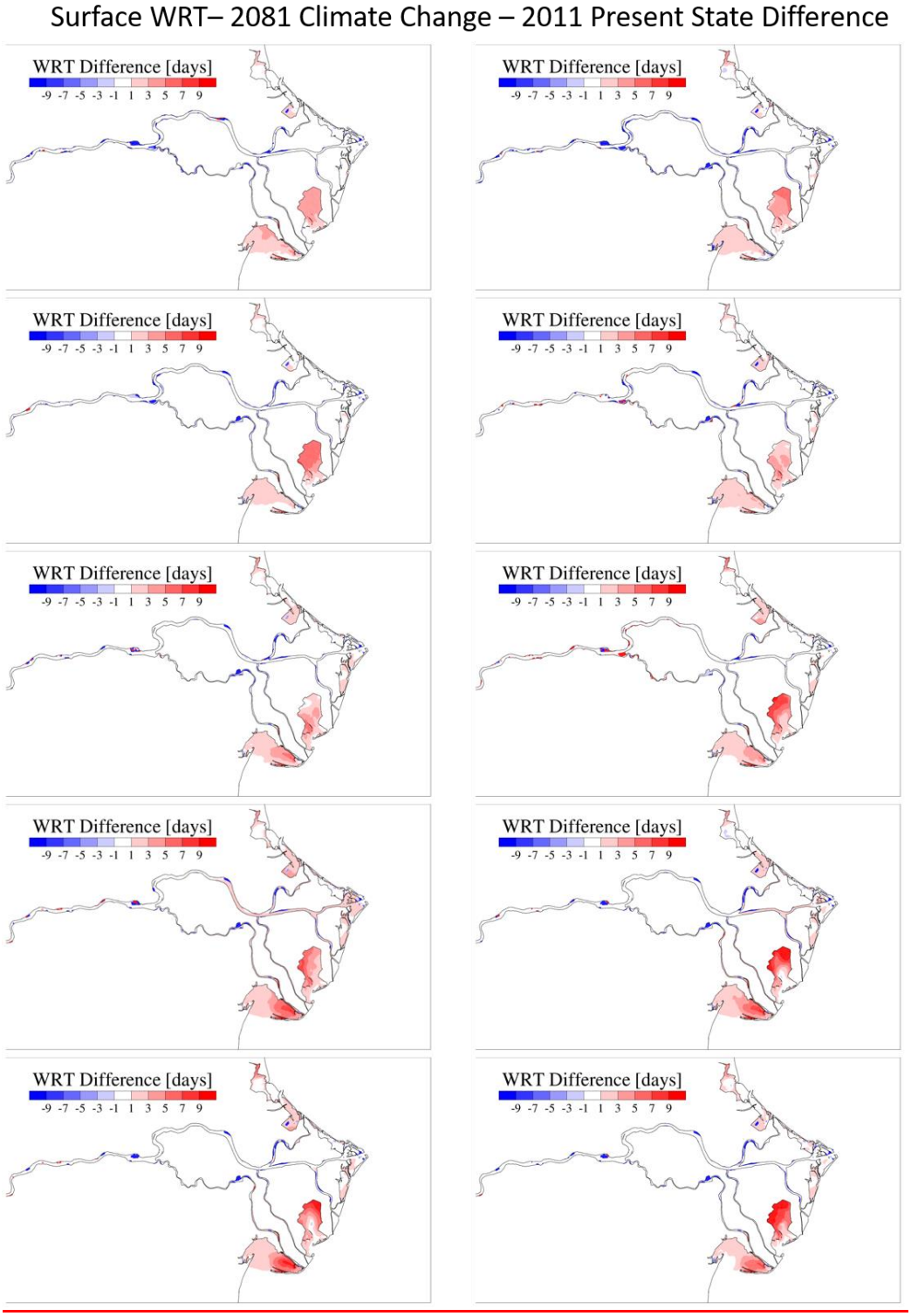

Figure 5.20: Surface Water Residence Time Differences within the Po River Delta between the Climate Change Scenario and the Present State case for the second year. Computation for each month.

5.2. REPORT ON HYDROLOGICAL AND PHYSICAL QUANTITIES OF RIVER JADRO UNDER CLIMATE CHANGE SCENARIOS (RERA)

5.2.1. Introduction

About 80 – 95 % of river Jadro flow is generated by Jadro spring discharge. In wet winter period of year about 80 % and in summer dry period about 95 %. Therefore, the impact of climate change on the hydrological regime of the Jadro river water is reduced to the analysis of the impact of climate change on the discharge of the Jadro spring, source of stream. This also means that climate change impacts in the Jadro spring basin and not in the coastal area (Kaštela Bay) are dominant for forecasts of the quantities and fluxes of the Jadro River. The relatively small coastal topographic basin of the river from the spring to the sea has little impact on the hydrological regime of the waters of the Jadro River (hydrological quantities). Likewise, the influence of the sea on the water regime of the Jadro River is manifested only on the regulated riverbed at a length of about 1.2 km upstream from the mouth. Namely, at a distance of 1.2 km from the mouth there are man-made and natural dams-barriers over which the river overflows into the downstream part of the riverbed towards the sea. These dams with their height of 3-5 m a.s.l. prevent the influence of the sea water on the upstream part of the river. This means that the interaction between the sea and the surface water of the river Jadro takes place only in the area of the estuary (about 1.2 km) and the Kaštela Bay. The rest of the river or the upstream part of the river is not affected by the sea and thus by climate change that will change the sea level. In addition, the mouth of the river Jadro is located deep in the eastern part of the Kaštela Bay, so that the waves and sea fluctuations due to the wind will also not significantly affect the river water flow regime. All impacts will occur in the regulated riverbed in the area of the estuary which bottom/riverbed is at elevation below the middle sea level, as is happening today.

However, the local groundwater that runs parallel to the river towards the sea, as well as those that are created in the hinterland of Kaštela Bay and in the area of the town of Solin, will rise as the middle sea level rises. These are small coastal aquifers with fragile interface fresh water – salt water whose water table is very little above sea level, so the resulting changes in sea level are manifested only through a small rise in groundwater tables. The same will affect the local biogenesis as well as the built structures whose foundations reach the groundwater level.

As the spring of the river is at an elevation of about 33 m a.s.l. it is obvious that the sea and changes in the sea caused by climate change have no effect on the water regime of the river Jadro. Therefore, river fluxes refer to discharge fluxes at spring Jadro. This is an atypical situation as already mentioned because the local topographic basin of the river generates only small amounts of water during rains. Most are generated by water from spring located at a distance of 4.41 km from the coast.

When considering the issue of physical quantities and fluxes of water substances (sediment, nutrients, pollutants, and other watershed system components) the situation is different. Topographic watershed

of rivers is a significant contributor and especially occasionally during rainy period when significantly quantities and fluxes of water substances is transported into river and sea. If there is no precipitation in the topographic watershed area, then there is no washout of sediment and substance into the river and sea. However, the leakage of the sewerage system network (pipes, canals and other structures) constantly affect the quality of groundwater and thus indirectly the quality of river and sea water. The most significant impact occurs during and immediately after rain. The constant impact on the sea comes with water from the Jadro spring, depending on the processes in its groundwater basin.

The permanent contribution of the spring water and the occasional contribution of the topographic basin waters have never been substantially and comprehensively considered, so there are no relevant studies and data. There are standard data on water quality at spring water and a small number of data on the river water quality. By analyzing these data and adapting them to the problem being addressed, quantities and fluxes and trends of changes in the future can be reproduced to some extent.

5.2.2. The key hydrological quantities and fluxes

5.2.2.1. Material and methods

Jadro karst aquifers are open natural water systems that constantly and rapidly exchange water with its environment and within the system. Such hydrology systems are generally never completely known, so it is difficult to study and manage them. The behaviour of aquifers is most often explained through three types of porosity, which include the porosity of micro pores, the porosity of small cracks and fractures, and the porosity of large fractures, openings. The density, frequency and number of cracks in the Dinarides vary with depth so that it is greatest on the surface and decreases significantly with depth. Due to these characteristics, the aquifer is rapidly filling, about 1 m h^{-1}, and at high water levels it empties relatively quickly, about 0.25 m s^{-1}, while at low water levels it is much slower (Milanović 2004). Well-developed cracks/openings of different dimensions from 1 mm up to openings of several meters enables fast water transport while the storage capacity is large and varies greatly (effective porosity is 0.5-3.5%) (Milanović 2004). As the water level of the aquifer decreases, the velocity of the water slows down, and at lower water levels in the dry season the flow is laminar and occurs mainly through small cracks less than 5-15 mm.

Fluctuations in the water level in the aquifer during the year are significant, and the aquifer responds relatively quickly to rainfall (random variable) in the spring watershed area, Figure 1. The discharge hydrograph is characterized by a very dynamic rainy period in which the discharge increases and decreases rapidly with each significant rainfall and the base flow are significant, and the long drought period in which the discharge decreases steadily and stays around the minimum values. In the wet season, the aquifer gradually fills up to maximum levels with some oscillations due to long rainfall, and with the onset of the drought period it is emptied. The upper part of the aquifer empty and draw down very quickly, the middle part has slightly slower reaction and the lower part has very slow discharge. Such features of the discharge hygrogram and aquifer behavior define the main features of the spring hydrological quantities and fluxes.

Given that the spring generates by far the largest part of the flow of the Jadro River (more than 90%), all of the above applies to the river itself.

Upper part of aquifer (discharge coefficient α_1) characterizes outflow from well-developed caves and channel system. Turbulent flow prevails with fast transport of suspended mater (turbidity). The great volume of water is stored in the karst system. However, outflow is fast (because of the high potential

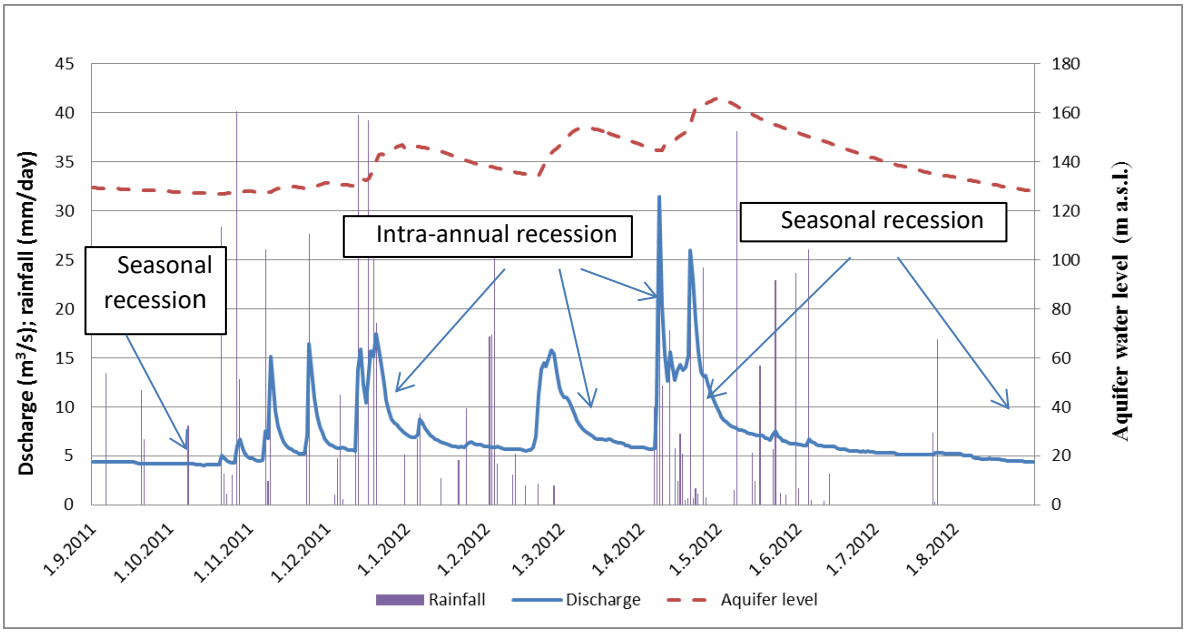

Figure 5.21: Discharge hydrograph, rainfall, aquifer water level in the period 1 September 2011 – 31 August 2012.

energy). Outflow lasted about one to two weeks. This means that inflow resulting from winter rainfall as a result of climate change will discharge quickly and will not have a major impact on the summer drought. Middle part of aquifer (coefficient of discharge α_2) characterizes the emptying of well-connected fractures and smaller caves. Due to decrease in aquifer potential energy the empting duration is longer. This part of aquifer has partial impact on summer discharge. The most significant impact has water reserves stored in lower part of aquifer structures (α_3). The coefficient α_3 characterised the outflow of water reserve which are scattered over the entire rock mass. They are stored in the system of fractures (matrix porosity), in sandy and send-clayey material deposited in the less active porosity structures, channels, caves and siphons. Part of the water reserve relates to condensed water vapor in the terrain layers above the aquifer. Outflow in this period integrated and the corresponding outflow from reserves represented by coefficients α_1 and α_2.

The recession curve of Jadro spring, (Figure 5.21) has several different slopes, and corresponding discharge coefficient (α_1, α_2, α_3, … α_n). This type of recession curve is a complex function:

$$Q_t = Q_{01}e^{-\alpha_{1t}} + Q_{02}e^{-\alpha_{2t}} + \cdots + Q_{0n}e^{-\alpha_{nt}} \quad (1)$$

The discharge coefficient can be estimated if values Q_t and Q_0 are known:

$$\alpha = \frac{logQ_0 - logQ_t}{0.4343(t-t_0)} \quad (2)$$

Where:
Q_t – the spring discharge ($m^3\ s^{-1}$) during the period $t - t_0$
Q_0 – the spring discharge at time t_0 ($m^3\ s^{-1}$)
t – the end of time period
t_0 – time representing the start of calculation
α – the coefficient of aquifer discharge patterns
e – the base of natural logarithm

Such curves represent complex characteristics of aquifer karst system and discharge regimes.

It has been found that recession curve consists of three characteristic outflow spring regime and has the corresponding three discharge coefficient. The values of coefficients for year 2011 are: α_1=0.0948 (17-29 March 2011), α_2=0.01327 (30 March-27 April 2011), α_3= 0.003004 (28 April-10 October 2011). Such curves are characteristic of well-developed karst system. Smaller oscillations in seasonal recession period as results of rare short rainfalls are neglected in recession curve fitting. The very fast release and big fluxes of water from Jadro karst system last about 13 days, the less fast and smaller fluxes 27 days and slow and small flow of water last 165 days. Such curve indicates that aquifer has large retardation capability which is characterised for permanent karst springs. Climate change will therefore affect these fluxes and their duration differently. How much there could be changes in relation to the current trend is explained below.

If, to simplify the analysis, the hydrograph of permanent spring is divided into two basic components, base flow and fast flow (concentrated flow in conduits) (Hartmann *et al.* 2014), then spring outflow can be simplified presented base on such physical reality of the system. The small outflows of the dry season mainly result from base flow effluence (groundwater storage). They have relatively small variation. During the flow recession, the flow at particular time is a fraction of the flow at a previous time period.

Based on the available data and the assumptions made related to behavior of the hydrological system an approach combining qualitative and quantitative assessment for climate impact and risk analysis for river Jadro system was used.

5.2.2.2. Results

Minimum discharge mainly occurs in period July-September up to the first significant autumn rains. The minimum discharge (about 4 $m^3\ s^{-1}$) generally does not change significantly, with the same difference as the total rainfall during the year. During this period, about 50% of the discharge of spring water is withdrawal for water supply, which means that only 50% of the water is discharged downstream to the

sea (about 2 $m^3 s^{-1}$). Changes in the amount of water flowing into the sea are small. It is a period of stable and relatively small fluxes of water into the sea.

In the wet period from October to June, with the occurrence of significant precipitation in the watershed area, increasing flows occur, which in shorter time intervals after December reach sizes of 70 $m^3 s^{-1}$ and even more. The oscillations of the flow at spring are large and sudden and thus the fluxes of river water into the sea. This is the period when large amounts of water flow into the sea with extremely variable dynamics depending on the dynamics of precipitation and water table of aquifer. This means that the magnitude but variability of precipitation will significantly affect the variability and quantity of water fluxes into the sea. As it is currently impossible to predict the magnitude and variability of precipitation due to climate change, it is not possible to define more precisely the magnitude and variability of water fluxes into the sea. So it is only possible to determine the character of possible changes for the dry and rainy period of the year. This is confirmed by the results obtained from the analysis of two consecutive years, extremely dry in 2012 and extremely rainy in 2013. These two years faithfully depict the magnitudes of variability that could occur in the future due to climate change.

Total rainfall in 2012 was approximately 796 mm, which is 34% less than the long-term average (1200 mm), average annual discharge of 7.06 $m^3 s^{-1}$ was 28% less than the long-term average (9.95 $m^3 s^{-1}$), the maximum was 31.5 $m^3 s^{-1}$, and minimum 4.1 $m^3 s^{-1}$. The total annual volume of water discharge at the spring was 222,762,205 $m^3 yr^{-1}$. The minimum flow of 4.08 $m^3 s^{-1}$ was reported on 14 October 2011, while on 1 September 2012 it was 4.41 $m^3 s^{-1}$.

The hydrological year 2013 was extremely wet. Total precipitation was about 1775 mm, which is 48% more than the long-term average, and the average annual discharge was about 12.2 $m^3 s^{-1}$ (25% more than the long-term average), maximum was 43.5 $m^3 s^{-1}$ and minimum 4.3 $m^3 s^{-1}$. The total annual volume of water discharge at the spring was 384,056,640 $m^3 yr^{-1}$. The minimum discharge was 4.32 $m^3 s^{-1}$, occurred on 12 September 2012 while on 01 September 2012 it was 4.44 $m^3 s^{-1}$. It can be seen that the rainy year has a shorter recession period up to a minimum discharge, while the drought has a longer one, about 31 days.

Comparing the characteristic spring discharges between 2012 and 2013, it is found that rainfall was higher by 223%, mean flow $Q_{average}$ by 73%, Q_{max} by 38%, Q_{min} by 5%, and total volume of water discharge at spring by 73%. It is the significant variability between two consecutive years that clearly present what could happen in the future with climate change and variability. It is also evident that the percentage of variability of discharge is greatest at average discharge, less at maximum and minimum at minimum discharge values. The characteristic values are presented in Table 5.2.

Within the considered period 2011-2015, low minimum flow (3.64 $m^3 s^{-1}$, 20 November 2015) occurred, although rainfall (1603 mm) was higher than the minimum, as well as higher flows (52.47 $m^3 s^{-1}$, 23 February 2015) although rainfall was slightly less than in maximum year. This clearly indicates the great variability of flow in karst systems, which depends not only on the size of the annual rainfall, but also on

the schedule during the year, and a number of other processes that take place within the system. Therefore, the occurrence and the amount of precipitation in the short-term period are the biggest problem and risk. Existing models could not reliably predict the short-term potential impacts of global warming on river flow and so impacts on sea.

Table 5.2. The main features of seasonal precipitation and flow in 2012 and 2013, within considered period 2011-2015.

Characteristic values	2011-2015	2013		2012	
		1.09.2012-5.06.2013.	6.06.2013-31.08.2013	1.09.2011-5.06.2012	6.06.2012-31.08.2012
Rainfall (mm)	6543	1634	118	767	29
Discharge ($m^3 s^{-1}$)					
- Average	9.72	14.18	5.72	7.42	5.19
- Max - Min	52.47 3.64	43.53 4.32	9.47 4.85	31.48 4.08	6.32 4.38
Total volume of discharge (m^3)	306,485,741	339,452,074 89 (%)	42,886,497 11 (%)	184,175,565 83 (%)	38,088,717 17 (%)

Analyzing the amounts of water that in the wet and dry period (Table 5.2) it is obtained that about 80-90 (%) of flow into the sea in the period September-May, and about 20-10% June - August. These relationships apply regardless of whether the year was wet or dry.

The obtained results show that the processes in the system in summer do not yield an output proportional to the change of wet period inputs. So the impact of the extremely higher winter rainfalls do not change summer minimum flow significantly, generally about 5-10%. Since minimal seasonal flow at the end of dry season has small changes we may conclude that they are close to being independent. This means that a forecast increase in rainfall in winter period of 2-7% by 2100 and a decrease in spring rainfall by 3-8% may not have a significant impact on summer discharges. Climate change predicts greater winter rainfall, so that the forecasted decrease in rainfall during spring and summer, which are already very small, should not significantly affect the minimum discharge value.

5.2.2.3. Conclusion

Under the influence of climate change, the volume of water that will flow into the sea by the river Jadro will gradually increase in winter and in the rest of the year will gradually decrease. The total annual volume will gradually decrease. The dynamics of decrease and increase depend on the dynamics of climate change and especially precipitation and evapotranspiration.

The increase in winter inflow will be proportional to the increase in precipitation while the decrease in summer inflow will be less than the relative decrease in summer precipitation due to the reteradion capacity of the aquifer and the size of the indirect catchment area of the Cetina River. Generally speaking, the changes will not be significant for the medium climate change scenario. Human interventions in the hydrological system of the Jadro River including water withdrawals, in the groundwater basin of spring

Jadro and in the topographic basin of the river downstream from the Jadro spring could have a much greater impacts.

5.2.3. Turbidity, total suspended solids and suspended solids quantities and fluxes

5.2.3.1. Turbidity dynamics at Spring Jadro

Substances that alter water quality at source are mainly generated by the interaction of factors such as soil characteristics and saturation levels, infiltration, dilution, dispersion, transport length, filtration and adsorption, and more. A cumulative watershed impact influences or is influenced by the flow of water through a watershed. Cumulative watershed effects, a phrase which has widely replaced reference to "impacts," can be additive or synergistic and involve modification of water, sediment, nutrients, pollutants, and other watershed system components. An example of such effects would be where roads, forest cutting and agriculture contributes to increased peak stream flows and sediment loads, leading to aggradation of downstream areas, which in turn results in lateral channel migration causing streambank and floodplain erosion, which entrains additional sediment.

Therefore, it is very difficult to reliably predict water quality and turbidity (Massei et al. 2006; Göppert and Goldscheider 2008). Climate change will alter the characteristics of the basin (biocenosis and biotope), susceptibility to erosion, hydrological magnitude and thus the entire process of water quality and turbidity. Over time, socio-economic activities in the basin will change and thus the sources of pollution. Due to climate change (severe droughts) more frequent occurrence of fires and destruction of flora are possible, which together will create conditions for greater soil erosion and a greater deposit of ash and other substances.

The same thing is happening in the topographic (lowland) catchment area of river Jadro, with the dominant influence of urbanization and urban infrastructure and activities. The overland flow from the such catchment area that flow into the river are more polluted than the waters of the Jadro spring itself. Because of this, the waters of the Jadro spring dilute and reduce the concentration of pollution that inflows from the topographic river basin.

Turbidity may be beneficial as a surrogate for suspended-sediment concentration (SSC) in the river Jadro. The issue of sediment-load is considered mostly base on turbidity data and data of total suspended solids (TSS). Relevant data are available only for the years 1999-2002, and 2017 and 2018. Only during this period did the turbidity be measured continuously and in other years by single daily grab sampling. Due to the high variability of turbidity within one day and even several hours, individual daily data are not relevant for studying the incidence/occurrence of turbidity and suspended-sediment quantities and load.

Precipitation generates a turbidity that occurs constantly at the spring, significantly immediately after sudden and heavy rainfall, Figure 5.22. The rule of thumb is that the highest turbidity occurs after heavy rainfall, when the aquifer is at high groundwater table levels and when high discharge at the spring as a result of rapid flow dominates through large cracks system. This is the period November-May. High

turbidity occurs regularly during this period. In such hydrological conditions, significant leaching and erosion of the basin surface and rapid turbulent flow of water through the underground structures take place. Turbidity occurs abruptly, similar to a discharge that is several hours late (2-4 hours), as shown in Figure 5.22. High turbidity can occur during periods of heavy rainfall and thus discharge, without the aquifer being significantly filled. However, the amount of precipitation must then be very high. This is the case after a long summer drought period.

The relationship between rain, discharge and turbidity for the period of low aquifer water table levels (minimum base turbidity) is best observed by the example of the occurrence of the first significant turbidity in autumn 2017, Figure 5.23. Turbidity and discharge measurement data were available every half hour, and only total daily precipitation (Dugopolje station).

The first significant autumn rain that fell on 6 and 7 November 2017 (22.4 mm + 103.9 mm = 126.3 mm) generated a maximum flow of 39.02 $m^3 s^{-1}$ and a turbidity of 28.93 NTU. Flows increased from 4.45 $m^3 s^{-1}$ on 6 November at 10:00 for a period of 22 hours to 39.02 $m^3 s^{-1}$ on 7 November at 08:00, which lasted until 7 November at 10:30. The turbidity began to increase four hours later at 6 November at 14:00 when it was 0.40 NTU and peaked on 7 November at 13:00 with a value of 28.93 NTU, meaning that the rise to the maximum NTU level was almost the same as for the flow. Rain that came later in the month, namely on 14 November (26.8 mm), and at the end of the month, on 30 November (49.8 mm) did not significantly increase water turbidity.

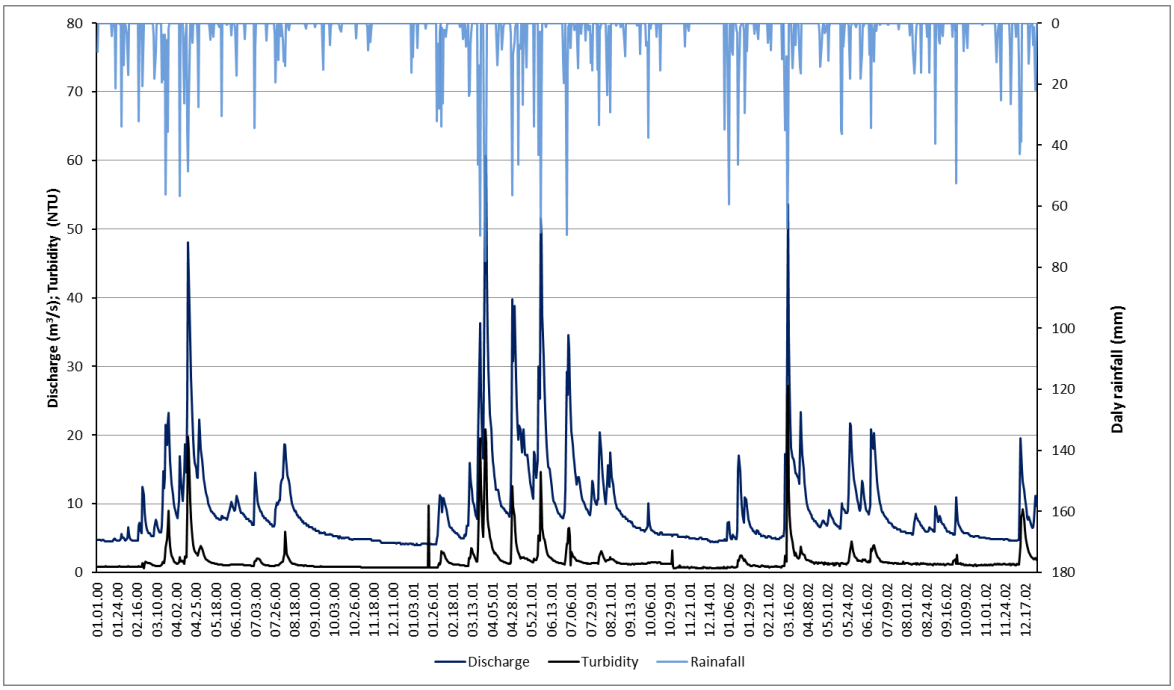

Figure 5.22. Relation between rainfall, discharge and turbidity of the Jadro spring for the period between 1999 and 2002.

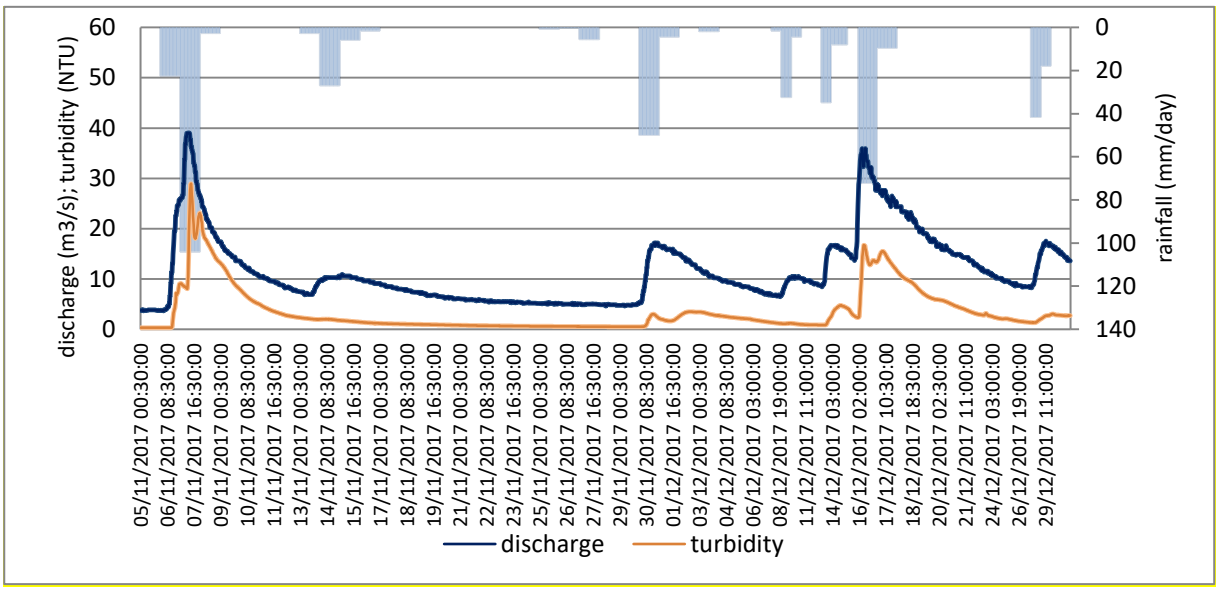

Figure 5.23. Rainfall, discharge and turbidity in the period from 5 November to 31 December 2017.

This example clearly shows that the first heavy rain washed away the surface and subsurface part of the basin after the long dry period, so that each subsequent rain as well as the flow generates a slightly less turbidity until the aquifer is full and base flow significant. Under these conditions, the flow and turbidity are generated through the concentrated flow in conduits, the part with priority flow of water through the pipe system, and partly from the rest of the aquifer that has a slower flow to the source (system with small cracks). Therefore, the turbidity as well as the flow rate decreases rapidly to smaller values. This is a phenomenon where rapid flow produces turbidity but the contribution of base flow is generally very small. However, some of the washed suspended matter together with water is through exchange processes between matrix and conduits retained in the aquifer and gradually increase the turbidity of the water in the base flow.

In the case of the Jadro spring, a total of about 30 days in the year, turbidity exceeds the permitted level of 4 NTUs (European Commission 2017), and extreme values, > 15 NTUs, occur only a few times a year (2-6 times) in the rainy season, November-May.

The simplified analysis clearly indicates that current turbidity (T) at spring is primarily a function of spring discharge (flow-turbidity coefficient of correlation = 0.86) and less precipitation (precipitation-turbidity coefficient of correlation = 0.48), and as expected since precipitation-flow correlation is also small, 0.42. Functional ratio of flow and turbidity (Q); $T_t = f(Q_t)$ is presented in Figure 5.24.

In the period of small spring flows, the autocorrelation component is more significant and strong, while in the periods of larger water flows impact of rainfall is significant and the mixed autoregressive and moving process is significant, so the scatter of the values of turbidity is greater (Margeta and Fistanić 2004).

During the late winter and early spring when base flow is significant, turbidity reached a size of 40.2 NTU and rise extremely fast, 29 NTU units in a period of 9 hours (3.2 NTU hr^{-1}). The main impact on such high turbidly has base turbidity. During this period the aquifer was at the highest water table levels which were a prerequisite for generating high flow and turbidity. During the summer rains are rare and small, so the

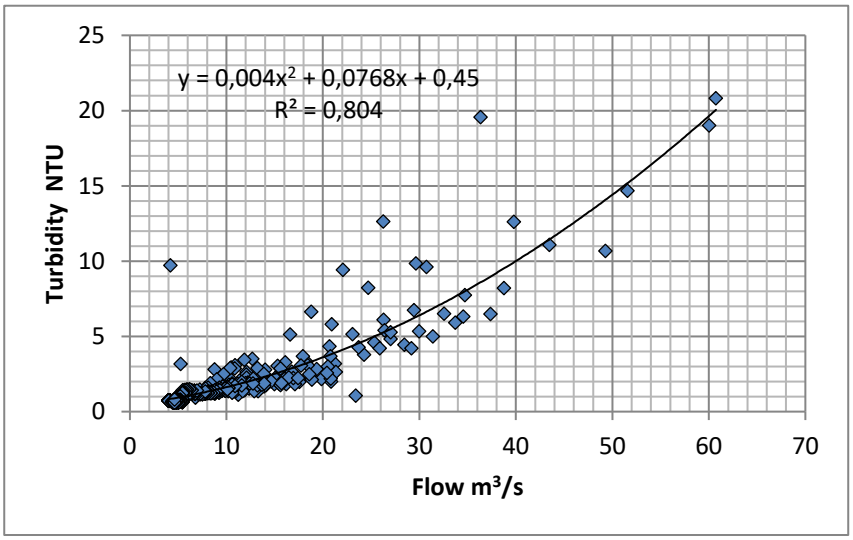

Figure 5.24. Turbidity dependence on flow (1999-2002).

aquifer is gradually emptied through small cracks partly filled with sediment, so that flow and turbidity gradually decrease with smaller oscillations in case of higher rainfall. Therefore, rainfall in the dry season cannot generate higher flows or turbidity because the water level in the aquifer in that period is the lowest in the year.

5.2.3.2. Relationship between turbidity, total suspended solids and suspended-solid concentration

Turbidity measurements are often used as an indicator of water quality based on clarity and estimated total suspended solids (TSS) and suspended-solid concentration in water.

Turbidity and total suspended solids refer to particles present in the water column. Turbidity and water clarity are both visual properties of water based on light scattering and attenuation. All three parameters are related to particles in the water column, whether directly or indirectly.

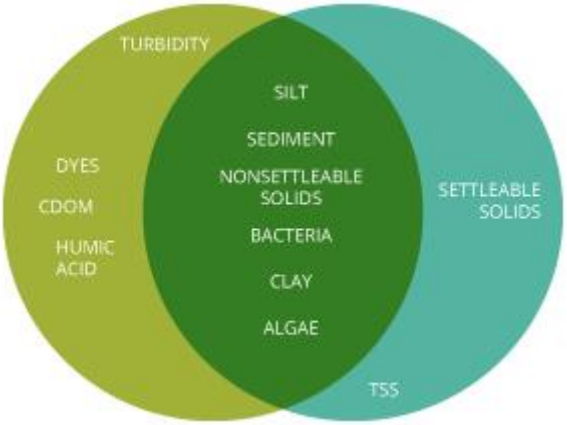

While turbidity and total suspended solids often overlap, there are a few outlying factors that only contribute to one or the other.

Turbidity is determined by the amount of light scattered off of these particles. While this measurement can then be used to estimate the total dissolved solids concentration, it will not be exact. Turbidity does not include any settled solids or bedload (sediment that "rolls" along the riverbed). In addition, turbidity measurements may be affected by colored dissolved organic matter. While this dissolved matter is not included in TSS measurements, it can cause artificially low turbidity readings as it absorbs light instead of scattering it.

Total suspended solids, on the other hand, are a total quantity measurement of solid material per volume of water. This means that TSS is a specific measurement of all suspended solids, organic and inorganic, by mass. TSS includes settleable solids, and is the direct measurement of the total solids present in a water body. As such, TSS can be used to calculate sedimentation rates, while turbidity cannot. Both organic and inorganic particles of all sizes can contribute to the suspended solids concentration.

Water clarity is strictly relative to sunlight penetration. While this is usually determined by the amount of suspended solids in water, it can also be affected by CDOM and other dissolved solids. Water clarity is the most subjective measurement of these three parameters, as it is usually determined by human observation.

The estimation of SS concentrations from turbidity measurements with optical backscatter sensors depends on the content of fine particulate organic matter as well as grain size distribution of the SS and colour and shape of the grains. Accordingly, turbidity measurements require calibration at individual test sites. Numerous studies have been conducted on fine sediment dynamics and fine sediment infiltration and accumulation in different part of the world. The results of those empirical studies of fine sediment infiltration rates are difficult to generalize mostly due to different measurement methodologies.

Turbidity and total suspended solids refer to particles present in the water column which means that there is a significant correlation between these quantities. Knowing the magnitude of the dependence, it

is possible to generate the magnitudes of TSS on the basis of NTU and predict the magnitudes of suspended-sediment loads. Starting from these assumptions, it follows that the fluxes of suspended solids are very variable and large in the wet winter period of the year, while in the dry summer period they are stable and small as well as turbidity.

Suspended-sediment concentration SSC is not the same as TSS although both measures solid phase material within the water column. The difference stems from the method of measurement and determination. That why analytical results are not interchangeable. For approximate estimates of the state of SSC quantities, both SSC load and TSS load sizes can be used to some extent.

5.2.4. Suspended solids dynamics of River Jadro

5.2.4.1. Introduction

The morphology of Spring Jadro is significantly modified: about 45% of the ecomorphology is close to natural or natural, 25% is little affected and 30% is strongly affected or even artificial due to urbanisation. The bedrock of the watershed consists of limestone and dolomite.

The morphology of the river Jadro (downstream from spring until sea) is even strongly modified: about 15% of the ecomorphology is close to natural or natural, 20% is little affected and 65% is strongly affected or even artificial due to strong urbanization. The bedrock of the watershed consists of limestone and dolomite and marl. Therefore, a significant contribution of this basin to the pollution of the river and the coastal sea is to be expected.

Sediment is moved from slopes to stream channels and through stream networks by a great variety of processes. Some of these processes are pervasive and persistent, such as the removal of fine-grained weathering products in suspension. Other processes operate infrequently and even catastrophically, as in the case of rapid excavations and landslides. Sediment transport through stream systems involves a variety of processes ranging from transfer of dissolved material, to movement of fine particulate material in the water column, to rolling of coarse particles along the streambed. Thus, the movement of these materials through a watershed involves a series of linked transfer processes and storage sites, such as gravel bars and floodplains. As with hydrological and biogeochemical cycling, the routing of sediment through watersheds has both long-term, average properties and very significant fluxes during extreme events.

The dynamic sediment of the river Jadro is unknown because it has not been explored so far. There is no adequate measurement of the sediment. Several times in each season of the year, quality tests of the river Jadro in its lower course are performed in order to be able to define the state of watercourses in accordance with the EU Water Framework Directive. Suspended-sediment data are not collected. One of the parameters measured is TSS. At the Jadro spring, TSS and turbidity as grab samples are constantly measured several times per week. For several years, there are also data on continuous turbidity measurements. These are the most reliable data for estimating suspended-sediment concentration and

estimating load. Therefore, the flux of Jadro river sediment can only be generally estimated on the basis of available data for TSS and turbidity and streamflow data at stream-gage Majdan.

In accordance with literature (Elison et al. 2014) in general SSC data are larger than median values of TSS. Overall percent difference value between SSC and TSS was 50 percent, varying from 40 to 60. In this report we assume that it is 40 % since Jadro belongs to karst water resources. Appling a simple linear regression model (SLR) results with indication that SSC is constantly larger than TSS concentration. SLR slope coefficient in the regression models is greater than 1. In order to determine the state and relationship between SSC and TSS for the river Jadro, it is necessary to carry out appropriate causation and measurement of SSC and TSS at different times of the year (wet, dry). For now, there is no such data.

Turbidity, SSC and TSS inherently are related given that each principally is a measure of suspended sediment in stream. The association of SSC and TSS to streamflow typically is used in the calculation of suspended-sediment and TSS load. Suspended-sediment loads also are calculated using regression approach based on relation between SSC or TSS with streamflow and other variables using appropriate models. In this report we computing daily TSS load base on the relationship between TSS and streamflow. Suspended-sediment load is estimated to be about 40% higher than TSS load. In order to create such an account, we need to generate daily values of TSS. This can be calculated using a regression approach based on the relation between turbidity and TSS. Namely, only continuous data for one year for turbidity have been used. In accordance with literature (Elison et al. 2014) turbidity was superior to streamflow in estimation of SSC and that turbidity may be used as a surrogate to SSC estimation.

Suspended-sediment, TSS, suspended-send, and suspended-fine sediment loads were estimated using direct calculation as well as literature data and expert assumptions.

Based on the available data, calculations of fine sediment (<2 mm) load in river movement can be performed, which is mainly impacted both directly and indirectly by human activities. The consequences of climate and land use change on the transport of sediment into rivers on sediment transport in the river and on clogging processes are poorly known. Several studies have shown a strong correlation between sediment deposition and the occurrence of fine sediment in the water column. Higher fine sediment load in rivers generally lead to increased fine sediment infiltration into the riverbed especially at estuary and coastal sea area. The temporal and spatial dynamics of suspended sediment (SS) can be estimated from turbidity measurements if there are no adequate measurements and analyses of sediments.

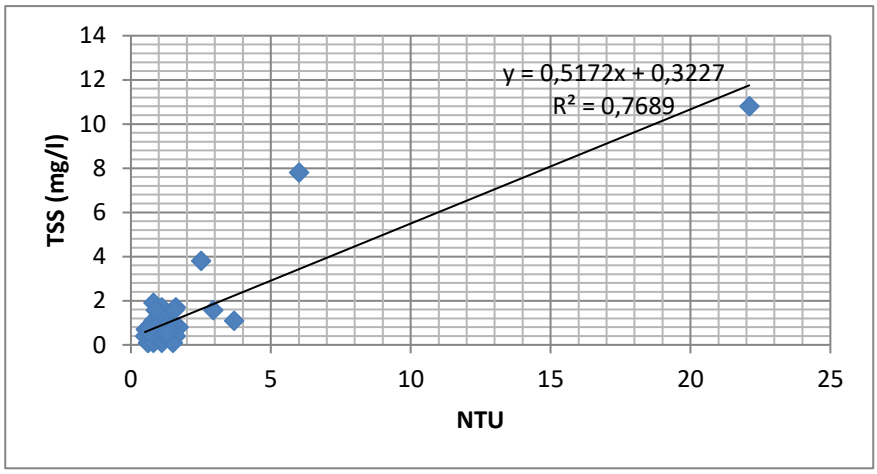

Figure 5.25. Correlation between turbidity (NTU) and total suspended solid (TSS) at spring Jadro.

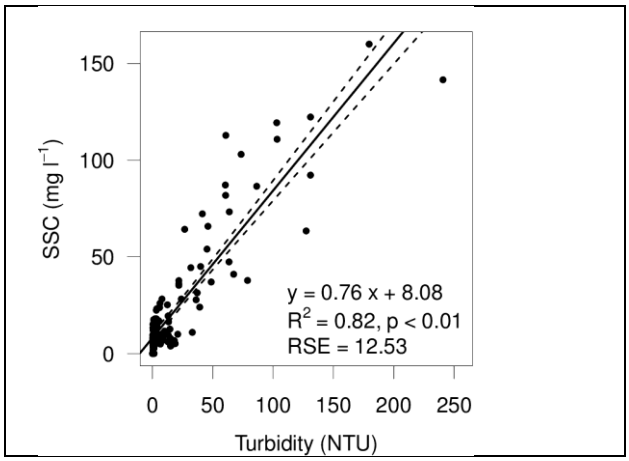

Figure 5.26. Example of turbidity (NTU) and suspended sediment concentration (SSC) (Schindler Wildhaber et al. 2012).

For an approximate calculation, it is necessary to calibrate the nephelometric turbidity unit (NTU) to total suspended sediment concentration in mg l^{-1}. In this study, the calibration was made based on the available data for NTU and TSSC at the source of the river Jadro, Figure 5. The calibration of NTU values to TSS concentration was difficult and associated with a high variance (Fig. 5). An average value TSS is 1.25 mg l^{-1}, while NTU is 1.79, medina of TSS is 0.7, and NTU 1.1. Average NTU value is higher about 40 % than TSS while for medina it is about 50%, what is expected in accordance with literature information (Elison et al. 2014).

In a similar way, a correlation is estimated between turbidity in NTU and suspended-solid concentration if data exists as shown in Figure 6 (Schindler et al. 2012). In this case, the SSC is slightly smaller than the NTU. Obviously, it is always necessary to conduct appropriate field research for a specific area. SSC and TSS change along watercourses, typically rising as the river flows toward the mouth due to sediment

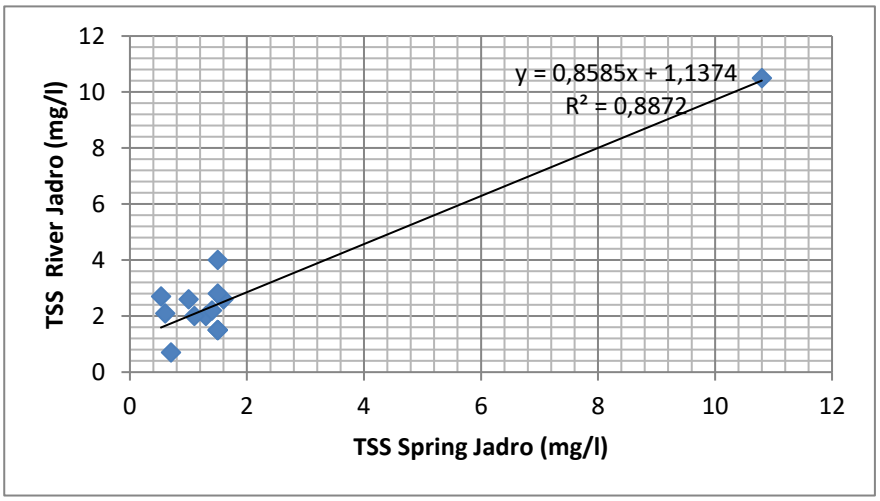

Figure 5.27. Correlation between TSS at spring Jadro and TSS in River Jadro.

contribution from the local morphological basin. So, SSC increased significantly from upstream to the two downstream. Based on the available data for 2014-2016, an analysis of the dependence of TSS at spring and location downstream in the river was made, Figure 5.27.

There is a clear increase in TSS downstream from the source as a result of the inflow of substances from the local topographic basin, ie. the city of Solin, although the increase is not large.

The available number of data is small so this result is only one possible approximation that confirms the expectations. With the increase of urbanization, the concentration of TSS in the lower course of the river (lowlands) will increase even more in relation to the concentration at the spring Jadro. From this it can also be concluded that urbanization will increase all other indicators of water pollution of the river Jadro.

5.2.4.2. TSS and SS load of River Jadro

Based on the available data on turbidity measurement (NTU) and the defined NTU-TSS ratio (Figure 5.25), it is possible to predict TSS loads and dynamic of river Jadro and flux of sediment during the year. In accordance with the established relationship between NTU and TSS at spring Jadro values of TSS were generated for the year 2018, Figure 5.28. It is accepted that the magnitudes of turbidity at profile Majdan and at spring are the same (distance of measuring station Majdan from spring is only 1.3 km).

Using data on the size of the TTS and water flow at the river Jadro at profile / site Majdan (Figure 5.29), the temporal variation of the TSS for the year 2018 was calculated (Figure 5.30).

Estimated annual TSS load, wet period load (October-May) and dry period load (June-September) is presented in Table 5.3. The table shows the results for SS load considering that NTU is a good surrogate for SSC. According to the literature, SSC is higher than turbidity by about 40%.

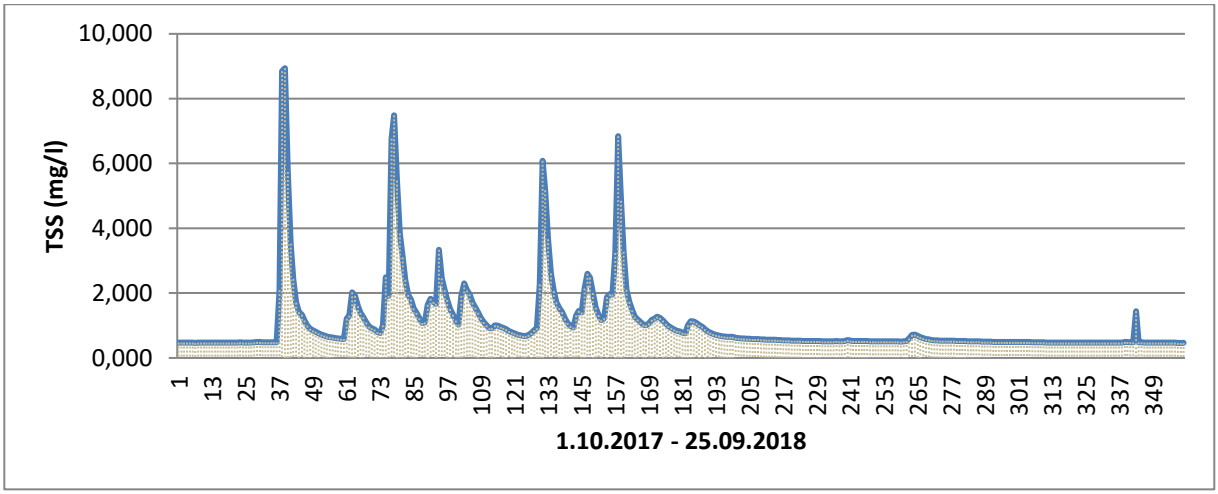

Figure 5.28. The temporal variation of the TSS concentration at spring Jadro for 2018.

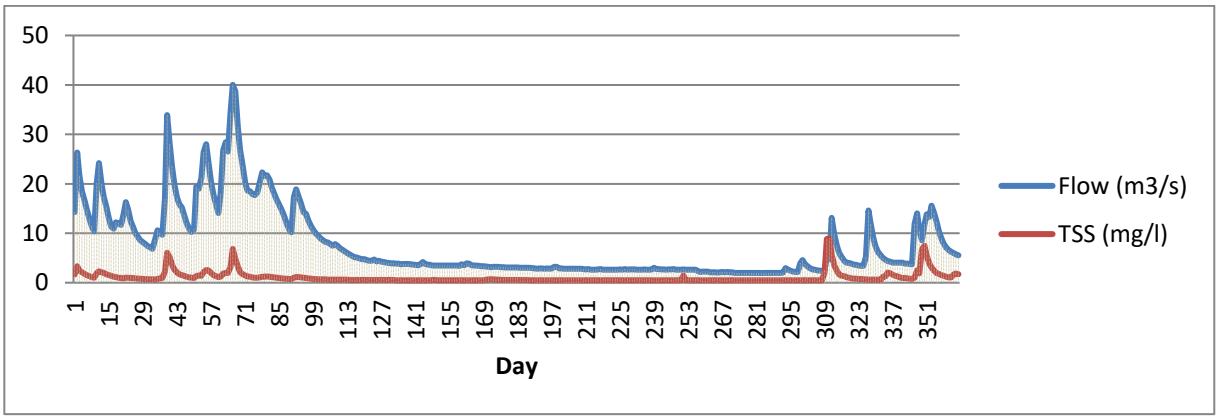

Figure 5.29. The temporal variation of the TSS concentration and water flow of river Jadro at measuring station Majdan for 2018.

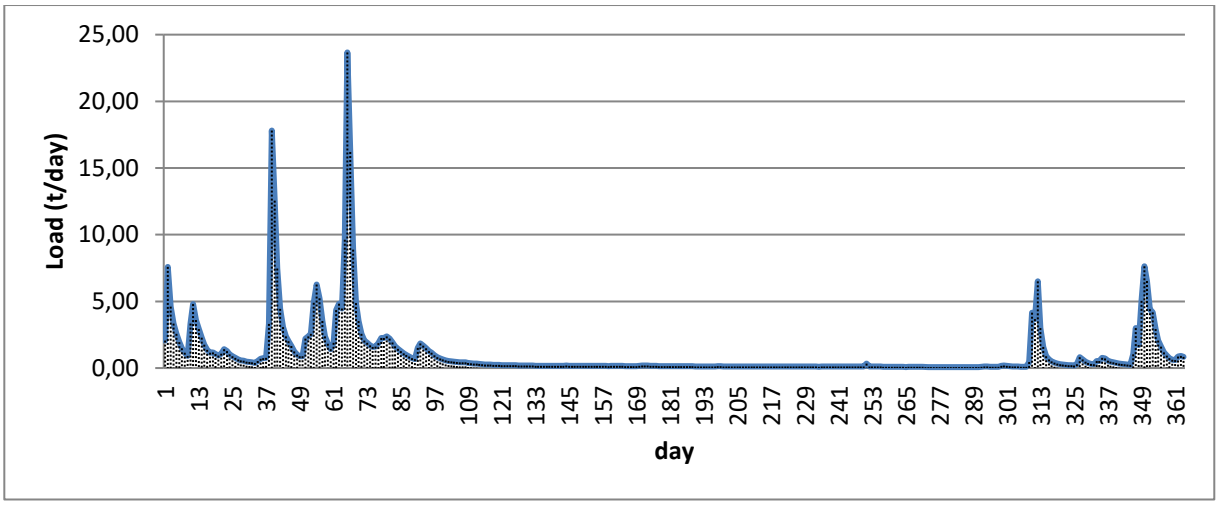

Figure 5.30. Example of the temporal variation of the TSS load of river Jadro at measuring station Majdan for 2018.

Table 5.3. Annual and seasonal sizes SS load and TSS load of river Jadro at measuring station Majdan for 2018.

	SS (tons)	TSS (tons)
Period October-May	526.540 (95.5 %)	376.100 (95.7 %)
Period June-September	23.164 (4.5 %)	16.546 (4.3 %)
Annual	549.704 (100%)	392.646 (100 %)

Table 5.4. Annual and seasonal quantities of SS loads and TSS loads of river Jadro at estuary for 2018 and estimation for Suspended-sand and Suspended-fines loads in tons.

	SS	TSS	Suspended-sand	Suspended-fines
Wet period October-May	783.886 (91.7 %)	559.919 (91.7 %)	223.967	559.919
Dry period June-September	71.551 (8.3 %)	51.107 (8.3 %)	20.443	51.107
Annual	855.437 (100 %)	611.027 (100 %)	244.410	611.027

Analysing the quantities in the wet and dry period (Table 5.3), it is obtained that about 95.5 (%) of annual of SS and TSS loads is discharge into the river in the period October-May, and about 4.3% June - September, which roughly corresponds to the seasonal variation of water quantities.

Since station Majdan is located about 3.5 km upstream from estuary at beginning of urbanized topographic catchment area of river Jadro, estimated loads is lower than at estuary. Using determined dependence between TSS at spring and river estimated load was corrected and estimation for estuary is presented in Table 5.4.

In general, for particle sizes, suspended-fines (sediment smaller than 0.0625 mm) had higher percentages than suspended-sands comprised an appreciable amount of the total suspended-sediment concentration (Elison et al. 2014).

It is assumed that:

- Suspended-fines load ≈ TSS load
- SS load ≈ Suspended-fines load + Suspended-sand load

Analysing the amounts in the wet and dry period (Table 5.4) it is obtained that about 92 % of annual quantities of SS and TSS flow into the sea in the period October-May, and about 8 % June - September.

The obtained quantities are approximate estimate of quantities and their variations over time. Much data is missing for more detailed analyses and estimations. We think that these values can also be used to estimate the order of magnitude of sediment loads and variations during the year. Climate change will change sediment loads. However, the biggest changes will be generated by urbanization processes in the catchment area of spring and river Jadro.

Climate change will change turbidity and thus sediment fluxes in the same way that it will change hydrological quantities. The correlation coefficient is very high and indicates a direct dependence. The character of the change will be the same, so everything said for hydrological values applies to turbidity and sediment too.

5.2.4.3. Conclusion

Under the influence of climate change, the volume of suspended-sediment that will flow into the sea by the river Jadro will gradually increase in winter and in the rest of the year will gradually decrease. The dynamics of the increase depends on the dynamics of climate change and especially precipitation as well as changes in the watershed. Expected increase in precipitation variability will contributes to increased peak streamflows and sediment loads. The increase in winter inflow will be proportional to the increase in precipitation while the decrease in summer inflow will be less than the relative decrease in summer precipitation due to retardation capacity of the aquifer and the size of the indirect catchment area of the Cetina River. Generally speaking, the changes will not be significant for the medium climate change scenario.

Human interventions in the hydrological system of the Jadro River, in the spring watershed area and especially in the topographic of the river downstream from the Jadro spring could have the greatest

impact on the sedimentary load. The topographic basin gradually becomes an urban basin and the water and sediment runoff regime changes significantly as do pollution loads.

In order to obtain more reliable magnitudes o suspended sediment fluxes it is necessary to carry out continuous measurements of the turbidity of the river Jadro on a watercourse where the elevation of the river bottom is around or above geodetic zero. In addition, sampling and analysis of SSC, TSS as well as Turbidity, and measurement of river flow should be performed at that location in order to estimate regression models of SSC and current flow, SSC and NTU, SSC and TSS and Turbidity and SSC in order to define dynamic properties of suspended-sediment fluxes and loads and sizes of suspended-sand and suspended-fines.

5.2.5. Water quality parameters quantities and loads

5.2.5.1. Introduction

The chemical characteristics of stream water depend on its source and the flow path and transit time to the stream. In general, the concentrations of dissolved solids decrease with increasing discharge and increase with the length of the flow path and the amount of time the water has travelled across the landscape. These generalizations are especially true of highly soluble and typically nonbiologically limiting ions—like calcium (Ca^{+2}), magnesium (Mg^{+2}), sodium (Na^{+1}), silica (SiO_2), chloride (Cl^{-1}), bicarbonate (HCO_3^{-1}), and sulfate SO_4^{-2} — associated with chemical weathering. They are also generally true for chemicals derived from point sources that enter streams at relatively constant rates. In contrast, the concentrations of sediment and particulate matter derived from physical detachment and chemicals derived from the flushing of the land surface or shallow subsurface tend to increase with stream discharge and the proportion of surface or storm runoff in the stream as have been determined previously in the report.

Once in the stream, constituents may be transported in solution, in suspension, or attached to particles. Metabolic activity in a stream depends on upstream inputs, internal (algae, aquatic plants), and external (leaves, dissolved organic carbon) sources of food and nutrients.

In the case of a river Jadro, the water first flows over the surface of the terrain in the spring catchment basin, then underground through the karst aquifer and then again by the regulated riverbed to the sea. Since surface flow in spring catchment area (karst hydrological system) is temporary flow only during precipitation period metabolic activities are limited in upper part of basin. The processes affecting dissolved oxygen (DO) are limited and DO concentration at spring is good. The major processes affecting dissolved oxygen (DO) in a stream downstream from spring to the sea are reaeration, carbonaceous and nitrogenous deoxygenation, sediment oxygen demand, and plant photosynthesis and respiration. Period of flow from spring to the sea (transit time) is short, about 1-3 hours, and impact of these processes on DO in the river water is small. Flow is mostly turbulent and reaeration is high while nitrogenous deoxygenation, sediment oxygen demand is small. The main process that takes place is the rapid transport of substances from headwater and lowlands into the sea of Katela Bay.

From headwaters to lowlands, streams change in their morphology, water chemistry, and biotic communities. In downstream areas from spring, the amount of light entering the river, the contribution of ground water and anthropogenic contaminants generally increase. This is area that most affected water quality of the river and sea water. As dissolved constituents are quickly transported downstream to the sea of Kaštela Bay, where they are converted to organic forms and accumulated in organisms until they die and are recycled.

That is why the coastal sea is under the greatest and direct influence of all substances that are quickly transported to the sea by river. The character of substances from headwater and lowland areas to the sea is slightly changed.

5.2.5.2. Water temperature

The water temperature is around 14 °C and varies slightly throughout the year. The flow from the source to the sea (4.41 km) changes depending on the air temperature. The flow lasts on average about 1.5 hours so that the air temperature does not significantly affect the change in temperature of the water flowing into the sea. In summer it is slightly higher around 15-16 °C and in winter slightly lower 14-13 °C.

5.2.5.3. Organic matter

Organic matter characteristic values are shown in Table 5.5. Sampling is carried out periodically in accordance with water quality control regulations and for some parameters every day. There are no continuous measurements so that the pollution load cannot be calculated more precisely. Table 5.5 shows the data from the spring and downstream in the river for the period 2014-2016. These are individual measurements several times a year, a total of 15 for spring and 33 on river.

As it can be seen the water quality downstream from the spring to the mouth is significantly deteriorating. It follows that the topographic catchment area of the river Jadro (City of Solin) contributes much more to the pollution of the river water than the catchment area of the spring although the spring

Table 5.5. Water quality of spring and River Jadro in the period 2014-2016.

Parameter	Spring				River			
	max	average	min	median	max	average	min	median
COD-Mn (mg l^{-1})	1.45	0.62	0.4	0.61	4.57	1.96	O.5	1.42
BOD_5 (mg l^{-1})	3.4	1.2	0.1	0.8	4.19	2.08	0.67	1.06
TSS (mg l^{-1})	10.8	2.0	0.53	1.57	13.5	3.27	0.53	3.23
TN (mg l^{-1})	0.6	0.534	0.372	0.566	1.64	0.80	0.45	0.25
TP (mg l^{-1})	0.027	0.012	0.005	0.015	0.095	0.022	0.003	0.025

catchment area (130 km^2) is much larger than the topographic (28.2 km^2). Such a trend is expected in the future due to the activity of the coastal area and the development of tourism.

The dependence of the concentration and magnitude of the flow or precipitation is not large so that it cannot be used to define the temporal variation of the parameters, Figure 5.31. In addition, there are no significant measurements of the water quality of the Jadro River in the estuary area, so no variation of quality parameters is known due to the influence of the topographic river basin that includes the city of Solin and suburbs of neighbouring administrative units. These impacts are significant especially during precipitation. Therefore, data on water quality are insufficient for a more detailed interpretation of water quality and fluxes of different parameters into Kaštela Bay. If reliable data are to be obtained, it is necessary to conduct multi-year research on water quality, sediment and other parameters, taking into account the hydrological regime of the Jadro River and the variation of urban water flow during the dry and wet period of the year.

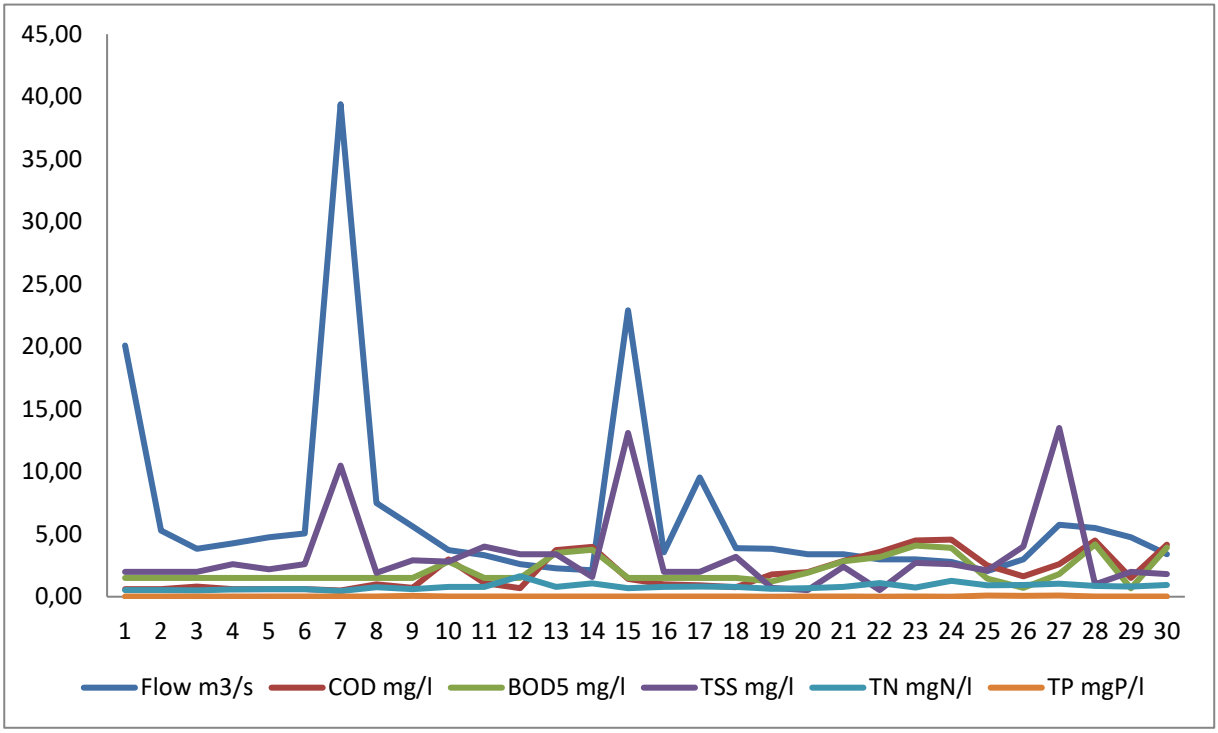

Figure 3.31. River Jadro water quality in the period 2014-2016 (total number of data: 33).

Based on the available data, an analysis will be made to assess the trend of changes and oscillations of the pollution load during the year. Based on older data for the Jadro spring, the dependence analysis was made, ie the correlation coefficient between specific indicators (turbidity, KMnO4, BOD5, N nitrate, phosphorus P) and it was determined that the dependence is very small; the highest for nitrates and turbidity (0.31) and even lower for other indicators.

The calculated correlation coefficients (Table 5.6) show that there is a strong relationship between flow and turbidity, since the correlation coefficient is high (0.85). All other coefficients are very small and statistically insignificant, which indicates the absence of correlation between flow and other parameters.

From the obtained results it can be concluded that the increase in flow does not result in a significant change in water quality parameters BOD_5, COD-Mn, nitrates and total P, since the concentration of parameters does not change. The burden of pollution that is brought into groundwater daily is higher during the period of higher precipitation that washes away the soil, but the dilution is also higher, so the concentration does not increase. However, in this period, increasing the flow significantly increases the turbidity of the water, and to a lesser extent the concentration of nitrates as a result of leaching of the terrain and substances from the groundwater.

Analysing the data for the period 2014-2016, the same conclusions are reached. The correlation between Flow ($m^3\ s^{-1}$) and parameters is only visible for TSS (mg l^{-1}) (0.35) and TN (0.29). It was also obtained that for all parameters except TSS with increasing flow the concentration of the parameter decreases. For measurements on the river in the period 2014-2016, the corresponding loads per day, (t d^{-1}) were calculated for all parameters, and the dependence between loads and flow by linear regression model was analysed. In this case the relations between Flow ($m^3\ s^{-1}$) and different parameters is variable among parameters but significant, Table 5.7. This is quantified with regression model and regression coefficient. Loads are consistently larger with larger flow for each parameter, Table 5.7. Only COD-Mn and flow relation is weak.

Table 5.6. Correlation coefficients and degrees of significance between water quality (organic matter) and flow parameters (1979-2000).

	Turbidity	KMnO4	BPK5	Total N	Total P
Flow	0.8451	-0.0568	-0.0555	0.1896	-0.0472
	N=1096	N=69	N=66	N=69	N=69
	p=0.00	p=0.643	p=0.658	p=0.119	p=0.700

Table 5.7. Regression models between flow (Q) and parameter loads (y) at river Jadro.

	COD-Mn	BOD5	TSS
Regression model (t d^{-1})	y = 0,0435Q + 0,4966 R^2 = 0,3126	y = 0,1217Q + 0,215 R^2 = 0,8952	y = 0,9128Q - 2,8233 R^2 = 0,8424
	TN	TP	
Regression model (t d^{-1})	y = 0,0408Q + 0,119 R^2 = 0,9107	y = 0,0018Q + 0,0005 R^2 = 0,6665	

It follows from the obtained data that the magnitude of water quality parameters loads is controlled by timing, magnitude, and frequency of streamflow, so the periods of the years, as well as years with larger or frequent precipitation events may on occasion generate higher loads during wet seasons.

So, the loads of all analyses parameters will be significantly greater in period October-May than in dry period June-September. Fluxes of parameters can be estimated by linear regression models. However,

linear regression model is *very limited* for karst hydrological system which varied widely among days and years, since it is estimated base on only 33 values of data.

5.2.5.4. Conclusion

Under the influence of climate change the loads of organic matter parameters that will flow into the sea by the river Jadro will gradually increase in winter and in the rest of the year will gradually decrease. The dynamics of the increase depends on the dynamics of climate change and especially precipitation as well as changes in activity in the basin/watershed area. The increase in winter inflow will be proportional to the increase in precipitation and the level of urbanization in the catchment area. Generally speaking, changes from precipitation will not be significant for the medium scenario of climate change. However, the changes will be significant and loads will increase with urban development in the topographic basin of the river which will significantly increase overland flow (or surface flow) and pollution, partly interflow (or subsurface stormflow), and less the ground water flow.

Human interventions in the hydrological system of the Jadro River, in the spring basin and especially in the topographic basin of the river downstream from the Jadro source could have the greatest impact on the load. The topographic basin gradually becomes an urban basin and the runoff regime of water and water quality parameters changes significantly as well as pollution loads.

In order to obtain more reliable quantities of pollution fluxes it is necessary to carry out continuous measurements of the river Jadro on a watercourse where the elevation of the river bottom is around or above geodetic zero. In addition, sampling and analysis of the most important water quality parameters in relation to environmental impacts and measurement of river flow should be carried out regularly at this location in order to define the dynamic properties of pollution fluxes and loads.

5.2.5.5. Heavy metals

Metals are introduced in aquatic systems as a result of the weathering of soils and rocks, from volcanic eruptions, and from a variety of human activities involving the processing, or use of metals and/or substances that contain metal pollutants. The most common heavy metal pollutants are arsenic, cadmium, chromium, cooper, nickel and mercury. So far, we have only been able to collect data for Cu, K and Mn concentration in the river Jadro. In the period 2014-2016 only 29 data were collected. The characteristics of data are shown in Table 5.8.

The main sources of contamination in Jadro River are landfill leaches, municipal wastewater, urban runoff (traffic) and industrial wastewaters, particularly from the electroplating, electronic and metal-finishing industries.

Table 5.8. Characteristic values for Cu, K and Mn.

Parameter	Spring				River			
	max	average	min	median	max	average	min	median
Cu (µg l^{-1})	2,0	0,878	0,224	0,559	2.51	1.0	0.13	0.90
K (mg l^{-1})*	81,0	76,9	71,0	75,5	84.6	73.9	65.7	73.5
Mn (mg l^{-1})	10	6,59	4,29	6,63	9.0	5.46	2.63	5.4

*The data is not reliable

Table 5.9. Regression models between flow (Q) and metal parameter concentration (y) at river Jadro.

	Cu (µgCu l^{-1})	K (mg l^{-1})	Mn (mg l^{-1})
Regression model	y = -0,0148Q + 1,0909 R^2 = 0,0347	y = -0,0999Q + 74,535 R^2 = 0,02	y = -0,1045Q + 6,1361 R^2 = 0,2822

Table 5.10. Regression models between flow (Q) and metal parameter loads (y) at river Jadro.

	Cu	K	Mn
Regression model (t d^{-1})	y = 0,0612Q + 0,0701 R^2 = 0,6608	y = 5,9262Q + 2,4464 R^2 = 0,9935	y = 0,2345Q + 1,001 R^2 = 0,8476

It can be seen that the concentration of metals in the water increases downstream of the source as a result of pollution from the topographic river basin. The differences are not large which shows that most heavy metals come from the headwater basin of the river (spring watershed area) and not from the lowland-topographic river basin. Given the small number of measurements we can only reliably assess general trends.

The dependence between concentration of parameters and flow was analysing by linear regression, Table 5.9.

From the obtained results it can be concluded that the increase in flow decrease concentration of parameters. The chemical characteristics of stream water depend on its source and the flow path and transit time to the stream. In general, the concentrations of dissolved solids decrease with increasing discharge. Length of the flow path and amount of time the water has travelled across the landscape is short and most of the metal fluxes very fast reach the sea.

For measurements on the river in the period 2014-2016, the corresponding loads per day, (t d^{-1}) were calculated for all three parameters, and the dependence between loads and flow by linear regression model was analysed. In this case the relations between Flow (m^3 s^{-1}) and parameters is significant (Table 5.10). This is quantified with regression model and regression coefficient. Loads are consistently larger with larger flow for each parameter (Table 5.10).

It follows from the obtained data that the magnitude of metal parameters loads is controlled by timing, magnitude, and frequency of streamflow, so the periods of the years, as well as years with larger or frequent precipitation events may on occasion generate higher loads during wet seasons.

So, the loads of all analyses parameters will be significantly greater in period October-May than in dry period June-September. Fluxes of parameters can be estimated by linear regression models. However, linear regression model is *very limited* for karst hydrological system which varied widely among days and years, since it is estimated base on only 29 values of data.

The chemical loads of stream water depend on its source and the flow path and transit time to the stream. In general, the loads of dissolved solids increase with increasing discharge. The transient time is short and metal loads reach sea water very quickly. Impact is proportional to the pollution source strength. Flow path of water in karst hydrological system is simple and direct without significant filtration and retardation capacity.

5.2.6. Conclusions and recommendations

Assessment of hydrological and physical quantities of the river Jadro under climate change scenarios is a complex and difficult task. There are several reasons for this, the most important of which are:

Hydrological system of the river Jadro is complex and still insufficiently defined due to the complex configuration and hierarchy of hydrological elements which gradually change under the influence of man.

Most of the hydrological quantities and fluxes are generated by the ground water basin of the spring Jadro and only a smaller topographic catchment area of the river Jadro. However, ground water basin divides are not firmly fixed since surface water divides are fixed by topographic highs and due to the construction of hydroelectric power plants and reservoirs on the river Cetina, there was a limited surface water inflow in karstic aquifers.

In this way the watershed of the spring Jadro was indirectly extended to the river Cetina. That why the components karst surface water/ground water system are in region of fluviokarst and doline karst. The association of these basins in the wet and dry period of the year is not fully known so it is very difficult to study the influence of climate on hydrological quantities and fluxes.

Climate of river Cetina, groundwater basin of spring Jadro and topographic basin of river Jadro are very different so it is difficult to define input into the system (precipitation (P)– evapotranspiration (ET)). For now, climate change forecasts are still general and difficult to apply locally to determine / predict interseasonal and interdecade hydrological magnitudes and fluxes of groundwater (Gw) and surface water (R).

In Dinarid karst region, surface water becomes ground water when it sinks into the streambed and into swallets. After a relatively short stay in the underground karst ground water becomes surface water when it emerges from springs. The springs are of very dynamic discharge and form the headwaters of sizable surface streams. Karst springs are very distinguished features of karst topography due to highly porous aquifers formed in soluble limestone and dolomite rocks. Specific hydrogeological settings are responsible for a very dynamic recharge system manifested in springs highly responsive to rainfall and very sudden and substantial changes in water discharge.

The formed **Jadro watercourse flows** to a lesser extent through the natural catchment of the basin and to a greater extent through the urbanized catchment basin, which is constantly being urbanized. Topographic catchment area and river basin gradually becomes urban basin. Changes in the basin are constant and thus changes in climate and hydrological quantities and fluxes.

The relationship between the trend of changes in the groundwater basin and the topographic basin of the river Jadro has not been studied and is relatively unknown. The topographic basin is small and its area is within the scope of regional climate forecasts and sizes. However, due to the impact of urbanism / city on the local climate, regional climate change needs to be adapted to local characteristics in order to be used for calculations of future hydrological quantities and fluxes. This is especially true for the dry period of the year in which the local ratio (P-ET) changes significantly relative to regional forecasts. For the time being, there are no such modified local climate variables for the area of the topographic river basin Jadro (town of Solin). Therefore, the quantities (Gw) and (R) cannot be calculated / predicted.

In conclusion, there are currently no inputs that could seriously analyse future changes in hydrological quantities and fluxes. Only general guidelines in principle as given in this document can be given. When analysing the quantities and fluxes of sediment and water quality parameters (substances), the situation with the necessary data for analysis is even more unfavorable. Therefore, the quantities and the impact of climate change on them, as well as the relevant quantities and fluxes, cannot be more reliably determined. Only a general overview of the possible state and trend of changes can be made in this document.

Overland, interflow and ground water flow rapidly transferred water and water constituents to river Jadro. Once in river stream, constituents are transported in solution, in suspension, or attached to particles in the sea. The fastest and the most transfer occurred in the wet period of the year. Water in river is short-lived (several hours) and no significant metabolic activity takes place that changes the characteristics of water quality parameters (water chemistry). All substances, as well as sediment, quickly end up in the sea where they are integrated into coastal water metabolic activities. This means that climate change will not have a significant impact on the state of the water in the river itself (fresh water resources). However, the concentrations of sediment and particulate matter derived from physical detachment and chemicals derived from the flushing of the land surface or shallow subsurface tend to increase with stream discharge and the proportion of surface or storm runoff in the stream. This means that any future changes and increases in precipitation will result in a greater impact on the sea. The

greatest loads of substances and sediment will occur during the winter period in days with heavy rains, as much as today.

6. SUMMARY AND CONCLUSIONS

The present report describes the activity performed to address the effects of climate change on hydrological and hydrodynamic processes at the Adriatic basin scale and in Pilot Sites. Predictions for future periods in the 21st century are compared to 'present' (i.e. late 20th century) climate conditions under the IPCC RCP2.6, 4.5 and 8.5 scenarios, in order to assess the climate change impact on the basin ocean properties. First, the study on waves and surges is described, then the attention is devoted to the thermohaline properties and derived variables as the potential density and the ocean heat content.

The projections concerning the wind wave regimes include the assessment of the variations in the significant wave height induced by the climate change in all conditions, and a more specific study of the variations of significant wave height and peak wave period in stormy conditions.

Mean conditions are studied by means of the SWAN modelling system. based on the implementation of a climatological control run for 1971-2000 and a run under the IPCC RCP8.5 climate scenario for 2071-2100. Overall, predicted significant wave height statistics generally consists in a decrease in mean, calm, and storm conditions throughout the basin, but with the exception of an increase in the extreme values along the northeastern coastal regions, associated with the variations in Sirocco wind regimes. This local effect is attributed to higher relative weight of Sirocco with respect to Bora due to a northbound migration of the Mediterranean cyclone tracks.

Stormy conditions are specifically addressed using the AdriSC modelling suite, applied to selected storms occurred in 1979-2019. The present climate conditions are those obtained using the reanalyses, while the future climate conditions are obtained with the Pseudo-Global Warming method, that is adopting projected atmospheric temperatures for 2060-2100 in the RCP4.5 and RCP8.5 scenarios. During Bora events both the significant wave height and the peak wave period are predicted to decrease except in the southern basin under the RCP4.5 scenario. In case of Sirocco storms, under both scenarios a certain decrease is predicted of both significant height and peak period in the northern Adriatic, while both variable are predicted to increase in the rest of the basin. Sirocco-driven storm surges on the norther Adriatic coast are predicted to decrease in height and also to be less frequent.

Thermohaline properties are addressed using two approaches. The first one consists of a multidecadal continuous run performed with ROMS, from which the control period 1976-2005 (present climate) is adopted and two future periods are defined, namely 2020-2049 (Mid-Term Scenario, MTS) and 2070-2099 (Long-Term Scenario, LTS); the RCP8.5 scenario is adopted. The second approach involves the regional coupled model CNRM-RCSM4, with boundary conditions from CNRM-CM5; the control period is 1976-2005, and three future periods are defined, namely 2011-2040, 2041-2070 and 2071-2100.

From the multidecadal ROMS run, a basin-wide increase in SST (by approximately 0.5-1.5 °C in MTS, up to 3 °C in LTS) is found. Also SSS tends to increase (mostly not greater than 0.5), however in the northern basin a slight decrease appears. Considering the seasonal vertical structures of the water masses, projections suggesting that the warming and salinization trends at the surface actually involve the whole

water column. As a result, potential density anomaly is expected to decrease in the northern Adriatic by about 0.1 kg m^{-3} in MTS and 0.3 kg m^{-3} in LTS, with slightly smaller values in the southern basin. Preliminary results suggest that the Ocean Heat Content tends to increase, showing that the Adriatic Sea warming involves the whole water column.

In the regional CNRM-RCSM4 simulation the average SST of the Adriatic is increasing in all scenarios, namely +1.0, 1.7 and 2.7 °C for RCP2.6, 4.5 and 8.5, respectively. However, in scenario RCP2.6 the SST rises until mid-century, and after 2070 it slowly decreases. Salinity is generally predicted to increase in all scenarios. At the end of the century it is from 0.26 (RCP2.6) to 0.71 (RCP8.5) higher than in the control period, however, scenarios RCP2.6 and RCP4.5 exhibit the highest increase by mid-century with 0.64 and 0.58, respectively. Concerning the mixed-layer depth, in the near and middle future term, the RCP2.6 and RCP4.5 scenarios predict more pronounced variability and stronger convection compared to the reference period, while in the far future convective processes weaken. In the RCP8.5 scenario, no events of pronounced deep convection is recorded, with a maximum mixing depth of up to 400 m. The behaviour of the Adriatic-Ionian Bimodal Oscillating System (BiOS) in the future climate was analysed using the simplified BiOS index defined in Gačić et al. (2010). Particularly the RCP4.5 and RCP8.5 scenarios predicts an increase in the index towards the end of the 21st century, suggesting a more frequent occurrence of anticyclonic circulation in the northern Ionian Sea and greater advection of less saline waters from the western Mediterranean to the Adriatic.

A specific high-resolution study relative to the Po Delta Pilot Site is performed with the SHYFEM model under the RCP8.5 scenario. The period modelled covers the 2080-2081 period and represents a synthetic reproduction of the conditions of the years 2010-2011, with forcing obtained by imposing the climate change rate of change of the selected scenario relative to the time period 2080-2100. A water temperature increase is found, from +2-3 °C in winter to +6 °C in summer.

Although different approaches and models are used, the general picture is consistent, namely the Adriatic is likely to became warmer and saltier. Deep convection is expected to be less frequent and a more frequent occurrence of anticyclonic circulation in the northern Ionian Sea should favour the advection of less saline waters from the western Mediterranean into the Adriatic. The wave and storm surges induced by Bora are predicted to be less severe over the whole basin, while the severity of those induced by Sirocco may be expected to decrease in the north and increase in the rest of the Adriatic Sea.

7. REFERENCES

Adloff F, Jordà G, Somot S, et al (2018). Improving sea level simulation in Mediterranean regional climate models. Clim Dyn 51:1167–1178. doi: 10.1007/s00382-017-3842-3.

Androulidakis YS, Kombiadou KD, Makris CV, Baltikas VN, Krestenitis YN (2015). Storm surges in the Mediterranean Sea: Variability and trends under future climatic conditions. Dyn Atmos Oceans 71:56–82. doi: 10.1016/j.dynatmoce.2015.06.001.

Antonioli F, Anzidei M, Amorosi A, Lo Presti V, Mastronuzzi G, Deiana G, De Falco G, Fontana A, Fontolan G, Lisco S, Marsico A, Moretti M, Orrù PE, Sannino GM, Serpelloni E, Vecchio A (2017). Sea-level rise and potential drowning of the Italian coastal plains: Flooding risk scenarios for 2100. Quat. Sci. Rev. 158:29-43. doi: 10.1016/j.quascirev.2016.12.021.

Argueso D, Evans JP, Fita L, Bormann KJ (2014). Temperature response to future urbanization and climate change. Clim Dyn 42:2183–2199. doi:10.1007/s00382-013-1789-6.

Artegiani A, Bregant D, Paschini E, Pinardi N, Raicich F, Russo A (1997). The Adriatic Sea General Circulation. Part I: Air–Sea Interactions and Water Mass Structure. J Phys Oceanogr 27:1492–1514. doi:10.1175/1520-0485(1997)027<1515.

Balsamo G, Albergel C, Beljaars A, Boussetta S, Brun E, Cloke H, Dee D, Dutra E, Muñoz-Sabater J, Pappenberger F, de Rosnay P, Stockdale T, Vitart F (2015). ERA-Interim/Land: a global land surface reanalysis data set. Hydrol Earth Syst Sci 19:389-407. doi:10.5194/hess-19-389-2015.

Ban N, Schmidli J, Schär C (2015). Heavy precipitation in a changing climate: Does short-term summer precipitation increase faster? Geophys Res Lett 42:1165– 1172. doi: 10.1002/2014GL062588.

Bellafiore D, Bucchignani E, Gualdi S, Carniel S, Djurdjević V, Umgiesser G (2012). Assessment of meteorological climate models as inputs for coastal studies. Ocean Dyn 62:555–568. doi:10.1007/s10236-011-0508-2.

Belušić D, Klaić ZB (2006). Mesoscale dynamics, structure and predictability of a severe Adriatic bora case. Meteorol Zeit 15:157–168.

Belušić Vozila A, Güttler I, Ahrens B, Obermann-Hellhund A, Telišman Prtenjak M (2019). Wind over the Adriatic region in CORDEX climate change scenarios. J Geophys Res Atmos 124:110–130. doi:10.1029/2018JD028552

Bencivenga M, Nardone G, Ruggiero F, Calore D (2012). The Italian Data Buoy Network (RON). Advances in Fluid Mechanics IX, WIT Trans Engineering Sciences 74:321–332.

Benetazzo A, Fedele F, Carniel S, Ricchi A, Bucchignani E, Sclavo M (2012). Wave climate of the Adriatic Sea: A future scenario simulation. Nat. Hazards Earth Syst. Sci. 12:2065–2076. doi:10.5194/nhess-12-2065-2012.

Bernstein L, Bosch P, Canziani O, Chen Z, Christ R, Riahi K (2008). IPCC, 2007: Climate Change 2007: Synthesis Report. Geneva. ISBN 2-9169-122-4.

Bertotti L, Bidlot J-R, Buizza R, Cavaleri L, Janousek M (2011). Deterministic and ensemble-based prediction of Adriatic Sea sirocco storms leading to 'acqua alta' in Venice. Q J R Meteorol Soc 137:1446-1466. doi:10.1002/qj.861.

Beuvier J, Sevault F, Herrmann M, Kontoyiannis H, Ludwig W, Rixen M, Stanev E, Béranger K, Somot S (2010). Modeling the Mediterranean Sea interannual variability during 1961–2000: Focus on the Eastern Mediterranean Transient. J Geophys Res Atmos 115:C08017. doi:10.1029/2009JC005950.

Bonaldo, D, Bucchignani, E, Pomaro, A, Ricchi, A, Sclavo, M, Carniel, S (2020). Wind waves in the Adriatic Sea under a severe climate change scenario and implications for the coasts. Int J Climatol 2020:1-18. doi:10.1002/joc.6524.

Bonaldo D, Orlić M, Carniel S (2018). Framing Continental Shelf Waves in the southern Adriatic Sea, a further flushing factor beyond dense water cascading. Scientific Reports 8:660. doi:10.1038/s41598-017-18853-2.

Bonaldo D, Bucchignani E, Ricchi A, Carniel S (2017). Wind storminess in the Adriatic Sea in a climate change scenario. Acta Adriatica, 58(2):195–208.

Booij N, Ris RC, Holthuijsen LH (1999). A third-generation wave model for coastal regions, Part I, Model description and validation. J. Geophys. Res. 104:7649-7656.

Brogli R, Sørland SL, Kröner N, Schär C (2019a). Causes of future Mediterranean precipitation decline depend on the season. Environ Res Lett 14:114017. doi:10.1088/1748-9326/ab4438.

Brogli R, Kröner N, Sørland SL, Lüthi D, Schär C (2019b). The role of Hadley circulation and lapse-rate changes for the future European summer climate. J Clim 32:385–404. doi:10.1175/JCLI-D-18-0431.1.

Bucchignani E, Montesarchio M, Zollo AL, Mercogliano P (2016). High-resolution climate simulations with COSMO-CLM over Italy: Performance evaluation and climate projections for the 21st century. Int J Climatol 36(2):735-756. doi:10.1002/joc.4379.

Buongiorno Nardelli B, Tronconi C, Pisano A, Santoleri R (2013). High and Ultra-High resolution processing of satellite Sea Surface Temperature data over Southern European Seas in the framework of MyOcean project. Remote Sensing of Environment, 129: 1–16. doi:10.1016/J.RSE.2012.10.012.

Cavaleri L (2000). The oceanographic tower Acqua Alta activity and prediction of sea states at Venice. Coastal Eng 39(1):29–70. doi:10.1016/S0378-3839(99)00053-8.

Cavaleri L, Bertotti L, Buizza R, Buzzi A, Masato V, Umgiesser G, Zampieri M (2010). Predictability of extreme meteo-oceanographic events in the Adriatic Sea. Q J R Meteorol Soc 136:400–413. doi:10.1002/qj.567.

Conte D, Lionello P (2013). Characteristics of large positive and negative surges in the Mediterranean Sea and their attenuation in future climate scenarios. Global and Planetary Change 111:159-173.

Cushman-Roisin B, Gačić M, Poulain P-M, Artegiani A (2001). Physical Oceanography of the Adriatic Sea: Past, Present and Future. Springer, New York, 304 pp.

Darmaraki S, Somot S, Sevault F, Nabat P (2019). Past variability of Mediterranean Sea marine heat-waves. Geophys. Res. Lett., 46, 9813–9823. doi: 1029/2019GL082933.

Denamiel C, Šepić J, Ivanković D, Vilibić I (2019). The Adriatic Sea and Coast modelling suite: Evaluation of the meteotsunami forecast component. Ocean Model 135:71–93. doi:10.1016/j.ocemod.2019.02.003.

Dietrich JC, Tanaka S, Westerink JJ, et al (2012). Performance of the Unstructured-Mesh, SWAN+ADCIRC Model in computing hurricane waves and surge. J Sci Comput 52:468–497. doi:10.1007/s10915-011-9555-6.

Elison CA, Savage BE, Johnson GD (2014). Suspended-sediment Concentration, Loads, Total Suspended Solid, Turbidity, and Particle-size Fractions for selected Rivers in Minnesota, 2007 through 2011. USGS Scientific Investigation Report 2013-5205. USA.

Fosser, G, Khodayar S, Berg P (2016). Climate change in the next 30 years: what can a convection-permitting model tell us that we did not already know? Clim Dyn 48:1987–2003. doi:10.1007/s00382-016-3186-4.

Gačić M, Borzelli GLE, Civitarese G, Cardin V, Yari S (2010). Can internal processes sustain reversals of the ocean upper circulation? The Ionian Sea example. Geophys Res Lett 37, L09608. doi:10.1029/2010GL043216.

Giorgi F, Lionello P (2008). Climate change projections for the Mediterranean region. Global Planet Change 63:90-104.

Giorgi F, Jones C, Asrar GR (2009). Addressing climate information needs at the regional level: the CORDEX framework. *WMO Bull.* 58:175–83. doi: 10.1146/annurev-environ-102014-021217.

Giorgi F, Gutowski WJ (2015). Regional Dynamical Downscaling and the Cordex Initiative. Ann. Rev. Environ. Res. 40:467-490. doi: 10.1146/annurev-environ-102014-021217.

Gohm A, Mayr GJ, Fix A, Giez A (2008). On the onset of bora and the formation of rotors and jumps near a mountain gap. Q J R Meteorol Soc 134:21–46.

Göppert N, Goldscheider N (2008). Solute and Colloid Transport in Karst Conduits under Low- and High-Flow Conditions, Ground Water, 46 (1):61–68.

Grisogono B, Belušić D (2009). A review of recent advances in understanding the meso- and microscale properties of the severe Bora wind. Tellus A 61:1–16. doi:10.1111/j.1600-0870.2008.00369.x.

Gualdi S, Somot S, Li L, Artale V, Adani M, Bellucci A, Braun A, Calmanti S, Carillo A, Dell'Aquila A, Déqué M, Dubois C, Elizalde A, Harzallah A, Jacob D, L'Hévéder B, May W, Oddo P, Ruti P, Sanna A, Sannino G, Scoccimarro E, Sevault F, Navarra A (2013). The CIRCE simulations: Regional climate change projections with realistic representation of the Mediterranean Sea. Bull Am Meteor Soc 94:65–81. doi:10.1175/BAMS-D-11-00136.1.

Haidvogel, D. B., Arango, H., Budgell, et al (2008). Ocean forecasting in terrain-following coordinates: Formulation and skill assessment of the Regional Ocean Modeling System. J Comput Phys, 227(7):3595–3624. doi:10.1016/j.jcp.2007.06.016.

Hartmann A, Goldscheider N, Wagener T, Lange J, Weiler M (2014). Karst water resources in a changing world: Review of hydrological modelling approaches, Rev. Geophys., 52:218–242, doi:10.1002/2013RG000443.A.

Hintze HL, Nelson RD (1998). Violin plots: A box plot-density trace synergism. Am Stat 52(2):181–184. doi:10.1080/00031305.1998.10480559.

Horvath K, Ivatek-Šahdan S, Ivančan-Picek B, Grubišić V (2009). Evolution and Structure of Two Severe Cyclonic Bora Events: Contrast between the Northern and Southern Adriatic. Weather and Forecasting, 24(4), 946–964. doi:10.1175/2009WAF2222174.1.

Hourdin F, Musat I, Bony S et al (2006). The LMDZ4 general circulation model: climate performance and sensitivity to parametrized physics with emphasis on tropical convection. Clim Dyn 27:787–813. doi:10.1007/s00382-006-0158-0.

Janeković I, Mihanović H, Vilibić I, Tudor M (2014). Extreme cooling and dense water formation estimates in open and coastal regions of the Adriatic Sea during the winter of 2012. J Geophys Res Oceans 119:3200–3218, doi:10.1002/2014JC009865.

Jenkins C, Trincardi F, Hatchett L, Niedoroda A, Goff J, Signell R, McKinney K (2005). http://instaar.colorado.edu/~jenkinsc/dbseabed/coverage/adriaticsea/adriatico.htm

Jiang Q, Doyle JD (2005). Wave breaking induced surface wakes and jets observed during a bora event. Geophys Res Lett 32:L17807. doi:10.1029/2005GL022398.

Jordà G, Gomis D (2013). On the interpretation of the steric and mass components of sea level variability: The case of the Mediterranean basin. J Geophys Res Oceans 118:953– 963. doi:10.1002/jgrc.20060.

Jurčec V, Ivančan-Picek B, Tutiš V, Vukičević V (1996). Severe Adriatic jugo wind. Meteor Z 5:67–75.

Kendon EJ, Fowler HJ, Roberts MJ, Chan SC, Senior CA (2014). Heavier summer downpours with climate change revealed by weather forecast resolution model. Nat Clim Change 4:570–576. doi:10.1038/nclimate2258.

Kendon EJ, Ban N, Roberts NM, Fowler HJ, Roberts MJ, Chan SC, Evans JP, Fosser G, Wilkinson JM (2017). Do convection-permitting regional climate models improve projections of future precipitation change? Bull Am Meteor Soc 98:79–93. doi:10.1175/BAMS-D-15-0004.1.

Komen GJ, Hasselmann S, Hasselmann K (1984). On the existence of a fully developed wind-sea spectrum. J Phys Oceanogr 14:1271-1285.

Kröner N, Kotlarski S, Fischer E et al (2017). Separating climate change signals into thermodynamic, lapse-rate and circulation effects: theory and application to the European summer climate. Clim Dyn 48:3425–3440. doi:10.1007/s00382-016-3276-3.

Kuzmić M, Janeković I, Ivančan-Picek B, Trošić T, Tomažić I (2005). Severe northeastern Adriatic bura events and circulation in greater Kvarner region. Croat Meteorol J 40:320–323.

Leder N, Smirčić A, Vilibić I (1998). Extreme values of surface wave heights in the Northern Adriatic. Geofizika 15:1–13.

Lipizer M, Partescano E, Rabitti A, Giorgetti A, Crise A (2014). Qualified temperature, salinity and dissolved oxygen climatologies in a changing Adriatic Sea. Ocean Sci. 10, 771-797. doi:10.5194/os-10-771-2014.

Lionello P, Cavaleri L, Nissen K, Pino C, Raicich F, Ulbrich U (2012a). Severe marine storms in the northern Adriatic: characteristics and trends. Phys. Chem. Earth A/B/C 40-41:93–105. doi:10.1016/j.pce.2010.10.002.

Lionello P, Galati MB, Elvini E (2012b). Extreme storm surge and wind wave climate scenario simulations at the Venetian littoral. Phys Chem Earth 40-41:86–92. doi:10.1016/j.pce.2010.04.001.

Macias D, Stips A, Garcia-Gorriz E, Dosio A (2018). Hydrological and biogeochemical response of the Mediterranean Sea to freshwater flow changes for the end of the 21st century. PLoS ONE 13(2): e0192174. doi:10.1371/journal.pone.0192174.

Madsen OS, Poon Y-K, Graber HC (1988). Spectral wave attenuation by bottom friction: Theory. Proceedings of the 21th International Conference on Coastal Engineering, ASCE 492–504.

Marcos M, Jordà G, Gomis Bosch D, Pérez Gómez B (2011). Changes in storm surges in southern Europe from a regional model under climate change scenarios. Glob. Planet. Change 77:116-128. doi: 10.1016/j.gloplacha.2011.04.002.

Margeta J, Fistanić I (2004). Water quality modelling of Jadro spring, Water Science and Technology, 50 (11):59-66.

Massei N, Dupont J, Mahler B, Laignel B, Fournier M., Valdes D, Ogier S (2006). Investigating transport properties and turbidity dynamics of a karst aquifer, Journal of Hydrology 329:244– 257.

Međugorac I, Pasarić M, Orlić M (2015). Severe flooding along the eastern Adriatic coast: the case of 1 December 2008. Ocean Dyn 65:817–830. doi:10.1007/s10236-015-0835-9.

Meehl GA, Stocker TF, Collins WD, Friedlingstein P, Gaye AT, Gregory JM, Kitoh A, Knutti R, Murphy JM, Noda A, Raper SCB, Watterson IG, Weaver AJ, Zhao Z-C (2007). Global Climate Projections. In: Climate Change 2007: The Physical Science Basis. Contribution of Working Group I to the Fourth Assessment Report of the Intergovernmental Panel on Climate Change. Solomon S, Qin D, Manning M, Chen Z, Marquis M, Averyt KB, Tignor M, Miller HL (eds.). Cambridge University Press, Cambridge, UK and New York, NY, USA.

Milanović, P. 2004. Water resources engineering in karst. CRC Press, London.

Pan L-L, Chen S-H, Cayan D, Lin M-Y, Hart Q, Zhang M-H, Liu Y, Wang J (2011). Influences of climate change on California and Nevada regions revealed by a high-resolution dynamical downscaling study. Clim Dyn 37:2005–2020. doi:10.1007/s00382-010-0961-5.

Parker BB (1991). The Relative Importance of the various nonlinear mechanisms in a wide range of tidal interaction (review). Tidal Hydrodynamics, Wiley, New York 237–268 pp.

Pasarić M, Orlić M (2004). Meteorological forcing of the Adriatic: present vs. projected climate conditions. Geofizika 21:69–86.

Penzar B, Penzar I, Orlić M (2001). Vrijeme i klima hrvatskog Jadrana. Nakladna kuća 'Dr. Feletar', Zagreb, 258 pp.

Pinardi N, Allen I, Demirov E, De Mey P, Korres G, Lascaratos A, Le Traon P-Y, Maillard C, Manzella G, Tziavos C (2003). The Mediterranean ocean Forecasting System: first phase of implementation (1998-2001). Ann Geophys 21:3–20. doi:10.5194/angeo-21-3-2003.

Pisano A, Buongiorno Nardelli B, Tronconi C, Santoleri R (2016). The new Mediterranean optimally interpolated pathfinder AVHRR SST Dataset (1982–2012). Remote Sens Environ 176:107–116. doi:10.1016/J.RSE.2016.01.019.

Poje D (1992). Wind persistence in Croatia. Int J Climatol 12:569–586.

Pomaro A, Cavaleri L, Lionello P (2017). Climatology and trends of the Adriatic Sea wind waves: analysis of a 37-year long instrumental data set. Int J Climatol 37:4237-4250. doi:10.1002/joc.5066.

Pomaro A, Cavaleri L, Papa A, Lionello P (2018). Data Descriptor: 39 years of directional wave recorded data and relative problems, climatological implications and use. Scientific Data 5:1–12.

Prein AF, Langhans W, Fosser G, et al (2015). A review on regional convection-permitting climate modeling: Demonstrations, prospects and challenges. Rev Geophys 53:323–361. doi:10.1002/2014RG000475.

Raicich F (1994). Note on the flow rates of the Adriatic rivers. Tech. Rep. 561 RF 02/94, CNR Istituto Sperimentale Talassografico, Trieste.

Raicich F (2015). Long-term variability of storm surge frequency in the Venice Lagoon: an update thanks to 18th century sea level observations. Nat Hazards Earth Syst Sci 15:527–535. doi:10.5194/nhess-15-527-2015.

Raicich F, Colucci RR (2019). A near-surface sea temperature time series from Trieste, northern Adriatic Sea (1899-2015). Earth Sys Sci Data 11(2):761–768. doi:10.5194/essd-11-761-2019.

Rasmussen R, Liu C, Ikeda K, Gochis D, Yates D, Chen F, Tewari M, Barlage M, Dudhia J, Yu W, Miller K, Arsenault K, Grubišić V, Thompson G, Gutmann E (2011). High-resolution coupled climate runoff simulations of seasonal snowfall over Colorado: A process study of current and warmer climate. J Clim 24:3015–3048. doi:10.1175/2010JCLI3985.1.

Rasmussen R, Ikeda K, Liu C, Gochis D, Clark M, Dai A, Gutmann E, Dudhia J, Chen F, Barlage M, Yates D, Zhang G (2014). Climate change impacts on the water balance of the Colorado headwaters: High-resolution regional climate model simulations. J Hydrometeor 15:1091–1116. doi:10.1175 /JHM-D-13-0118.1.

Ravdas M, Zacharioudaki A, Korres G (2018). Implementation and validation of a new operational wave forecasting system of the Mediterranean Monitoring and Forecasting Centre in the framework of the Copernicus Marine Environment Monitoring Service. Nat Hazards Earth Syst Sci 18:2675–2695. doi:10.5194/nhess-18-2675-2018.

Robinson AR, Tomasin A, Artegiani A (1973). Flooding of Venice: Phenomenology and prediction of the Adriatic Sea storm surge. Q J R Meteorol Soc 99:688–692. doi:10.1002/qj.49709942210.

Rockel B, Will A, Hense A (2008). The regional Climate Model COSMO-CLM (CCLM). Meteorol Zeit 17: 347–348. doi:10.1127/0941-2948/2008/0309.

Ruti PM, Somot S, Giorgi F, et al (2016). Med-CORDEX initiative for Mediterranean climate studies. Bull Am Meteorol Soc 97:1187–1208. doi:10.1175/BAMS-D-14-00176.1.

Schär C, Frei C, Luthi D, Davies HC (1996). Surrogate climate-change scenarios for regional climate models. Geophys Res Lett 23:669–672.

Schindler Wildhaber Y, Michel C, Burkhardt-Holm P, Bänninger D, Alewell C (2012). Measurement of spatial and temporal fine sediment dynamics in a small river, Hydrol. Earth Syst. Sci., 16:1501–1515, doi:10.5194/hess-16-1501-2012.

Signell RP, Carniel S, Cavaleri L, Chiggiato J, Doyle JD, Pullen J, Sclavo M (2005). Assessment of wind quality for oceanographic modelling in semi-enclosed basins. J Mar Sys 53:217–233. doi:10.1016/j.jmarsys.2004.03.006.

Sikirić MD, Janeković I, Kuzmić M (2009). A new approach to bathymetry smoothing in sigma-coordinate ocean models. Ocean Modelling 29(2):128–136. doi:10.1016/j.ocemod.2009.03.009.

Simoncelli S, Fratianni C, Pinardi N, Grandi A, Drudi M, Oddo P, Dobricic S (2019). Mediterranean Sea Physical Reanalysis (CMEMS MED-Physics) [Data set]. Copernicus Monitoring Environment Marine Service (CMEMS). doi:10.25423/MEDSEA_REANALYSIS_PHYS_006_004.

Somot S, Sevault F, Déqué M (2006). Transient climate change scenario simulation of the Mediterranean Sea for the twenty-first century using a high-resolution ocean circulation model. Clim. Dyn. 27:851–879. doi:10.1007/s00382-006-0167-z.

Soomere T, Bishop SR, Viska M, Raametm A (2015). An abrupt change in winds that may radically affect the coasts and deep sections of the Baltic Sea. Clim Res 62(2):163–171.

Steppeler J, Doms G, Schättler U, Bitzer HW, Gassmann A, Damrath U, Gregoric G (2003). Meso-gamma scale forecasts using the nonhydrostatic model LM. Meteor Atmos Phys 82:75-96. doi:10.1007/s00703-001-0592-9.

Tolle MH, Gutjahr O, Busch G, Thiele JC (2014). Increasing bioenergy production on arable land: Does the regional and local climate respond? Germany as a case study. J Geophys Res Atmos 119:2711–2724. doi:10.1002/2013JD020877.

Trenberth KE, Dai A, Rasmussen RM, Parsons DB (2003). The Changing Character of Precipitation. BAMS 84 (9), 1205-1217.

Trošić T (2015). The onset of a severe summer bora episode near Oštarijska Vrata Pass in the Northern Adriatic. Meteorol Atmos Phys 127: 649–658. doi:10.1007/s00703-015-0393-1.

Tsimplis M, Marcos M, Somot S, Barnier B (2008). Sea level forcing in the Mediterranean Sea between 1960 and 2000. Global Planet Change 63(4):325–332. doi:10.1016/j.gloplacha.2008.07.004.

Umgiesser G, Ferrarin C, Cucco A, De Pascalis F, Bellafiore D, Ghezzo M, Bajo M (2014). Comparative hydrodynamics of 10 Mediterranean lagoons by means of numerical modeling. J. Geophys. Res. Oceans, 119(4):2212–2226.

Vilibić I, Šepić J, Proust N (2013). Weakening thermohaline circulation in the Adriatic Sea. Clim Res 55(3): 217–225. doi:10.3354/cr01128.

Warner JC, Armstrong B, He R, Zambon, JB (2010). Development of a Coupled Ocean-Atmosphere-Wave-Sediment Transport (COAWST) modeling system. Ocean Model 35:230–244.

Zuliani A, Zaggia L, Collavini F, Zonta R (2005). Freshwater discharge from the drainage basin to the Venice Lagoon (Italy). Environment International. doi:10.1016/j.envint.2005.05.004.